Effect of Surface State on Radiative Properties of Advanced High Strength Steel Strips

by

Kaihsiang Lin

A thesis

presented to the University of Waterloo

in fulfillment of the

thesis requirement for the degree of

Doctor of Philosophy

in

Mechanical and Mechatronics Engineering

Waterloo, Ontario, Canada, 2021

Examining Committee Membership

The following served on the Examining Committee for this thesis. The decision of the Examining Committee is by majority vote.

External examiner	Liping Wang Associate Professor
Supervisor	Kyle. J. Daun Professor
Internal member	Elizabeth Weckman Professor
Internal member	Elliot Biro Assistant Professor
Internal-external member	Irene Goldthorpe Associate Professor

Author's Declaration

I hereby declare that I am the sole author of this thesis. This is a true copy of the thesis, including any required final revisions, as accepted by my examiners.

I understand that my thesis may be made electronically available to the public.

Abstract

Automotive manufacturers increasingly turn to light-weighting through galvanized advanced high strength steels (AHSS) to improve fuel efficiency and reduce pollutant emissions without compromising passenger safety. Unfortunately, Canadian steel manufacturers report unacceptably high AHSS rejection rates due to substandard mechanical properties, both in terms of strength and zinc layer adhesion. Much of the issue can be traced back to temperature excursions during intercritical annealing, caused by improper heating control and errors in the pyrometrically-inferred temperatures used to control the furnaces. These errors, in turn, originate from the changing surface state of the steel strip, in terms of roughness and oxide formation, during thermal processing. This causes issues of steel heating control and wavelength-dependent variations in spectral emissivity, which are unaccounted for in the pyrometry measurement model.

A large number of studies have been performed on correlating the surface state (e.g. oxide, roughness) and radiative properties of metals in the context of electromagnetic wave (EM) theory. The exact EM solution, along with other more approximate physical models, have been investigated to deal with the issue. Nevertheless, most of these studies are restricted to the modeling of bi-directional radiative properties, instead of wavelength-dependent spectral emissivity, which is critical to the improvement of heating control and pyrometry measurement. In addition, very few of these studies are related to AHSS, while none of them have been performed on correlating the surface state with radiative properties of AHSS subject to different alloy compositions and annealing conditions. As a consequence, the physical correlation between the surface state and radiative properties of AHSS still remain unclear.

This study aims to improve the robustness of industrial pyrometry measurement and heating control of AHSS during continuous galvanizing, by determining how spectral emissivity depends on surface state, AHSS alloy composition, and annealing atmosphere. To achieve this, the relationship between AHSS surface topography and spectral emissivity is elucidated in the context of EM wave theory. First, the correlation between the surface roughness and radiative properties of several as-received and oxidized AHSS samples are investigated using the Davies' model with wavelet-filtering technique. Secondly, the radiative properties of as-received AHSS having different surface topographies are interpreted using geometric optics approximation (GOA) ray tracing and EM diffraction models. Finally, the effect of alloy composition and annealing atmosphere on selective oxidation and radiative properties of AHSS having polished and as-received substrate states are interpreted *via* the thin film interference model and a hybrid thin film/geometric optics model, respectively.

It is found that the geometric optics ray tracing can effectively predict the spectral emissivity of as-received AHSS within its validity domain. These findings will be useful for improving heating control *via* a correlation between the spectral absorptivity, heat absorption, and the roughness profile of the surface. The thin film interference model is applicable to the estimation of spectral emissivity of samples annealed in their smooth state. This provides a potential means to understand oxide formation kinetics in-situ through optical measurements during annealing, as well as to improve pyrometry measurements. The hybrid thin film/geometric optics model, however, is unable to capture the spectral emissivity of oxidized samples having rough states. This highlights the need for a more rigorous model which accounts for the complex oxide profile upon the rough substrate, and the complex wave interference mechanism underlying that scenario.

This research provides valuable insights into the development of an *in-situ* emissivity model during annealing that can be used to improve pyrometry measurement and heating control for industrial continuous galvanizing lines.

Acknowledgements

The completion of this thesis would not have been possible without the help of numerous people.

First of all, I would like to sincerely thank my supervisor, Professor Kyle Daun, for his continuous support throughout my PhD study. His constructive ideas, comments and insights are always helpful. Under his guidance, my research ability, presentation skill, knowledge, and field of vision have been improved. His supervision has also led me toward an independent researcher myself. For me, he is a benevolent supervisor, a heartful mentor, a true friend that have accompanied me and helped me grow substantially in the past four years. From the bottom of my heart, I much appreciate the opportunity to experience the life here and the chance to work among a friendly, talented team under his leadership. I would also never forget the delightful moments when we were taking the nice hiking tours together around the "mysterious, but splendid" trails.

I would also like to thank my fellow researchers and colleagues from Waterloo Laboratory for Inverse Analysis and Thermal Sciences (WatLIT), for their valuable feedbacks, suggestions, accompanies and friendships. To name just a few: Sina Moghaddam, Rodrigo Miguel, Fatima Suleiman, Roger Tsang, Stephen Robinson-Enebeli, Cameron Klassen, Tom Zhao, Stanislav Musikhin, Tim Sipkens, Samuel Grauer, Weizhi Zhu, Mohit Verma, Cory Yan, Nishant Narayanan, Arpan Singh, Michael Nagorski, and Nigel Singh.

Of particular note, thanks to Fatima Suleiman, and Nishant Narayanan, for their contribution and participation in the research project. Their engagements in the meetings and discussions have been so beneficial to this research topic.

Many thanks to Prof. Joseph McDermid and Dr. Maedeh Pourmajidian from McMaster University. I am much grateful to their help on the sample annealing and oxide thickness

measurement as part of the task depicted in this thesis, as well as their supportive ideas and remarkable insight regarding to selective oxidation. Their expertise in this field had been considerably influential and helpful.

Special thanks to Prof. Myriam Brochu and her research team from Polytechnique Montréal, for their helpful discussion on the research progress through the GAP meetings which often came with inspiring thoughts with respect to the direction of the research.

Also, I would like to thank Dr. Frank Goodwin from International Zinc Association, for his valuable feedbacks and advice during the Galvatech meetings. And I would like to thank Thomas Larrick from Williamson as well, for his beneficial thoughts and advice on the pyrometry measurement. Also, thanks to Dr. Joyce C. Niedringhaus from AK steel, for her supportive ideas and her invitation to the tour of industry, and thanks to Christopher Martin-Root from Stelco, for his continuous support on the research project.

I would also like extend thanks to the members of my examination committee, including Prof. Kyle Daun, Prof. Elizabeth Weckman, Prof. Elliot Biro, Prof. Irene Goldthorpe, and Prof. Liping Wang. Your willingness to review and comment on this thesis is greatly appreciated.

Special thanks to Frédéric Chopin, whose musical work: *Piano Sonata No. 3 in B minor, Op. 58,* has consistently brought me immense mental strength and confidence over these years.

Finally, I would like to thank my family for their never-ending support. Your love is important for me to complete this not-so-easy work. I am sincerely grateful to what all you have done over these years.

Dedication

To my parents,

Jinwen Lin and Lipin Chen

Table of Contents

Examining Committee Membership ii
Author's Declaration iii
Abstract iv
Acknowledgements vii
Dedication ix
List of Figures and Tables xiii
List of Figures xiii
List of Tables xix
Nomenclature xx
List of Abbreviations xxvii
Chapter 1 Background 1
1.1 Introduction to AHSS 1
1.2 Continuous galvanizing line 2
1.3 Existing issue regarding to temperature control in industry 5
1.4 Objectives 6
1.5 Organization of the thesis 6
Chapter 2 Selective Oxidation and Principles of Pyrometry 8
2.1 Influence of selective oxidation on AHSS 8
2.2 Principle of pyrometry 15
Chapter 3 EM Theories and Models 23
3.1 Surface roughness parameters 24
3.2 Thin film effect 27
3.3 Surface roughness effect 30
3.3.1 Agababov model 33
3.3.2 Fractal theory 35
3.3.3 Definition of directional reflectances 39
3.3.4 Kirchhoff-Helmholtz diffraction theory 40
3.3.5 Criterion of Kirchhoff approximation 43
3.3.6 Davies' and Beckman's model 44
3.3.7 Criterion for rough surfaces 47
3.3.8 Geometric optics approximation 49

3.3.9 Kirchhoff EM diffraction models 55
3.4 Hybrid thin film/roughness effect 57
Chapter 4 Interpreting the Spectral Reflectance of Advanced High Strength Steels using the Agababov and Davies' Model 63
4.1 Introduction 63
4.2 Sample preparation and measurement 66
4.3 Radiation properties of annealed samples 72
4.4 Results and discussion 74
4.4.1 Agababov model 74
4.4.2 Criterion of Kirchhoff approximation 75
4.4.3 Comparison of optically-derived and wavelet-filtered surface roughness 76
4.4.4 Comparisons of reflectance predictions and measurements 82
4.5 Conclusions 86
Chapter 5 Interpreting the Radiative Properties of Advanced High Strength Steel using the Geometric Optics Ray-tracing Approximation 88
5.1 Introduction 88
5.2 Sample preparation and measurement 92
5.3 Results and discussion 96
5.3.1 AFM and optical profiler surfaces, Kirchhoff criterion 96
5.3.2 Measured directional-hemispherical reflectances 98
5.3.3 Comparison of 1-D and 2-D GOA modeling, incident azimuthal angle effect 100
5.3.4 Reflectance measurements and predictions using GOA and diffraction models 103
5.3.5 Comparison of 1-D and 2-D bi-directional functions 109
5.4 Conclusions 110
Chapter 6 Effect of Annealing Atmosphere and Steel Alloy Composition on Oxide Formation and Radiative Properties of Advanced High Strength Steel Strip 112
6.1 Introduction 112
6.2 Sample preparation and measurement 118
6.3 Refractive indices of Fe and MnO 122
6.4 Results and discussion 123
6.4.1 Microscopy and optical profilograms 123
6.4.2 Measured reflectance of samples having polished and rough state 126
6.4.3 Scanning electron micrographs, measured refractive indices of oxides 127
6.4.4 Comparison of thin film interference predictions and measurements 130

6.5 Conclusions 133

Chapter 7 Interpreting the Radiative Properties of Advanced High Strength Steel Strip using Hybrid Thin Film/Geometric Optics Model 134

7.1 Introduction 134

7.2 Methodology, sample preparation and measurement 139

7.2.1 Methodology of hybrid model 139

7.2.2 Sample preparation 140

7.2.3 Measurement techniques 140

7.3 Results and discussion 142

7.3.1 Scanning electron micrographs and oxide thickness histograms 142

7.3.2 Comparisons of CDF curves for local oxide thickness 145

7.3.3 Constructed 1-D oxide profile employed in the hybrid model 146

7.3.4 Comparisons of reflectance measurements and predictions 148

7.3.5 Effect of surface roughness parameters on the predictions 152

7.4 Conclusions 153

Chapter 8. Conclusions and future work 154

8.1 Summary and key findings 154

8.1.1 Thin film effect 154

8.1.2 Surface roughness effect 156

8.1.3 The hybrid effect 157

8.2 Future work 158

8.2.1 Modeling the spectral emissivity variations across the surface underlying GOA 158

8.2.2 Improving the reflectance predictions of oxidized AHSS having rough states 159

8.2.3 Investigation of temperature effect on radiative properties 161

8.2.4 Industrial impact of research 161

References 163

List of Figures and Tables

List of Figures

Figure 1-1. Comparison of Stress-strain curve between Dual Phase and HSLA steels [4]..... 2
Figure 1-2. Schematic view of continuous galvanizing line (CGL). 4
Figure 2-1. Thermodynamic stability of oxygen potential (in logarithmic scale) with respect to annealing temperature. (p_{O2} in atm.) The curves are calculated and derived based on the Gibbs energy equations of FeO, MnO, SiO_2 and Cr_2O_3 formation [15]. Curves of the dew points (−30°C and +10°C) shown in red dashed lines are derived underlying 95%/5% N_2/H_2 atmosphere, while curves corresponding to Mn-Si ternary oxides (e.g. $MnSiO_3$, Mn_2SiO_4) exist in the grey shaded area between the curves of MnO and SiO_2, but are not shown in the plot. Note that the metallic oxide curves were calculated based on the alloy compositions of the present study. 11
Figure 2-2. Schematic view of pyrometer receiving radiation from the object having temperature T. The voltage, S, induced by the pyrometer is proportional to received total energy, Q_e emitted from the object that is affiliated with the object's temperature via spectral intensity, I_λ (λ_d,T,θ), and spectral emissivity, $\varepsilon_\lambda(\lambda_d, T,\theta)$. The temperature of the object is therefore inferred from received voltage, through Eq. (1.18). 19
Figure 2-3. The bandwidth $\Delta\lambda$ with respect to spectral intensity curve of a blackbody, $I_{b\lambda}(\lambda,T)$ and a real surface, $I_\lambda(\lambda,T)$. Parameters such as $\kappa_\lambda(\lambda_d,T)$, $\varepsilon_\lambda(\lambda_d,T)$ and $I_{b\lambda}(\lambda_d,T)$ in Eq. (1.14) can be taken out of the integral, in case $\Delta\lambda$ is sufficiently small. 19
Figure 2-4. Graphs of blackbody radiation at three different radiator temperatures. The spectral intensity increases with temperature, and the peak of the spectrum shifts toward the shorter wavelength spectrum. 20
Figure 3-1. Schematic view of one dimensional surface roughness profile with reference and mean line. The plot is depicted based on a random surface in one dimension. Surface parameters derived based on the reference line can be different from that of derived based on the mean line. 26
Figure 3-2. Schematic view of radiation incident on oxide film formed upon a substrate material [47]. .. 29
Figure 3-3. Experimentally measured spectral emissivity variations with time as oxide growth on metal surface [51]. 29
Figure 3-4. Schematic view of the theory upon which Agababov model is derived [112]. Parameters A_r and A_s denote the surface area of the roughness cavity and that of the corresponding imaginary smooth surface above the cavity. Based on the scenario of radiative energy balance between the total energy radiation from the rough surface and that of from smooth surface, the formula that relates the emissivity from a rough surface, ε_r, to that of a smooth surface, ε_s, can be derived. 35
Figure 3-5. Schematic of E-M wave scattering from a rough surface. Points A and B show cases where the radius of curvature is large and small compared to the wavelength of interest. The scattered electrical field can be obtained by solving Helmholtz's integrand incorporating Kirchhoff's boundary conditions that assumes the surface is locally flat relative to the incident EM wave, depicted as the scenario of point A. 43
Figure 3-6. Schematic view of single scattering (dashed arrows) and multiple scattering (solid arrows) at a rough surface. 50

Figure 3-7. Illustration of bidirectional reflection under the hemispherical area in a global reference frame. 52
Figure 3-8. Schematic view of ray tracing on the 2-D rough surface in a global coordinate. The surface nodes incorporated in the GOA model are obtained directly from the measured profilogram data. 54
Figure 3-9 Flowchart of 2-D ray tracing framework. 55
Figure 3-10. Depiction of a uniform oxide film upon a rough metal surface. In the hybrid model, the oxide film is assumed to be uniform in thickness across the substrate, which makes both profiles identical to each other. 59
Figure 3-11. Schematic of rough surface with uniform oxide film in one dimension. The profiles of the two interfaces are assumed to be identical, $z=\zeta(x,y)$, and $z=\zeta(x,y)+h$. The system contains three layers: air, oxide film, and substrate, having refractive indices of n_1, $\tilde{n}_2$, $\tilde{n}_3$, respectively. The local film thickness relates to global thickness as $D=h\cos\alpha$. In this thesis, the substrate is treated as iron (Fe). 61
Figure 3-12. 1-D schematic view illustrating the relation between the global oxide thickness, *h*, and the local oxide thickness, *D*, underlying the uniform oxide scenario. The correlation between the global thickness and the measured averaged local thickness is given by Eq. (2.63). 61
Figure 3-13. Flowchart of GOA ray tracing with thin film interference (hybrid method) 62
Figure 4-1. Surface topography obtained by optical profilometer (a) before (b) after removing of global texture. (c) the relation between wave-filtered surface roughness and measured emissivity [156]. The global texture shown in (a) is mainly caused by artifact of rolling effect, while the tiny, local roughness texture observed in (b) is formed by oxide nodules during inter-critical annealing. The global emissivity appears to have an exponential correlation with the roughness scale of filtered surface shown in (c). 65
Figure 4-2. McMaster galvanizing simulator used to anneal the samples in present work. 68
Figure 4-3. DP980 Heating cycles for the annealed samples [154]. 69
Figure 4-4. Optical microscopy (left) and optical profilograms (right) of the DP980 samples: as-received (a, b), polished (c, d), roughened (e, f), annealed "A" (g, h) and "Full" (i,j) surfaces. Rolling striations are clearly visible in the as-received sample, which have been removed by polishing or are obscured by roughening or oxide growth in the remaining samples. 70
Figure 4-5. Scanning electron micrographs of the DP980 annealed "A" sample, highlighting the oxide nodules formed during annealing. The image on the right corresponds to the white boxed region in the image on the left. 71
Figure 4-6. Configuration of the integrating sphere 72
Figure 4-7. Reflectance of DP980 specimens from NIR and FTIR measurement (left) and reflectance of NIR measurement with corresponding visible surface images (right). Measured data were obtained by using the UV-VIS-NIR spectrophotometer (0.25-2.5 μm) and Bruker Invenio-R spectrometer (2.5-25 μm). It is observed that the brightness of each image correlates with ρ_{vis}, the spectral reflectance averaged over the visible spectrum, 0.4-0.7 μm. 73
Figure 4-8. Measured spectral emissivity of annealed "A" (left), annealed "Full" (middle) and annealed "Full 0°C" (right) in order to compensate for the specimen orientation effect due to rolling direction, addition measurement was made by rotating the sample by 90°. Slight difference (less than 5%) is observed between the data of 0° and 90° within the entire spectrum for the three samples. The final spectral emissivity is determined by averaging both data, as shown in dashed line. 74
Figure 4-9. Examination of the correlation between surface roughness parameters and spectral emissivity predicted using the Agababov model for the DP980 as-received sample. Different sampling lengths and measuring locations presented as circle, triangle, diamond and square symbols were used to derive the surface parameters that were incorporated into Eq. (2.15) to obtain roughness parameter, *Y*. The solid line represents the case when Eq. (2.64) is satisfied. The results demonstrate that the estimated roughness

ratio, Y_s/Y_r, via its relationship with measured spectral emissivity in Eq. (2.64), are not in line with the measured data from the surface profiler, indicating that Agababov model does not work in some cases of present study. 75
Figure 4-10. Verification of the applicability of the Kirchhoff approximation using Eq. (2.31) using profilometry-derived surface parameters. 76
Figure 4-11. (a) Plot of ρ_λ vs λ and (b) plot of $\ln\rho_\lambda$ vs $1/\lambda^2$. The trends found through linear regression via Eq. (2.65) are shown as dashed lines. The spectral reflectance of the "A" and "full" samples are nearly indistinguishable. 78
Figure 4-12. Surface profiles obtained using wavelet filtering for the as-received sample. The original profile is decomposed into a set of different levels of wavelets (1^{st}, 2^{nd}, 3^{rd}, 4^{th}), where the lower level stands for wavelet with higher frequency and less amplitude. The "high-pass filtered surface" is recovered by reconstructing the 1^{st} level wavelet into a new profile. 80
Figure 4-13. Surface topography of roughened sample before (left) and after (right) the removal of global texture. The topography is recovered via the surface profile data obtained from the optical profiler. Daub2 wavelet mode is employed in the high-pass filtering process for the removal of global roughness texture. The filtered surface profile composed of local scale roughness, which is caused by random process, has RMS roughness of around 0.1 μm in general. 80
Figure 4-14. Comparison of statistical heights between filtered surface profile (left) with that of measured by atomic force microscope (right) for annealed "A" sample. Although the optical profiler cannot capture the detained surface data at lateral resolutions below 1.6 μm, similar distributions are observed from both profiles that result in almost same surface height deviation, σ. This demonstrates the robustness of using optical profiler and filtering techniques to obtain the overall surface parameters. 81
Figure 4-15. Comparison of AFM (left) and SEM (right) images of annealed "A" sample. It can be seen that the oxide nodules observed from SEM reflect to the pattern presented in the AFM derived profile, demonstrating the existence of oxide nodules and consistent surface topography measured from two techniques. 81
Figure 4-16. Probability density of surface roughness from filtered and unfiltered profilograms. The histograms for the unfiltered surface profile are distinguished by how they were processed. The surface roughness of the annealed sample follows a near-normal distribution, and exhibits less skewness than the as-received and roughened samples. It can be seen that surface profile becomes normally-distributed After removing the global roughness for the as-received, roughened, and annealed samples, suggesting that the surface features at the micrometer length scale originate through random processes, and, in this respect, more in line with the assumptions that underlie Eq. (2.47). 82
Figure 4-17. Comparison of measured and estimated reflectance for (a) polished, (b) as-received, (c) roughened, (d) annealed "A" and (e) annealed "Full" samples. The long dash line in (a) denotes the estimation of Eq. (2.47) with constant $\rho_{\lambda,s}$. The estimations from (b)-(e) were achieved by applying Eq. (2.47), using Hagen-Rubens derived $\rho_{\lambda,s}$ with profiler measured σ (dotted line) and filtered σ (dashed line), respectively. The Fraunhofer criterion based on the optical roughness is shown as a vertical dashed line for all cases. 85
Figure 4-18. Comparison of estimated spectral reflectance given different temperatures with the same surface roughness, σ=0.134, found from Eq. using Eq. (2.38)-(2.39) and Eq. (2.47). It can be seen that the temperature-dependent electrical resistivity of steel significantly affects the modeled spectral reflectance, even excluding the additional variation one would expect as the surface phase evolves during annealing. Such result highlights how the temperature-dependent electrical resistivity can affect the predictions and motivates the development of strategies for measuring the spectral reflectance of AHSS samples at high temperatures during annealing. 86

Figure 5-1. Optical microscopy (left) and optical profilograms (right) of sample #1 (a, b), sample #4 (c, d), sample #5 (e, f), sample #6 (g, h) sample #7 (i, j) and sample #8 (k, l). Artifacts from the cold-rolling process are evident in sample #4, #6, #7, and #8. Note that samples #4, #6, #8 underwent ground rolling in the last stand rolling finish, and appear different from sample #7, which underwent electro-discharge (EDT) rolls in the last stand finish. 95
Figure 5-2. RMS roughness of tested samples measured using the optical profilometry. 96
Figure 5-3. Comparison of probability density function for heights between the filtered surface profile (left) with that of measured by atomic force microscopy (right) for sample #2. Although the optical profilometer cannot capture the detailed surface data at lateral resolutions below 1.5 μm, similar distributions are observed from both profiles, resulting in almost the same surface height deviation, σ. This demonstrates the robustness of using optical profilometry to obtain the overall surface parameters required for GOA modeling. 97
Figure 5-4. Verification of the applicability of the Kirchhoff approximation using Eq. (2.31). 98
Figure 5-5. Comparisons of measured directional-hemispherical reflectance of all tested samples (left) and measured reflectance of polished surfaces of the three alloys (right) used in the tested rough samples. The yellow shaded area in the left plot represents the spectrum of pyrometry interest, while the gray shaded area contains the GOA valid domain of sample #5 and sample #6. The square symbols in the right plot represent the GOA predictions and the two dash curves are the refractive indices for iron from Refs. [42,43]. 100
Figure 5-6. Directional-hemispherical reflectance predictions with GOA for (a) sample #1, (b) sample #4, (c) sample #7 and (d) sample #8. The solid and dash lines in each plot represent the prediction results using 1-D and 2-D GOA methods, respectively. 102
Figure 5-7. Effect of incident azimuthal angles on 2-D GOA predictions for (a) sample #1, (b) sample #4, (c) sample #7 and (d) sample #8. The black, red and purple lines in each plot represent the directional-hemispherical reflectance predictions using 2-D GOA with an incident azimuthal angle of 0°, 45°, 90°, respectively. 103
Figure 5-8. Comparison of measured and estimated reflectance for (a) sample #1, (b) sample #4, (c) sample #5, (d) sample #6, (e) sample #7 and (f) sample #8. The solid red lines represent the measured directional-hemispherical reflectance at near normal incidence. The blue dashed line represents predictions using the regression model described in Ref. [33]. The solid purple lines represent the reflectance of iron. The black long dash lines denote the boundary of the GOA validity regime defined in Ref. [169], and the gray-shaded areas represent the GOA regime. The directional-hemispherical and specular reflectance predictions using GOA are shown as circle and triangles symbols, respectively. ... 108
Figure 5-9. Contour maps of BRDF with respect to the scattered polar angle, θ_s, and azimuthal angle, φ_s, for (a) sample #1, (b) sample #4, (c) sample #5, (d) sample #7, (e) sample #8. The BRDF is obtained via Eq. (2.53) with incident polar and azimuthal angles fixed at θ_o=10°, φ_o=45°. 109
Figure 5-10. BRDF results with respect to the scattered azimuthal directions for (a) sample #1, (b) sample #4, (c) sample #5, (d) sample #7, (e) sample #8. The incident polar and azimuthal angles are fixed at θ_o=10°, φ_o=45°. In these plots the scattered polar angle is fixed at θ_s=30°. All samples exhibit coherent peaks of BRDF in the proximity of specular directions (φ_s=225°). 110
Figure 6-1. Schematic view of the thin film interference model where an oxide layer is formed on the metal surface; (b) surface topography (e.g. roughness) effect on EM wave scattering. 115
Figure 6-2. Annealing schedule for the tested samples. The samples were heated to 800°C and soaked for 180 s before quenching. 120

Figure 6-3. Images showing the process of Focused Ion Beam (FIB) technique (a) defining the region of interest (ROI) (b) tilted to 54˚ (c) trench milling (d) magnification of image for measurement. The dashed white lines denote the oxide. 122
Figure 6-4. Refractive indices of (a) ferrite [194] and (b) MnO [193]. 123
Figure 6-5. Comparison of measured reflectances of polished surfaces for different alloys: (a) DP980, Si/Mn=0.23; (b) DP780, Si/Mn=0.10; and (c) DP980, Si/Mn=0.04. The surfaces of the samples were polished to the same roughness scale (σ=0.09 μm) before the measurements. The dashed lines denote the reflectance of ferrite derived using Fresnel's equation with refractive indices from Ref. [194]. 123
Figure 6-6. Optical microscopy and optical profilograms of the samples. Samples annealed in a polished state (sample #1, #3, #5, #7, #9, #11) have similar appearance, while artifacts from the cold-rolling process are evident in sample #2, #4, #6, #8, #10, #12. Note that samples #4, #6, #10, #12 underwent ground rolling in the last stand rolling finish, and appear different from sample #2 and sample #8, which underwent electro-discharge (EDT) rolling in the last stand. Overall, samples with identical Si/Mn share a similar color and brightness attributed to oxide speciation obtained during annealing. For polished substrates, samples annealed at low dew points (−30°C) appear darker compared to those annealed at high dew points (+10°C). 125
Figure 6-7. Comparisons of measured directional-hemispherical reflectances for samples annealed in their polished (left) and as-received (right) states. The thin film interference effect is more pronounced on the samples annealed in their polished state. 127
Figure 6-8. Scanning electron micrographs of cross-sectional surfaces of the annealed samples. (a) sample #1 (b) sample #5 (c) sample #7 and (d) sample #11. Oxides are outlined by the white dashed lines. Sample 1 has a film-like oxide, while isolated nodules oxides are formed on sample #5 and #11. The oxide structure of sample #7 shares characteristics of both a nodular and film-like structure, but more inclined towards film-like. Oxide formations of sample #3, #9 (not shown) are film-like. 129
Figure 6-9. Measured refractive indices of oxide film via ellipsometry are shown for (a) Si/Mn=0.23, (b) Si/Mn=0.10, and (c) Si/Mn=0.04 for the samples annealed in a polished state. The solid and dash curves in the plots represent samples annealed at -30°C and +10°C atmosphere, respectively. The long-short dash lines in (c) are derived from [193]. The refractive indices shown in (a) should be interpreted with some skepticism, since the oxide has a nodular as opposed to a film-like morphology. 130
Figure 6-10. Comparisons of measured and predicted reflectances for samples annealed in their polished state: (a) sample #1, (b) sample #3, (c) sample #5, (d) sample #7, (e) sample #9, (f) sample #11. The black solid curves in the plots represent reflectance of ferrite derived using Fresnel's equation. The red curves and black dotted curves represent measurements and predictions using the thin film interference model, Eq. (2.9)-(2.13), with measured refractive indices, respectively. The blue dashed curves in (b) and (e) denote predictions via the thin film interference model with refractive indices of MnO obtained from reference [193]. 132
Figure 7-1. Schematic view of how EM waves interact with oxidized AHSS surfaces: (a) thin film interference effect; (b) surface topography dominates the wave/surface interaction when the wavelength is much larger than the oxide film thickness; (c) rough oxidized surface where the global oxide thickness across the surface area is uniform upon the substrate; and (d) rough oxidized surface where the global oxide thickness across the surface area is non-uniform upon the substrate. In scenarios (a) and (c), thin film interference dominates the wave/surface interaction. In scenario (d), both interference and non-interference reflections are important, depending on the profiles of the oxide and substrate. 138
Figure 7-2. Scanning electron micrographs of cross-sectional surfaces of the annealed samples: (a) sample #2 (b) sample #4 (c) sample #6 and (d) sample #8 (e) sample #10 (f) sample #12. Oxides are outlined by the white dashed lines. 144

Figure 7-3. Measured local oxide thickness histogram for: (a) sample #2; (b) sample #4; (c) sample #6; (d) sample #8; (e) sample #10; and (f) sample #12. The grey bars denote the histogram of oxide thickness measured via FIB milling..... 145
Figure 7-4. Comparisons of cumulative distribution function curves of local oxide thickness for: (a) sample #2; (b) sample #4; (c) sample #8; (d) sample #10; The blue curve represents the empirical CDF generated from the measured data. The red curve represents CDF generated by constant global oxide thickness, *h* and measured surface parameters, σ, τ listed in Table 7-1. 146
Figure 7-5. 1-D profiles of oxide and substrate for: (a) Sample 2; (b) Sample 4; (c) Sample 8; (d) Sample 10; The oxide profile is generated using the calculated universal (global) oxide thickness, *h*, while the substrate profile is generated using the measured surface parameters (σ, τ). The incident wavelength is fixed at λ=0.4 μm. The red and black curves represent the generated oxide and substrate profiles, respectively. 148
Figure 7-6. Comparisons of measurements and the predictions using thin film interference model, hybrid model, and modified hybrid model for (a) sample #2 (b) sample #4 (c) sample #8 (d) sample #10 and (e) sample #3. Predictions are made with measured surface parameters and measured averaged oxide thickness. Description of the thin film interference model, which assumes a uniform oxide layer deposited on a smooth surface, can be found in Ref. [203]. The refractive indices employed are from those of the samples having a polished surface state. The results for the sample having polished state (sample #3) shown in (e) are retrieved directly from Ref. [203].The refractive indices of MnO are derived from Ref. [193]. 151
Figure 7-7. Comparisons of predictions using hybrid model through parametric analysis. Effect of (a) surface slope (b) root-mean-square roughness on the reflectance predictions. The analysis is performed on sample #4 having measured parameters μ_h=91.2 nm, σ_h=34.1 nm, σ=0.62 μm, σ/τ=0.49. 152

List of Tables

Table 1-1. Lists of life cycle cost for the existing corrosion-protection coating systems [9]. 4
Table 2-1. Summary of the oxide formations subject to annealing conditions from relevant literatures. .. 14
Table 4-1. Chemical composition of tested sample [159]..... 69
Table 4-2. RMS roughness inferred by linear regression of measured $\rho_{\lambda,d\text{-}h}$ via Eq. (2.65), along with surface RMS roughness and correlation length inferred from the profilograms before and after filtering. 77
Table 5-1. List of tested AHSS alloys with chemical compositions (weight %) based on the ASTM standards [41]. The Si/Mn ratio is measured using inductively-coupled plasma spectroscopy. 94
Table 5-2. List of samples with measured surface parameters from optical profilometry. 94
Table 5-3. Variance between the predictions using Monte Carlo ray tracing. 98
Table 6-1. Tested samples with different alloy compositions, annealing atmospheres, measured pre-annealed and post-annealed roughness, and measured oxide thickness and oxide species. The uncertainty in μ_h represents the margin of error at 95% confidence interval of the mean. 121
Table 7-1. Tested samples with different alloy compositions, annealing atmospheres, measured pre-annealed and post-annealed roughness, and measured oxide thickness and oxide species. The uncertainty in μ_h represents the margin of error at 95% confidence interval of the mean. 142

Nomenclature

This section indicates the nomenclature used throughout this thesis. As this thesis draws from multiple bodies of literature, there are occasionally conflicts in the symbols used. In these cases, the chapter restriction indicates the chapters in which a specific definition applies. In cases where no chapter is specific, the symbol applies universally throughout the document.

Latin Characters

Symbol	Chapter Restrictions	Definition
A	-	Surface area
A	2.1	Coeffiecient in Gibbs energy formula
A_d	2.2	Detection area
A_r	-	Area of roughness cavity
A_s	-	Area of imaginary smooth surface
B	2.1	Coeffiecient in Gibbs energy formula
B	3	Parameter in Beckmann's diffuse model
C	2.1	Coeffiecient in Gibbs energy formula
C	3	Autocorrelation function
C_1	-	Constant in Plank's spectral enery distribution
C_2	-	Constant in Plank's spectral enery distribution
$C_{\lambda d}$	-	Calibration constant for pyrometry
D	-	Fractal dimension
D	3.4	Local oxide thickness
E	2.1	Coeffiecient in Gibbs energy formula
E	3	Electric field
E_1	-	Incident electric field
E_2	-	Reflected electric field

E_2	3.3.6	Reflected electric field in specular direction from a Gaussian stationary rough surface
E_{20}	-	Electric field scattered from a smooth surface
E_{flat}	3.3.6	Reflected electric field from a smooth surface
E_{s}	-	Electric field at the surface
e	3	Euler's number
F	2.1	Coeffiecient in Gibbs energy formula
F	3	Coefficient in the electric field formula
$f_{\text{bi-d}}$	-	Bi-directional function of reflectance
f_{d}	-	Diffuse function of reflectance
f_{sp}	-	Specular function of reflectance
G	2.1	Coeffiecient in Gibbs energy formula
G	3	Parameter in Beckmann's diffuse model
ΔG	-	Gibbs energy
G	-	Scaling constant of Weiestrass-Mandebrot function
G_{i}	-	Incident energy
G_{r}	-	Scattered energy
$G_{\text{i,p}}$	-	Incident energy of *p*-polarized component
$G_{\text{i,s}}$	-	Incident energy of *s*-polarized component
$G_{\text{r,p}}$	-	Reflected energy of *s*-polarized component
$G_{\text{r,s}}$	-	Reflected energy of *s*-polarized component
H	3	Parameter in Beckman's diffuse model
h	2.2	Plank's constant
h	-	Global oxide thickness
I_{λ}	2	Radiation spectral intensity
$I_{\text{b}\lambda}$	-	Balck body intensity
$I_{\lambda,\text{gen,i}}$	-	Generated spectral irradiance
$I_{\lambda,\text{meas,i}}$	-	Measrued spectral irradiance
K	2	Equilibrium constant of chemical reaction
K_{mean}	-	Mean surface curvature
$\mathbf{k}_1$	-	Incident wave vector

$\mathbf{k}_2$	-	Reflected wave vector
k_1	-	Modulus of the incident wave vector
L	-	Surface length
M	-	Metal element
m	2	Coefficient in chemical equilibrium formula
m	3.1	Mean value of surface height
m	-	Number of summation in Beckman's diffuse model
n	2	Coefficient in chemical equilibrium formula
n	-	Refractive index
n	3.3.3	Surface normal
$\mathbf{n}$	-	Surface normal vector
n_s	-	Total number of surface point
P	-	Power spectral density fuction
p	2	Partial pressure
p	3	Parameter in Fresnel's equation
Q_e	-	total emitted energy
q	-	Parameter in Fresnel's equation
R	2	Universal gas constant
R	3.1	Auto covariance function
R	3.3.4	Radius of curvature
R_a	-	Arithmetic average surface roughness
R_q	-	Root-mean-square roughness
R_{RMS}	3.3.4	Root-mean-square radius of curvature
r	3.3.3	Distance between scattered point and surface
r_e	-	Temperature-dependent electrical resistivity
r_o	-	Electrical resistivity at a reference temperature
r_p	-	Fresnel amplitude reflectivity of *p*-polarization
r_s	-	Fresnel amplitude reflectivity of *s*-polarization
S	-	signal received by the pyrometer
s	-	RMS slope of surface profile
T	-	Temperature

T_{dp}	-	Dew point temperature
T_o	3.3.5	Reference temperature
Y	-	Surface parameter in Agababov model
Y_r	-	Surface parameter for rough surface area
Y_s	-	Surface parameter for smooth surface area
z	-	Surface height profile

Greek Characters

Symbol	Chapter Restrictions	Definition
α	2	Atomic fraction
α	3.1	Constant representing correlation length in autocorrelation function
α	-	Local incident angle
β	-	Correlation length
β_x	-	Correlation length in *x* direction
β_y	-	Correlation length in *y* direction
ε	-	Emissivity
ε_λ	-	Spectral emissivity
$\varepsilon_{\lambda d,B}$, $\varepsilon_{\lambda d,A}$	2.2	Emissivity of detection wavelengths in dual-wavelength pyrometry
ε_r	-	Emissivity from a rough surface
ε_s	-	Emissivity from the imaginary smooth surface
Φ_i	-	Incident radiant power
Φ_s	-	Reflected radiant power
ϕ	-	Global grazing angle
ϕ_g	-	Local grazing angle

γ	-	Parameter which determines the density of the spectrum
η	3.3.2	Parameter in bi-directional reflectance model based on fractal theory
η_{12v}, η_{23v}, η_{12p}, η_{23p}	-	Reflectance parameters in Airy's formula
φ_i	-	Incident azimuthal angle
φ_s	-	Reflected azimuthal angle
κ	3.3.5	Temperature coefficient of resistivity
κ_λ	2.2	optoelectronic efficiency of the pyrometer
$\boldsymbol{\kappa}_i$	-	Incident ray vector
$\boldsymbol{\kappa}_r$	-	Reflected ray vector
λ	-	wavelength
λ_d	2.2	Detection wavelength
$\lambda_{d,A}$, $\lambda_{d,B}$	2.2	Detection wavelengths in dual-wavelength pyrometry
μ_h	-	Mean local oxide thickness
ν	3.3	Number of intersections between the mean line and the surface profile
θ	-	polar angle
θ_1, θ_2, θ_3	3.2	Incident and refracted angles in Snell's equation
θ_i	-	Incident polar angle
θ_s	-	Reflected polar angle
ρ	-	Reflectance
ρ_p	-	Parallel-polarized reflectance
ρ_{pp}	-	Co-polarized (*p*-polarization) reflectance
ρ_{ps}	-	Cross-polarized (*p*-s-polarization) reflectance
ρ_{ss}	-	Co-polarized (*s*-polarization) reflectance
ρ_{sp}	-	Cross-polarized (*s*-*p*-polarization) reflectance
ρ_v	-	Vertical-polarized reflectances
ρ_λ	-	Spectral reflectance
$\rho_{\lambda,diffuse}$	-	Diffuse reflectance

$\rho_{\lambda,d\text{-}h}$	-	Directional-hemispherical reflectance
$\rho_{\lambda,s}$	-	Reflectance from a smooth surface
$\rho_{\lambda,sp}$	-	Specular reflectance
σ	-	Root-mean-square roughness
σ_h	-	Standard deviation of oxide thickness
τ	3.1	Variable spatial separation
τ	-	Correlation length
υ	-	Parameter in bi-directional reflectance modelbased on fractal theory
Ω	-	Detection solid angle
ω	-	Frequency of roughness spectrum
ω_i	-	Incident solid angle
ω_s	-	Reflected solid angle
ψ	-	Specular reflectance by Fresnel's equation
ζ	-	Phase difference of reflected wave
ζ	-	Surface height function
ζ'_x	-	Derivative of surface height in the *x* direction
ζ'_y	-	Derivative of surface height in the *y* direction
ζ''_x	-	Second derivative of surface height in the *x* direction
$\zeta''_{x,y}$	-	Second derivative of surface height in both *x* and *y* direction
ζ''_y	-	Second derivative of surface height in *y* direction

Common Superscripts and Subscripts

Character	Definition
a	Arithmetic
b	Blackbody
bi-d	Bi-directional
d	Detection
d	Diffuse
d-h	Directional-hemispherical
e	Emission
g	Global
h	Thickness
i	Incident
p	Parallel
q	Root-mean-square
RMS	Root-mean-square
r	Rough
r	Reflected
s	Smooth
s	Scattered
sp	Specular
v	Vertical
λ	Spectral

List of Abbreviations

Abbreviation	Definition
AFM	Atomic force microscopy
AHSS	Adavnced high strength steel
ASTM	American Society for Testing and Materials
BRDF	Bi-directional distribution function
CDF	Culmulative distribution function
DP	Dual phase
dp	Dew point
EM	Electromagnetic
FEM	Finite element method
FIB	Focused ion beam
FMM	Fast multipole method
FTIR	Fourier-transform infrared spectroscopy
GOA	Geometric optics approximation
ICP	Inductively Coupled Plasma
MIR	Mid-infrared
NIR	Near-infrared
PDFs	Probability density functions
RMS	Root-mean-square
SEM	Scanning electron miscroscopy
TRIP	Transformation Induced Plasticity
UTS	Ultimate tensile strength
UV	Ultra-violet
VIS	Visible
XPS	X-ray photoelectron spectroscopy
YS	Yield strength

Chapter 1 Background

1.1 Introduction to AHSS

Improving fuel economy and reducing emissions and their effect on the environment have become priorities and a major objective for industrial, academic, and national research centers. To achieve these goals, automakers are developing new strategies and advanced technologies to improve engines, drivetrains, transmissions, aerodynamics, tire rolling resistance, and vehicle weight. Among these, vehicle weight reduction is the most effective means for improving fuel economy and reducing energy consumption [1]. Reducing vehicle weight lowers the inertial forces that the engine has to overcome to accelerate and decelerate the vehicle.

To meet these demands, advanced high strength steel (AHSS) alloys have been incorporated into nearly every new road vehicle. In most cases, the superior strength of these alloys allows thick-gage components to be replaced by thin-gage material without any loss of performance. On average this has reduced vehicle body structure mass by at least 25% [2], which has significantly improved the fuel efficiency and reduce greenhouse gas emissions, without compromising passenger safety.

One of the earliest types of AHSS to be developed are Dual Phase (DP) steels, which have a microstructure of hard martensite in a soft ductile ferrite matrix. DP steels are an improvement on high strength low alloy (HSLA) steels since they have improved elongation and ductility while exhibiting similar strengths. In addition, unlike HSLA steels, DP steels also exhibit desirable continuous yielding [3, 4]. The comparison is illustrated in Figure 1-1. As more types of AHSS

alloys continue to be developed, researchers and steel producers will be challenged to identify the most cost efficient and high-performance steel types and processing routes.

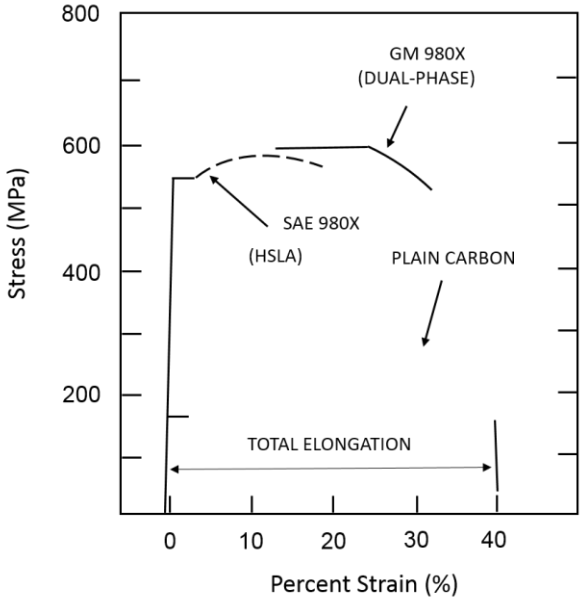

Figure 1-1. Comparison of Stress-strain curve between Dual Phase and HSLA steels [4].

1.2 Continuous galvanizing line

Hot-dip galvanizing, which is often carried out in a continuous galvanizing line (CGL), is a particularly effective way to protect AHSS parts from corrosion. This is crucial since any lost material represents a greater portion of the total cross-section compared to a thicker part made of traditional steel. Prior to annealing, steel strips normally go through a series of upstream processes including hot-rolling, cold-rolling, cleaning to improve the formability and surface finishes of the strips [5]. In the continuous galvanizing line, as shown in Figure 1-2, cold-rolled steel strip undergoes cleaning and annealing prior to immersion in a molten zinc bath, within which a protective zinc layer is fused to the steel [6]. In the cleaning process, steel strips undergo rinsing, degreasing and pickling to get rid off the dirt and contaminants on the surface before entering the

entry accumulator, which provides storage areas between static steel coils and continuous strip running through the furnace sections. The annealing furnace normally contains heating, soaking, and cooling sections to anneal the full-hard strip and impart the desired mechanical properties and microstructure to the steel, with reduced atmosphere to prevent the steel strips from oxidation in order to achieve complete wetting of the steel surface by the liquid Zn alloy in the process of galvanizing. In the furnace, the gas atmosphere is typically composed of 5-20 vol. % hydrogen and nitrogen. The gas atmosphere is controlled by the dew point which is a measure of the water vapour content of the atmosphere at a specific temperature [7].

Dual-phase steels generally contain low carbon (0.06–0.15 wt.% C) along with alloying element additions such as Mn to increase the hardenability and improve the ultimate tensile strength (UTS) to yield strength (YS) ratio [8]. Accordingly, some of the alloying elements can selectively diffuse to the external surface to form oxides during annealing, which is of particular concern since the existing industrial CGL annealing atmosphere can not reduce MnO or other alloying element oxides [7]. The formation of selective oxide with respect to the annealing atmosphere is discussed in the following chapter. After the annealing procedure, the steel strips are immersed into the zinc bath to form a protecting layer in prevention of corrosion. At the exit point of the bath, a set of gas knives (e.g. high pressure air) wipe off any excess molten metal to control the thickness of the zinc coating. The coating is then cooled to allow the metal to freeze on the steel surface.

Hot-dip galvanizing normally has both lower initial and life-cycle costs compared to other competing systems (e.g. Epoxy, Polyurethane, Metallizing). Table 1-1 shows the comparisons of the life cycle cost for all the existing corrosion-protection coating techniques [9].

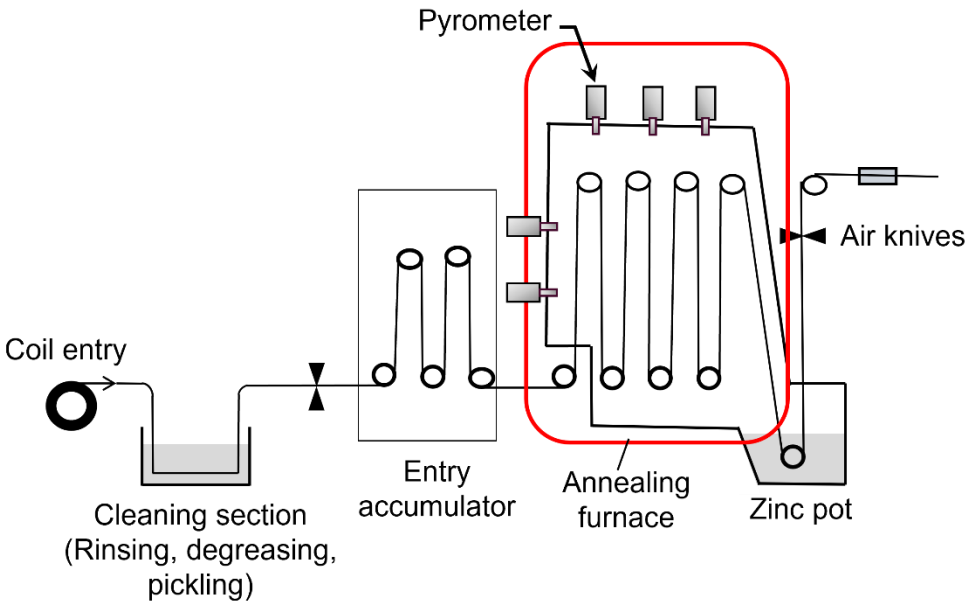

Figure 1-2. Schematic view of continuous galvanizing line (CGL).

Table 1-1. Lists of life cycle cost for the existing corrosion-protection coating systems [9].

Life cycle cost (75 years)	$/ft	Total ($)	AEAC (Average Annual Equivalent Cost)
Hot-dip galvanizing	4.29	214550	0.11
Epoxy/Epoxy	51.91	2595500	1.34
Inorganic Zinc/Epoxy	39.92	199000	1.03
Epoxy/Polyurethane	57.73	2886500	1.49
Inorganic Zinc/Epoxy/ Polyurethane	41.53	2076500	1.07
Galvanizing/Epoxy/Polyurethane	22.84	1142500	0.59
Metallizing	62.80	3140000	1.62

1.3 Existing issue regarding to temperature control in industry

Both the AHSS mechanical properties and zinc-adhesion to the base steel are sensitive to process temperature, especially during intercritical annealing that immediately precedes the zinc pot. In the annealing furnace of CGL, the steel strip temperature is controlled with inputs from non-contact temperature sensors, most often single- or multi-wavelength pyrometers (Figure 1-2). However, inferior zinc adhesion and substandard product mechanical properties have been frequently reported by industry. Much of this problem is attributed to thermal excursions of the strip during annealing, caused by improper heating control and erroneous pyrometrically-inferred temperatures used to control the furnace. Thermal excursions arising from improper heating control and pyrometry errors are principally due to wavelength-dependent variations in spectral emissivity caused by the evolving surface state of the steel strip in terms of roughness and oxide formation during annealing [10, 11].

Although a number of studies have attempted to correct these effects, very few of them are essentially related to AHSS. None of these studies have investigated the effect of alloy composition, annealing condition, and pre-annealed surface state on the selective oxidation, surface morphology, and radiative properties of AHSS alloys. In addition, none of them have clarified how the surface states (roughness, selective oxidation) of AHSS alloys are physically linked to the variations of wavelength-dependent emissivity, through modeling or experiment. Wavelength-dependent radiative properties, which are critical for pyrometry, are often excluded from these studies. In order to improve temperature control in industrial continuous galvanizing line, it is thus crucial to develop a robust spectral emissivity model that is correlated with these effects; this is the overriding purpose of this thesis.

1.4 Objectives

The aim of this thesis is to clarify the evolution of spectral emissivity of AHSS with surface state and roughness during continuous galvanizing, in order to improve the robustness of pyrometrically-inferred temperature and heating control in the furnace. The major objectives are to:

1. Determine how radiative properties (e.g. spectral emissivity) depend on surface state, roughness, AHSS composition through ex-situ measurement, and how the radiative properties are physically linked to these effects through EM theories.
2. Determine how annealing atmosphere, alloy components (Mn/Si ratio), and pre-annealed surface roughness affect the selective oxidation, surface topography and spectral emissivity of AHSS.
3. Determine how the spectral emissivity is physically linked to the selective oxidation and surface topography.

1.5 Organization of the thesis

The organization of this thesis is presented as follows: Chapter 2 illustrates the theories regarding to the selective oxidation of AHSS and the principle of pyrometry. Chapter 3 explores how surface topography impacts EM wave scattering, including the surface characterization, thin film effect, surface roughness effect, and hybrid thin film/roughness effect. Physical models and approaches used to correlate the surface state and radiative properties, which are adopted in this dissertation, are indicated in this chapter. Chapter 4 investigates how the radiative properties of AHSS can be

interpretated using the Davies' model with wavelet-filtering techniques. Although the model works to predict the directional-hemispherical reflectance over the optically-smooth region, as what was found in Ham's study [12] that the filtered roughness is exponentially correlated to the measured emissivity, there is still no reliable explanation to why the hemispherical reflectance can be estimated using a specular reflectance model. This leads to Chapter 5, which is focused on the geometric optics approximation (GOA) that adopts the Monte Carlo ray tracing technique to interpret the radiative properties of rough AHSS samples. Apart from most of the EM approximations, this technique can effectively capture the multiple reflections as the incident ray bundles interact with the surface boundaries. The estimations of radiative properties of rough surfaces are found to comply with the measurements when the parameters are within the validity domain of GOA. Chapter 6 illustrates the effect of alloy composition, annealing atmosphere and pre-annealed surface state on selective oxides and radiative properties of AHSS. This chapter is focused on oxidized AHSS having polished state where the thin film interference effect dominates the radiative properties and good agreements are found between the predictions and measurements. Chapter 7 is focused on a hybrid thin film/geometric optics model in the prediction of radiative properties of oxidized AHSS having rough states. The comparisons between the measurements and predictions are made. It is found the hybrid model generally underestimates the reflectance by overpredicting of interference effect due to the non-uniformity of the rough oxide layer. Chapter 8 summarizes the important findings of this thesis, and illustrates the future work based on the present findings.

Chapter 2 Selective Oxidation and Principles of Pyrometry[1]

This chapter illustrates the selective oxidation and principles of pyrometry. During industrial annealing, the emissivity varies according to the change of surface states due to selective oxidation, which depends on the annealing atmosphere and alloy composition of AHSS. Such phenomenon would further affect the pyrometry measurement in the furnace. As a consequence, it is important to know the mechanism of selective oxidation as well as the principle of pyrometry prior to the improvement of the temperature measurements. Topics regarding to selective oxidation and pyrometry are illustrated in Section 2.1 and Section 2.2, respectively.

2.1 Influence of selective oxidation on AHSS

When AHSS alloys are annealed in a controlled dew-point (i.e. controlled p_{O2}) atmosphere, alloying elements segregate from the bulk material toward the surface and grain boundaries, forming oxides at the surface and in the subsurface of the steel. Since the annealing atmosphere is reductive with respect to the native oxide on the steel, FeO, this phenomenon is called *selective oxidation* [13]. This process depends on a variety of factors such as alloy composition, annealing temperature and process atmosphere composition. Underlying the thermodynamic stability for metal/oxide equilibrium, the oxidation potential at a given temperature is determined by [18]

$$m\mathrm{M} + \frac{n}{2}\mathrm{O}_2 \rightleftarrows \mathrm{M}_m\mathrm{O}_n \quad (+\Delta G_1) \tag{1.1}$$

[1] Information presented in this chapter can be found in a paper submitted to Metall. Mater. Trans. B:
K. Lin, M. Pourmajidian, F. K. Suleiman, J. R. McDermid, K. J. Daun, Effect of annealing atmosphere and steel alloy composition on oxide formation and radiative properties of advanced high strength steel strip. (2021)

The Gibbs free energy, ΔG_1, (J/mol), and the equilibrium constant, K_1, of this reaction at annealing temperature, T (K), can be written as

$$\Delta G_1 = -RT \ln K_1 \tag{1.2}$$

$$K_1 = \frac{\alpha_{M_mO_n}}{\alpha_M^m \, p_{O_2}^{n/2}} = \frac{1}{\alpha_M^m \, p_{O_2}^{n/2}} \tag{1.3}$$

where R is the universal gas constant, R=8.314 J/(mol ·K). The oxide is assumed to be a pure condensed species with an activity of unity ($\alpha_{M_mO_n} = 1$), and α_M^m denotes the atomic fraction of M in the alloy.

With a fixed hydrogen content at a given T, the oxygen potential of the process atmosphere, p_{O2} [atm], is determined by the partial pressures of water vapor, p_{H2O}, and hydrogen, p_{H2}, in the atmosphere [18]

$$H_2 + \frac{1}{2}O_2 \rightleftarrows H_2O\,(g) \quad (+\Delta G_2) \tag{1.4}$$

$$\Delta G_2 = -RT \ln K_2 \tag{1.5}$$

$$K_2 = \frac{p_{H_2O}}{p_{H_2} \, p_{O_2}^{1/2}} \tag{1.6}$$

where p_{H2} is 0.05 in the case of a 95%/5% N_2/H_2 atmosphere and p_{H2O} is determined by the process atmosphere dew point, T_{dp}, which is the temperature at which the liquid water-water vapour reaction is at equilibrium,

$$H_2O\,(l) \rightleftarrows H_2O\,(g) \quad (+\Delta G_3) \tag{1.7}$$

$$\Delta G_3 = -RT_{\mathrm{dp}} \ \ln\left(p_{\mathrm{H_2O}}\right) \tag{1.8}$$

where liquid water is assumed to be a pure condensed species, i.e, $\alpha_{p\mathrm{H_2O}}$ =1.

The Gibbs energy for each compound can be approximated using [14]

$$\Delta G = AT\ln(T) + BT + CT^2 + DT^{-1} + ET^{\frac{1}{2}} + F\times10^{-7}T^3 + G \tag{1.9}$$

where coefficients *A, B, C, D, E, F, G* corresponding to each compound (FeO (s), MnO (s), SiO_2 (s), Cr_2O_3 (s), H_2O (l), H_2O (g)) derived from the experimental fits [14] are listed in Table 2-1. Consequently, the curves of oxygen potential for each oxide and for a given atmospheric condition with respect to the annealing temperature can be derived using Eqs (1.1)-(1.9), as depicted in Figure 2-1. If the atmospheric oxygen potential at a given temperature and dew point exceeds the oxygen potential of a specific compound, the oxide will form since the oxygen potential in the environment is greater than the equilibrium oxygen partial pressure of species *M*. As shown in Figure 2-1, when the alloy is annealed with either dp=−30°C or dp=+10°C, the atmospheric oxygen potentials exceed those of Mn and Si oxides. (Additional curves corresponding to ternary oxides, i.e. $MnSiO_3$ and Mn_2SiO_4, exist in the shaded area between the MnO and SiO_2 curves but are not shown). In this scenario, Mn, Si, and possibly Cr, could form stable oxides, while FeO is less likely to form on the metal substrate. It should be remembered that these calculations are based on thermodynamic equilibrium between the substrate and the atmosphere and do not account for the kinetics of segregation of the alloying elements, which can cause the oxide layer composition to vary with time and location.

Table 2-1. Corresponding coefficients used to obtain the Gibbs energy for each compound via Eq, (1.9), derived from Ref. [14].

Compound	A [J/mol·K]	B [J/mol·K]	C [J/mol·K^2]	D [J/mol·K^{-1}]	E [J/mol·K$^{0.5}$]	F [J/mol·K^3]	G [J/mol]
FeO (s)	-312.37974	2289.59246	0.1296543	35023345.2	1042.28461	5.85664	-536965.33
MnO (s)	1.3662852	36.6929348	0.00481023	352614.968	1042.28461	-3.9889179	-395773.02
SiO_2 (s)	8.21930022	79.2570095	-0.0009297	1322689.18	2084.56922	-1.1798608	-932891.64
Cr_2O_3 (s)	297.799334	-2306.3214	-0.1006328	4175977.18	23712.6364	119.406	-1292002.1
H_2O (l)	-2304.0466	18256.7583	1.4416257	-8161063.5	-121879.48	-3158.67	245617.101
H_2O (g)	14.5914916	-49.440744	-0.0053297	-122643.5	-76.542088	3.47762	-236434.09

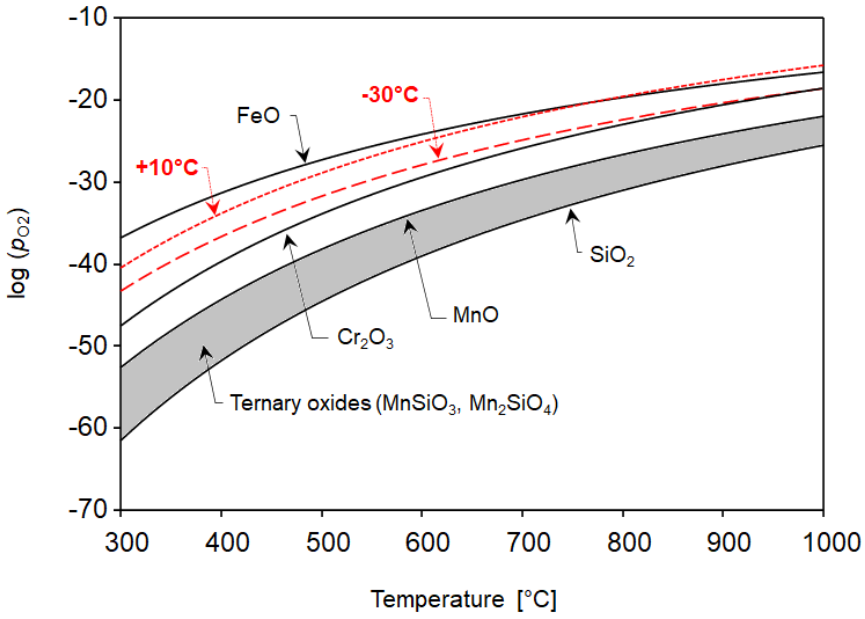

Figure 2-1. Thermodynamic stability of oxygen potential (in logarithmic scale) with respect to annealing temperature. (p_{O2} in atm.) The curves are calculated and derived based on the Gibbs energy equations of FeO, MnO, SiO_2 and Cr_2O_3 formation [15]. Curves of the dew points (−30°C and +10°C) shown in red dashed lines are derived underlying 95%/5% N_2/H_2 atmosphere, while curves corresponding to Mn-Si ternary oxides (e.g. $MnSiO_3$, Mn_2SiO_4) exist in the grey shaded area between the curves of MnO and SiO_2, but are not shown in the plot. Note that the metallic oxide curves were calculated based on the alloy compositions of the present study.

Table 2-1. lists the summary of the relevant studies with respect to the alloy composition, annealing conditions, and oxide formations. The selective oxidation of DP AHSS during intercritical annealing has been investigated extensively as described in Refs. [16-25]. These works show that annealing atmosphere and Si/Mn ratio strongly influence the chemistry and morphology of oxides that form during intercritical annealing. Suzuki et al. [26] interpreted the selective oxidation behavior of Si and Mn using a thermodynamic equilibrium calculation based on the chemical potential of the Fe-Mn-Si-O system. Their model showed that, in alloys with a Si/Mn ratio below 0.5, formation of SiO_2 as the dominant surface oxide species could be avoided when annealing under conventional, dew-point controlled process atmospheres. In this scenario, Mn-rich oxides, such as MnO, tend to form on the surface under high process atmosphere dew points, while ternary oxides, e.g. $MnSiO_3$ and Mn_2SiO_4, become prevalent at lower dew points. It was also found that as the Si/Mn ratio increases, the oxide species gradually transform from Mn-rich oxides to ternary oxides and SiO_2.

Seyed Mousavi et al. [16] studied the selective oxidation of a 2 wt.% Mn, 1.3 wt.% Si AHSS having a Si/Mn ratio of 0.64 during annealing heat treatments at 820°C. It was found that the external oxides consisted of film-like $MnSiO_3$, Mn_2SiO_4, SiO_2, and nodule-like MnO at outermost layer when the samples were annealed with dp=−50°C atmosphere, while nodule-like $MnSiO_3$, Mn_2SiO_4, and MnO were formed within the external surface region when the samples were annealed in a dp=+10°C atmosphere. Further work by Seyed Mousavi et al. [17] was carried out on the effects of dew point (−50°C , −30°C, +5°C), and Sn as a micro-addition on the selective oxidation of a 2 wt.% Mn, 1.7 wt.% Si AHSS having a Si/Mn ratio of 0.87 during annealing heat treatments at 840°C. They found that the thickness of the external oxides formed at lower dew points was smaller than those formed at a higher dew point. The external oxides consisted of MnO,

while internal oxide networks comprised $MnSiO_3$ and SiO_2 for both the bulk internal and grain boundary oxides. Pourmajidian and McDermid [27] investigated the effect of annealing atmosphere (−50°C , −30°C, +5°C) on the selective oxidation of a 3G AHSS model alloy with Si/Mn=0.32 during annealing heat treatments at 800°C. The measured external oxide thicknesses varied between 40-300 nm across different dew points and soaking times, and the outermost external oxide layer was found to be MnO for all process atmospheres. Surface oxides formed under a T_{dp} = −50°C atmosphere consisted of a layered configuration of SiO_2, $MnSiO_3$, and MnO, while the oxides formed under a +5°C dew point only comprised nodule-like MnO. Similar findings were reported at a lower annealing temperature of 690°C [25], where the external oxides were MnO and the internal oxide networks comprised a multi-layered structure of $MnSiO_3$ surrounding a SiO_2 core. Alibeigi et al. [28] found that only MnO appears on the external surface of high Mn (Si/Mn<0.06) steels annealed under different dew points (−50°C, −30°C, −10°C, +5°C) at annealing temperatures ranging from 630-770°C. The external oxide thickness was below 100 nm in all cases. Oh et al. [29] investigated the oxide formation on a 1.64 wt.% Mn, 1.48 wt.% Si TRIP steel (Si/Mn=0.9) annealed at 820°C under a dew point of −60°C. It was found that a thick Mn-rich oxide layer formed on the surface and Si-rich oxides formed in the subsurface region. The thickness of the Mn-rich oxide layer ranged from 20 to 50 nm, while the thickness of the Si-rich oxide layer was found to be less than 20 nm.

Table 2-1. Summary of the oxide formations subject to annealing conditions from relevant literatures.

Ref No.	Si/Mn [wt%]	Annealing Temperature	Atmospheric dew point, T_{dp}	Oxygen potential, p_{O2} [atm]	Oxide thickness, D [nm]	Surface oxide species	Oxide Morphology
[16]	0.64	820°C	-50°C -30°C +5°C	1.96×10^{-24} 1.21×10^{-22} 3.45×10^{-20}	-	dp=-50°C, -30°C: MnO, $MnSiO_3$, $MnSiO_4$, SiO_2; dp=+5°C: MnO, $MnSiO_3$, $MnSiO_4$;	dp=-50°C, -30°C: film-like; dp=+5°C: nodular
[17]	0.87	840°C	-50°C -30°C +5°C	5.52×10^{-24} 3.41×10^{-22} 9.68×10^{-20}	20-100 nm	MnO, $MnSiO_3$, SiO_2	dp=-50°C, -30°C: film-like; dp=+5°C: nodular
[20]	0.65 1.0	797°C, 777°C	-50°C -30°C +5°C	4.13×10^{-26} 4.05×10^{-23} 1.41×10^{-20} 7.16×10^{-27} 1.40×10^{-23} 3.95×10^{-21}	-	MnO, $MnSiO_4$, SiO_2	dp=-50°C, -30°C: widely spaced nodules; dp=+5°C: closely spaced nodules;
[23]	0.64	820°C	-60°C -10°C +5°C	1.29×10^{-26} 7.38×10^{-22} 8.33×10^{-21}	dp=-60°C: 30-40 nm; dp=+5°C: 5 nm	MnO, $MnSiO_3$, $MnSiO_4$, SiO_2	dp=-60°C: film-like; dp=-10°C, +5°C: fine-grained;
[24]	0.64	820°C	-60°C -30°C -10°C 0°C +5°C	1.29×10^{-26} 1.58×10^{-23} 7.38×10^{-22} 4.09×10^{-21} 8.33×10^{-21}	-	dp=-60°C: MnO, $MnSiO_3$, $MnSiO_4$, SiO_2; dp=-30°C: $MnSiO_3$, $MnSiO_4$, SiO_2; dp=-10°C: $MnSiO_3$, $MnSiO_4$, SiO_2; dp=0°C: $MnSiO_3$, $MnSiO_4$; dp=+5°C: $MnSiO_3$, $MnSiO_4$;	dp=-60°C, -30°C: film-like; dp=0°C, +5°C: nodules;
[27]	0.32	800°C	-50°C -30°C +5°C	6.87×10^{-25} 4.39×10^{-23} 1.29×10^{-20}	40-300 nm	dp=-50°C, -30°C: MnO, $MnSiO_3$, SiO_2; dp=+5°C: MnO, $MnSiO_3$;	dp=-50°C, -30°C: film-like; dp=+5°C: nodular
[28]	0.005 - 0.064	630°C, 685°C, 724°C, 750°C, 770°C;	-50°C -30°C -10°C +5°C	2.05×10^{-29} - 2.62×10^{-21}	5-35 nm (Si/Mn=0.05) 30-80 nm (Si/Mn=0.064) 35-95 nm (Si/Mn=0.015) 38-65 nm (Si/Mn=0.005) 55-95 nm (Si/Mn=0.01)	MnO	dp=-50°C, -30°C, -10°C: film-like; dp=+5°C: nodular
[29]	0.90	820°C	-60°C	1.71×10^{-25}	20-50 nm (Mn-rich) 0-20 nm (Si-rich)	MnO, $MnSiO_3$, $MnSiO_4$, SiO_2	Film-like

2.2 Principle of pyrometry

The previous section is focused on the selective oxidation of AHSS, which would cause the change of emissivity during annealing and affect the pyrometry measurements. The principle of pyrometry is thus important to be understood in order to improve and optimize the temperature measurements in the furnace.

Increasingly stringent demands for product material properties, surface quality, dimensional tolerances, and productivity require manufacturers to monitor and control critical process parameters, chief among them temperature. The ability to effectively and accurately measure steel strip temperature in continuous galvanizing without contacting the strip is critical to ensure the mechanical properties of the steel [30-32]. Non-contact infrared pyrometers are used extensively in continuous galvanizing to carry out near-instantaneous non-contact measurement of temperatures of surfaces. However, the pyrometry measurements are affected by the change of radiative properties during annealing. In addition, the temperature control of the furnace is also influenced by the radiative heating of the steel strips due to the change of radiative properties (e.g. emissivity, absorptivity).

In pyrometry, as shown in Figure 2-2, surface temperature is inferred with the signal generated at a given detection wavelength, which is found by integrating the spectral intensity over the spectral width $\Delta\lambda$ of a bandpass filter centered at the detection wavelength. At a given detection wavelength, the signal (voltage) received by the pyrometer is proportional to the total emitted energy from the surface,

$$S \propto Q_e \tag{1.10}$$

where S is the signal received by the pyrometer and Q_e is the total energy emitted by the object's surface. Since S is proportional to Q_e at a given detection wavelength, Eq. (1.10) can be rewritten as

$$S = \kappa_\lambda(\lambda_d) \cdot Q_e \tag{1.11}$$

where κ_λ is the optoelectronic efficiency of the pyrometer. Note that the total energy, Q_e, is related to the integral of emitted spectral intensity over the spectral width $\Delta\lambda$ of a bandpass filter centered at the detection wavelength, and the solid angle, $d\Omega$ and detection area, dA.

$$\begin{aligned} Q_e &= \int_{A_d}\int_{\Delta\Omega_d}\int_{\Delta\lambda} I_\lambda(\lambda_d, T, \theta)\cos\theta \, d\lambda \, d\Omega \, dA \\ &= \int_{A_d}\int_{\Delta\Omega_d}\int_{\Delta\lambda} \varepsilon_\lambda(\lambda_d, T, \theta)\cdot I_{b\lambda}(\lambda_d, T)\cos\theta \, d\lambda \, d\Omega \, dA \end{aligned} \tag{1.12}$$

where A_d and $\Delta\Omega_d$ are the detector area and detection solid angle, respectively, $I_{b\lambda}$ is the blackbody intensity, T is the surface temperature, $\varepsilon_\lambda(\lambda, T, \theta)$ is the spectral emissivity, and θ is the angle formed between the optical axis of the pyrometer and the surface normal of the streel strip, as indicated in Figure 2-3.

Combing Eq. (1.11) and Eq. (1.12) results in

$$\begin{aligned} S &= \int_{A_d}\int_{\Delta\Omega_d}\int_{\Delta\lambda} \kappa_\lambda(\lambda_d)\cdot\varepsilon_\lambda(\lambda_d, T, \theta)\cdot I_{b\lambda}(\lambda_d, T)\cos\theta \, d\lambda \, d\Omega \, dA \\ &= \Delta\Omega_d A_d \cdot \int_{\Delta\lambda} \kappa_\lambda(\lambda_d)\cdot\varepsilon_\lambda(\lambda_d, T, \theta)\cdot I_{b\lambda}(\lambda_d, T)\cos\theta \, d\lambda \end{aligned} \tag{1.13}$$

Note that it is reasonable to assume $\theta=0°$ if the pyrometry measurements are carried out at near-normal incidence, which is often the case. Consequently, Eq. (1.13) can be stated as,

$$S = \Delta\Omega_d A_d \cdot \int_{\Delta\lambda} \kappa_\lambda(\lambda_d) \cdot \varepsilon_\lambda(\lambda_d, T) \cdot I_{b\lambda}(\lambda_d, T)\, d\lambda \tag{1.14}$$

In practice the spectral width of the bandpass filter is sufficiently narrow, as depicted in Figure 2-4. In such case Eq. (1.14) can be expressed by

$$S = \kappa_\lambda(\lambda_d)\Delta\Omega_d A_d \cdot \varepsilon_\lambda(\lambda_d, T) \cdot I_{b\lambda}(\lambda_d, T)\Delta\lambda \tag{1.15}$$

Note that at sufficiently small values of λT, the blackbody spectral intensity, $I_{b\lambda}$, is given by the Planck distribution [33].

$$I_{b\lambda}(\lambda, T) = \frac{C_1}{\lambda^5\left[\exp\left(\frac{C_2}{\lambda T}\right) - 1\right]} \approx \frac{C_1}{\lambda^5\left[\exp\left(\frac{C_2}{\lambda T}\right)\right]} \tag{1.16}$$

where $C_1 = 2hc_0^2 = 1.19\times10^{-16}$ W·m^2 and $C_2 = hc_0/k_B = 1.439$ μm·K, and h and k_B are the Planck and Boltzmann constants, respectively, and c_0 is the speed of light in vacuum. A plot of blackbody radiation at three different radiator temperatures is shown in Figure 2-4. Substituting Eq. (1.16) into Eq. (1.15) results in

$$S = \Delta\Omega_d A_d \cdot \kappa_\lambda(\lambda_d) \cdot \varepsilon_\lambda(\lambda_d, T) \cdot \Delta\lambda \frac{C_1}{\lambda_d^5\left[\exp\left(\frac{C_2}{\lambda_d T}\right)\right]} \tag{1.17}$$

By re-organizing Eq. (1.17), the final form the signal can be expressed as

$$S = C_{\lambda d} \cdot \frac{\varepsilon_\lambda(\lambda_d, T)}{\lambda_d^5\left[\exp\left(\frac{C_2}{\lambda_d T}\right)\right]} \tag{1.18}$$

where $C_{\lambda d}$ is the calibration constant.

The scheme used to relate T from S depends on the number of wavelengths at which the spectral irradiance is measured. Typically, there are three main categories of pyrometers that

employ Eq. (1.18) to derive target temperature: single wavelength, dual-wavelength, and multi-wavelength pyrometers. Single wavelength pyrometry utilizes intensity measured at a single wavelength to determine the surface temperature directly through Eq. (1.18). Dual-wavelength pyrometry was first introduced in steel making applications. It requires intensity measurements at two wavelengths coupled with an emissivity compensation algorithm to infer the temperature [34],

$$T = C_2 \left(\frac{1}{\lambda_{d,B}} - \frac{1}{\lambda_{d,A}} \right) \Bigg/ \ln \left[\frac{S_A}{S_B} \left(\frac{\lambda_{d,A}}{\lambda_{d,B}} \right)^5 \frac{\varepsilon_{\lambda d,B}}{\varepsilon_{\lambda d,A}} \right] \tag{1.19}$$

where $C_2 = hc_0/k_B = 1.439\ \mu m \cdot K$, S_A and S_B are the signal voltages measured at the two detection wavelengths $\lambda_{d,A}$ and $\lambda_{d,B}$, and $\varepsilon_{\lambda d,B}/\varepsilon_{\lambda d,A}$ is the ratio of spectral emissivity at these wavelengths, which must be specified. Thus, understanding the spectral variation of ε_λ with respect to λ, and how it evolves as the steel is processed, is critical for accurate pyrometry. Knowing the fact that spectral, directional emissivity can be related to the spectral, directional-hemispherical reflectance given the same incident angle according to Kirchhoff's law [33],

$$\varepsilon_\lambda(\Omega_i) = 1 - \rho_{\lambda,d\text{-}h}(\Omega_i) \tag{1.20}$$

where Ω_i denotes the incident direction. At normal incidence, for example, Eq. (1.20) becomes,

$$\varepsilon_\lambda = 1 - \rho_{\lambda,d\text{-}h} \tag{1.21}$$

A number of studies have been carried out on the effectiveness of using dual-wavelength emissivity compensation algorithms for aluminum and steel surfaces [34-36]. In general, for the industrial pyrometers, the detection angle is near normal and the detection wavelengths are between 0.6 μm and 3.0 μm.

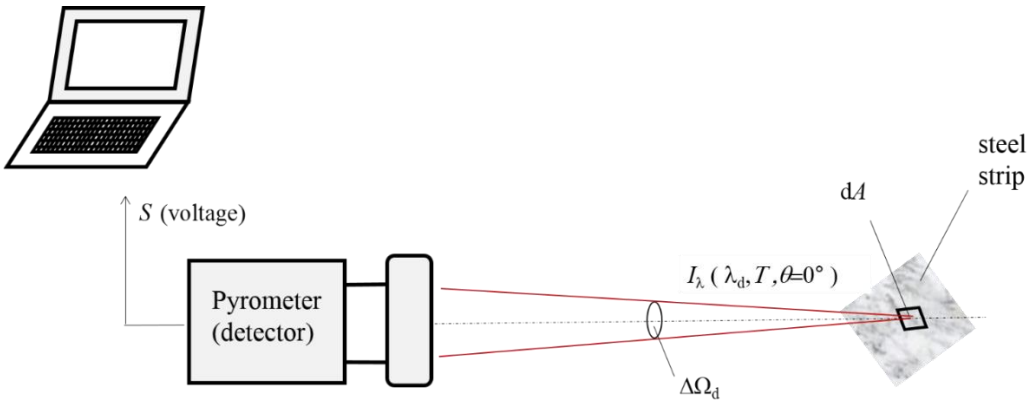

Figure 2-2. Schematic view of pyrometer receiving radiation from the object having temperature T. The voltage, S, induced by the pyrometer is proportional to received total energy, Q_e emitted from the object that is affiliated with the object's temperature via spectral intensity, $I_\lambda(\lambda_d, T, \theta)$, and spectral emissivity, $\varepsilon_\lambda(\lambda_d, T, \theta)$. The temperature of the object is therefore inferred from received voltage, through Eq. (1.18).

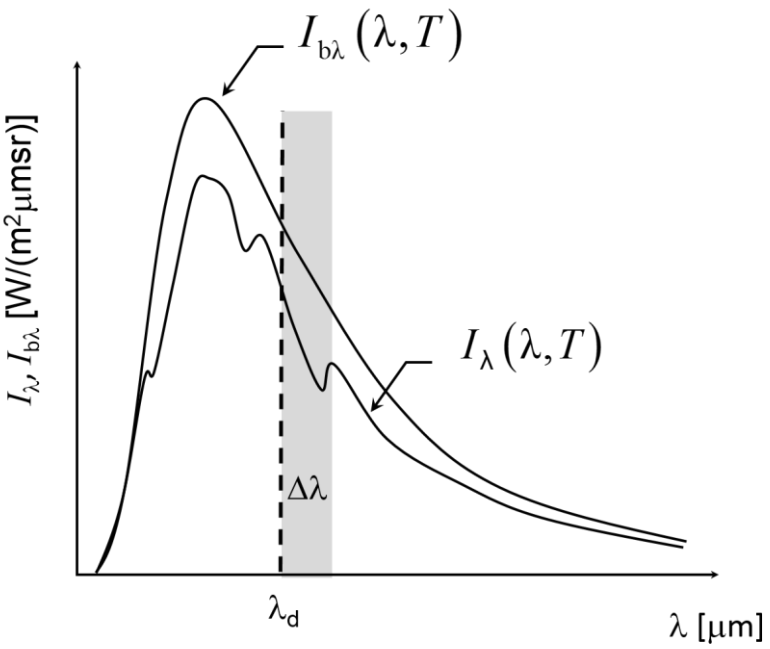

Figure 2-3. The bandwidth $\Delta\lambda$ with respect to spectral intensity curve of a blackbody, $I_{b\lambda}(\lambda,T)$ and a real surface, $I_\lambda(\lambda,T)$. Parameters such as $\kappa_\lambda(\lambda_d,T)$, $\varepsilon_\lambda(\lambda_d,T)$ and $I_{b\lambda}(\lambda_d,T)$ in Eq. (1.14) can be taken out of the integral, in case $\Delta\lambda$ is sufficiently small.

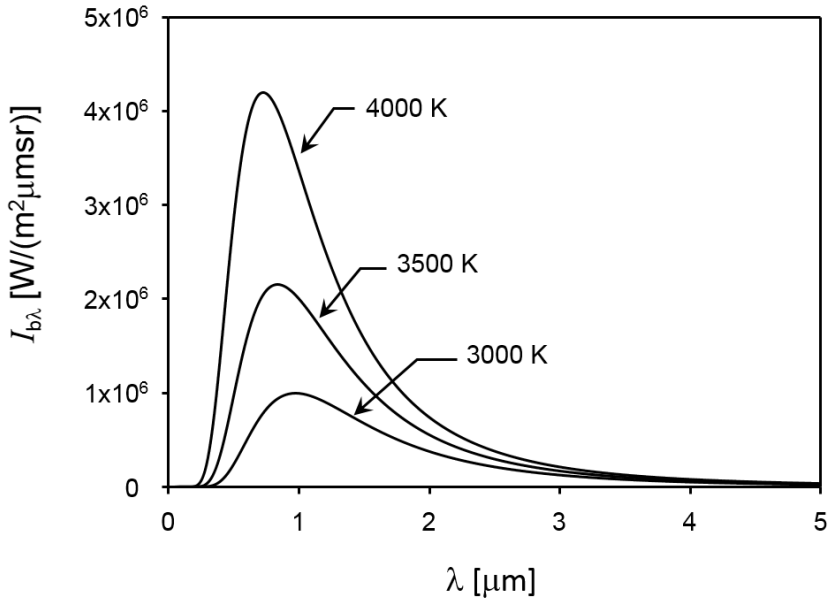

Figure 2-4. Graphs of blackbody radiation at three different radiator temperatures. The spectral intensity increases with temperature, and the peak of the spectrum shifts toward the shorter wavelength spectrum.

Dual-wavelength pyrometers are generally more reliable than single wavelength pyrometers with respect to highly oxidized metallic and nonmetallic surfaces, due to the grey surface characteristic and emissivity compensation algorithm. Some studies highlight that single and dual-wavelength methods yield unacceptable errors in surface temperature measurement as a result of their inability to capture the complex spectral emissivity behavior of aluminum alloy surfaces [37]. This gives rise to multi-wavelength pyrometry, which can compensate for spectral variations in emissivity [38]. In general, two mathematical methods are used to infer the surface temperature from simultaneous spectral radiosity measurements: the exact technique and the least-squares technique [39]. The exact technique employs an emissivity model with n unknown coefficients and spectral intensity measurements from $n + 1$ wavelengths, and then incorporates these into Eq. (1.19) to solve the unknown coefficients along with target temperature. On the other hand, the least squares technique utilizes an emissivity model with up to n unknown coefficients

and spectral intensity measurements carried out at a minimum of $n + 2$ wavelengths to infer the spectral emissivity and temperature of the target surface by minimizing the least square function.

$$(T, \varepsilon_\lambda) = \arg\min \left\{ \sum_{i=0}^{p} [\ln(I_{\lambda,meas,i}) - \ln(I_{\lambda,gen,i})]^2 \right\} \tag{1.22}$$

where $I_{\lambda,\mathrm{meas,i}}$ is the measured spectral irradiance and $I_{\lambda,\mathrm{gen,i}}$ is the generated spectral irradiance that minimizes the sum of squared errors using the emissivity compensation algorithm.

This technique avoids the over-fitting errors of the exact technique when more than three wavelengths are used. Several studies had evaluated the robustness of these techniques [39-43]. The conclusion that can be drawn from these studies is that at present no promising emissivity models exist that can be employed by the pyrometer for purpose of accurate temperature measurement, underlying a variety of target's surface conditions. Therefore, knowing the exact correlation between the spectral emissivity and surface state of the target is of paramount importance for the improvement of pyrometry.

Overall, the main problem in the application of radiation pyrometry to the measurement of true surface temperatures is the large error arising from the uncertain spectral emissivity of the surface that varies with time during annealing. A secondary issue concerns the fact that the background radiation in the furnace will reflect off the steel strip to the pyrometer, resulting in an erroneous temperature reading. The wedge pyrometer configuration is largely unaffected by background radiation or emissivity changes in the steel strip. However, this method is also very sensitive to alignment and the measured temperature is a combination of strip and roller. In addition, it is not always possible to implement the device for any designated measuring locations of the strip.

It is well known that the variation of spectral emissivity depends not only on temperature, but also surface topography (which may include contributions from an oxide) of the target. To this end, further work is needed to connect the evolution of spectral emissivity and surface topography of the target surface, in order to obtain desirable emissivity functions to apply in pyrometry algorithms.

Chapter 3 EM Theories and Models[2]

Chapter 2 illustrates the selective oxidation and principles of pyrometry that are critical to the change of radiative properties and the improvement of temperature measurement. The correlation between the surface states and the radiative properties of steel strips, however, is also important to understand prior to the development of a robust emissivity model for the pyrometry and furnace heating control. For this purpose, this chapter is focused on the link between the surface state and radiative properties of AHSS alloys in the context of numerical models underlying the electromagnetic (EM) wave theory.

When an EM wave impinges on a plane interface between two media, it is reflected according to well-known laws: the reflected field depends on the wavelength, angle of incidence and the electrical properties of the two adjoining media. In the case of smooth interfaces Maxwell's equations can be used directly to derive the reflected field and radiation properties (e.g. spectral emissivity) based on the complex refractive indices of the bulk material. However, this method cannot predict the properties of non-smooth surfaces [44-46], or surfaces contaminated by an oxide layer, both of which prevail for AHSS steel strip undergoing intercritical annealing [47]. In general, radiative properties are dominated by two effects: the thin film effect, and the roughness effect. The radiative properties can be interpreted *via* thin film interference theory for the case of a smooth

[2] Some of the contents in this chapter are presented in the following papers:

K. Lin, K.J. Daun, Interpreting the spectral reflectance of advanced high strength steels using the Davies' model, J. Quant. Spectrosc. Radiat. Transf., vol. 242, pp. 106796, 2020. (doi.org/10.1016/j.jqsrt.2019.106796)

K. Lin, F.K. Suleiman, K.J. Daun, Interpreting the radiative properties of advanced high strength steel using the geometric optics ray-tracing approximation, Int. J. Heat Mass Transf., 176 (2021) 121429. (doi.org/10.1016/j.ijheatmasstransfer.2021.121429)

oxide film deposited on a smooth substrate. In the case of a rough metal surface, models derived from electromagnetic wave scattering theory with approximations can be used to evaluate the radiative properties. When a rough oxide is deposited on a rough metal surface, the radiative properties are affected by both thin film and roughness effects, and therefore, ideally, these two effects should be considered simultaneously via a hybrid thin film/geometric optics model when the oxide layer has the same surface profile as that of the substrate.

3.1 Surface roughness parameters

Parameters used to characterize surface roughness can be categorized into two groups: amplitude parameters and spatial parameters. Amplitude parameters include arithmetic average surface roughness, R_a, root-mean-square roughness, R_q, and the surface height deviation, σ. If we consider a surface profile $z(x)$ in which profile heights are measured from a reference line in Figure 3-1 (e.g. using a contact or optical profilometer), these parameters are found from

$$R_a = \frac{1}{L}\int_0^L |z - m|\, dx$$

$$R_q = \frac{1}{L}\int_0^L z^2\, dx \tag{2.1}$$

and

$$\sigma = \frac{1}{L}\int_0^L (z - m)^2\, dx \tag{2.2}$$

where L is the sampling length and m is the mean value of surface height. For the special case where the mean of surface height is zero,

$$\sigma = R_q \tag{2.3}$$

In many cases, σ can be expressed in terms of the mean arithmetic deviation, R_a of the profile according to the relationship $\sigma=1.25R_a$ [48].

The most commonly used spatial parameter is correlation length, which describes the lateral distribution of the surface. The exact definition and derivation of correlation length may differ based on different theories and interpretations. Nevertheless, the most general definition is the measure of how quickly the random event decays, and the derivation of it is associated with the autocorrelation function, $C(\tau)$[49],

$$C(\tau) = \frac{R(\tau) - m^2}{\sigma^2} \tag{2.4}$$

where τ is the variable spatial separation and $R(\tau)$ is the autocovariance function, which is a measure of how well future values of the function can be predicted based on past observations. In general, the autocovariance function is given by

$$R(\tau) = \frac{1}{L}\int_0^L z(x)\, z(x+\tau)\, dx \tag{2.5}$$

For engineering surfaces, the autocorrelation function often obeys

$$C(\tau) = \exp(-\tau / \alpha) \tag{2.6}$$

where α is a constant. The correlation length can thus be defined as the value that makes autocorrelation function equal to 1/e, which is equal to α for the exponential autocorrelation function. Besides the autocorrelation function, the other commonly used function to evaluate the spatial information of a surface is the power spectral density function, which can be derived by a Fourier transform of the profile data $z(x)$

$$P(\omega) = \frac{1}{L}\left[\int_0^L z(x)\ \exp(-i\omega x)\ dx\right]^2 \tag{2.7}$$

where ω is the wave frequency. The physical meaning of the power spectral density function is that the surface consists of a superposition of different levels of frequencies (wavelengths) of waves having magnitudes that decline with increasing frequency so that the amplitude is proportional to wavelength. The power spectral density itself represents the amplitude of the wave at a given frequency, and is related to autocorrelation function by

$$R(\tau) = \frac{1}{2\pi}\int_{-\infty}^{\infty} P(\omega)\ \exp(i\omega\tau)\ d\omega \tag{2.8}$$

Therefore, using Eq. (2.4), the correlation length, β, can be obtained from a given surface profile, $z(x)$.

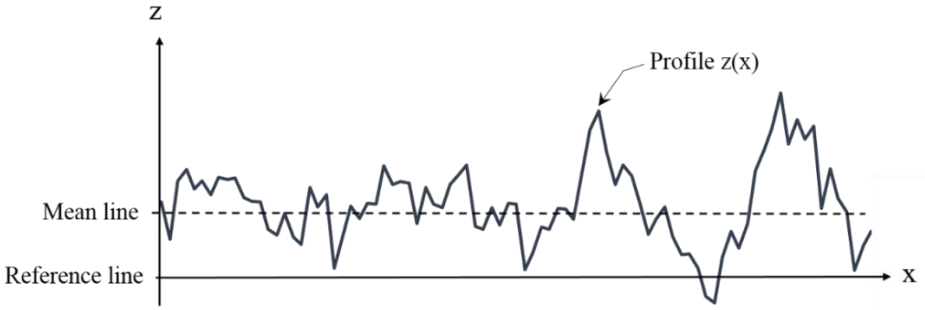

Figure 3-1. Schematic view of one dimensional surface roughness profile with reference and mean line. The plot is depicted based on a random surface in one dimension. Surface parameters derived based on the reference line can be different from that of derived based on the mean line.

3.2 Thin film effect[3]

When a clean metallic surface is exposed to air, a thin oxide film is formed. The growth of it is assumed to be driven by an electric field created by quantum mechanical effect on the metal surface, and the growth is stopped when electrons are not allowed to pass through the thickness of the film [50]. However, the oxide film can continue to grow when the temperature increases due to annealing. When a plane EM wave is incident upon the oxide film with thickness h, as illustrated in Figure 3-2, the reflected electric field is obtained by solution of Maxwell's equations as a boundary problem composed of parallel media, where n_1, k_1, n_2, and k_2 are the real and imaginary components of the complex refractive index of the oxide film and substrate metal, respectively, assuming homogeneous and absorbing media. On the other hand, the growth of oxide film during annealing will cause constructive and destructive interferences to the incident wave at the interface of the metal surface and oxide film, resulting in oscillations in the sample reflectivity values on a time-resolved basis [51]. Consequently, an oscillatory effect can be found in the measured spectral emissivity, as shown in Figure 3-3.

Consider the scenario of an oxide film of thickness h and uniform composition forming on a smooth metal surface. If the oxide film thickness is relatively thin where the thickness is on the order of, or less than the incident wavelength, Figure 3-2, the film causes a phase shift, leading to oscillations in the spectral reflectivity with respect to wavelength [47] that depend on the complex refractive index of the oxide film, $\tilde{n}_2 = n_2 + ik_2$, and the substrate steel, $\tilde{n}_3 = n_3 + ik_3$. (The refractive index of air is $n_1 = 1$.) Maxwell's equations can be solved to obtain the vertical and parallel-polarized reflectances (also known as Airy's formula [52]),

[3] Information presented in this section can be found in a paper submitted to *Metall. Mater. Trans. B*:
K. Lin, M. Pourmajidian, F. K. Suleiman, J. R. McDermid, K. J. Daun, *Effect of annealing atmosphere and steel alloy composition on oxide formation and radiative properties of advanced high strength steel strip.* (2021)

$$\rho_v(\lambda) = \left| \frac{\eta_{12v} + \eta_{23v} \exp(-i\zeta)}{1 + \eta_{12v}\eta_{23v} \exp(-i\zeta)} \right|^2, \quad \rho_p(\lambda) = \left| \frac{\eta_{12p} + \eta_{23p} \exp(-i\zeta)}{1 + \eta_{12p}\eta_{23p} \exp(-i\zeta)} \right|^2 \tag{2.9}$$

where the reflectance parameters, η_{12v}, η_{23v}, η_{12p}, η_{23p} at the interfaces are expressed by

$$\eta_{12v} = \frac{n_1 \cos\theta_1 - \tilde{n}_2 \cos\theta_2}{n_1 \cos\theta_1 + \tilde{n}_2 \cos\theta_2}, \quad \eta_{23v} = \frac{\tilde{n}_2 \cos\theta_2 - \tilde{n}_3 \cos\theta_3}{\tilde{n}_2 \cos\theta_2 + \tilde{n}_3 \cos\theta_3} \tag{2.10}$$

$$\eta_{12p} = \frac{\tilde{n}_2 \cos\theta_1 - n_1 \cos\theta_2}{\tilde{n}_2 \cos\theta_1 + n_1 \cos\theta_2}, \quad \eta_{23p} = \frac{\tilde{n}_3 \cos\theta_2 - \tilde{n}_2 \cos\theta_3}{\tilde{n}_3 \cos\theta_2 + \tilde{n}_2 \cos\theta_3} \tag{2.11}$$

and

$$\zeta = \frac{4\pi \tilde{n}_2 h \cos\theta_2}{\lambda} \tag{2.12}$$

where ζ is the phase difference of reflected wave. The incident angle, θ_1, is taken to be 10° (the angle of incidence for the spectrophotometer and spectrometer) and is related to θ_2 and θ_3 by Snell's law,

$$n_1 \sin\theta_1 = \tilde{n}_2 \sin\theta_2 = \tilde{n}_3 \sin\theta_3 \tag{2.13}$$

In the case of unpolarised incident radiation, the specular reflectance can then be obtained from $\rho_\lambda = [\rho_v(\lambda) + \rho_p(\lambda)]/2$, and, since emission is always unpolarised, $\boldsymbol{\varepsilon}_\lambda = 1 - \rho_\lambda$.

To sum up, amongst roughness, many studies have shown that oxidation has the most important influence on the spectral emissivity of metals, and the observed variation of spectral emissivity could be related to the increase of the oxide layer thickness [51, 53-56].

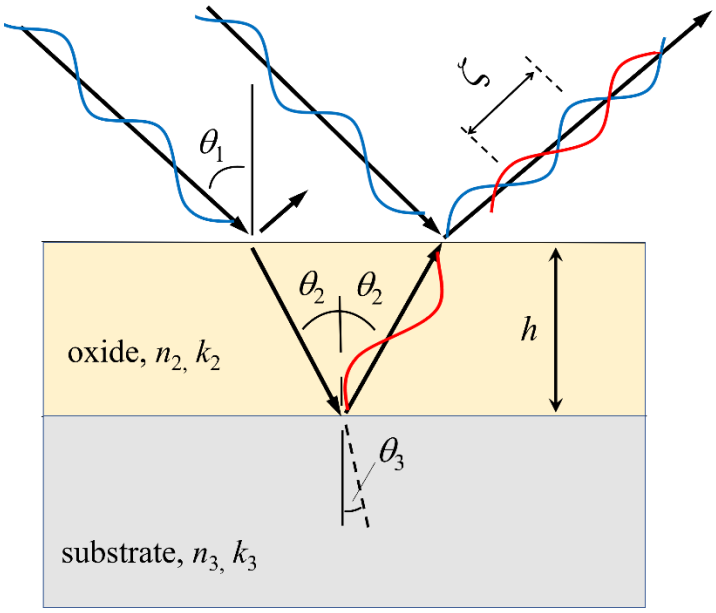

Figure 3-2. Schematic view of radiation incident on oxide film formed upon a substrate material [47].

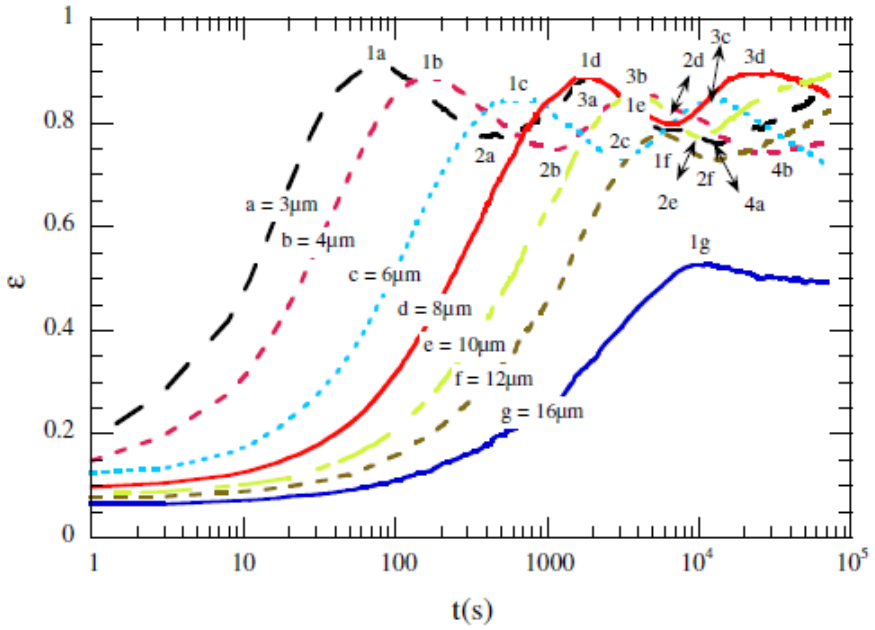

Figure 3-3. Experimentally measured spectral emissivity variations with time as oxide growth on metal surface [51].

3.3 Surface roughness effect

No real surface is perfectly smooth due to irregularities ranging from the atomic scale, caused by inner structure of the material, to the mesoscopic and macroscopic scale caused by the defects in processing [57]. These effects greatly impact the way in which EM waves are reflected by surfaces, depending on the wavelength of the waves [58-61]. The first work on this subject was done by Lord Rayleigh, who considered the issue of light incident upon a sinusoidal surface at normal incidence [62]. The Rayleigh roughness criterion has been used in several models thereafter to describe this scattering phenomenon. Today, the problem of rigorous computation of the field scattered by randomly rough surfaces remains one of the most difficult to handle, and, owing to its considerable impact on a variety of engineering applications, numerous studies had been carried out over the past decades. An overall review of these studies can be found in [63], while McGinn and Sykes [64] summarizes the techniques used to model the scattering of EM waves from rough surfaces. These models are mainly derived from Maxwell's equations using either analytical or numerical approaches [44-46, 65-108]. However, the models proposed or examined in these studies are subject to important restrictions, and often require intensive computational time. In addition, the models limited to one-dimensional surfaces [77, 82-84, 86-89, 102, 107], or on two-dimensional surfaces in limited cases [90, 91, 97, 98, 105, 106, 108].

Due to the urgent need to obtain rigorous, computationally-effective solutions to EM wave scattering problems, several models with approximations had been developed. One of the most straightforward approaches is due to Agababov [109], based on an approximation that the radiant energy leaving the roughness cavity of the surface is equal to that of a smooth surface line located right above the cavity. While the Agababov model can predict the variation of spectral emissivity with respect to wavelength and roughness for certain types of mechanically-roughened aluminum

surfaces [48], it does not constitute a rigorous solution to EM wave scattering problems. It was suggested that more work should be done to examine the reliability of the model subject to a broader range of measurements, materials and surface conditions.

In general, there are two approximations used in analytical models: the small roughness perturbation approximation (or Rayleigh-Rice approximation) and Kirchhoff approximation (or Kirchhoff's tangent approximation) [80, 110]. The perturbation approach is valid when the root-mean-square roughness is small compared to the incoming wavelength. It has been verified in the case of low-frequency acoustic scattering from the sea surface [111]. The Kirchhoff approximation, on the other hand, is not restricted to the ratio of RMS roughness and incident wavelength per se, and therefore it has been used for applications involving a broad range of roughness scales and wavelengths [112-114]. To this end, the present study is focused on this approximation.

The Kirchhoff approximation is valid for surfaces having large radius of curvature compared to the incident wavelength, and has been used to predict the spectral, bi-directional reflectance of rough metal surfaces. The two most widely used are Davies's model and Beckmann's model [115]. Davies's model is applicable to both slightly rough surfaces ($\sigma/\lambda<<1$) and very rough surfaces ($\sigma/\lambda>1$) with two separate forms, where σ is the surface height deviation (RMS roughness). Beckmann's model applies to all levels of surface roughness with a general form, which is more complicated in terms of evaluation compared with Davies's model. Both models were derived by solving the Helmholtz integral of scattered field based on Kirchhoff's tangent plane approximation and the assumption of a Gaussian surface roughness; they are thus closely related and reduce to the identical form under certain conditions. Typically, Beckmann's model applies to wide range of optical roughness while Davies model is restricted to surface

contours with very small slopes and to the limiting cases of very small and very large optical roughness.

The geometric optics approximation, often simply referred to as “ray tracing”, is an approximation to the exact numerical integration methods underlying the electromagnetic wave theory [116]. In contrast to many other approximate methods, including the Kirchhoff approximation, the geometric optics approximation incorporates both shadowing and multiple scattering, which is easily implemented for computational purposes through intuitive geometrical arguments. It generally serves as a multiple scattering solution which traces energy of incident EM ray bundles until they leave the surface. At each local interaction between the wave and surface points, the wave is reflected in a specular manner and Fresnel’s equation is used to predict the amount of energy absorbed by the surface. This approach has also been proposed to effectively obtain the bidirectional or directional-hemispherical reflectance from a period or statistically rough metal surface [117, 118], and can reproduce experimental data under certain conditions [119-122]. This approximation was considered valid when the normalized correlation length, τ/λ, as well as the normalized rms roughness, σ/λ, are larger than unity [123].

Although these models have been deployed to predict the scattering of EM waves from rough surfaces, few studies have actually confirmed if they are applicable to rough AHSS samples. In addition, most of the predictions are for bidirectional or specular reflectance [58, 115, 124-129], and not the directional-hemispherical reflectance, which is related to the spectral, directional emissivity important to pyrometry measurement (Eq. (1.20)). The diffuse and specular behavior underlying the wavelength-dependent radiative properties are also worth investigating.

To this end, this thesis investigates the effect of surface roughness on radiative properties of AHSS samples underlying the above-mentioned approaches. The detailed approaches and

background are illustrated in the following sections starting with Agababov's model (Section 3.3.1), which serves as a potential approach to relate the radiative properties with surface roughness parameters. Following that, fractal theory (Section 3.3.2) will be introduced; any real surfaces have fractal characteristics, which are unaccounted for by the Agababov model. The contribution of fractal geometry to the radiative properties of rough metal surfaces is presented, and the disadvantages of using these models are drawn. The concepts of bi-directional and directional-hemispherical reflectance, which are important to the characterization of radiative properties, are illustrated in Section 3.3.3. Following that, Kirchhoff-Helmholtz diffraction theory (Section 3.3.4), as a general theory applied to the analytical solution of EM wave scattering problem, is presented. The criterion of employing this theory (Kirchhoff approximation), for rough metal surfaces is illustrated thereafter in Section 3.3.5. Models derived by using this theory to obtain the spectral reflectance are then illustrated in Section 3.3.6, and the criteria that define a "rough" surface are presented in Section 3.3.7. Due to the fact that the Kirchhoff approximation does not account for multiple scattering, which is an important factor specifically when the surface becomes optically rough, the geometric optics approximation along with its detailed algorithm are defined in Section 3.3.8. Finally, the EM diffraction models for diffuse and specular reflectances, which become more prominent as the wavelength becomes large and is greater than the surface roughness, are illustrated Section 3.3.9.

3.3.1 Agababov model

Using geometric optics, Agababov developed a model for the emissivity of gray-diffuse rough surfaces having thermal and optical homogeneity [48, 109, 130-132]. As illustrated in Figure 3-4, the local surface roughness is regarded as a depression of area A_r while the smooth surface area

A_s is that of a membrane that covers the surface. Based on the scenario of energy balance between the total energy radiation from the rough surface and that from a smooth surface, it can be shown that

$$\varepsilon_r = \left[1 + \left(\frac{1}{\varepsilon_s} - 1 \right) \frac{Y_s}{Y_r} \right]^{-1} \tag{2.14}$$

where Y_s, Y_r are the surface parameters used to approximate the smooth and rough surface area, respectively. Specifically, for an isotropic rough surface having small surface inclinations, the surface parameter Y is defined as,

$$Y = (1 + \pi^2 \nu^2 \sigma^2)^{-1} \tag{2.15}$$

where ν is the number of intersections between the mean line and the surface profile per unit length of the mean line, and σ is the surface height deviation or RMS roughness defined by Eqs. (3.1)-(3.2).

In principle, Eqs. (2.14)-(2.15) can be used to predict the emissivity of a rough surface from the known emissivity of a surface made of the same material but having a different roughness, provided the surface roughness parameters (ν and σ) of both surfaces are known. It should be noted that this model is derived based on assumptions of a grey surface and isotropic surface distributions, and the analysis is restricted to one dimension. Furthermore, the roughness parameters (ν, σ) used to approximate the surface area A_r and A_s, may not be physically robust. Therefore, this approach would not be expected to work well for non-grey or non-isotropic surfaces as the roughness parameters vary with location and direction. In this scenario it would not be possible to obtain a set of unified roughness parameters from all directions of the surface, in the estimation of radiation properties. As a result, the non-uniform distribution of these parameters

across each direction of the surface could lead to inaccurate results. The ability of Agababov's model to predict the emissivity of the dual phase steel of interest to this study is presented in Section 4.1.

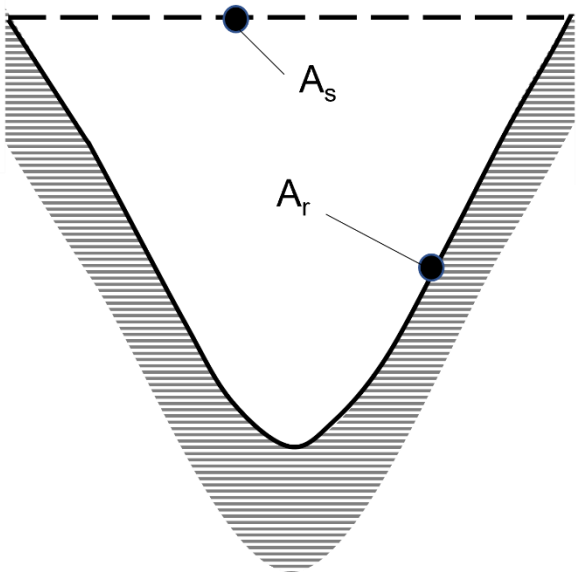

Figure 3-4. Schematic view of the theory upon which Agababov model is derived [112]. Parameters A_r and A_s denote the surface area of the roughness cavity and that of the corresponding imaginary smooth surface above the cavity. Based on the scenario of radiative energy balance between the total energy radiation from the rough surface and that of from smooth surface, the formula that relates the emissivity from a rough surface, ε_r, to that of a smooth surface, ε_s, can be derived.

3.3.2 Fractal theory

When the surface roughness arises from random processes, the deviation of a surface from its mean plane is also assumed to be a random process, for which statistical parameters such as variances of the height, the slope and the curvature can be used to describe the surface topography [133]. However, surface topography is often a *non-stationary* random process, and the variances of height, the slope and curvature depend intensively on resolution of roughness-measuring instrument or any other implicit filter and are thus not unique [134]. In addition, the surface height distribution may vary with sampling length [135, 136]. Consequently, measurements using different sampling

lengths or resolution would yield different values of these statistical parameters for identical surfaces [137].

Randomly rough surfaces also exhibit geometric self-similarity and self-affinity. Similar appearances of the surface could be observed when the same area of the surface is repeatedly magnified; consequently, any point on the surface is, technically, non-differentiable [49]. These fractal-like surface features can be encoded by the Weiestrass-Mandebrot function (W-M function) [138]

$$\zeta(x) = G^{D\text{-}1} \sum_{k=k_1}^{\infty} \frac{\cos 2\pi\gamma^k x}{\gamma^{k(2\text{-}D)}} \tag{2.16}$$

where G is the scaling constant that depends on the roughness structure and γ determines the density of the spectrum and the relative phase differences between the spectral modes, and D represents the fractal dimension. Eq. (2.16) is therefore capable of providing information on the roughness structure at all length scales within the fractal regime by making measurements at one scan length. The fractal dimension, D, ranges from 1 to 2 and is primarily related to the relative power of the frequency contents (power spectrum) [135]. Based on Eq. (2.16), the power spectrum of the W-M function is given by

$$P(\omega) = \frac{G^{2(D\text{-}1)}}{\ln\gamma} \frac{1}{\omega^{5\text{-}2D}} \tag{2.17}$$

This power law behavior of Eq. (2.17) is the essence of a fractal characterization of rough surfaces. The fractal dimension, D, can thus be obtained from the slope of $P(\omega)$ plotted as a function of ω on a log-log scale. Fractal dimension plays critical role in characterizing the fractal degree of a surface [135, 136].

The scattering of waves by fractal surfaces has been studied for both monochromatic waves [139] and pulses [140]. The essential difference between the theory for fractal surfaces and the usual rough surface is attributed to the assumptions about the correlations on the surface: there are infinite correlation lengths along the fractal surface due to the fact that the fractal features exhibit long range order [63]. Consequently, it is not appropriate to use correlation functions and associated correlation lengths to describe fractal surface properties. Employing the theory proposed by Berry and Blackwell [140], it was found that a pulse scattered from a fractal surface will decay in a different manner than if the surface were non-fractal; the power decays as $\tau^{-(3-D)}$ for a fractal surface, instead of exponentially as for a non-fractal surface. In reality, surfaces may be fractal over a local size range, such that the limit of geometrical optics still applies for small enough wavelengths, and an upper cut-off limit exists for the longest wavelength in the surface spectrum. Therefore, the RMS roughness does not have useful meaning for fractal surfaces and thus the profilometry-measured roughness is virtually useless in relating the surface with the scattering properties. Instead, the scattering properties of a surface will depend strongly on a range of roughness scales around the wavelength of the incident wave and the presence of extremely fine structure or very long range order will not affect the scattering behaviour to an appreciable degree [63].

A more recent and comprehensive study on the reflection of EM waves from fractal surfaces was carried out by Majumdar and Tien [148], who developed a model with fractal dimension for the prediction of bidirectional and specular reflectance of metal surfaces. Like other typical reflection models, it incorporates Helmholtz-Kirchhoff diffraction theory to solve the scattered field, by assuming the surface roughness is randomly distributed according to a Gaussian statistical profile. Accordingly, the bi-directional reflectance model was obtained by replacing the

averaged statistical height difference of two random surface points in the Helmholtz integral of scattered field with power spectrum of Weiestrass-Mandebrot (W-M) function from Eq. (2.17),

$$<(\zeta_1 - \zeta_2)^2> = \int_{-\infty}^{\infty} P(\omega)(e^{i\omega(x_1 - x_2)} - 1)d\omega \tag{2.18}$$

By incorporating Eq. (2.17) and Eq. (2.18) into the Kirchhoff-Helmholtz integral of scattered intensity, the bi-directional reflectance can be expressed as

$$<\rho\rho^*> = \frac{T^2}{4L^2}\int_{-L}^{L}\int_{-L}^{L} e^{i\eta(x_1 - x_2)} e^{-\upsilon|x_1 - x_2|^{(4-2D)}} dx_1 dx_2 \tag{2.19}$$

where $<\rho\rho^*>$ is the bi-directional reflectance of a perfectly conducting rough surface, L is the sampling length, and x_1 and x_2 are two random points on the surface. The parameters η and υ are given as

$$\eta = \frac{2\pi}{\lambda}(\sin\theta_i - \sin\theta_s) \tag{2.20}$$

$$\upsilon = \frac{4\pi^2}{L^{4-2D}}\left[\frac{\sigma}{\lambda}(\cos\theta_i + \cos\theta_s)\right]^2 \Gamma(2D-3)\sin(2D-3)\frac{\pi}{2} \tag{2.21}$$

where θ_i and θ_s are off-normal incident and reflected angle, respectively, and σ is the surface RMS roughness and λ is the radiation wavelength.

Therefore, with given fractal dimension, D, and optical roughness, σ/λ, bidirectional reflectance can be estimated for any rough metal surface. By letting $\theta_i = \theta_s$, the model can be further simplified to find specular reflectance. In this case, Eq. (2.19) reduces to

$$< \rho\rho^{*} >= 2\sum_{m=0}^{\infty} \frac{(-1)^{m}(2^{4-2D}\hat{\upsilon})^{m}}{m![(4-2D)m+1][(4-2D)m+2]} \tag{2.22}$$

where $\hat{\upsilon} = \upsilon L^{4-2D}$. This formula serves as a general solution for specular reflectance for any given fractal dimension and optical roughness.

It should be noted that evaluating Eq. (2.22) is computationally-intensive. These models also assume one-dimensional roughness, and do not account for two-dimensional artifacts. In addition, with respect to estimating the diffuse reflection component, surface spatial parameters such as correlation length are crucial, whereas the proposed fractal model offers insufficient information about the correlation length, but only fractal dimension. Furthermore, precise evaluation of the fractal dimension, *D*, is challenging and is sensitive to the resolution limit of the instrument among other sources of measurement uncertainty. Overall, effective and precise estimation of directional-hemispherical reflectance through the fractal model is quite challenging. The model is, therefore, not useful in the present study.

3.3.3 Definition of directional reflectances

The radiative properties of a surface are often described by both bi-directional reflectance distribution function (BRDF) and directional-hemispherical reflectances that feature the variation of reflectance with respect to the incident and scattered light directions. The BRDF is defined as the ratio of the radiance scattered by a surface into the direction to the collimated irradiance incident on a unit area of the surface. In practice, the BRDF is equal to the scattered power per unit solid angle normalized by the product of the incident power and the cosine of the detector view angle,

$$f_{bi-d}(\theta_{\mathrm{i}}, \varphi_{\mathrm{i}}, \theta_{\mathrm{s}}, \varphi_{\mathrm{s}}) = \frac{I_{\lambda,\mathrm{s}}(\theta_{\mathrm{s}}, \varphi_{\mathrm{s}})}{I_{\lambda,\mathrm{i}}(\theta_{\mathrm{i}}, \varphi_{\mathrm{i}})\cos\theta_{\mathrm{i}} d\Omega_{\mathrm{i}}} \tag{2.23}$$

Where θ_i, φ_i, θ_s, φ_s, $d\Omega_i$ denote the incident polar angle, incident azimuthal angle, scattered polar scattered azimuthal angle, and solid angle of incident, respectively. And $I_{\lambda,s}(\theta_s,\varphi_s)$, $I_{\lambda,s}(\theta_s,\varphi_s)$ are the scattered and incident intensity. Note that the reflectance also depends on the surface temperature, but the *T* notation is omitted here for simplicity.

The directional-hemispherical reflectance, which is defined as the energy scattered into all solid angles divided by the energy incident from a specific direction (θ_i, φ_i),

$$\rho_{\lambda,d\text{-}h}(\theta_i,\varphi_i) = \int f_{bi-d}(\theta_i,\varphi_i,\theta_s,\varphi_s)\cos\theta_s d\Omega_s \tag{2.24}$$

Note that the directional-hemispherical reflectance, $\rho_{\lambda,d\text{-}h}$, is related to the directional emissivity via Eq. (1.20).

Besides BRDF and directional-hemispherical reflectance, another important radiative property is the specular reflectance, which is defined as the ratio of reflected energy in specular direction ($\theta_s = \theta_i$; $\varphi_s = \varphi_i$) to the incident energy,

$$\rho_{\lambda,sp} = \frac{dQ_s(\theta_s=\theta_i;\varphi_s=\varphi_i)}{dQ_i(\theta_i,\varphi_i)} \tag{2.25}$$

3.3.4 Kirchhoff-Helmholtz diffraction theory

Modeling the interaction of EM wave with a material boundary requires solution of the Maxwell equations with appropriate boundary conditions. For surface profiles as complicated as those produced by normal finishing operations on metals, Kirchhoff's diffraction theory, based on Kirchhoff's tangent plane approximation [44], presents a practical method of accounting for randomly-rough surfaces. This theory is based on the Helmholtz integral equation, which serves as

an integral form of the Maxwell equations. The solution to the integral equation requires knowledge of the surface contour and the electric field as well as its normal derivative at each point of the surface. The common procedure adopted to ascertain approximate solutions is to introduce an assumption regarding the total field at the surface in terms of the known incident field.

When an EM wave impinges a rough surface, as shown in Figure 3-5, the waves are reflected off of each point source, and interfere constructively and destructively in the far-field. The surface profile, $\zeta(x,y)$, determines the manner in which the waves interfere, and thus the spectral reflectivity of the surface. In particular, the scattered far-field wave E_2 at any point P at a distance r far away from the surface is given by the Helmholtz integral [141]

$$E_2(P) = \frac{1}{4\pi}\iint_A \left[E\frac{\partial}{\partial n}\left(\frac{e^{ikr}}{r}\right) - \frac{e^{ikr}}{r}\frac{\partial E}{\partial n}\right] dA \tag{2.26}$$

where both time variation and polarization of the wave are ignored. This analysis hinges on modeling the local reflection of the wave at every point on the surface. If the surface is locally flat relative to the incident wave, the integral can be solved by invoking the Kirchhoff tangent plane approximation,

$$E_s = (1+\psi)E_1, \frac{\partial E_s}{\partial n} = (1-\psi)E_1\mathbf{k}_1\cdot\mathbf{n} \tag{2.27}$$

where E_s is the field intensity at the surface, E_1 the incident field, $\mathbf{k}_1$ is the incident wave vector, $\mathbf{n}$ is the local surface normal vector, and ψ is the specular reflectance found by locally-applying Fresnel's equation. For a rectangular surface having an area A, with randomly-distributed heights, after some manipulation it can be shown that the bi-directional reflectance is given by

$$\rho_\lambda = \left\langle \left| \frac{E_2^{\,2}}{E_{20}^{\,2}} \right| \right\rangle = \frac{F^2}{A^2}\int_{-X}^{X}\int_{-X}^{X}\int_{-Y}^{Y}\int_{-Y}^{Y} e^{iv_x(x_1-x_2)+iv_y(y_1-y_2)}\left\langle e^{iv_z(\zeta_1-\zeta_2)}\right\rangle dx_1 dx_2 dy_1 dy_2 \tag{2.28}$$

where E_{20} is the electric field scattered from a smooth surface, $\mathbf{v} = \mathbf{k}_1 - \mathbf{k}_2$ is the difference between the incident and scattered wave vectors, $\zeta_1 = \zeta(x_1, y_1)$, $\zeta_2 = = \zeta(x_2, y_2)$, and F is a coefficient that depends on the incident and scattered angles θ_i and θ_s, which has the following form:

$$F = \frac{1+\cos(\theta_i + \theta_s)}{\cos\theta_i(\cos\theta_i + \cos\theta_s)} \tag{2.29}$$

Equation (2.28) provides a general solution to the spectral, bi-directional reflectance given any surface profile and θ_i and θ_s. This equation is derived by making four basic assumptions:

I. The surface is perfectly conducting, therefore no absorption occurs during each incident reflection on the surface;

II. Mutual interaction of the irregularities, including shadowing and multiple scattering, is neglected.;

III. The incident wave is plane and linearly polarized; and

IV. The point of observation is sufficiently far removed from the surface to regard the scattered waves as plane.

Note that "these assumptions can be withdrawn at the cost of exactness and simplicity, since they do not intensively impair the generality of the solution", quoted in [44].

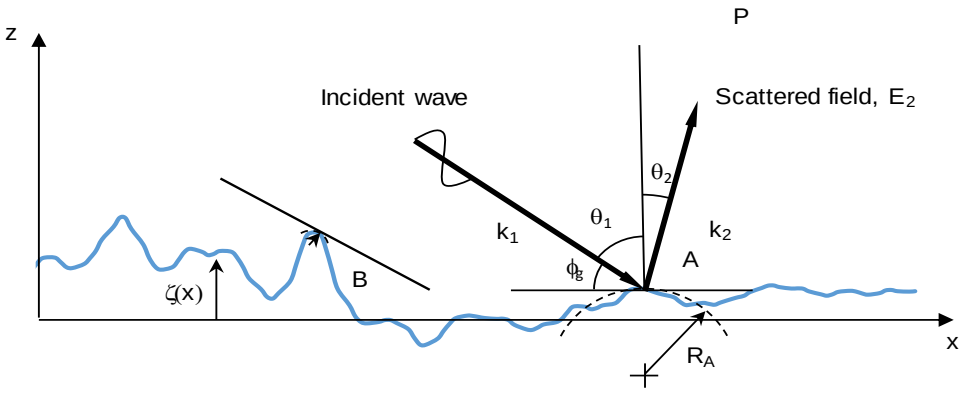

Figure 3-5. Schematic of E-M wave scattering from a rough surface. Points A and B show cases where the radius of curvature is large and small compared to the wavelength of interest. The scattered electrical field can be obtained by solving Helmholtz's integrand incorporating Kirchhoff's boundary conditions that assumes the surface is locally flat relative to the incident EM wave, depicted as the scenario of point A.

3.3.5 Criterion of Kirchhoff approximation

The above result relies on Kirchhoff's approximation, which is reasonable as long as the local radius-of-curvature, *R*, of the surface is larger compared to the projection of the incoming wavelength onto the surface [81]. This is locally-enforced by condition that [112]

$$2k_1 |R| \sin^3 \phi_g \gg 1 \tag{2.30}$$

where R is the local radius of curvature, $k_1 = 2\pi/\lambda$ is the modulus of the incident wave vector, and ϕ_g is local grazing angle of incident field. This criterion can be globally-enforced by

$$2k_1 R_{RMS} \sin^3 \phi \gg 1 \tag{2.31}$$

where R_{RMS} denotes the root-mean-square radius of curvature for the analyzed points on surface and ϕ represents a global grazing angle which equals to $\pi/2-\theta$. Considering $\zeta(x,y)$ is a function of x and y, the mean curvature of any specific point for a two dimensional surface is [142]

$$K_{\text{mean}} = \frac{(1+\zeta_y'^2)\zeta_x'' - 2\zeta_x'\zeta_y'\zeta_{x,y}'' + (1+\zeta_x'^2)\zeta_y''}{2(1+\zeta_x'^2+\zeta_y'^2)^{3/2}} \tag{2.32}$$

and radius of curvature is equal to the inverse of curvature,

$$R = \frac{1}{K_{\text{mean}}} \tag{2.33}$$

If ζ is normally-distributed,

$$R_{RMS} = \left(\frac{\beta^2}{\sqrt{12}\sigma}\right)\left(1+\frac{2\sigma^2}{\beta^2}\right)^{3/2} \tag{2.34}$$

where β is the correlation length. Finally, for a randomly rough surface, the correlation length can be related to the RMS surface slope by [143]

$$\left\langle \left(\zeta'(x)\right)^2 \right\rangle^{1/2} = \frac{\sqrt{2}\sigma}{\beta_x} \tag{2.35}$$

where $\zeta'(x)$ is the derivative of surface height in the x direction, which can be calculated from the surface profile data. The same procedure is applied to obtain the correlation length in the y direction, and the equivalent correlation length β, is taken as the average value of β_x and β_y.

The applicability of Kirchhoff's approximation to a two-dimensional rough surface can be verified through Eq. (2.31)-(2.35).

3.3.6 Davies' and Beckman's model

Since Eq. (2.28) is computationally difficult to evaluate for an unknown surface statistical profile, Davies assumed a Gaussian distribution of heights of surface irregularities about the mean level

and finally derived a bi-directional reflectance model for the limiting cases of slightly rough and very rough surfaces [46]. For slightly rough surfaces ($\sigma/\lambda<<1$), the bi-directional reflectance model contains a specular component, f_{sp}, and a diffuse component, f_d.

$$f_{sp}(\theta_i,\theta_s)=\frac{\rho_{\lambda,s}}{\cos\theta_i\Delta\omega_i}\exp\left[-\left(\frac{4\pi\sigma\cos\theta_i}{\lambda}\right)^2\right] \tag{2.36}$$

$$\begin{aligned} f_d(\theta_i,\varphi_i,\theta_s,\varphi_s)=&\frac{\rho_{\lambda,s}}{\cos\theta_i\cos\theta_s}\pi^3(\frac{\beta}{\lambda})^2(\frac{\sigma}{\lambda})^2\left(\cos\theta_i+\cos\theta_s\right)^4 \\ &\times\exp\left\{-\left(\frac{\pi\beta}{\lambda}\right)^2\left[\sin^2\theta_i+\sin^2\theta_s+2\sin\theta_i\sin\theta_s\cos(\varphi_i-\varphi_s)\right]\right\} \end{aligned} \tag{2.37}$$

where θ_i, θ_s are normal incident and reflection angle, respectively, and φ_1, φ_2 are azimuthal incident and reflected angles, respectively. The parameter β in Eq. (2.37) represents the correlation length and $\rho_{\lambda,s}$ is the reflectance for a smooth surface which is determined by the Hagen-Rubens relations

$$\rho_{\lambda,s}(T)=1-\left\{36.5\left[\frac{r_e(T)}{\lambda}\right]^{0.5}-464\left[\frac{r_e(T)}{\lambda}\right]\right\} \tag{2.38}$$

where

$$r_e=r_0+\kappa\times r_0(T-T_0) \tag{2.39}$$

is the temperature-dependent resistivity, r_0 denotes resistivity at a reference temperature T_0, and κ is the temperature coefficient of resistivity.

Note that $\rho_{\lambda,s}$ does not exist in the original Davies model, which was developed assuming a perfectly conducting metal [126].

Based on Eq. (2.37), the reflectance model for very rough surfaces with $\sigma/\lambda>1$ can be derived in the following expression,

$$f_{\text{bi-d}}(\theta_{\text{i}},\varphi_{\text{i}},\theta_{\text{s}},\varphi_{\text{s}}) = \frac{\rho_{\lambda,\text{s}}}{\cos\theta_{\text{i}}\cos\theta_{\text{s}}}\frac{1}{16\pi}\left(\frac{\beta}{\sigma}\right)^2 \times \exp\left[-\left(\frac{\beta}{2\sigma}\right)^2 \frac{\sin^2\theta_{\text{i}} + \sin^2\theta_{\text{s}} + 2\sin\theta_{\text{i}}\sin\theta_{\text{s}}\cos(\varphi_{\text{i}}-\varphi_{\text{s}})}{\left(\cos\theta_{\text{i}}+\cos\theta_{\text{s}}\right)^2}\right] \tag{2.40}$$

Based on Eq. (2.40), Beckmann derived an expression for the bi-directional reflectance, which is valid for arbitrary values of optical roughness (σ/λ). The model contains a specular component and a diffuse component. The specular component is identical to that of Davies model, Eq. (2.36), while the diffuse model can be expressed in the following form [44, 115],

$$f_{\text{d}}(\theta_{\text{i}},\varphi_{\text{i}},\theta_{\text{s}},\varphi_{\text{s}}) = \frac{\rho_{\lambda,\text{s}}}{\cos\theta_{\text{i}}\cos\theta_{\text{s}}}\pi B\left(\frac{\beta}{\lambda}\right)^2 \times \exp\left[-\left(\frac{\sigma}{\lambda}G\right)^2\right]\sum_{m=1}^{\infty}\frac{1}{m(m!)}\left(\frac{\sigma}{\lambda}G\right)^{2m}\exp\left[-\frac{\pi^2}{m}\left(\frac{\beta}{\lambda}\right)^2 H\right] \tag{2.41}$$

where the parameters *B*, *H*, and *G* are given as

$$B = \left[\frac{1+\cos\theta_{\text{i}}\cos\theta_{\text{s}}+\sin\theta_{\text{i}}\sin\theta_{\text{s}}\cos(\varphi_{\text{i}}-\varphi_{\text{s}})}{\cos\theta_{\text{i}}+\cos\theta_{\text{s}}}\right]^2 \tag{2.42}$$

$$H = \sin^2\theta_{\text{i}} + \sin^2\theta_{\text{s}} + 2\sin\theta_{\text{i}}\sin\theta_{\text{s}}\cos(\varphi_{\text{i}}-\varphi_{\text{s}}) \tag{2.43}$$

$$G = 2\pi(\cos\theta_{\text{i}}+\cos\theta_{\text{s}}) \tag{2.44}$$

It can be seen that Davies's model and Beckmann's model have similar forms, although Davies's model is restricted to the limiting cases of very small and very large optical roughness, while Beckmann's model applies to a wide range of surface roughness. Further insight into the role of the various parameters in Davies' and Beckmann's bidirectional reflectance model can be acquired by considering the results they yield for directional-hemispherical reflectance, $\rho_{\lambda,\text{d-h}}$.

$$\begin{aligned}\rho_{\lambda,\text{d-h}} &= \rho_{\lambda,\text{sp}} + \int_{\Lambda\omega} f_{\text{d}}\ \cos\theta_{\text{s}}\ d\omega \\ &= \rho_{\lambda,\text{sp}} + \int_0^{2\pi}\int_0^{\pi/2} f_{\text{d}}\ \cos\theta_{\text{s}}\ \sin\theta_{\text{s}}\ d\theta_{\text{s}}\ d\varphi\end{aligned} \tag{2.45}$$

where $\rho_{\lambda,\text{sp}}$ denotes the contribution of the specular component to ρ_{dh} and is given by [46]

$$\rho_{\lambda,\text{sp}} = \rho_{\lambda,\text{s}} \exp\left[-\left(\frac{4\pi\sigma\cos\theta_{\text{i}}}{\lambda}\right)^2\right] \tag{2.46}$$

For near normal incidence, Eq. (2.46) can be simplified to

$$\rho_{\lambda,\text{sp}} = \rho_{\lambda,\text{s}} \exp\left[-\left(\frac{4\pi\sigma}{\lambda}\right)^2\right] \tag{2.47}$$

where σ is the root-mean-square (RMS) roughness and ρ_λ and $\rho_{\lambda,\text{s}}$ are the specular reflectances of a slightly rough and a hypothetical perfectly-smooth surface, respectively. Note that in Eq. (2.47), $\rho_{\lambda,\text{s}}$ is obtained by employing Hagen-Rubens theory [33].

It should be noted that for small optical roughness ($\sigma/\lambda<<1$), the energy scattered into directions other than the specular direction can be neglected [115], giving rise to

$$\rho_{\lambda,\text{d-h}} \approx \rho_{\lambda,\text{s}} \exp\left[-(\frac{4\pi\sigma}{\lambda})^2\right] \tag{2.48}$$

3.3.7 Criterion for rough surfaces

Numerous criteria have been proposed for defining an "optically-rough" surface, which depend on surface profile, radiation wavelength, and angle of incidence. The most general and adopted criterion is the Rayleigh roughness criterion [62], which assumes the surface can be considered as slightly rough or optically smooth when the phase difference is much smaller than $\pi/2$, under which

condition the reflected waves interfere constructively. Based on this, the following equation for rough surface criterion can be derived,

$$\frac{\sigma}{\lambda}\cos\theta_i << \frac{1}{8} \tag{2.49}$$

where σ denotes the RMS roughness, θ_i denotes the incident angle.

From a more quantitative point-of-view, the mean reflected field in specular direction from a Gaussian stationary rough surface, $<E_2>$ can be expressed as [144],

$$< E_2 >= E_{\text{flat}} \exp\left[-8\left(\frac{\pi}{\lambda}\sigma\cos\theta_i \right)^2 \right] \tag{2.50}$$

where E_{flat} corresponds to the scattered field from a smooth surface. Note that the intensity is proportional to the square of the electric field strength, which leads to the coherent intensity attenuation of $\exp[-(4\pi\sigma\cos\theta_i/\lambda)^2]$. For a very rough surface, intensity is reflected into directions other than the specular one. However, the Rayleigh criterion of Eq. (2.49) gives rise to an attenuation of scattered intensity of $\exp(-\pi^2/4) \approx 0.08$, which is not negligible. Hence, a more rigorous criterion is provided as

$$\frac{\sigma}{\lambda}\cos\theta_i < \frac{1}{32} \tag{2.51}$$

which corresponds to $\exp(-\pi^2/64) \approx 0.85$. Equation (2.51) is also known as Fraunhofer criterion [144, 145] which can be employed to quantify a random surface as slightly rough. Under this criterion the coherent intensity is only slightly attenuated, which implies that the surface is optically-smooth.

3.3.8 Geometric optics approximation

All the EM models mentioned in the previous sections assume that the incident beam interacts only once with the rough surface before being scattered away from the surface. However, in reality subsequent interactions between the incident beam and the surface may occur during the scattering process as depicted in Figure 3-6. This scenario becomes important when: (i) the roughness of the surface increases, and (ii) the angle of incidence increases away from the surface normal [146]. This effect is wavelength-dependent; multiple scattering may be described using geometric optics in the case that incoming wavelengths are short. When the EM wavelength is comparable to, or greater than the surface roughness, however, diffraction effects will contribute to multiple scattering.

One of the few models that can effectively capture multiple scattering effects is the geometric optics approximation with ray tracing. This method is used in many instances to quantify thermal radiative properties such as transmission, absorption, reflection, and emission. Agreement of radiative property estimations found using the Kirchhoff approximation and geometric optics approximation was shown in the case of moderate ratios of correlation length to incident wavelength ($2<\tau/\lambda<4.75$; $0.045<\lambda<0.701$) [147]. This agreement, however, is limited to optically smooth or slightly rough surfaces as the Kirchhoff approximation is only valid when the surface slope is locally flat where the specular approximation dominates. The geometric optics approximation, in contrast, is both a specular and diffuse approximation and has a different validity domain from that of the Kirchhoff approximation. In addition, because it accounts for the multiple scattering effects, the geometric optics approximation can accurately capture diffuse behavior for even very rough surfaces [123].

In the geometric optics approximation, the energy of ray bundles is tracked throughout their interactions with the surface until they leave the surface. Each surface interaction is modeled as a reflection from a locally optically-smooth surface governed by specular reflection based on the local incidence angle, and the amount of reflected energy is determined by multiplying the incident energy with Fresnel's coefficient [52]. This approximation is reasonable if both normalized correlation length, τ/λ, and normalized surface roughness, σ/λ, are greater than unity [146]. Tang et al. further examined its domain of validity by comparing the bi-directional reflectance estimations with that of the exact solutions over a wide range of surface parameters ($\sigma\cos\theta_i/\lambda > 0.2$, $\sigma/\tau < 2$) [116].

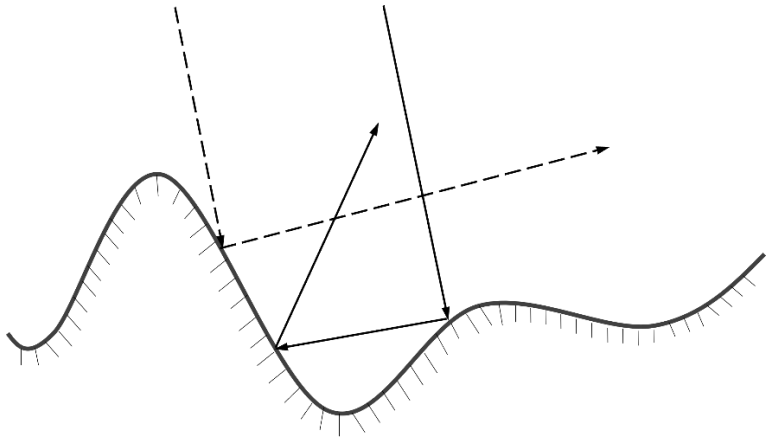

Figure 3-6. Schematic view of single scattering (dashed arrows) and multiple scattering (solid arrows) at a rough surface.

The energy of EM waves incident upon a surface is either reflected, transmitted, or absorbed. The angular distribution of the reflected component is defined by the bi-directional distribution function (BRDF) [52]

$$\rho''_{\lambda}\left(\Omega_{\mathrm{i}},\Omega_{\mathrm{s}}\right)=\frac{\pi}{\cos\theta_{\mathrm{s}}}\left(\frac{\frac{\mathrm{d}\Phi_{\mathrm{s}}}{\mathrm{d}\Omega_{\mathrm{s}}}}{\frac{\mathrm{d}\Phi_{\mathrm{i}}}{\mathrm{d}\Omega_{\mathrm{i}}}}\right) \tag{2.52}$$

where Φ, Ω and θ represent the radiant power, solid angle and polar angle, respectively, and the subscripts "i" and "s" denote incident and scattering (Figure 3-7). In the geometric approximation with ray tracing, the BRDF can be calculated in terms of the energies of the ray bundles,

$$\rho''_{\lambda}\left(\Omega_{\mathrm{i}},\Omega_{\mathrm{s}}\right)=\frac{G_{\mathrm{i}}\left(\theta_{\mathrm{i}},\varphi_{\mathrm{i}}\right)}{G_{\mathrm{r}}\left(\theta_{\mathrm{s}},\varphi_{\mathrm{s}}\right)\ \cos\theta_{\mathrm{s}}\ \Delta\Omega_{\mathrm{s}}} \tag{2.53}$$

where $G_{\mathrm{i}}(\theta_{\mathrm{i}}, \varphi_{\mathrm{i}})$, $G_{\mathrm{r}}(\theta_{\mathrm{s}}, \varphi_{\mathrm{s}})$ denote the total energy of the incident and scattered ray bundles, respectively, and $\Delta\Omega_{\mathrm{s}}$ denotes the scattered solid angle of the ray bundles. Integration of the bidirectional reflectance over the entire hemisphere yields the directional-hemispherical reflectance [33],

$$\rho_{\lambda,\mathrm{d-h}}\left(\Omega_{\mathrm{i}}\right)=\frac{1}{\pi}\int_{\Delta\omega}\rho''_{\lambda}\left(\Omega_{\mathrm{i}},\Omega_{\mathrm{s}}\right)\ \cos\theta_{\mathrm{s}}\ \mathrm{d}\Omega_{\mathrm{s}} \tag{2.54}$$

For a perfectly conducting surface (no energy absorption or transmission), the directional-hemispherical reflectance is unity [148]. For metals having opaque surfaces, the EM wave incident on the surface is either absorbed or reflected, and by conservation of energy and Kirchhoff's law, the spectral, directional emissivity can be found through Eq. (2.54).

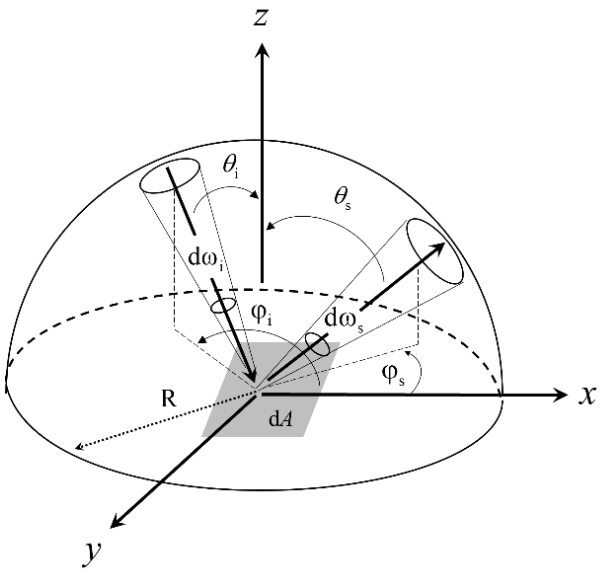

Figure 3-7. Illustration of bidirectional reflection under the hemispherical area in a global reference frame.

The framework of geometric optics approximation is often conceptualized by tracking the trajectory of an energy bundle, having an incident trajectory drawn from corresponding probability density functions (PDFs), as it undergoes multiple interactions with the surface, until it ultimately scatters away from the surface. Each local point of intersection on the surface is treated as a specular reflection, and Fresnel's equation is used to model the energy transfer between the wave and the surface. The GOA reduces to a single Fresnel reflection for a smooth surface, while for a rough surface the number of scattering events typically increases with surface slope.

The schematic view of 2D ray tracing on a rough surface is illustrated in Figure 3-8. First, a set of *x*, *y*, *z* surface points are used as surface nodes that form the 2D surface. Then a number of first reflection points, five times greater than the total number of surface nodes, are randomly sampled from the 2D surface from uniform PDFs. The incident polar angle, θ_i, and the azimuthal angles, ϕ_i, are prescribed, and an incident ray vector is then defined as

$$\boldsymbol{\kappa}_{\mathrm{i}} = -\left[\sin\left(\theta_{\mathrm{i}}\right)\cos\left(\varphi_{\mathrm{i}}\right),\ \sin\left(\theta_{\mathrm{i}}\right)\sin\left(\varphi_{\mathrm{i}}\right),\ \cos\left(\theta_{\mathrm{i}}\right)\right]^{\mathrm{T}} \tag{2.55}$$

The combination of (θ_{i}, φ_{i}) and the candidate incident point defines a plane of incidence. In the event of shadowing, the candidate ray is discarded and the first reflection point is resampled. As the angle between the incident and normal vectors is equal to the angle between the reflected and normal vectors, the direction of reflection, $\boldsymbol{\kappa}_{\mathrm{r}}$, is found by using Snell's Law,

$$\boldsymbol{\kappa}_{\mathrm{r}} = \boldsymbol{\kappa}_{\mathrm{i}} - 2\mathbf{n}\left(\boldsymbol{\kappa}_{\mathrm{i}} \cdot \mathbf{n}\right) \tag{2.56}$$

where **n** is the normal vector. The incident ray energy is weighted by the projected area of the surface on the plane according to Lambert's law. Bergström et al. [149] noted that the polarization of the incident and reflected energies should be considered due to the random orientations of the local surface normal vectors; accordingly, the incident energy is decomposed into *s*- and *p*-polarized components in a global reference frame defined by the *z*-axis unit vector. The relation between the incident and reflected energies are expressed as

$$\begin{bmatrix} G_{\mathrm{r,s}} \\ G_{\mathrm{r,p}} \end{bmatrix} = \begin{bmatrix} \rho_{\mathrm{ss}} & \rho_{\mathrm{ps}} \\ \rho_{\mathrm{sp}} & \rho_{\mathrm{pp}} \end{bmatrix} \begin{bmatrix} G_{\mathrm{i,s}} \\ G_{\mathrm{i,p}} \end{bmatrix} \tag{2.57}$$

where ρ_{ss} and ρ_{pp} are the co-polarized reflectances, and ρ_{sp} and ρ_{ps} are the cross-polarized reflectances. The co-polarized and cross-polarized reflectances can be calculated through the Fresnel amplitude reflectivities and the directions of incident and reflected rays described in [149, 150]. The Fresnel amplitude reflectivities, r_{s}, r_{p} are given by

$$r_{\mathrm{s}} = \frac{\left(n_1\cos\theta_{\mathrm{i}} - p\right)^2 + q^2}{\left(n_1\cos\theta_{\mathrm{i}} + p\right)^2 + q^2} \quad , \quad r_{\mathrm{p}} = \frac{\left(p - n_1\sin\theta_{\mathrm{i}}\tan\theta_{\mathrm{i}}\right)^2 + q^2}{\left(p + n_1\sin\theta_{\mathrm{i}}\tan\theta_{\mathrm{i}}\right)^2 + q^2} \times r_{\mathrm{s}} \tag{2.58}$$

where n_1=1, and n_2 and k_2 are the optical constants of substrate metal.

The reflected ray is then raytraced to determine whether it re-intercepts the surface. In this scenario, a new reflection point is found and the scattering calculation between the ray and the surface is repeated. This process continues until the ray leaves the surface, at which point the remaining energy of the incident ray is restored under its respective direction within the hemisphere for the BRDF calculation, as defined by Eq. (2.53). After all of the first reflection points from the surface have been traced at a given incident angle, the specular reflectance can be found by dividing the total energy restored in the specular direction by the total incident energy. The directional-hemispherical reflectance can therefore be obtained via Eq. (2.54), or simply by dividing the total reflected energy of all directions by the total incident energy. The flow chart of the ray tracing model is shown in Figure 3-9.

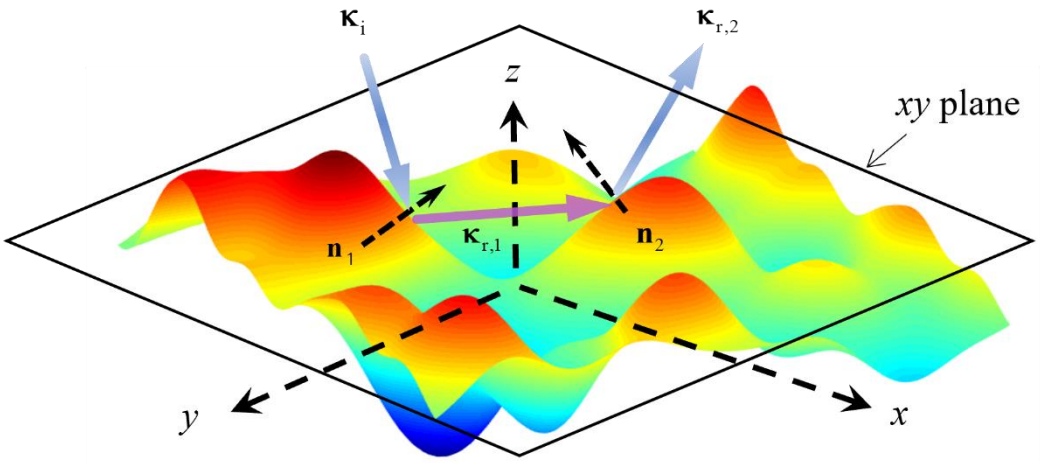

Figure 3-8. Schematic view of ray tracing on the 2-D rough surface in a global coordinate. The surface nodes incorporated in the GOA model are obtained directly from the measured profilogram data.

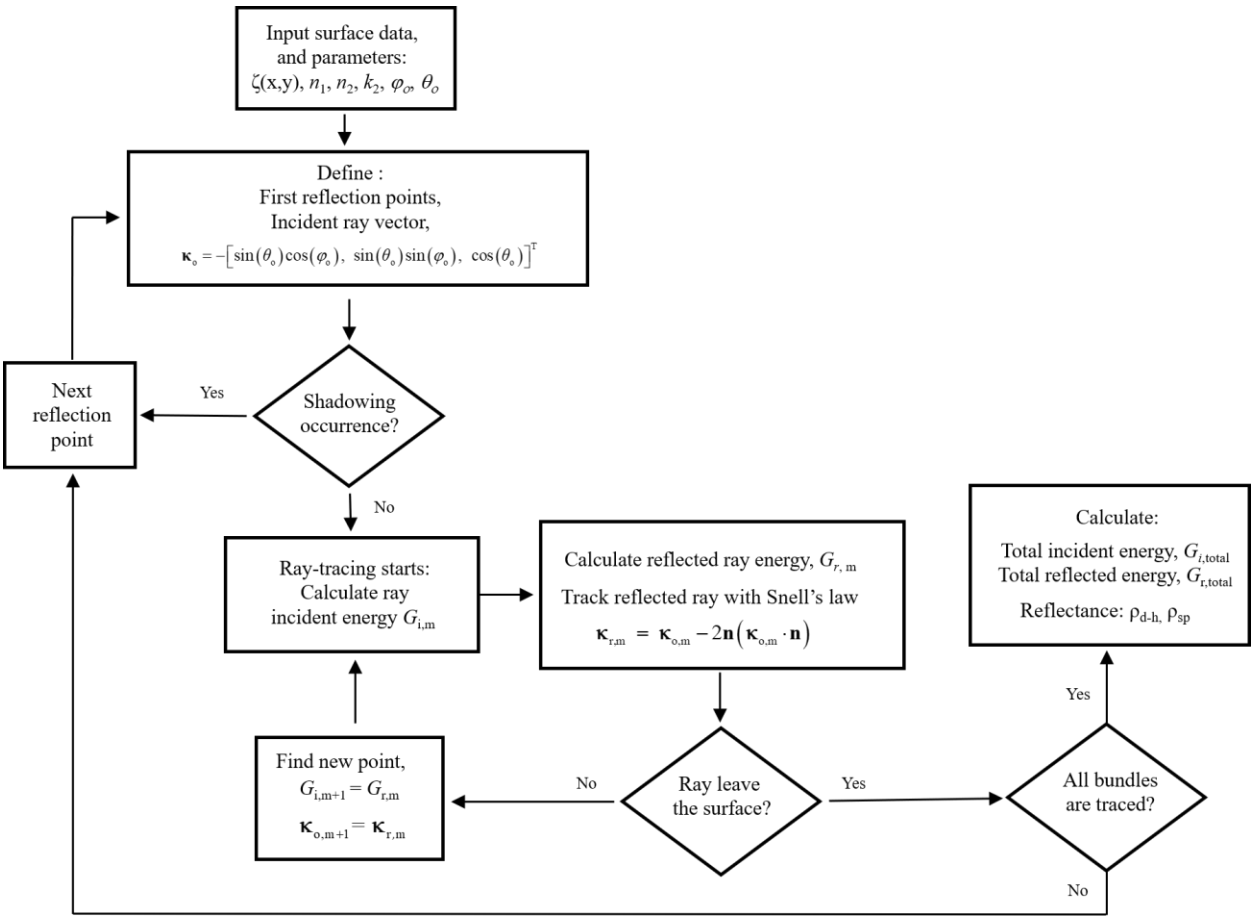

Figure 3-9 Flowchart of 2-D ray tracing framework.

3.3.9 Kirchhoff EM diffraction models

Although GOA provides a computationally-efficient way to predict the spectral reflectance and BRDF, it does not account for wave diffraction and therefore it should not be applied outside of its valid domain. As mentioned in Section 3.3.7, the diffraction effects will contribute to multiple scattering when the EM wavelength is comparable to, or greater than the surface roughness. Accordingly, the radiative properties cannot be evaluated using the geometric optics alone. Instead, Kirchhoff's diffraction theory, based on Kirchhoff's tangent plane approximation, presents a practical method to derive effective solutions of specular and diffuse reflections for randomly-rough surfaces [151]. This approximation assumes that the surface is locally flat relative to the incident waves, i.e.

the local curvature radius is large compared to the wavelength, as described in Section 3.3.4. A closed form relationship between reflectance and root-mean-square (RMS) roughness is described by Eq. (2.46). The angular dependence of diffusely-reflected EM waves can also be obtained using Davies' theory, keeping in mind that the experimentally-determined normal reflectance corresponds to a finite instrumental acceptance angle $\Delta\theta$. Accordingly, the complete expression for the specular reflectance with specular and diffuse terms at normal incidence for a rough metal surface is presented by Bennett and Porteus [126],

$$\rho_{\lambda,sp} = \rho_{\lambda,s} \exp\left[-\left(\frac{4\pi\sigma}{\lambda}\right)^2\right] + \rho_{\lambda,s} \frac{2^5\pi^4}{s^2}\left(\frac{\sigma}{\lambda}\right)^4 (\Delta\theta)^2 \tag{2.59}$$

where s represents RMS slope of surface profile, which can be calculated from the derivative of surface profile data. At sufficiently long wavelengths ($\sigma/\lambda<<1$), Eq. (2.59) reduces to Eq. (2.46) as the surface becomes optically-smooth. At shorter wavelengths, however, the specular reflectance is influenced by both roughness and the slope of the surface irregularities.

The specular reflectance model was further improved by Houchens and Hering in the following form for off-normal incidence [148]:

$$\rho_{\lambda,sp} = \rho_{\lambda,s} \exp\left[-\left(\frac{4\pi\sigma}{\lambda}\cos\theta_i\right)^2\right] + \rho_{\lambda,s} f_d \cos\theta_i \frac{\Delta\Omega}{\pi} \tag{2.60}$$

where $\Delta\Omega$ is the instrument acceptance of solid angle, which can be approximated by $\Delta\Omega = \pi(\Delta\theta)^2$ [129]. The diffuse function of reflectance, f_d, is

$$f_d = \frac{4\pi^2}{\cos^2\theta_i}\left(\frac{\tau}{\lambda}\right)^2 \exp\left[-\left(\frac{4\pi\sigma}{\lambda}\cos\theta_i\right)^2\right]\left[\sum_{m=1}^{\infty}\frac{\left(\frac{4\pi\sigma}{\lambda}\cos\theta_i\right)^{2m}}{m(m!)}\right] \tag{2.61}$$

where τ is the surface autocorrelation length, which is related to the RMS roughness and RMS slope for a randomly rough surface through Eq. (2.35). Finally, the diffuse reflectance can be obtained by subtracting the specular reflectance from the hemispherical reflectance,

$$\rho_{\lambda,\text{diffuse}} = \rho_{\lambda,s} - \rho_{\lambda,sp} \tag{2.62}$$

In summary, Eq. (2.60)-(2.62) are proposed to evaluate the specular and diffuse reflectance when the incident EM wavelength is greater than the surface roughness parameters and the diffraction effect dominates the scattering, in which scenario the geometric optics approximation is invalid. It should be noted that multiple reflections may still exist between the interactions of EM waves and surface boundaries even if the wavelength is greater than the roughness. As a consequence, predictions of specular and diffuse reflectances at long wavelength region *via* Eq. (2.60)-(2.62) may still deviate from the actual values as the models do not account for the aspects of geometric optics.

3.4 Hybrid thin film/roughness effect[4]

As mentioned in Section 3.3.8, the radiative properties of an unoxidized rough metal surface can be estimated using the geometric optics approximation with ray tracing. When a flat, absorbing thin oxide film deposited on a flat metal substrate, the radiative properties can be interpreted using the thin film interference model described in Section 3.2. A more complex scenario occurs when a rough, absorbing thin oxide film is deposited on a rough metal substrate, in which case EM wave scattering is influenced by both the oxide film and roughness.

[4] Information presented in this section can be found in a paper submitted to *J. Quant. Spectrosc. Radiat. Transf.:* K. Lin, M. Pourmajidian, F. K. Suleiman, J. R. McDermid, K. J. Daun, *Interpreting the radiative properties of advanced high strength steel strip using a hybrid thin film/geometric optics model.* (2021)

Unfortunately, very few studies in the literature have been performed on the case of a rough, thin film upon a rough surface, and the only existing model developed to physically correlate the radiative properties and thin film/roughness effect is the hybrid thin film/geometric optics model (hybrid model). This hybrid method incorporates thin film interference theory into the framework of geometric optics ray tracing, assuming a uniform, absorbing oxide film deposited upon a rough substrate (i.e. the profile of the substrate is consistent to that of the oxide film having a uniform global thickness), as illustrated in Figure 3-10. The thickness of the oxide film is assumed to be on the order of, or less than, the incident wavelength. In this scenario, two aspects need to be considered in the modeling of EM wave scattering: multiple reflection and interference. In terms of the geometric optics, as the ray bundle strikes the top surface of the oxide film, some of the energy is reflected and some is transmitted through the film. As the transmitted energy hits the bottom interface of the oxide film, some of the energy is reflected from the substrate. Based on this, the interaction of the wave with each interface is repeated each time the wave hits an interface, and reflection of interference incorporating the phase difference between all waves reflected from the top interface of the thin film is considered. As a consequence, the fraction of reflected energy each time the ray bundle hits the interface is calculated using the interference model, dictated by Eq. (2.9)-(2.13), instead of Fresnel's equation.

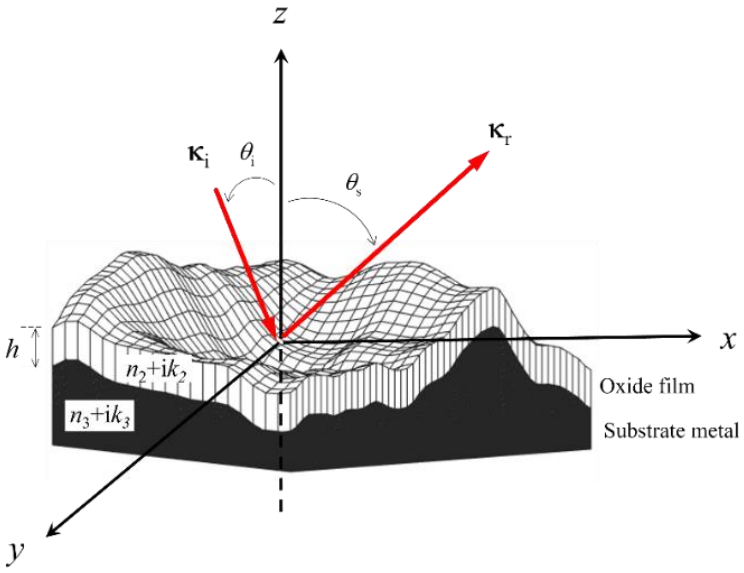

Figure 3-10. Depiction of a uniform oxide film upon a rough metal surface. In the hybrid model, the oxide film is assumed to be uniform in thickness across the substrate, which makes both profiles identical to each other.

In the hybrid thin film/geometric optics model, both wave interference and multiple reflections must be taken into account as an energy bundle incident upon a rough surface with an oxide film deposited on it. For a one-dimensional view of the profile, as shown in Figure 3-11, the film-substrate interface is described by $z = \zeta(x, y)$, and its mean surface is located on the $z = 0$ plane. The air–film interface is described by $z = \zeta(x, y)+h$ with a mean surface located on the $z = h$ plane, where h is the average film thickness. Given the local surface inclination angle, α, the local oxide film thickness is found by $D = h \cos\alpha$. The ray is incident from air, which has a refractive index n_1=1. The direction of incident, refracted, and reflected rays is found by using Snell's law and Eq. (2.56). An oxide film with refractive indices $\tilde{n}_2$ forms on top of the substrate, $\xi(x,y) < z < \xi(x, y) + h$. The substrate in this study is treated as ferrite (Fe), with a complex refractive index $\tilde{n}_3$. The relation between the global thickness and averaged local thickness of oxide layer shown in Figure 3-12 can be expressed by

$$h = \frac{\mu_h \times n_s}{\sum_{i=1}^{n_s} \cos(\alpha_i)} \tag{2.63}$$

where μ_h and n_s represent the mean local oxide thickness and total number of surface points, respectively. The subscript i denotes the i^{th} incident point.

The hybrid model algorithm is similar to the one from Section 3.3.8 with respect to tracing the ray bundles. First, a set of *x*, *y*, *z* surface points are used as surface nodes that form the 2D surface. Then a number of first reflection points, five times greater than the total number of surface nodes, are randomly sampled from the 2D surface from uniform PDFs. In the event of shadowing, the candidate ray is discarded and the first reflection point is resampled. For rough surfaces without a thin film, each time the ray bundle hits the surface, the local reflectivity can be derived using Fresnel's equation according to the local incidence angle and refractive index of the substrate, as discussed in Section 3.3.8. For 2-D rough surfaces with an uniform oxide film thickness, *h*, illustrated in Figure 3-10, when a ray bundle strikes the top surface of the oxide film, some of the energy is reflected and some is transmitted through the oxide film. In this case, the local reflectivity associated with each scattering event is obtained using the thin film interference model *via* Eq. (2.9)-(2.13), which incorporates the phase difference between all waves reflected from the top interface of the oxide film. The fraction of reflected energy at each scattering event is therefore calculated according to the local reflectivity of thin film interference. The reflected ray is then raytraced to determine whether it re-intercepts the surface. In this scenario, a new reflection point is found and the scattering calculation between the ray and the interface is repeated. This process continues until the ray leaves the surface, at which point the remaining energy of the incident ray is restored under its respective direction within the hemisphere for the BRDF calculation, as defined by Eq. (2.53).

After all of the first reflection points from the surface have been traced at a given incident angle, the specular reflectance can be found by dividing the total energy restored in the specular direction by the total incident energy. The directional-hemispherical reflectance can therefore be obtained via Eq. (2.54), or simply by dividing the total reflected energy of all directions by the total incident energy. The flowchart of the hybrid method employed in this study is illustrated in Figure 3-13.

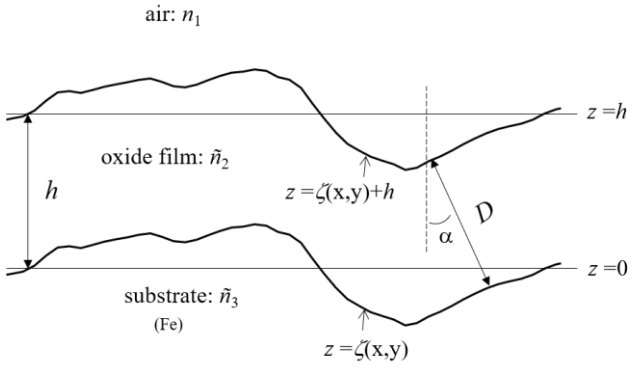

Figure 3-11. Schematic of rough surface with uniform oxide film in one dimension. The profiles of the two interfaces are assumed to be identical, $z=\zeta(x,y)$, and $z=\zeta(x,y)+h$. The system contains three layers: air, oxide film, and substrate, having refractive indices of n_1, $\tilde{n}_2$, $\tilde{n}_3$, respectively. The local film thickness relates to global thickness as $D=h\cos\alpha$. In this thesis, the substrate is treated as iron (Fe).

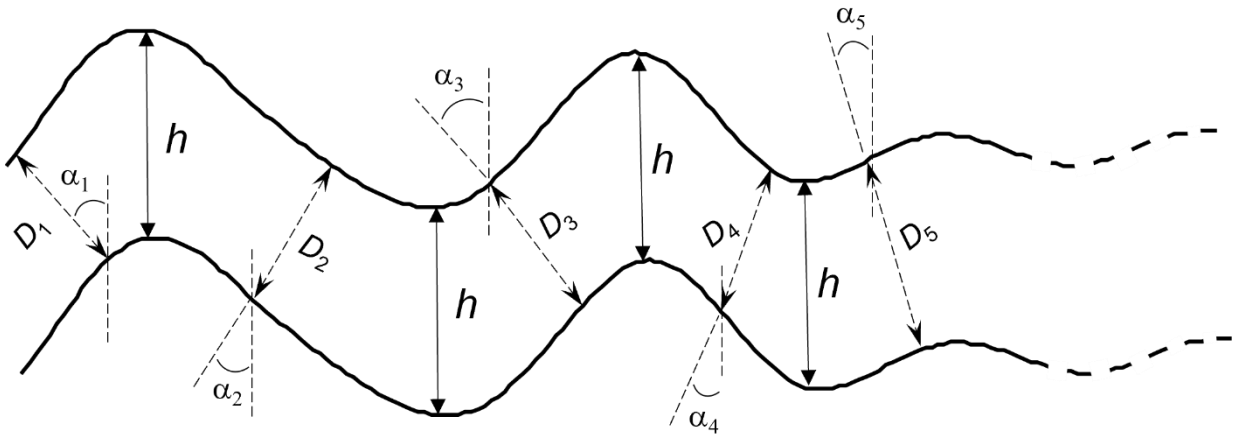

Figure 3-12. 1-D schematic view illustrating the relation between the global oxide thickness, *h*, and the local oxide thickness, *D*, underlying the uniform oxide scenario. The correlation between the global thickness and the measured averaged local thickness is given by Eq. (2.63).

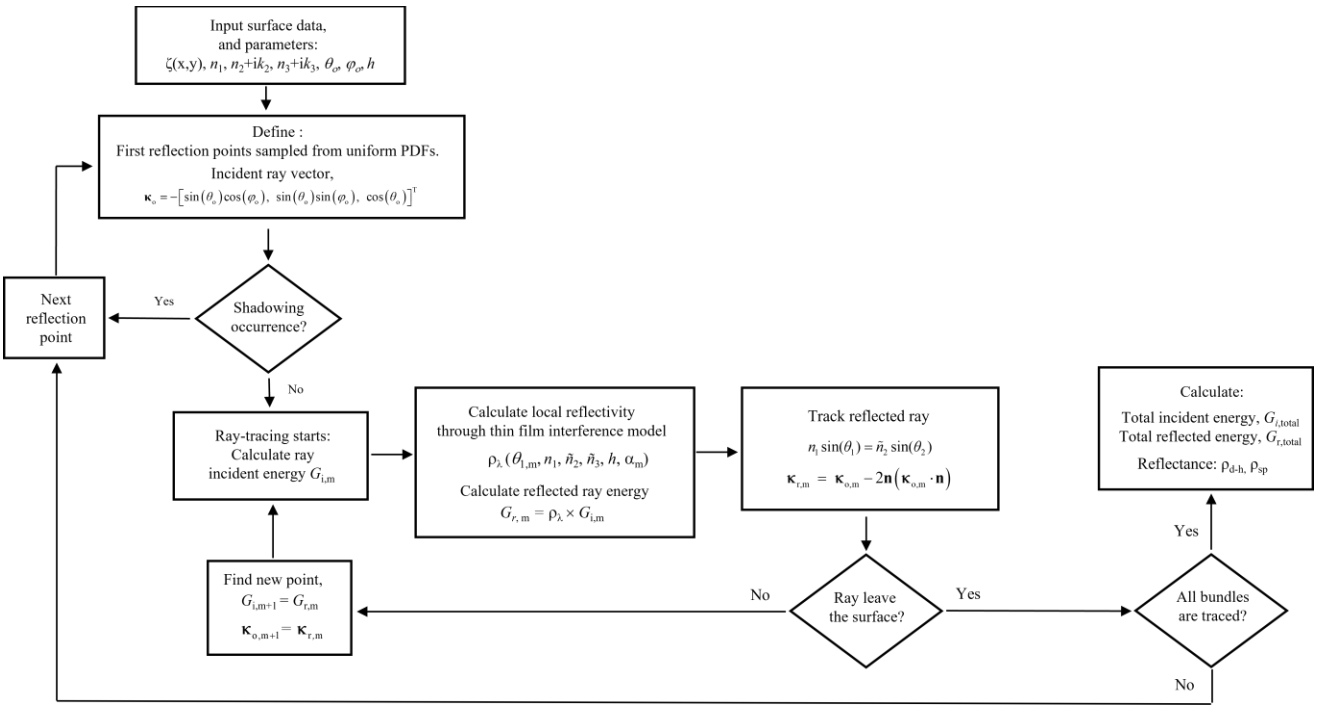

Figure 3-13. Flowchart of GOA ray tracing with thin film interference (hybrid method).

Chapter 4 Interpreting the Spectral Reflectance of Advanced High Strength Steels using the Agababov and Davies' Model[5]

4.1 Introduction

Although using the rigorous EM solution (exact solution) is the most accurate way to model the radiative properties of rough metal surfaces, it is extremely time- and computationally- demanding, which disallows its application for analyzing large amounts of surfaces. More approximate and efficient models are therefore critical to address this requirement. As mentioned in Chapter 3, the model proposed by Agababov, Eq. (2.14), was examined to be effective in the modeling of spectral emissivity of rough aluminum surfaces [152]. The Davies' model, Eq. (2.46), derived from the Kirchhoff approximation, can be used to model the specular reflectance of slightly rough metals.

It was shown in the previous chapter that a randomly rough surface is composed of different levels of roughness scales, and the radiation properties of a material could be affected by specific roughness scales from the surface. The derivation of Eq. (2.46) assumes that the surface roughness obeys a Gaussian distribution as well as Kirchhoff's approximation, which requires the surface to be locally-smooth (i.e. the radius of curvature at each point of surface is large relative to the wavelength). The application of Eq. (2.46) to metallic surfaces is limited to $\sigma/\lambda << 1$, under which conditions the surface can be modeled as optically-smooth and therefore a specular reflector [126]. A major challenge in incorporating these roughness parameters into the reflectance models concerns how to characterize them. In their study of aluminum alloys, Wen and Mudawar [48]

[5] The content of this chapter is an extended version of a paper published in:
K. Lin, K.J. Daun, Interpreting the spectral reflectance of advanced high strength steels using the Davies' model, *J. Quant. Spectrosc. Radiat. Transf.*, vol. 242, pp. 106796, 2020. (doi.org/10.1016/j.jqsrt.2019.106796)

measured σ using a contact profilometer. They applied Eq. (2.47) when $\sigma/\lambda < 0.2$, while for rougher surfaces they propose the theory of Agababov [109]. Alternatively, Majumdar and Tien [153] envision the surface roughness as having a fractal-like quality, and they apply the concept of fractal dimension in the derivation of specular reflectance model, Eq. (2.22). They found that the specular reflectance predictions follow the measured trends over a range of optical roughness parameters ($0.01 < \sigma/\lambda < 1.0$) and fractal dimensions ($1.2 \leq D \leq 2$).

In the context of advanced high strength steel, recent work by Somveille et al. [154] examined DP780 and DP980 samples heated in a reducing atmosphere of 95%/5% N_2/H_2 and a dew point of -30°C, and then quenched the samples at intermediate heating times using process gas. They found that ε_λ evolved with heating time even though the RMS roughness found from contact profilometry remained approximately constant. Ham et al. [155, 156] obtained similar results for DP and TRIP AHSS processed under similar conditions. They hypothesized that the surface roughness measured by profilometry is governed by near-macroscopic surface artefacts imparted by the rolling/forming process, while radiative properties are sensitive to submicron features associated with the formation and growth of oxide nodules. They employed wavelet filtering of optical profilograms to show the existence of a subscale roughness, ~ O(0.1 μm), that correlated with increases in ε_λ as the annealing time increases, as shown in Figure 4-1, where the original surface profilogram (Figure 4-1 (a)) and the profilogram after implementing the high-pass wavelet filtering (Figure 4-1 (b)) are presented. They supported their hypothesis through wavelet filtering of optical profilograms, which confirmed a exponential correlation between ε_λ and subsurface roughness (Figure 4-1 (c)).

This chapter presents the experimental results of this study. It shows that, of the as-received, polished, roughened, and annealed samples, only the specular reflectance of the polished surface

could be accurately modeled using Eq. (2.47) with the profilometer-derived RMS roughness, for wavelengths that satisfy the Fraunhofer criterion. Following Ham et al. [156], the influence of roughness scale on the radiative properties was explored by using wavelet filtering to numerically-filter the large-scale irregularities on the rough surfaces. The filtered surface under tiny, local scale has been compared to the profile measured by the Atomic Force Microscope (AFM), with vertical resolution of 0.1 nm, sampling length of 10 nm and lateral interval of 0.02 μm, to ensure the robustness of the results. Once this was done, the theoretical predictions closely matched the experimental values over wavelengths that satisfy the Faunhofer criterion.

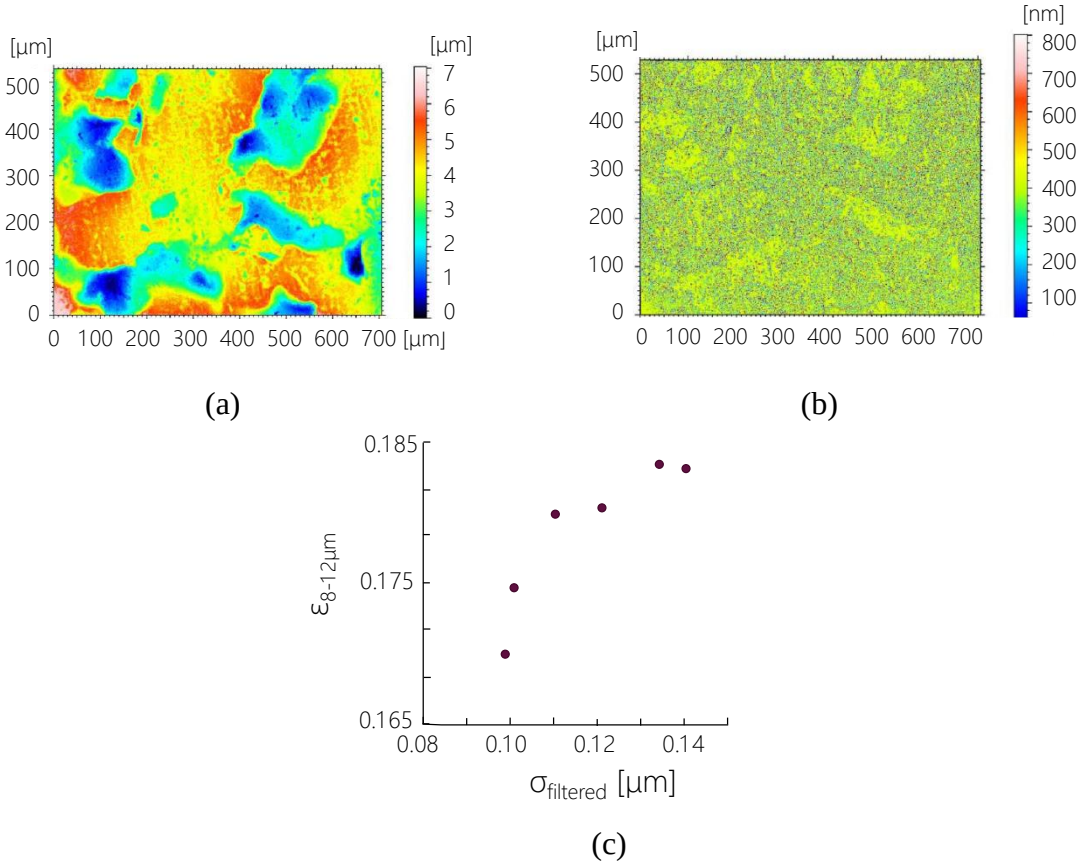

Figure 4-1. Surface topography obtained by optical profilometer (a) before (b) after removing of global texture. (c) the relation between wave-filtered surface roughness and measured emissivity [156]. The global texture shown in (a) is mainly caused by artifact of rolling effect, while the tiny, local roughness texture observed in (b) is formed by oxide nodules during inter-critical annealing. The global emissivity appears to have an exponential correlation with the roughness scale of filtered surface shown in (c).

4.2 Sample preparation and measurement

The focus of this chapter are DP980 samples having an elemental composition conforming to ASTM standard (ASTM, A1079 - 17) as indicated in Table 4-1. The samples were annealed in a McMaster galvanizing simulator described in Ref. [157, 158]. Figure 4-2 shows the galvanizing simulator, which was used for the annealing of the experimental samples. Using this apparatus, the industrial continuous galvanizing process can be fully simulated. This apparatus is fully automated and can manage complex thermal cycles in a variety of atmospheres. The oxygen potential of the atmosphere is controlled by adjusting the pH_2O/pH_2 ratio. The samples are annealed using infrared furnace radiant tube heating, which was designed to avoid contamination resulting from direct contact between the sample and the heating source. The sample temperature is measured by a K-type thermocouple welded to the sample panel. Rapid cooling is performed by a flowing jet composed of a mixture of N_2+H_2 in the cooling chamber located at the upper portion of the simulator column.

The samples are annealed according to the heating cycles shown in Figure 4-3, under a 95%/5% N_2/H_2 atmosphere with a dew point of -30°C (except otherwise noted). The dew point implicitly controls the oxygen content through the reaction $2H_2 + O_2 \leftrightarrows 2H_2O$. In order to compare different levels of surface roughness and their effect on radiation properties, three other un-annealed samples were cut from a coil of cold-rolled DP980. One sample is left in the as- received state, while a second surface was polished using a series of five polishing wheels with progressively finer grit and particle size (240 grit SiC, 320 grit SiC, 400 grit SiC, 600 grit SiC, diamond compound, Gamma alumina), resulting in a mirror-like finish. The third, roughened sample was made by abrading the surface with 30 μm sand paper having 240 grit. Figure 4-4 shows optical micrographs and optical profilograms of the five DP980 surfaces: polished, as-received,

roughened, annealed “A” and annealed “Full”. Rolling striations are clearly visible in the as-received sample, which have been removed by polishing or are obscured by roughening or oxide growth in the remaining samples. Surface topography was measured using an optical surface profiler (WYKO NT1100) with a vertical measurement resolution of 0.1 nm and horizontal resolution of 1.6 μm, which provided both the RMS roughness, σ, and surface profile data that can be used to derive the radius of curvature in Eq. (2.32)-(2.33). The repeatability of the optical profilometer was confirmed by repeatedly performing several measurements on the same area of the sample surface. A total number of ten measurements were carried out on each sample, and the mean values and uncertainties of these measurements are listed in Table 4-2. Figure 4-5 shows an SEM image of the DP980 “A” sample, highlighting the oxide nodules that form during annealing.

The statistical data obtained from optical profilogram for annealed “A” surface is compared to the one obtained by using an atomic force microscope (AFM, Pacific Nanotechnology Nano-R™), with vertical resolution of 0.1 nm, lateral interval of 0.02 μm and scanning area of 10μm×10μm, to confirm the physical relevance of surface statistics. It is noted that, while the AFM can be employed to measure more detailed profiles under small scale, the small scan area makes it impractical to obtain the global profile needed to characterize the surface. Consequently, all other surface profiles are acquired from the optical profilometer measurements.

All samples were cleaned in isopropanol before the optical measurement, and then rinsed with acetone and distilled water to remove any additional particles and contaminants. The near-normal directional-hemispherical spectral reflectance of each sample was measured using a Varian Cary 5000 UV-Vis-NIR spectrophotometer (0.25-2.5 μm) and a Bruker Invenio-R spectrometer (2.5-20 μm), both equipped with an integrating sphere having diameter of 37.5 mm. The configuration of the integrating sphere is depicted in Figure 4-6. The light comes through the

entrance port and is reflected by the flip mirror. The reflected light from the mirror is incident upon the sample at an incident angle of 13° normal to the sample surface. Finally, all the light reflected by the sample will go through the detector port in back of the sphere. The measurement spot on the sample's surface is 180 mm in diameter, which is assumed to be large enough to derive the spatially-averaged values for emissivity. A gold reference sample is used as a reference in the calibration for both the NIR spectrophotometer and FTIR spectrometer, having calibration uncertainty of ±2% and repeatability accuracy of less than ±1% confirmed by repeating four reflectance measurements on each sample over the entire spectrum.

Figure 4-2. McMaster galvanizing simulator used to anneal the samples in present work.

Table 4-1. Chemical composition of tested sample [159].

% mass max.	C	P	S	Mn+Al+S	Cu	Ni	Cr+Mo	V+Nb+Ti
DP980	0.23	0.080	0.015	6.00	0.20	0.50	1.40	0.35

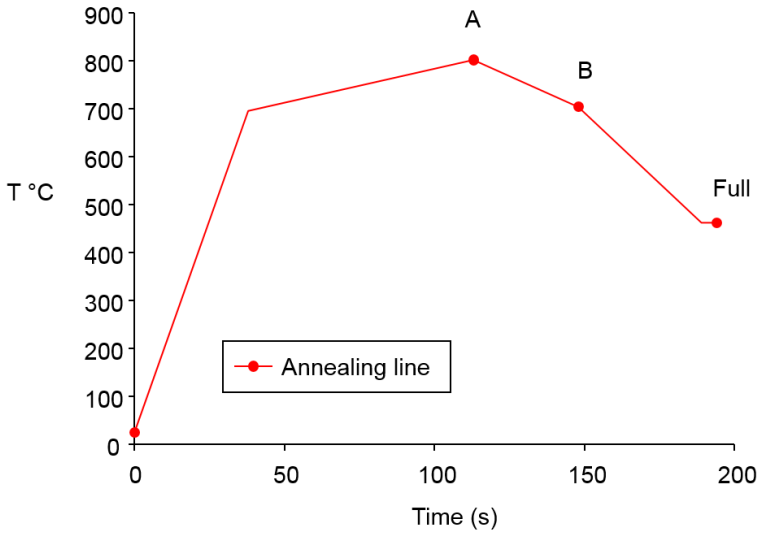

Figure 4-3. DP980 Heating cycles for the annealed samples [154].

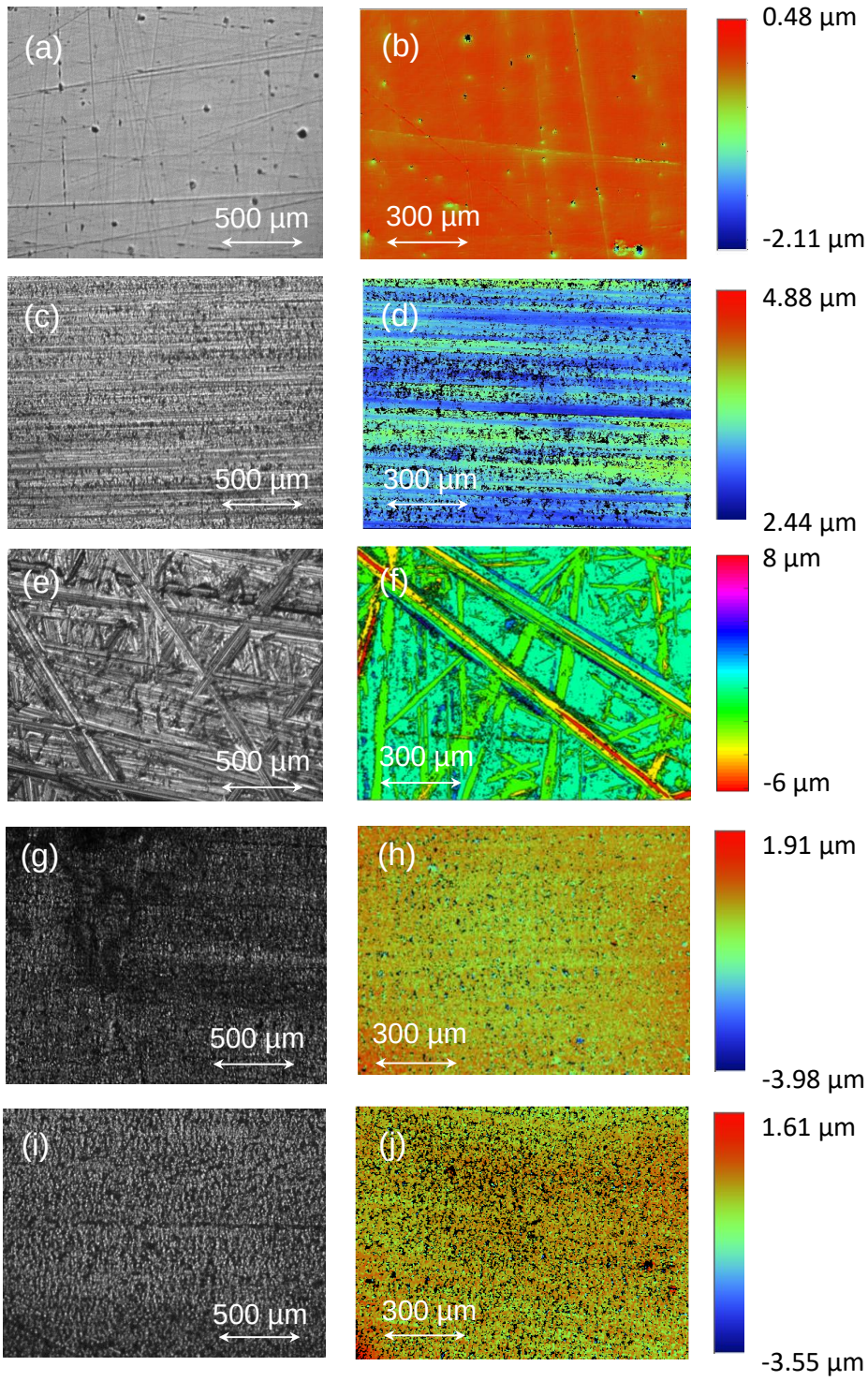

Figure 4-4. Optical microscopy (left) and optical profilograms (right) of the DP980 samples: as-received (a, b), polished (c, d), roughened (e, f), annealed "A" (g, h) and "Full" (i,j) surfaces. Rolling striations are clearly visible in the as-received sample, which have been removed by polishing or are obscured by roughening or oxide growth in the remaining samples.

Table 4-2. Measured RMS roughness of the samples using the optical profilometer. The repeatability of the measurement is confirmed by performing ten measurements on each sample, with mean value and standard deviation of all measurements.

	RMS roughness, $\sigma_{profiler}$
Polished	0.08±0.011 μm
As-received	0.61±0.031 μm
Roughened	1.55±0.028 μm
Annealed, A	0.37±0.014
Annealed, Full	0.34±0.015

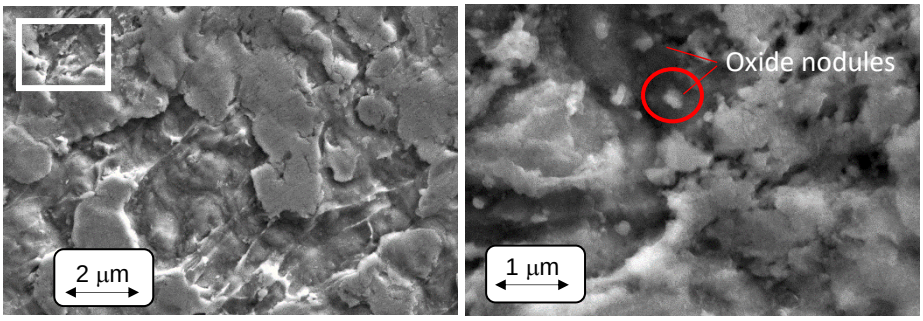

Figure 4-5. Scanning electron micrographs of the DP980 annealed "A" sample, highlighting the oxide nodules formed during annealing. The image on the right corresponds to the white boxed region in the image on the left.

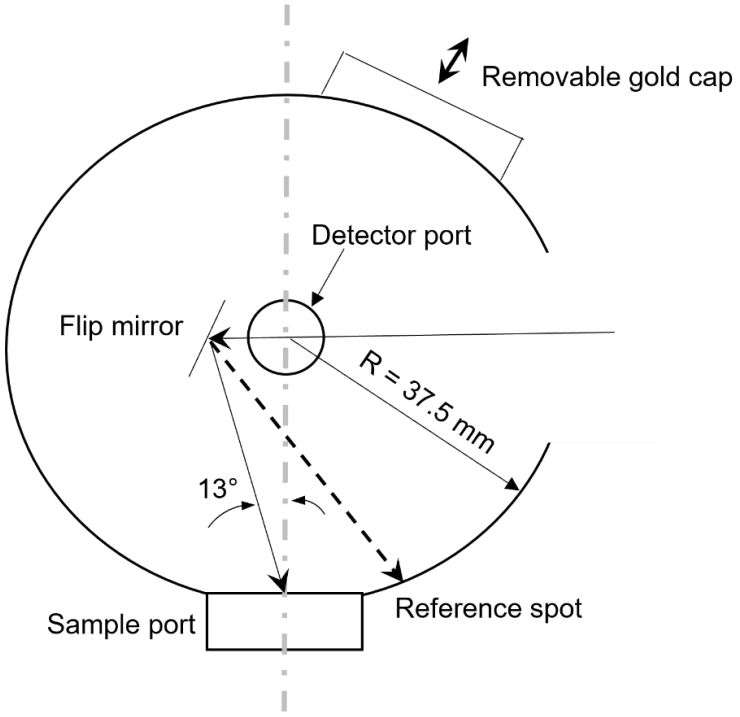

Figure 4-6. Configuration of the integrating sphere.

4.3 Radiation properties of annealed samples

Spectral emissivites of DP980 obtained using the spectrophotometer and Bruker Invenio-R spectrometer are shown in Figure 4-7 (left). Each curve is the average of measurements made by rotating the specimen by 90^o in order to compensate for the specimen orientation effect due to rolling direction. As shown in Figure 4-8, for tested samples of annealed "A", annealed "Full" and annealed "Full 0°C", the overall difference caused by rolling effect between the data of 0^o and 90^o is less than 5% within the entire spectrum, and are therefore averaged for subsequent analysis.

The radiative properties obtained using these two devices overlap at their crossover wavelength. In general ε_λ drops with increasing λ, which is consistent with diffraction theory, Eq. (2.47). Also, the spectral emissivity of the as-received sample stands out from the process samples; ε_λ increases with processing for $\lambda < 1$ μm, while ε_λ drops with processing for $\lambda > 1$ μm.

Figure 4-7 (right) also connects the spectral reflectance ($\rho_\lambda = 1-\varepsilon_\lambda$) among the specimens of DP980 subject to surface visible images obtained by stereo microscope. The brightness of each image correlates with ρ_{vis}, the spectral reflectance averaged over the visible spectrum, 0.4-0.7 μm. For samples processed at DP = -30°C the samples become progressively darker with processing. Notably, however, the samples processed at a dew point of 0°C remain nearly as bright/reflective as the as-received state. This seemingly counterintuitive result can be attributed to the transition from external to internal oxidation, which occurs at around -35°C for DP980 [7]. One can observe that ρ_{vis} decreases monotonically with processing time, the reflectance at longer wavelengths is highest for "B", which is intermediate between "A" and "Full". Overall, these results highlight the correlation between the visible appearance of the samples and the spectral reflectance at wavelengths important to pyrometry (1–2.5 μm).

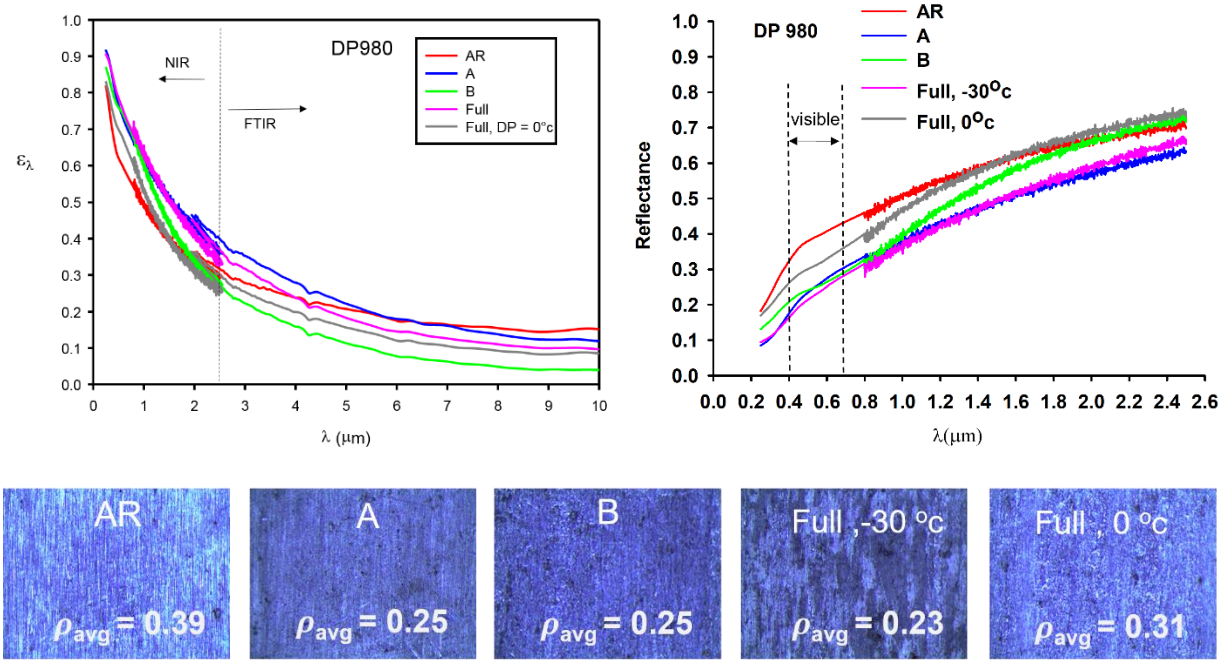

Figure 4-7. Reflectance of DP980 specimens from NIR and FTIR measurement (left) and reflectance of NIR measurement (right) with corresponding visible surface images (bottom). Measured data were obtained by using the UV-VIS-NIR spectrophotometer (0.25-2.5 μm) and Bruker Invenio-R spectrometer (2.5-25 μm). It is observed that the brightness of each image correlates with ρ_{vis}, the spectral reflectance averaged over the visible spectrum, 0.4-0.7 μm.

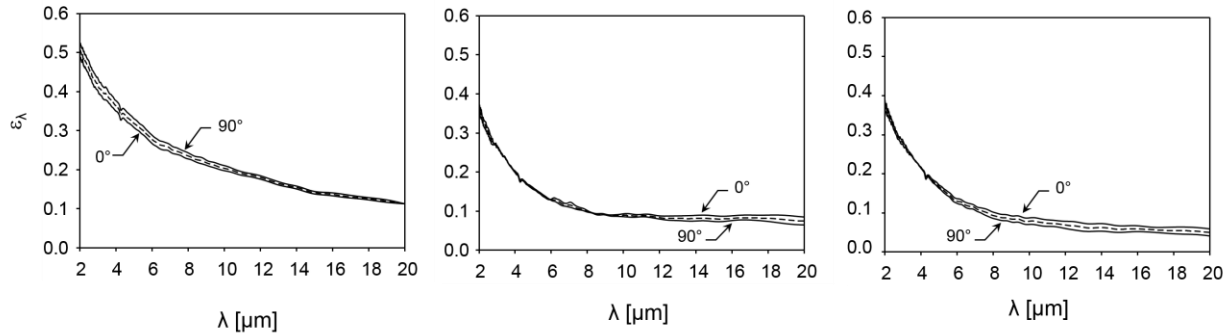

Figure 4-8. Measured spectral emissivity of annealed "A" (left), annealed "Full" (middle) and annealed "Full 0°C" (right) in order to compensate for the specimen orientation effect due to rolling direction, addition measurement was made by rotating the sample by 90°. Slight difference (less than 5%) is observed between the data of 0° and 90° within the entire spectrum for the three samples. The final spectral emissivity is determined by averaging both data, as shown by the dashed line.

4.4 Results and discussion

4.4.1 Agababov model

We first employ the Agababov model to examine the correlation between spectral emissivity and surface roughness. The following relationship is derived by rearranging Eq. (2.14),

$$\frac{Y_s}{Y_r} = \frac{\varepsilon_s(1-\varepsilon_r)}{\varepsilon_r(1-\varepsilon_s)} \tag{2.64}$$

Different measurements of roughness, taken at different sampling lengths and measurement locations on DP980 as-received samples obtained with the contact profilometer were used to derive the surface parameters that were incorporated into Eq. (2.15) to obtain the roughness parameter, *Y*. The results are compared to the roughness parameter derived through Eq.(2.64), as shown in Figure 4-9. It can be seen that the estimations obtained using Agababov's model are not in line with the values obtained directly through surface measurements. This indicates that the Agababov model

cannot predict the radiative properties of the AHSS samples. This may be due to the fact that the surface conditions of the DP980 samples deviate from the assumptions that underlie the Agababov model. One can also observe that surface parameters change with sampling length and measurement locations due to the nonstationary nature of the surfaces, implying that the surface parameters in the Agababov model cannot be reliably found from profilometry.

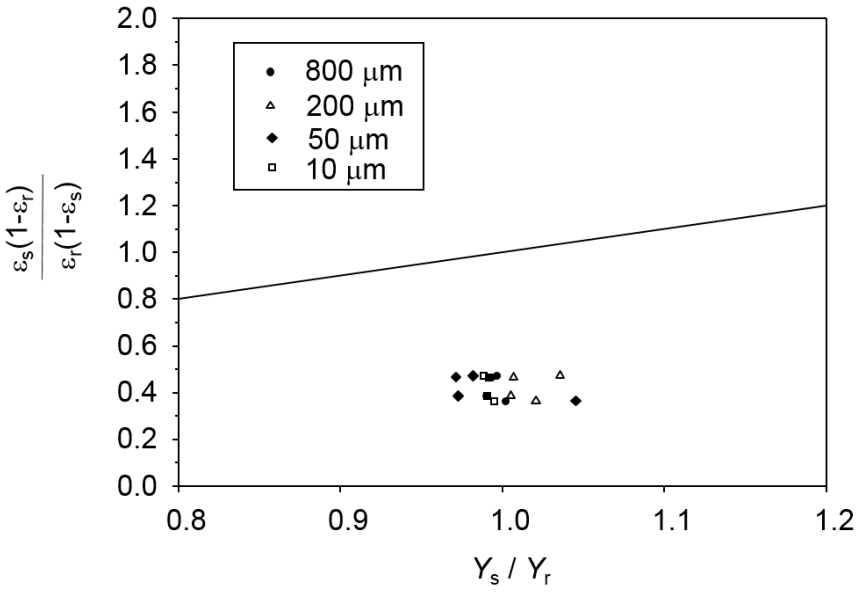

Figure 4-9. Examination of the correlation between surface roughness parameters and spectral emissivity predicted using the Agababov model for the DP980 as-received sample. Different sampling lengths and measuring locations presented as circle, triangle, diamond and square symbols were used to derive the surface parameters that were incorporated into Eq. (2.15) to obtain roughness parameter, *Y*. The solid line represents the case when Eq. (2.64) is satisfied. The results demonstrate that the estimated roughness ratio, Y_s/Y_r, via its relationship with measured spectral emissivity in Eq. (2.64), are not in line with the measured data from the surface profiler, indicating that Agababov model does not work in some cases of present study.

4.4.2 Criterion of Kirchhoff approximation

Next, Eq. (2.31)-(2.33) are employed to investigate the validity of the Kirchhoff approximation for the five tested DP980 samples (polished, as-received, roughened, annealed "A", annealed "Full"), assuming a global grazing angle of 80° since the incident light on the samples is near-

normal. The RMS radius of curvature of the surface is calculated through Eq. (2.34). The profilometer-inferred σ values are shown in Table 4-3. Figure 4-10 verifies that this condition is satisfied for all samples, although it is most in line with the polished sample.

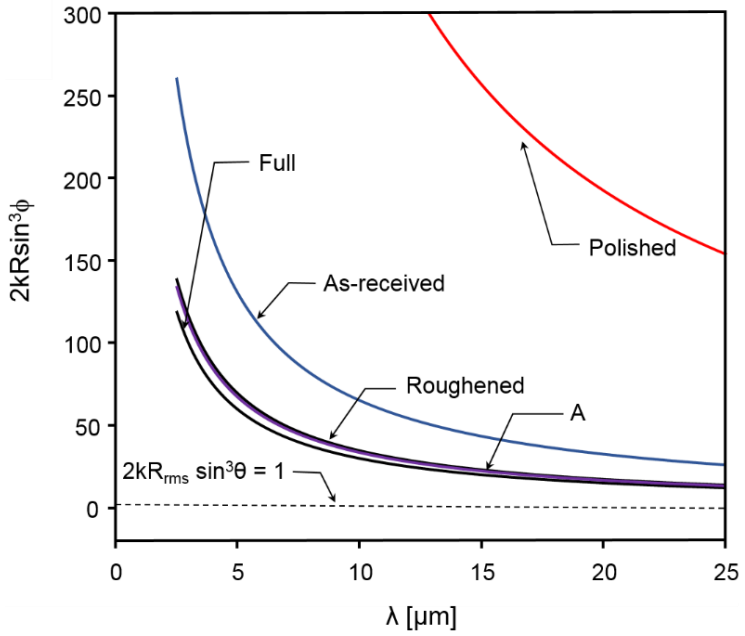

Figure 4-10. Verification of the applicability of the Kirchhoff approximation using Eq. (2.31) using profilometry-derived surface parameters.

4.4.3 Comparison of optically-derived and wavelet-filtered surface roughness

The measured spectral, directional-hemispherical reflectances for the five samples is plotted in Figure 4-11 (a), which qualitatively confirms the trend predicted by Eq. (2.47). Of the un-annealed samples, the polished sample has the highest reflectivity, followed by the as-received sample and roughened sample. The spectral reflectances of the two annealed samples, "A" and "Full", are nearly indistinguishable, and stand out from the others; they have a lower reflectance at short wavelengths, and approach the reflectivity of the polished sample at longer wavelengths. Further insights into these trends is found by taking the logarithm of Eq. (2.47),

$$\ln\left[\frac{\rho_\lambda}{\rho_{\lambda,s}(\lambda)}\right] = -\left(\frac{4\pi\sigma}{\lambda}\right)^2 \tag{2.65}$$

where the spectral reflectance of the smooth surface, $\rho_{\lambda,s}$, is found from Eq. (2.38)-(2.39) with $r_{e,0}$ = 1.43×10^{-7} Ω·m (carbon electrical steel at room temperature, [160]). Replotting the reflectance data accordingly in Figure 4-11 (b) shows nearly linear trends for the non-annealed samples, while the data obtained from the annealed sample is more curved. The σ values obtained from linear regression of $\ln(\rho\lambda/\rho_{\lambda,s})$ vs $1/\lambda^2$ are shown in Table 4-3, and are denoted "optical roughness". In the case of the polished sample, the RMS roughness measured with the profilometer closely matches the one found from Eq. (2.65), while for the other samples the profilometer-derived value is much larger.

Table 4-3. RMS roughness inferred by linear regression of measured $\rho_{\lambda,d\text{-}h}$ via Eq. (2.65), along with surface RMS roughness and correlation length inferred from the profilograms before and after filtering

	$\sigma_{profiler}$ [μm]	$\sigma_{optical}$ [μm]	$\sigma_{filtering}$ [μm]
Polished	0.08	0.091	-
As-received	0.61	0.092	0.106
Roughened	1.55	0.094	0.103
Annealed, A	0.37	0.131	0.138
Annealed, Full	0.34	0.129	0.118

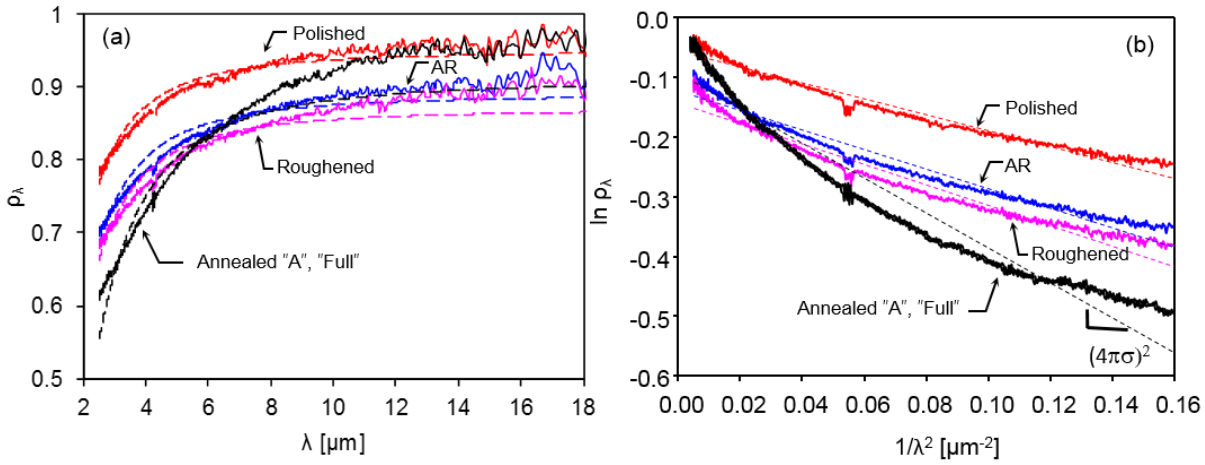

Figure 4-11. (a) Plot of ρ_λ vs λ and (b) plot of $\ln\rho_\lambda$ vs $1/\lambda^2$. The trends found through linear regression via Eq. (2.65) are shown as dashed lines. The spectral reflectance of the "A" and "full" samples are nearly indistinguishable.

Next, 2-D wavelet filtering is used to remove the low-frequency micrometer-scale roughness artifacts, following Ham et al. [156]. In this work the Daub2 wavelet transform technique was adopted wherein the surface is decomposed into four levels having different frequencies [161, 162]; the 2-D surface profile is then reconstructed using the highest frequency wavelets (first level wavelet) as illustrated in Figure 4-12 for the as-received surface. The surface topography of the roughened sample before and after wavelet filtering is shown Figure 4-13. As indicated in Table 4-3, the filtered RMS roughness values, σ, are much closer to the ones obtained via Eq. (2.65) compared to the unfiltered values.

In order to assess the robustness of surface data measured by optical profiler and the profile derived from wavelet filtering, the surface height statistical distribution is compared with that of the data measured by the AFM for annealed "A" sample, as shown in Figure 4-14. The contact mode was set as the scan mode for the measurement, with sampling length 10 μm, and lateral and vertical resolution of 0.02 μm and 0.1 nm, respectively, which is sufficient to resolve the oxide

nodules and other submicron features that are hypothesized to affect the radiative properties. The roughness distributions found through the AFM and filtered optical profilogram are very similar, while the RMS roughness, σ, is nearly identical. These results confirm the physical relevance of the surface statistics found from the filtered optical profilograms. As shown in Figure 4-15, the surface topography derived by using AFM and SEM techniques are compared on the same scale and the oxide nodules from both images can be obvious seen in similar patterns. This further demonstrates the existence of oxide nodules formed on the surface of annealed samples.

The histograms for the unfiltered surface profile, shown in Figure 4-16, are distinguished by how they were processed: the roughness of the polished sample is caused by random, cumulative manufacturing process and is more similar to the Gaussian spectrum curve, while surface artifacts imparted on the as-received (rolling) and roughened (abraded) surfaces exhibit anisotropically-distributed surface heights, and are much larger than the optically-inferred RMS roughness. The surface roughness of the annealed sample follows a near-normal distribution, and exhibits less skewness than the as-received and roughened samples. After removing the global roughness ζ becomes normally-distributed for the as-received, roughened, and annealed samples, suggesting that the surface features at the micrometer length scale originate through random processes, and, in this respect, are more in line with the assumptions that underlie Eq. (2.47).

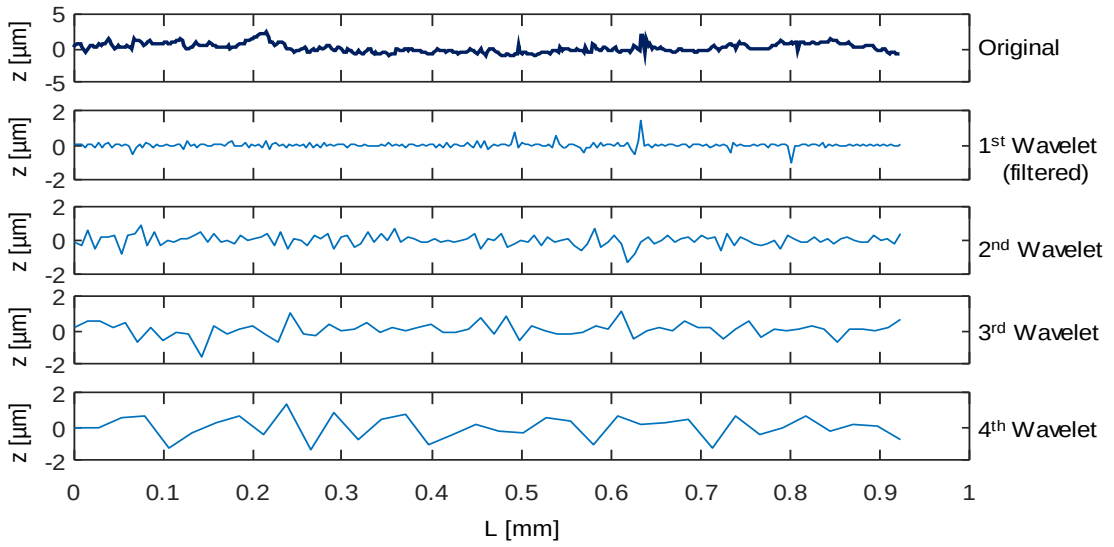

Figure 4-12. Surface profiles obtained using wavelet filtering for the as-received sample. The original profile is decomposed into a set of different levels of wavelets (1st, 2nd, 3rd, 4th), where the lower level stands for wavelet with higher frequency and less amplitude. The "high-pass filtered surface" is recovered by reconstructing the 1st level wavelet into a new profile.

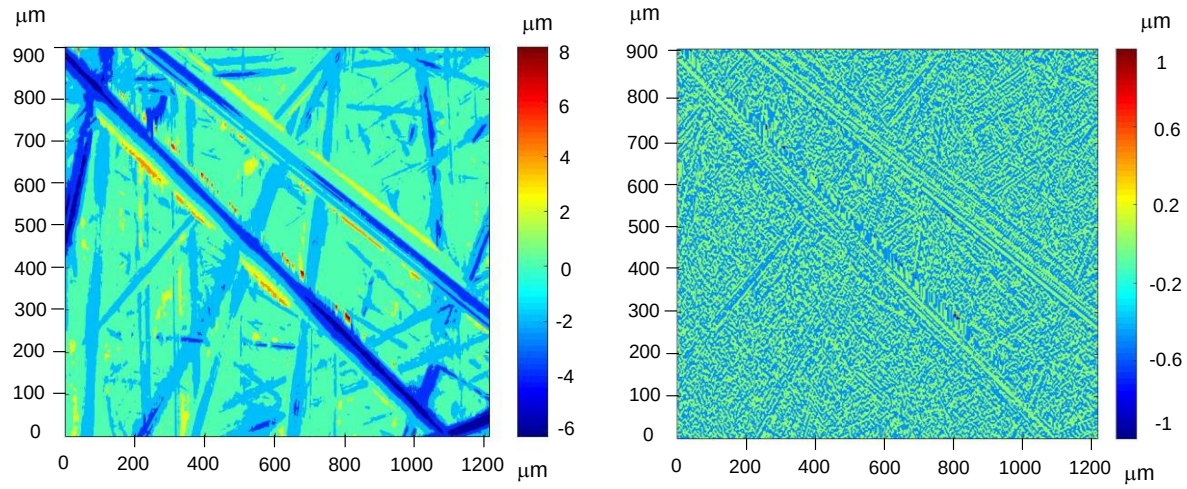

Figure 4-13. Surface topography of roughened sample before (left) and after (right) the removal of global texture. The topography is recovered via the surface profile data obtained from the optical profiler. Daub2 wavelet mode is employed in the high-pass filtering process for the removal of global roughness texture. The filtered surface profile composed of local scale roughness, which is caused by random process, has RMS roughness of around 0.1 µm in general.

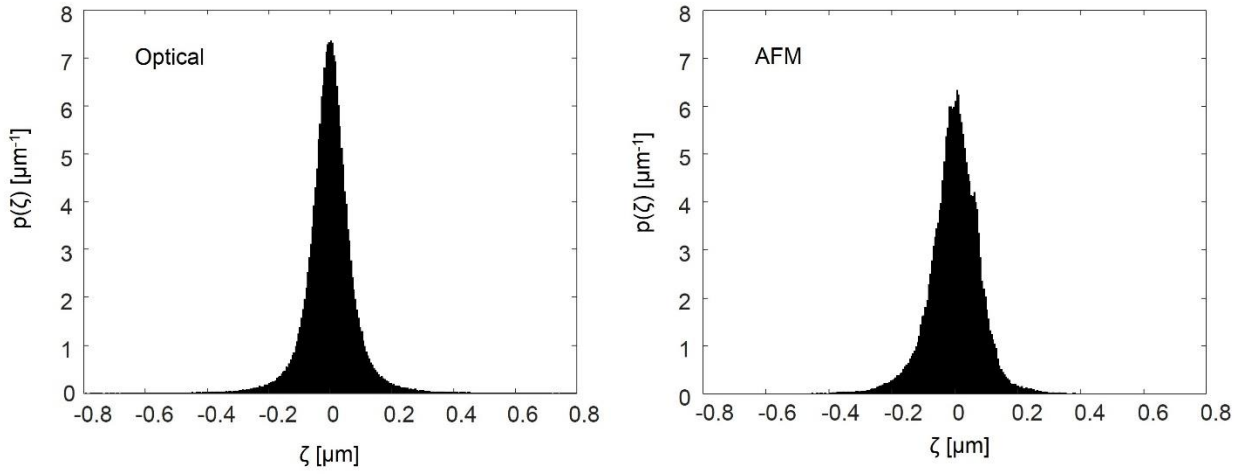

Figure 4-14. Comparison of statistical heights between filtered surface profile (left) with that of measured by atomic force microscope (right) for annealed "A" sample. Although the optical profiler cannot capture the detained surface data at lateral resolutions below 1.6 μm, similar distributions are observed from both profiles that result in almost same surface height deviation, σ. This demonstrates the robustness of using optical profiler and filtering techniques to obtain the overall surface parameters.

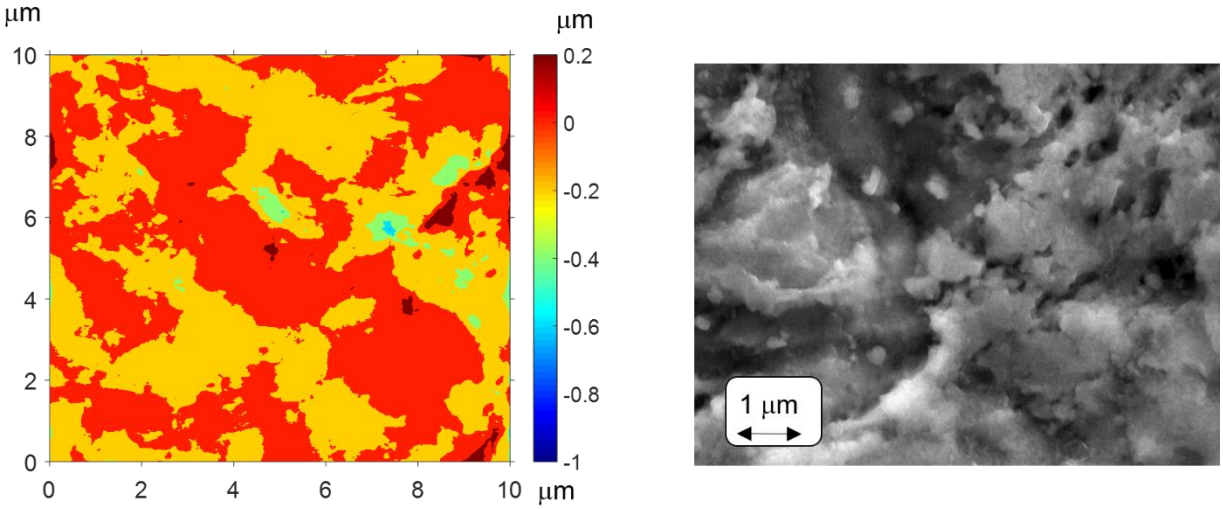

Figure 4-15. Comparison of AFM (left) and SEM (right) images of annealed "A" sample. It can be seen that the oxide nodules observed from SEM correspond to the pattern presented in the AFM derived profile, demonstrating the existence of oxide nodules and consistent surface topography measured from two techniques.

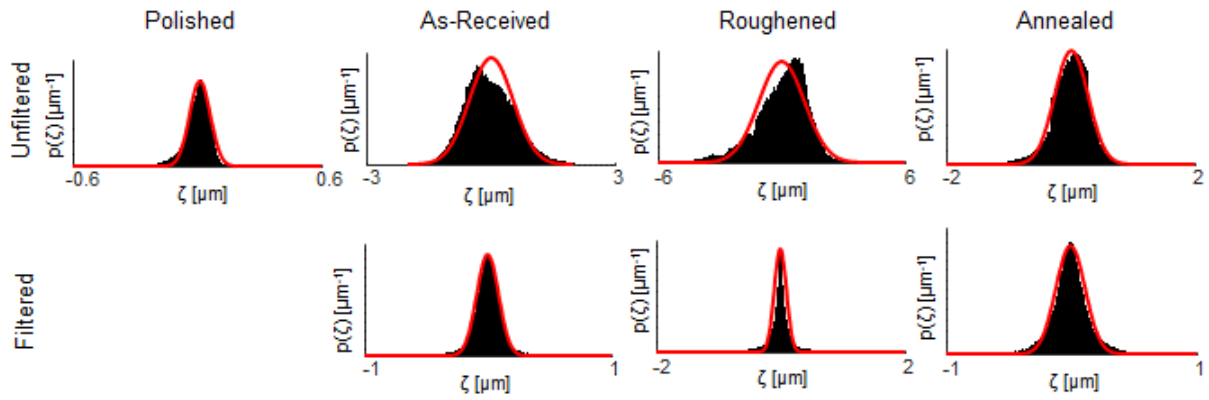

Figure 4-16. Probability density of surface roughness from filtered and unfiltered profilograms. The histograms for the unfiltered surface profile are distinguished by how they were processed. The surface roughness of the annealed sample follows a near-normal distribution, and exhibits less skewness than the as-received and roughened samples. It can be seen that surface profile becomes normally-distributed after removing the global roughness for the as-received, roughened, and annealed samples, suggesting that the surface features at the micrometer length scale originate through random processes, and, in this respect, are more in line with the assumptions that underlie Eq. (2.47).

4.4.4 Comparisons of reflectance predictions and measurements

The measured spectral, directional-hemispherical reflectance and modeled values found using Eq. (2.47) are plotted in Figure 4-17 (a)-(e). To comply with the testing condition, a normal incident angle ($\theta=0^{\circ}$) is assumed in the model. Figure 4-17 (*a*) compares the measured spectral reflectance of the polished surface to the modeled values obtained from Eq. (2.47) using the profilometer-derived RMS roughness. In this case the modeled specular reflectance matches the measured directional-hemispherical value for wavelengths that satisfy the Fraunhofer criterion, $\sigma/\lambda < 0.03$. In the case of RMS roughness of 0.10 μm, the modeled specular reflectance matches the measured directional-hemispherical value when $\lambda > 2$ μm. The surface is sufficiently optically-smooth over this range to model the interaction as specular [163]. At shorter wavelengths the modeled values underestimate the measured values because of the presence of a diffuse component of reflectance

which is captured by the integrating sphere but not accounted for by the Davies model. Similar results have been reported elsewhere [59, 164].

Figure 4-17 (a) also shows the fit one would obtain using the optical-derived roughness σ and a wavelength-independent value of $\rho_{\lambda,s}$ that is left as a fitting parameter, instead of the Hagen-Rubens relation. A nonlinear least-squares regression between the modeled and the portion of the measured spectral reflectances that satisfy the Fraunhofer criterion results in $\rho_{\lambda,s} = 0.96$ for the polished surface, but this modeled reflectance does not match the measurements as what is found when $\rho_{\lambda,s}$ is obtained from the Hagen-Rubens relation.

For the other samples, Figure 4-17 (b)-(e) show a significant discrepancy between the measured directional-hemispherical reflectance and modeled specular reflectance calculated using the profilometer-derived roughness, but show much better agreement when the filtered roughness is used in its place. This affirms the finding of Ham et al. [156] that, for optically-rough surfaces, the profiler-measured roughness is not directly relevant to the spectral emissivity; instead the directional-hemispherical reflectance can be modeled via Eq. (2.47) considering the interaction of the incident waves at a "locally rough" surface. In such a scenario, the surface profile is "optically smooth" and thus the global reflectance is reduced to Eq. (2.48). As the surfaces become globally rougher, based on their optical and filtered RMS roughness relative to the wavelength, a larger fraction of the incident energy is reflected outside of the specular direction, which gives rise to increased deviation between the prediction and measurement. The measured spectral reflectance of the two annealed surfaces, Figure 4-17 (d) and (e), stand out from the other samples; the reflectance of these surfaces at shorter wavelengths is significantly lower than that of the other surfaces, likely due to scattering by the oxide nodules shown in Figure 4-5. This is also reflected

by the larger values of σ shown in Table 4-3, indicating that these surfaces are optically rougher at local scale compared to the un-annealed surfaces.

Finally, we consider how the spectral reflectance may change with temperature. Figure 4-17 (a) showed that it is necessary to account for the spectral dependence of $\rho_{s,\lambda}$ according to the Hagen-Rubens relation in order to capture the spectral variation of ρ_{λ} for wavelengths that satisfy the Fraunhofer criterion. Given the wide range of temperatures encountered during intercritical annealing, this result suggests that the temperature dependence of the radiative properties via the electrical resistivity may also be important to consider. Figure 4-18 plots the estimated spectral reflectance using Eq. (2.38)-(2.39) and Eq. (2.47) at different temperatures (25°C, 400°C, 800°C), given the same surface roughness (σ=0.134) and assuming a value of α = 0.005 K^{-1}, which is typical for steel [165]. It can be seen that the temperature-dependent electrical resistivity of steel significantly affects the modeled spectral reflectance, even excluding the additional variation one would expect as the surface phase evolves with processing. This result motivates the development of strategies for measuring the spectral reflectance of AHSS samples at high temperatures, in order to derive results that are directly applicable to industrial conditions, and highlights the importance of including temperature-dependence in the pyrometry measurement equations.

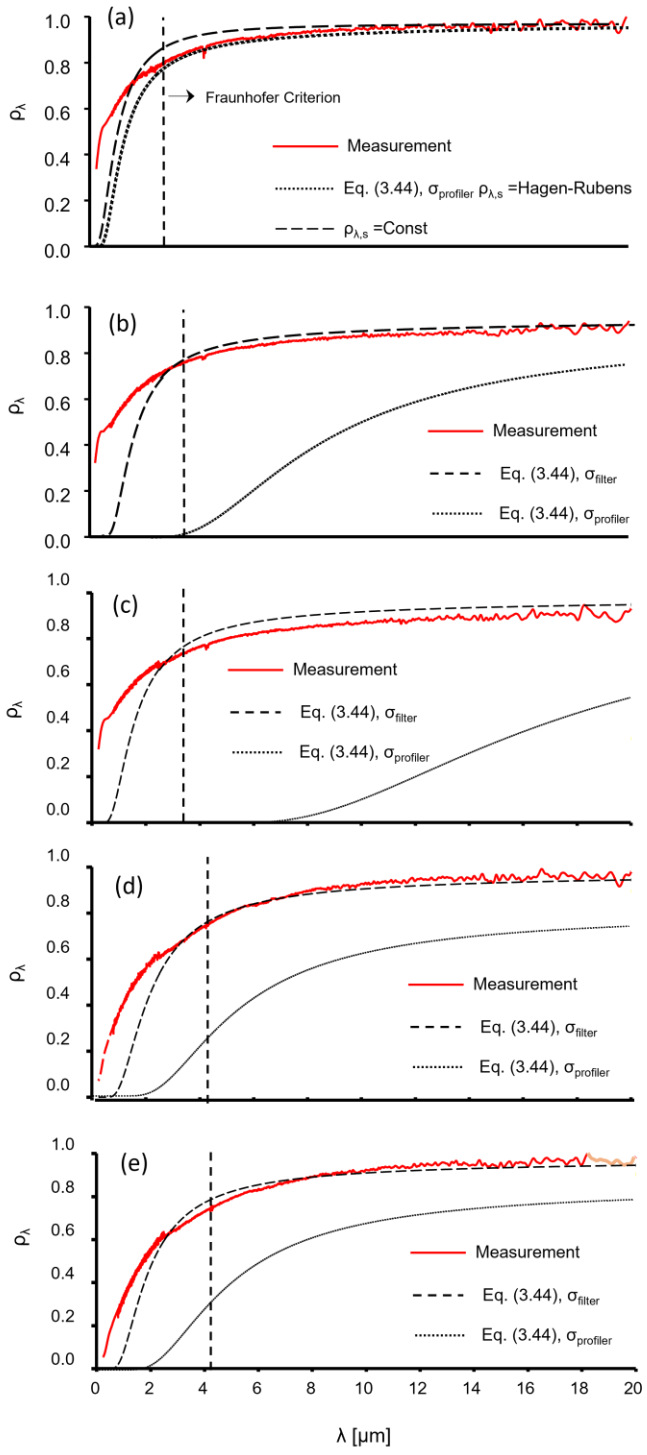

Figure 4-17. Comparison of measured and estimated reflectance for (a) polished, (b) as-received, (c) roughened, (d) annealed "A" and (e) annealed "Full" samples. The long dash line in (a) denotes the estimation of Eq. (2.47) with constant $\rho_{\lambda,s}$. The estimations from (b)-(e) were achieved by applying Eq. (2.47), using Hagen-Rubens derived $\rho_{\lambda,s}$ with profiler measured σ (dotted line) and filtered σ (dashed line), respectively. The Fraunhofer criterion based on the optical roughness is shown as a vertical dashed line for all cases.

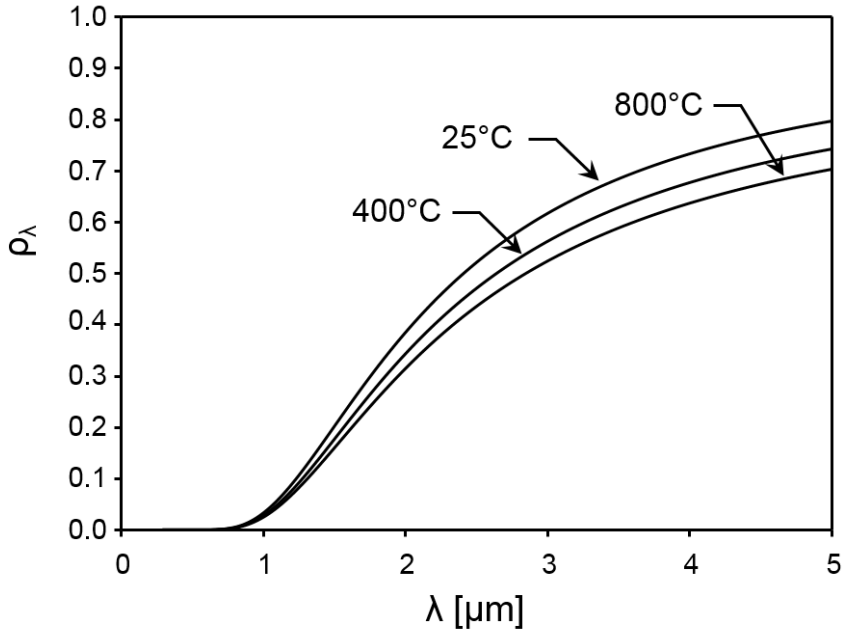

Figure 4-18. Comparison of estimated spectral reflectance given different temperatures with the same surface roughness, σ=0.134, found from Eq. using Eq. (2.38)-(2.39) and Eq. (2.47). It can be seen that the temperature-dependent electrical resistivity of steel significantly affects the modeled spectral reflectance, even excluding the additional variation one would expect as the surface phase evolves during annealing. Such result highlights how the temperature-dependent electrical resistivity can affect the predictions and motivates the development of strategies for measuring the spectral reflectance of AHSS samples at high temperatures during annealing.

4.5 Conclusions

This chapter examines the relationship between surface topography and the radiative properties of advanced high strength steel alloys having different surface states. The measured spectral reflectivity follows the expected trend with wavelength expected from Davies' model, and, in the case of the polished sample, the optical roughness inferred from this trend matches the value measured with an optical profilometer. For other surfaces, however, the profilometer-derived roughnesses are much larger than optically-inferred values, while the roughness of wavelet-filtered profilograms are more consistent with the optically-derived values. Although the high-pass

wavelet filtering provides a roughness scale that explains the spectral reflectance of the steel, it is not entirely clear how this parameter is related to the true surface features.

The Davies' model reproduces the experimentally-measured hemispherical-directional reflectance when the filtered roughness is used, provided the surface satisfies the Fraunhofer criterion so that the reflectance is mainly specular. This finding implies that, for the wavelengths important to steel pyrometry, the radiative properties of the steel are dominated by how the EM wave interacts with local (sub-micrometer) roughness scale artifacts. These results also show that it is important to account for the spectral dependence of $\rho_{s,\lambda}$ in Davies' model using the Hagen-Rubens relation; while the focus of this study is on how the evolving surface oxide may affect emissivity, this result also highlights that the temperature-dependent electrical properties of the substrate steel are also important. This finding motivates the development of strategies for measuring the spectral reflectance of AHSS samples at high temperatures in the context of industrial conditions.

Chapter 5 Interpreting the Radiative Properties of Advanced High Strength Steel using the Geometric Optics Ray-tracing Approximation[6]

5.1 Introduction

Although Chapter 4 shows the feasibility of applying Davies' model with wavelet-filtered roughness in the prediction of directional-hemispherical reflectance of AHSS, the physical aspect of this remains unclear as the applicability of a specular reflectance model to estimate hemispherical reflectance is questionable. In addition, the model fails to capture the reflectance in the short wavelength region as the surface becomes optically rough. Consequently, an alternate model is needed to account for the spectral emissivity of rough AHSS samples. As mentioned in section 3.3.8, the geometric optics approximation (GOA) with ray tracing serves as an effective approach to estimate the radiative properties of rough metals. This chapter is focused on the prediction of radiative properties using GOA ray-tracing for rough AHSS samples.

The presence of a thin oxide film on the surface influences the spectral emissivity via constructive and destructive interference discussed in Section 3.2. The importance of this effect depends on the film thickness relative to the wavelength, and may be significant when these two quantities are similar. The radiative properties become more sensitive to the surface irregularities (e.g. oxide nodules, roughness) at wavelengths larger than the oxide film thickness. In this scenario, EM waves are scattered by surface irregularities in a random way, leading to variations in

[6] The content of this chapter is an extended version of a paper published in:
K. Lin, F.K. Suleiman, K.J. Daun, Interpreting the radiative properties of advanced high strength steel using the geometric optics ray-tracing approximation, *Int. J. Heat Mass Transf.*, 176 (2021) 121429. (doi.org/10.1016/j.ijheatmasstransfer.2021.121429)

bidirectional reflectance subject to each scattered direction. In the case of an optically-smooth, perfectly-conducting surface, the variation of specular reflectance with wavelength can be described using Davies' model, Eq. (2.46). These conditions are satisfied when the wavelength is much larger than the roughness scale and the surface can be modeled as specular, in which case the directional-hemispherical reflectance of the surface is close to specular [166], as described by Eq. (2.48).

Diffuse reflections should be considered within the context of directional-hemispherical reflectance when the optical roughness exceeds the Fraunhofer criterion of optically smooth surfaces ($\sigma/\lambda > 0.03125$), [144, 145]. Scattering models derived with the Kirchhoff approximation can be used to predict the specular and diffuse components of reflectance [167], but shadowing effects and multiple scattering are usually neglected [168]. As the surface becomes optically rough, incident waves undergo multiple reflections, leading to more energy absorption during the scattering process. These effects can be captured through ray-tracing models derived using the geometric optics approximation (GOA) as indicated in Chapter 3.

This procedure has been extensively used to model the radiative properties of rough metal surfaces. Tang et al. [169] delineated the valid regime of the GOA approach ($\sigma\cos\theta_0/\lambda > 0.17$, $\sigma/\tau < 2.0$) by comparing the GOA solutions with more precise integral solutions of Maxwell's equations. They revealed that the one-dimensional GOA can yield accurate solutions even when both surface parameters are less than unity. Bruce [170] derived the Mueller matrix by employing a one-dimensional GOA simulation on rough metal surfaces subject to various scattered angles and surface slope parameter, σ/τ. These results were used to define the roughness domain of single scattering. Further work by Tang et al. [171] showed that bidirectional reflectances predicted using GOA within its valid regime were close to those found from a rigorous EM wave

solution. Fu and Hsu [172] further refined this regime of validity by comparing the GOA and finite-difference time-domain solutions. Bergström et al. [173] established a one dimensional ray-tracing model using artificially-generated one-dimensional Gaussian surfaces with various surface parameters and incident angles. It was found the overall absorptance depends on surface slope, roughness, and incident angles.

Increased computational capabilities enable GOA-based calculations on two dimensional surfaces. Studies on isotropic surfaces reveal minor differences compared to one dimensional cases [149, 174]. Tang and Bukius [174] developed a two-dimensional ray-tracing model for Gaussian rough surfaces with various roughness parameters (σ/τ) and incident angles, and compared the bi-directional reflectance results with those from EM scattering theory and experimental data. Modeled values closely approximated those derived via exact solutions and experimental findings. This approach was extended to a statistical model of wave scattering from random rough surfaces underlying the geometric optics approximation [143], in which the first, second, and higher orders of scattering events are predicted through a probability function dictated by the incident angles and surface parameters. The predicted results were found to be consistent with those obtained from geometric optics ray tracing as well as EM wave theory.

More recently, Parviainen and Muinonen [175] employed a Monte Carlo ray tracing (MCRT) method to investigate the reflectance and surface shadowing in porous random media with macroscale surface roughness. The bi-directional reflectances of various rough surfaces at different scattered azimuthal and grazing angles over the full hemisphere were investigated, although multiple scattering of the EM wave was not accounted for in the model. Zhang and Zhao [176] incorporated EM wave interference into a one-dimensional ray-tracing model of a randomly-sampled rough surface composed of a perfect electric conductor to obtain the bidirectional

reflectance distribution function (BRDF). The results were compared to those found using finite difference time domain (FDTD) methods. Sekiguchi and Kaneko [177] developed an advanced rough surface ray tracing (A-RSRT) model considering the shadowing and masking effect in terms of probability functions governed by the surface facet normal distribution. The model was compared to several other statistical models with respect to the BRDF and bi-directional scattering distribution function (BSDF). King et al. [178] employed a modified GOA to evaluate the total hemispherical and directional emissivity from artificially generated one-dimensional random rough surfaces. They found modeled emissivities to be sensitive to the surface geometry and incident angles. Jo et al. [179] extended King's [178] work to evaluate the spectral emissivity of oxidized rough surfaces and favourable comparisons between predictions and measurements were made. Warren el at. [180] applied MCRT to obtain the directional emissivity of a rough surface of Nextel high-emissivity black paint. The predictions were compared to the measured data and the effect of emission angle on directional emissivity was investigated at a specific EM wavelength. Lee [181] developed a simple regression model based on MRCT results for rough silicon and aluminum surfaces at normal incidence. The reflectance predicted using the regression model were within 4.4 % of the MCRT estimations for all surface slope conditions.

The above-mentioned emissivity models have been restricted to predicting the bi-directional reflectance at one wavelength, and they have not been applied to the AHSS alloys important to automotive manufacturing. This chapter evaluates the directional-hemispherical reflectance of AHSS specimens over visible, near-infrared, and mid-infrared wavelengths within the GOA framework described in Chapter 3, with the objective of developing a model that can account for variations in radiative properties due to surface roughness. Six different surface states were investigated: one polished, one roughened, and four as-received AHSS samples. The surface

profiles of the samples were characterized by optical profilometry, as well as optical, electron, and atomic force microscopy. Ex-situ directional-hemispherical reflectance measurements were done using a UV-Vis-NIR spectrophotometer (0.25–2.5 μm) and an FTIR infrared spectrometer (2.5–25 μm), both equipped with integrating spheres. Additional specular reflectance measurements were done using a second FTIR (2.5–15 μm) at an incident angle of 30°. These measurements are interpreted in the context of Kirchhoff diffraction models and two-dimensional GOA via Monte Carlo ray tracing on the rough surfaces, detailed in Section 3.3.8 and 3.3.9. The results show that the directional-hemispherical reflectances derived using the GOA closely match the reflectance data measured using an integrating sphere over wavelengths within the valid GOA regime and important to pyrometry. At wavelengths longer than the GOA regime, the GOA-predicted reflectances in the specular direction for the polished surface remain consistent with experimental measurements, while those for the roughened surfaces do not. In addition, EM wave models developed based on Kirchhoff diffraction theory can be used to estimate the specular and diffuse reflectances of rough samples at long wavelengths. Overall, GOA ray tracing is shown to be useful for parameterizing the wavelength-dependence of near-normal emissivity for multi-wavelength pyrometry, which is the primary objective of this study.

5.2 Sample preparation and measurement

The Chapter uses samples cut from two cold-rolled DP980 alloys (alloys A1 and A2) and one cold-rolled DP780 alloy (alloy A3), having elemental compositions consistent with the corresponding ASTM standards [182] as indicated in Table 5-1. Although the exact alloy composition is proprietary, the Si/Mn mass ratios specific to these alloys are found to be 0.23, 0.04, and 0.10 for A1, A2, and A3, respectively, using inductively coupled plasma (ICP) spectroscopy. Samples #1,

#2, and #3 are the polished surface samples from alloys A1, A2, and A3, respectively, obtained using a series of five polishing wheels with progressively finer grit and particle size (240 grit SiC, 320 grit SiC, 400 grit SiC, 600 grit SiC, diamond compound, gamma alumina), resulting in a mirror-like finish texture. Sample 5 was made by abrading Alloy A1 with 30 μm sand paper, while samples #4 (A1), #6 (A1), #7 (A3), and #8 (A2) remained in their as-received states. The rolling traces on their appearances can be observed in the optical microscopy and profilogram images in Figure 5-1.

Surface profiles and parameters were measured using an optical surface profiler (WYKO NT1100) with a vertical measurement resolution of 0.1 nm and horizontal resolution of 1.6 μm, which provides both the RMS roughness, σ, and the RMS surface slope, *s*, in Eq. (2.35). The derived surface parameters for these samples are listed in Table 5-2, and the optical profilograms are shown in Figure 5-2. Since Sample #1, #2, #3 have similar appearances as well as identical surface features, the latter two are excluded from the figure. The surface statistical data obtained from the optical profilogram for Sample #2 is consistent with the topography obtained from an atomic force microscope (AFM, Pacific Nanotechnology Nano-R™), with a vertical resolution of 0.1 nm, lateral interval of 0.02 μm and scanning area of 10μm ×10μm, which confirms the physical relevance of surface statistics. Consequently, the surface profiles of the tested samples in this study are acquired from optical profilometry. All samples were cleaned with isopropanol, and then rinsed with alcohol and distilled water to remove any additional particles and contaminants before the optical measurement. The near-normal directional-hemispherical spectral reflectance of each sample was measured using a Varian Cary 5000 UV-Vis-NIR spectrophotometer (0.25-2.5 μm) and a Bruker Invenio-R spectrometer (2.5-20 μm) detailed in Chapter 4, while the specular

reflectances at an incident angle of 30° were obtained using a Nicolet 6700 FTIR (2.5–15 μm) equipped with a VeeMAX III variable angle specular reflection apparatus.

Table 5-1. List of tested AHSS alloys with chemical compositions (weight %) based on the ASTM standards [41]. The Si/Mn ratio is measured using inductively-coupled plasma spectroscopy.

Alloy	C	P	**S**	**Cu**	**Ni**	**Cr+Mo**	**Mn+Al+Si**	**Si/Mn**
DP980 (A1)	0.23	0.08	0.015	0.20	0.50	1.40	6.00	0.23
DP980 (A2)	0.23	0.08	0.015	0.20	0.50	1.40	6.00	0.04
DP780 (A3)	0.18	0.08	0.015	0.20	0.50	1.40	5.40	0.10

Table 5-2. List of samples with measured surface parameters from optical profilometry.

Sample No	**#1**	**#2**	**#3**	**#4**	**#5**	**#6**	**#7**	**#8**
Alloy	A1	A2	A3	A1	A1	A1	A3	A2
σ [μm]	0.08	0.10	0.09	0.66	1.48	0.95	2.60	0.61
τ [μm]	3.03	2.96	3.02	2.02	2.85	2.71	7.65	1.33
σ/τ	0.02	0.03	0.03	0.33	0.52	0.35	0.32	0.46
Ratio of 1st order scattering	1	1	1	0.78	0.47	0.72	0.73	0.61
Ratio of 2nd order scattering	0	0	0	0.21	0.41	0.25	0.25	0.33
Ratio of 3rd (and above) order scattering	0	0	0	0.02	0.11	0.03	0.02	0.06

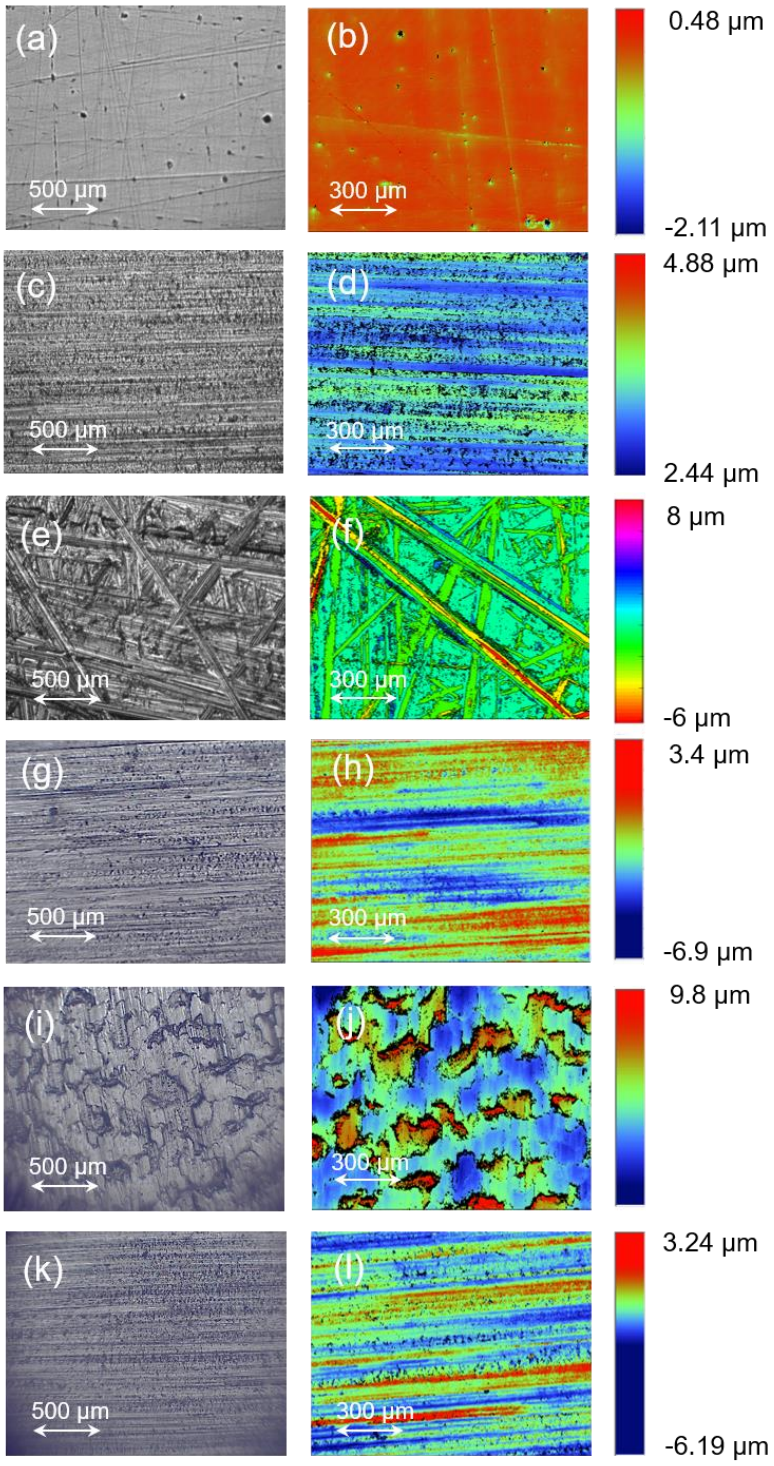

Figure 5-1. Optical microscopy (left) and optical profilograms (right) of sample #1 (a, b), sample #4 (c, d), sample #5 (e, f), sample #6 (g, h) sample #7 (i, j) and sample #8 (k, l). Artifacts from the cold-rolling process are evident in sample #4, #6, #7, and #8. Note that samples #4, #6, #8 underwent ground rolling in the last stand rolling finish, and appear different from sample #7, which underwent electro-discharge (EDT) rolls in the last stand finish.

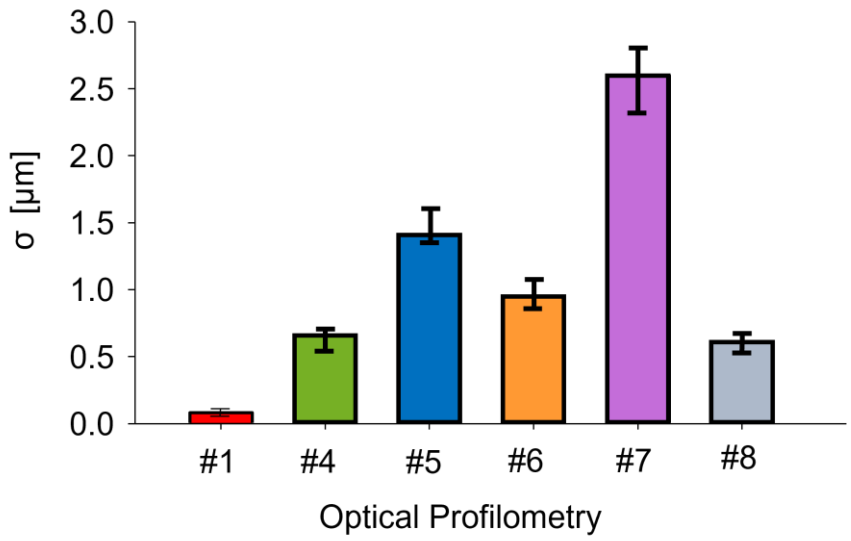

Figure 5-2. RMS roughness of tested samples measured using the optical profilometry.

5.3 Results and discussion

5.3.1 AFM and optical profiler surfaces, Kirchhoff criterion

Figure 5-3 compares the probability density function of surface heights for Sample #2 (as-received surface) derived using optical profilometry to the one obtained using the AFM. The AFM was set to contact mode, with a sampling length of 10 μm, and has a lateral and vertical resolution of 0.02 μm and 0.1 nm, respectively. The surface profile derived from optical profilometry is filtered under 10 μm using the 2D Fourier transform method [183] to match the AFM measurement scale. Both methods reveal similar surface height distributions, and the overall surface slope, σ/τ, of these two profiles are similar. These results indicate the physical relevance of surface statistics evaluated from the optical profilograms.

Figure 5-4 shows that Kirchhoff's approximation should be valid for all the samples based on Eq. (2.31), although it is most in line for the polished samples as the critical point value

($2kR\cos^3\theta_o$) for the roughened and as-received samples approaches unity with increasing wavelength.

The statistical variances of the predicted directional-hemispherical reflectance using Monte Carlo ray tracing are listed in Table 5-3, with incident angles θ_o=10º ,φ_o=45º, among wavelengths between λ =0.45 μm and λ =2.8 μm. A total number of 30 simulations were carried out on sample #8 (σ=0.61 μm, τ=1.33 μm, σ/τ=0.46) and the statistical data for each wavelength were derived. It is shown that the variances between all predictions are tiny, highlighting the robustness of the Monte Carlo method in this study.

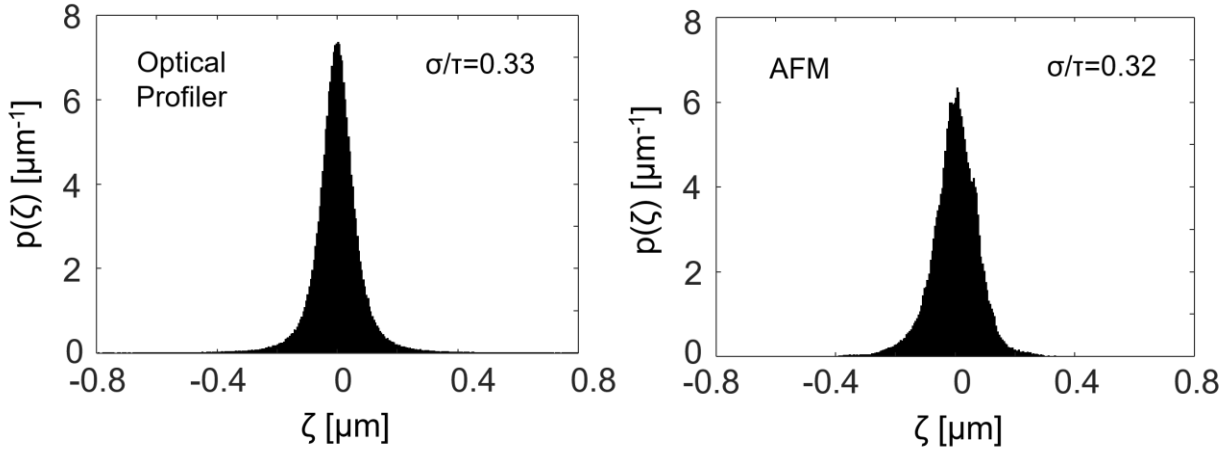

Figure 5-3. Comparison of probability density function for heights between the filtered surface profile (left) with that of measured by atomic force microscopy (right) for sample #2. Although the optical profilometer cannot capture the detailed surface data at lateral resolutions below 1.5 μm, similar distributions are observed from both profiles, resulting in almost the same surface height deviation, σ. This demonstrates the robustness of using optical profilometry to obtain the overall surface parameters required for GOA modeling.

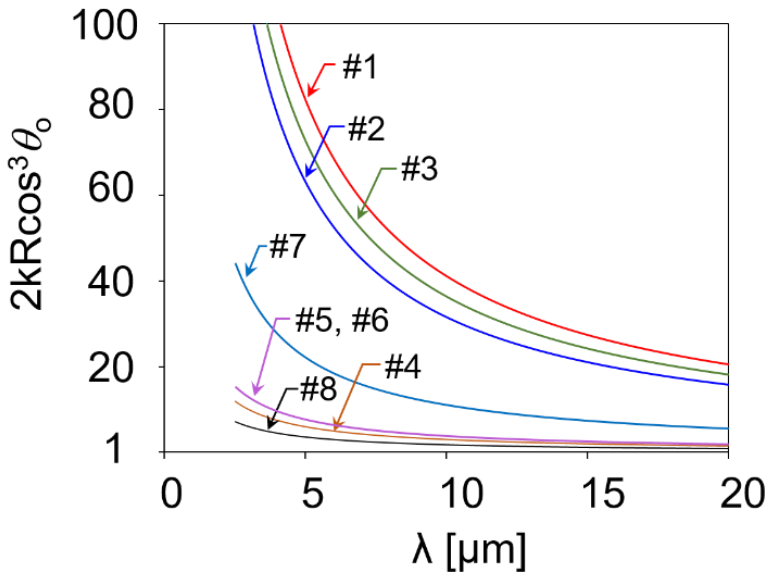

Figure 5-4. Verification of the applicability of the Kirchhoff approximation using Eq. (2.31).

Table 5-3. Variance between the predictions using Monte Carlo ray tracing.

	Wavelength, λ							
	0.45 μm	0.70 μm	0.90 μm	1.2 μm	1.7 μm	2.0 μm	2.4 μm	2.8 μm
Variance in ρ_λ	2.51×10^{-6}	2.51×10^{-6}	2.20×10^{-6}	1.94×10^{-6}	1.37×10^{-6}	1.12×10^{-6}	9.76×10^{-7}	8.32×10^{-7}

5.3.2 Measured directional-hemispherical reflectances

The measured directional-hemispherical reflectances of the surfaces are plotted in Figure 5-5 (a). The yellow shaded area represents the spectral range typically employed for industrial pyrometers used in steel manufacturing, which partially overlaps the gray shaded area defining the wavelengths over which the GOA model is valid for samples #5 and #6. The rough surfaces have a lower reflectance than the polished surface; this difference becomes more pronounced as the wavelength decreases, since, at short wavelengths EM waves (rays) undergo multiple reflections

at the surface, leading to more energy transfer between the waves and the surface. In contrast, at long wavelengths scattering is dominated by diffraction effects [126]. Consequently, diffraction models derived with the Kirchhoff approximation, such as Eq. (2.46), cannot be used to model radiative properties at shorter wavelengths since they do not account for the effect of multiple reflections [168], which are considered in GOA.

Figure 5-5 (b) compares the reflectance of pure iron, calculated using Fresnel's equation at normal incidence with optical constants obtained from Refs. [184, 185], and the predicted and measured directional-hemispherical reflectances found using the same optical constants in the GOA model. All polished samples have nearly identical measured reflectances, even though the alloy compositions are distinct. This suggests that differences in the directional-hemispherical reflectances of these samples will be dominated by differences in surface topography instead of their alloy composition. However, alloy composition strongly influences surface oxidation [26, 28].

The GOA results also demonstrate that first-order scattering dominates the radiative properties of these surfaces due to their smoothness ($\sigma/\tau=0.02$), as the predictions are similar to the reflectance of polished iron. These results also reflect the data in Table 5-2. Although the predicted results are slightly different from the measured reflectances of polished samples at longer wavelengths, they are close to the reflectances of polished samples at short wavelength region ($\lambda<2.5$ μm), which are the most important wavelengths for pyrometry.

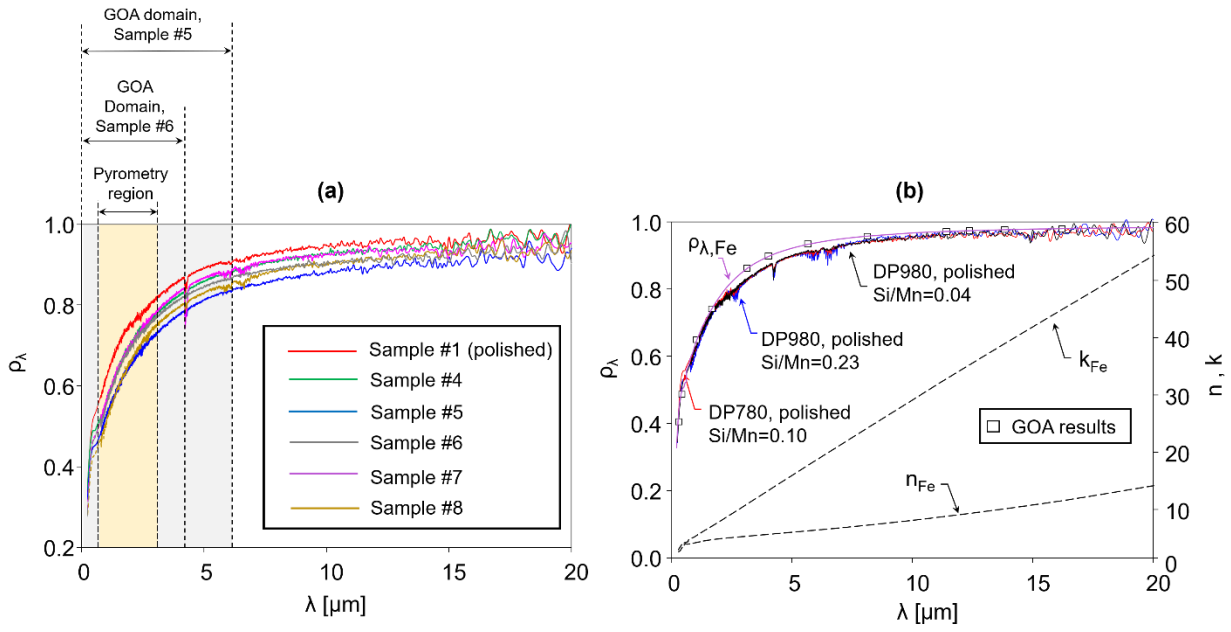

Figure 5-5. Comparisons of measured directional-hemispherical reflectance of all tested samples (left) and measured reflectance of polished surfaces of the three alloys (right) used in the tested rough samples. The yellow shaded area in the left plot represents the spectrum of pyrometry interest, while the gray shaded area contains the GOA valid domain of sample #5 and sample #6. The square symbols in the right plot represent the GOA predictions and the two dash curves are the refractive indices for iron from Refs. [42,43].

5.3.3 Comparison of 1-D and 2-D GOA modeling, incident azimuthal angle effect

Figure 5-6 (a)-(d) compare the predicted directional-hemispherical reflectance of four rough surfaces (Samples #1, #4, #7, and #8) over 0.25-2.50 μm for both 1D and 2D ray tracing. For the 1D surface models, the *x*-direction of the surface is parallel to the rolling direction. The reflectance predicted using 1D and 2D surface models are nearly identical for the polished sample, Figure 5-6 (a), but there are pronounced differences for the rough surfaces, Figure 5-6 (b)-(d). Slight differences in reflectance estimations between *x*- and *y*-directions of the 1D ray tracing model are seen for sample #4 and sample #8 (Figure 5-6 (b) and (d), respectively). The slightly lower reflectances in *y*-directions of these samples are due to the larger surface height variations caused

by cold-rolling. Overall, the 1D ray tracing predictions are different than those obtained from 2D models for non-smooth samples, and the 2D approach is more relevant for the purposes of developing a pyrometry model.

Figure 5-7 (a)-(d) show the effects of incident azimuthal angle (φ_o=0°, φ_o=45°, φ_o=90°) on the estimated directional-hemispherical reflectances of the samples. The incident azimuthal angle has a negligible effect on the predicted reflectances, even though some of the surfaces are anisotropic, as depicted in Figure 5-1. Consequently, this study adopts an arbitrary angle (φ_o=45°) for subsequent 2D modeling.

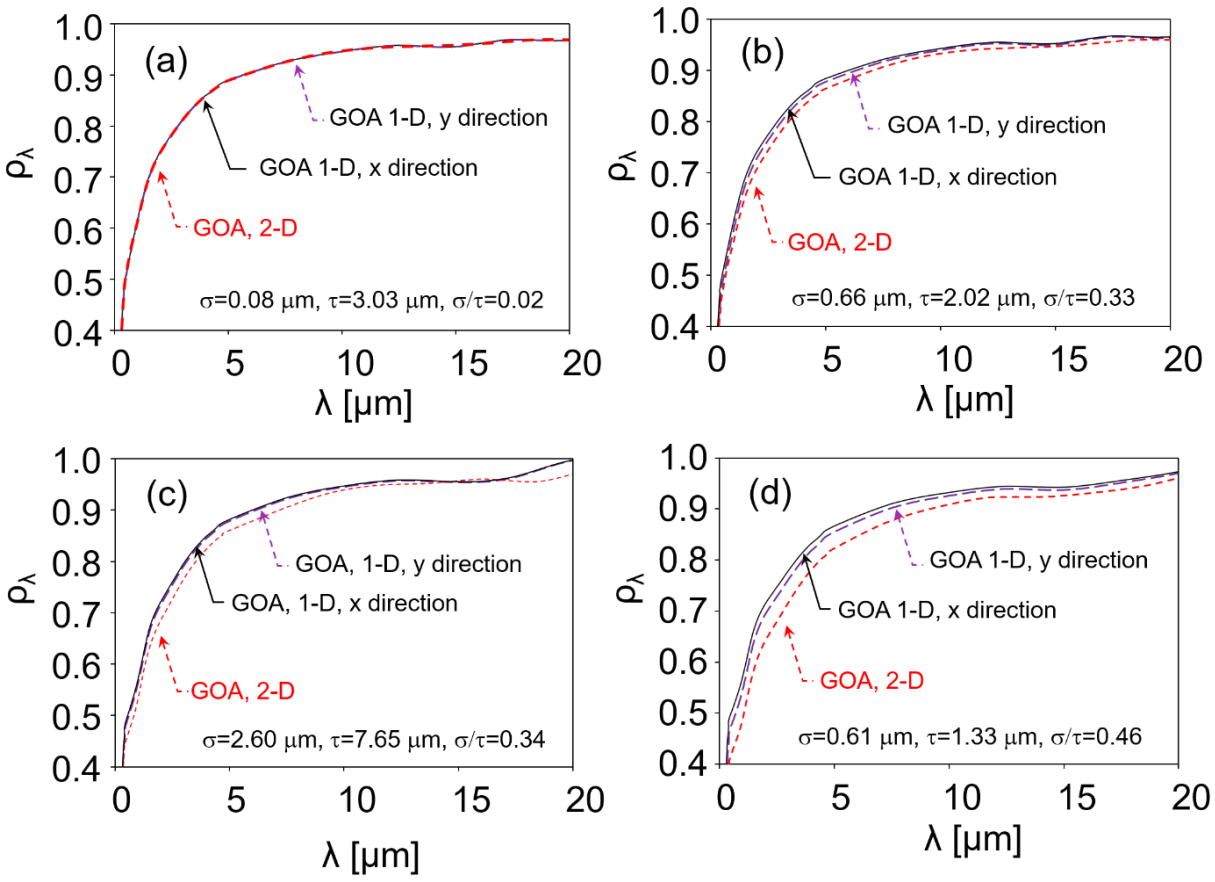

Figure 5-6. Directional-hemispherical reflectance predictions with GOA for (a) sample #1, (b) sample #4, (c) sample #7 and (d) sample #8. The solid and dash lines in each plot represent the prediction results using 1-D and 2-D GOA methods, respectively.

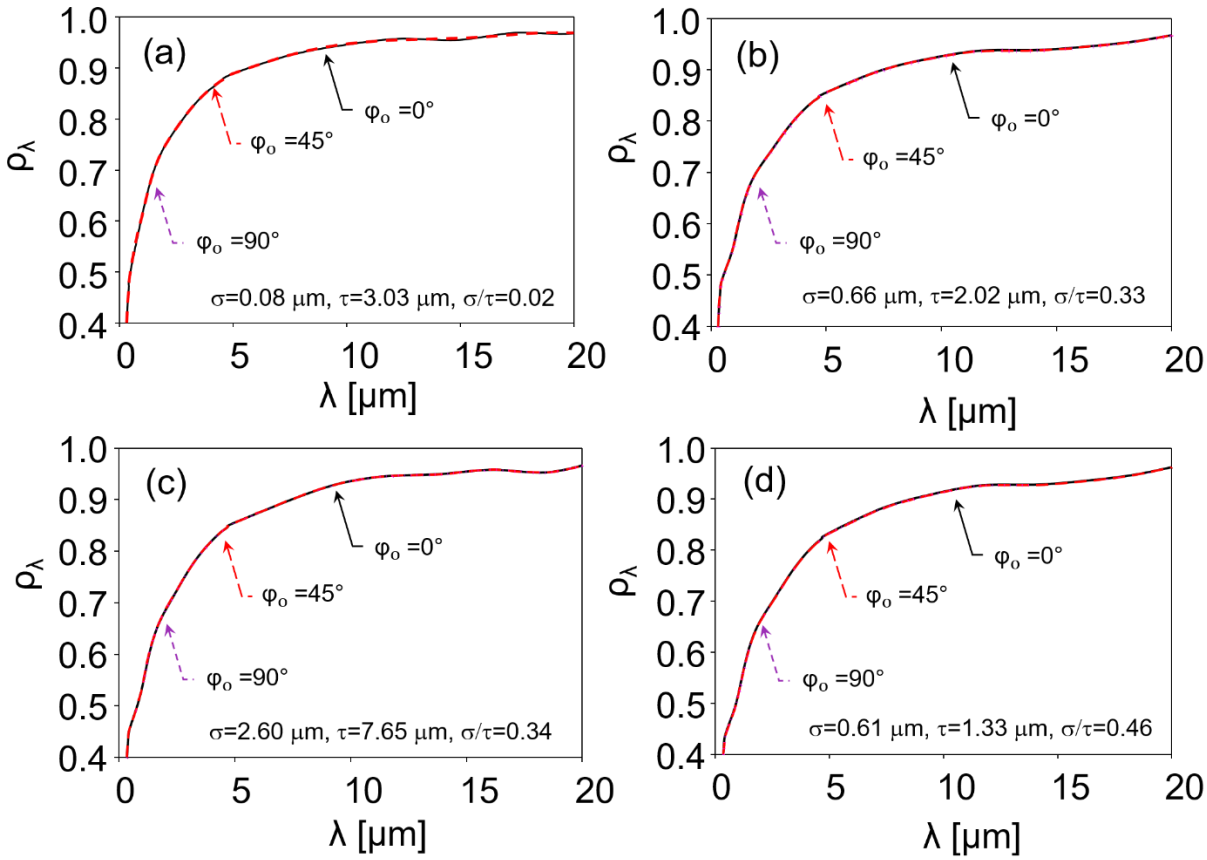

Figure 5-7. Effect of incident azimuthal angles on 2-D GOA predictions for (a) sample #1, (b) sample #4, (c) sample #7 and (d) sample #8. The black, red and purple lines in each plot represent the directional-hemispherical reflectance predictions using 2-D GOA with an incident azimuthal angle of 0°, 45°, 90°, respectively.

5.3.4 Reflectance measurements and predictions using GOA and diffraction models

Figure 5-8 (a)-(f) shows the measured directional-hemispherical reflectances and GOA predictions for all tested samples (#1, #4, #5, #6, #7, #8). The purple line in each plot denotes the reflectance of iron calculated using Fresnel's equation. The specular and diffuse reflectance measurements are also compared with predictions found using Eq. (2.60), with an instrument acceptance angle $\Delta\theta =$ 5°, which is consistent with the apparatus used to measure the specular component. To replicate the conditions of the FTIR measurements, the incident polar angle, θ_o, is set equal to 10° and 30°

for specular and diffuse predictions, respectively. For GOA specular reflectance predictions, the acceptance polar and azimuthal angles in the specular direction are taken as $\Delta\theta_s=\pm3°$, $\Delta\varphi_s=\pm3°$ ($\theta_s=\theta_o$, $\varphi_s=\varphi_o+\pi$). For the polished surface shown in Figure 5-8 (a), the directional-hemispherical reflectances are in line with the reflectance of iron due to its smoothness ($\sigma/\tau = 0.02$), as indicated previously in Figure 5-5. The deviation between the predictions and measurements beyond 2.5 μm can be attributed to differences in the refractive indices between pure iron and the AHSS alloys. According to Tang et al. [169], the valid domain spectrum ($\sigma\cos\theta/\lambda > 0.2$, $\sigma/\tau < 2$) for a polished surface is below 0.4 μm. However, the predicted directional-hemispherical reflectances at wavelengths greater than 0.4 μm using GOA still match the measurements. This is attributed to the fact that scattering events are governed by first-order scattering as a result of the small surface slope, leading to the conserved scattered energy in all directions from that of the polished surface. This finding is consistent with the data in Table 2.

As the surface slope increases, more higher-order scattering occurs. Given the fact that the polished surface lies in the specular approximation domain ($\sigma\cos\theta/\lambda < 0.2$, $\sigma/\tau < 0.06$) for wavelengths greater than 0.4 μm, the GOA specular reflectance predictions in this region are consistent with the measurements. Similarly, the diffuse reflectance predictions using GOA are close to the measured values. Note that the specular and diffuse reflectance measurements were carried out at different incident angles. As a result, one would not expect the sum of these two quantities to match the measured directional-hemispherical reflectance.

For the as-received surface (Sample #4) shown in Figure 5-8 (b), the GOA predicted directional-hemispherical reflectances approach the measured values for the domain of validity ($\lambda<3.3$ μm), although the small deviation observed for wavelengths longer than 2.5 μm is likely due to the difference between the refractive indices of iron and the AHSS alloys. Generally, the

GOA predictions are still close to the measurements even when the wavelengths are longer than the GOA regime. This phenomenon can be attributed to the fact that at long wavelengths, the scattered energy of EM waves in all directions is still close to that of the polished surface due to the dominance of first-order scattering. In addition, the GOA predictions using the AFM-derived surface profile are close to that of the optical profilometer, demonstrating the robustness of measured surface parameters employed in the GOA model. It is also shown that the measured specular reflectance of this surface is lower than that of the polished surface, due to larger RMS roughness, σ. However, the GOA predictions in the specular direction for the long wavelength regime are inconsistent with the measured specular reflectances, which is not surprising since the surface parameters, σ, τ, and optical roughness, σ/λ, are out of the specular approximation domain. For reflectances in the specular and diffuse directions, predictions using Eq. (2.60) are close to the measurements, specifically when the wavelength becomes longer. With increasing wavelength, the diffraction effect accounted for in Eq. (2.60) becomes increasingly important, but since this effect is excluded from the GOA framework [170, 186] the predictions become progressively inaccurate at longer wavelengths.

The comparisons of the predicted and measured reflectance of the roughened surface (sample #5) are shown in Figure 5-8 (c). This surface has a lower directional-hemispherical reflectance than the others, because higher-order reflections and energy absorptions are achieved as expected from the larger slope parameter, σ/τ. The measured specular reflectances are also lower, due to larger RMS roughness, σ. The directional-hemispherical reflectance predictions obtained using the GOA framework are consistent with the measured data when the wavelengths and surface parameters lie within the valid domain for the GOA ($\sigma\cos\theta/\lambda>0.2$, $\sigma/\tau<2$), but not at longer wavelengths. Also, the GOA reflectance predictions in the specular direction do not match

the measured data when the wavelength increases, again because the surface parameters are outside of the specular approximation domain. From a physical perspective, the wavelengths of the incident rays at this regime are large relative to the surface cavities, and thus the diffraction effect dominates scattering, which is not accounted for in the GOA technique. Scattering at this regime is governed by both diffraction and multiple reflections [63], which can not be captured by either GOA or diffraction models alone. The specular and diffuse reflectances at long wavelengths are accurately modeled by Eq. (2.60).

Similar trends can be observed from samples #4, #5, #6 in Figure 5-8 (b)-(d), where the measured directional-hemispherical reflectances are related to the surface slope parameter, σ/τ, and the GOA predictions of directional-hemispherical reflectances are consistent with the measurements within their respective GOA validity domain. These results also demonstrate that the directional-hemispherical reflectances are governed by the overall surface slope when the incident wavelength and surface parameters lie within the GOA domain. The measured specular reflectances are lowest in sample #5, since it has the largest RMS roughness. The GOA specular reflectance predictions for sample #4, sample #5, sample #7 and sample #8 are inconsistent with the measurements due to the fact that the surface parameters are out of the specular approximation domain at the long wavelength regime, even if they are partly inside the GOA domain as shown in Figure 5-8 (e). Note that the GOA domain is developed based on the averaged energy balance over all scattering directions, rather than a specific direction (specular). This might explain why the GOA predictions in the specular direction do not match the measurements even if the parameters are inside the GOA domain. Similarly, as the wavelength increases, the predictions of specular and diffuse reflectances using Eq. (2.60) approach the measured data, since the diffraction effect dominates multiple scattering as the optical roughness decreases.

The predictions using the regression model developed in Ref. [33] are also included in Figure 5-8 (b)-(f). The regression model agrees with the measurements and GOA predictions for samples having small surface slopes ($\sigma/\tau<0.4$), sample #4, sample #6, sample #7, but not for samples having large surface slopes ($\sigma/\tau>0.4$), sample #5, sample #8. This can be attributed to the fact that the regression model in Ref. [33] was developed for silicon and aluminum surfaces with the assumption of constant local reflectance over the surface, which may not be a reasonable assumption for AHSS samples with larger surface slopes, based on Fresnel's equation.

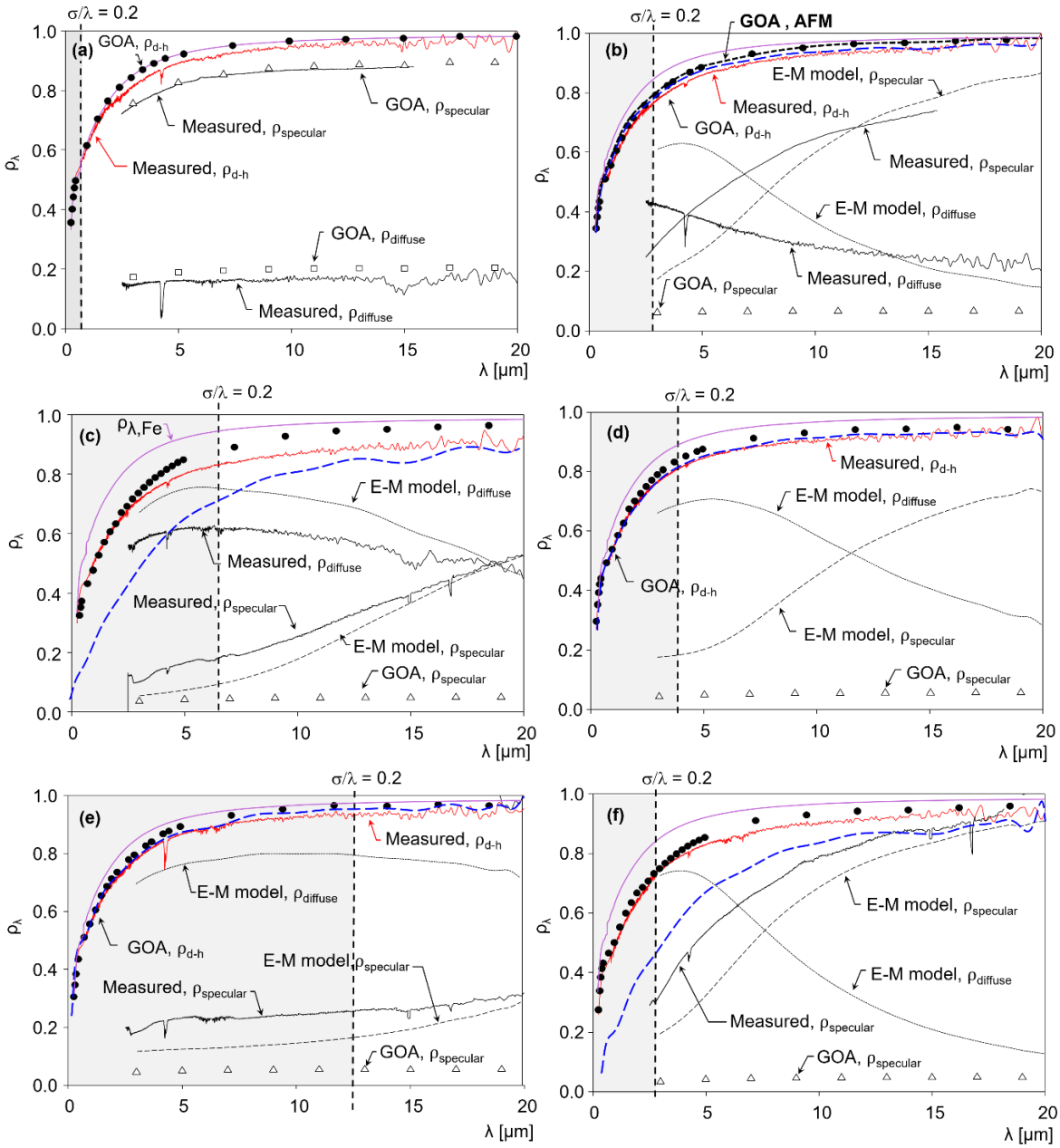

Figure 5-8. Comparison of measured and estimated reflectance for (a) sample #1, (b) sample #4, (c) sample #5, (d) sample #6, (e) sample #7 and (f) sample #8. The solid red lines represent the measured directional-hemispherical reflectance at near normal incidence. The blue dashed line represents predictions using the regression model described in Ref. [33]. The solid purple lines represent the reflectance of iron. The black long dash lines denote the boundary of the GOA validity regime defined in Ref. [169], and the gray-shaded areas represent the GOA regime. The directional-hemispherical and specular reflectance predictions using GOA are shown as circle and triangles symbols, respectively.

5.3.5 Comparison of 1-D and 2-D bi-directional functions

Figure 5-9 and Figure 5-10 illustrate the two-dimensional (contour maps) and one-dimensional variations of BRDF, respectively, with λ=5 μm, θ_o=30°, φ_o=45°. Figure 5-9 shows that the BRDF is symmetric with respect to the scattered polar and azimuthal directions, and peak values are observed around the specular angles (θ_s=30°, φ_s=225°). Higher and wider BRDF values are found in the specular region for the polished surface, in line with the measurement and predictions shown in Figure 5-8. Consequently, Figure 5-10 shows that, when the scattered polar angle is fixed at θ_s=30°, the BRDF distribution with respect to azimuthal direction exhibits coherent peaks in the specular region. The polished sample has the highest BRDF values in the specular direction while the other samples demonstrate nearly identical BRDF distributions, which are typical for the GOA prediction trends for specular reflectances shown in Figure 5-8 (b)-(f).

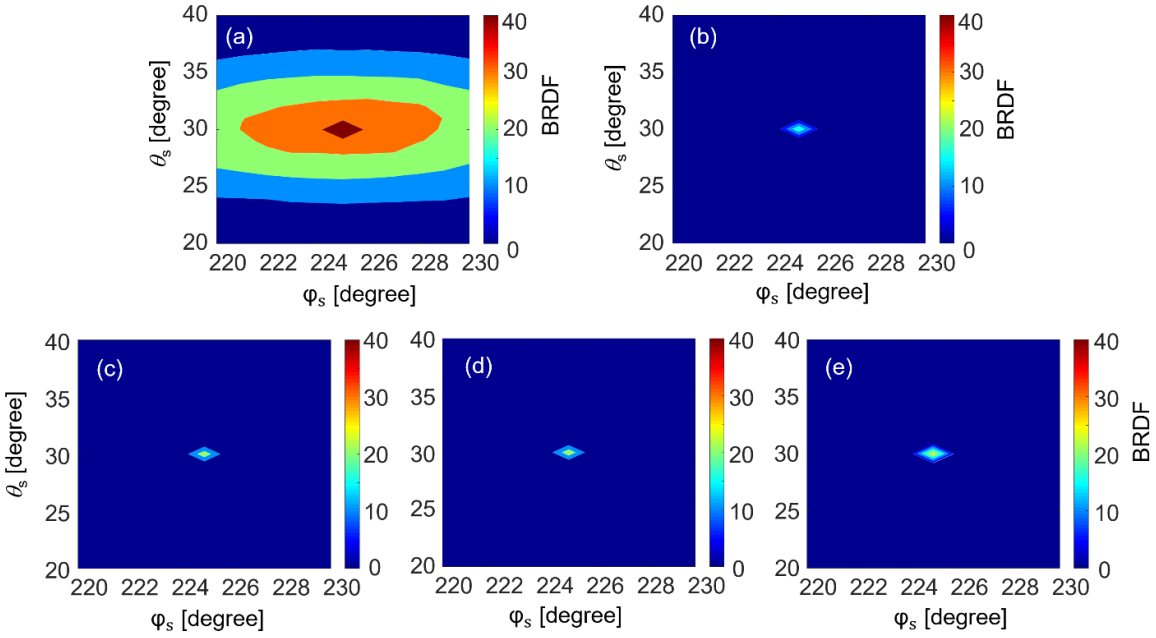

Figure 5-9. Contour maps of BRDF with respect to the scattered polar angle, θ_s, and azimuthal angle, φ_s, for (a) sample #1, (b) sample #4, (c) sample #5, (d) sample #7, (e) sample #8. The BRDF is obtained via Eq. (2.53) with incident polar and azimuthal angles fixed at θ_o=10°, φ_o=45°.

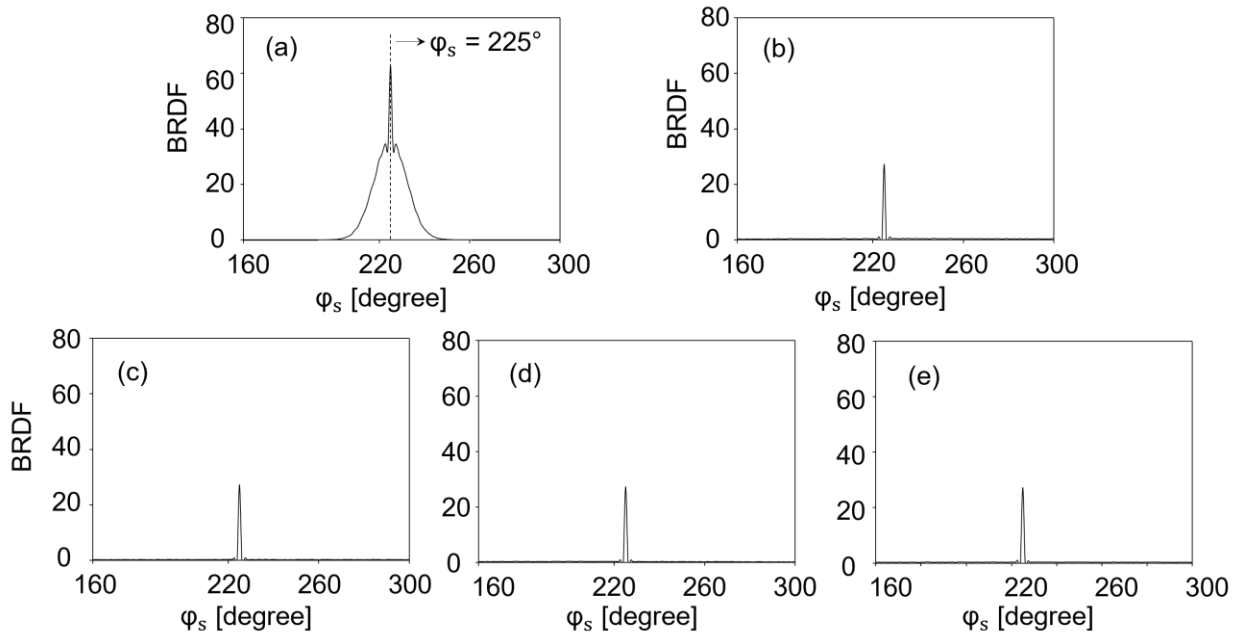

Figure 5-10. BRDF results with respect to the scattered azimuthal directions for (a) sample #1, (b) sample #4, (c) sample #5, (d) sample #7, (e) sample #8. The incident polar and azimuthal angles are fixed at θ_o=10°, φ_o=45°. In these plots the scattered polar angle is fixed at θ_s=30°. All samples exhibit coherent peaks of BRDF in the proximity of specular directions (φ_s=225°).

5.4 Conclusions

This chapter explores the relationship between surface topography and the radiative properties of dual-phase advanced high strength steel alloys in the context of the 2-D geometric optics approximation and EM wave diffraction theory. The surface profiles of tested samples have been examined under the criterion of the Kirchhoff approximation. Predictions of the directional-hemispherical reflectance using GOA with profilometry-derived surface profiles match the measured data over the wavelengths important to pyrometry, as long as the surface parameters and wavelengths

are within the valid domain for GOA. Predictions using the regression model developed in Ref. [33] also agree with measurements for samples having a small surface slope.

The GOA model can also accurately predict the specular and diffuse reflectance components for the polished surfaces over all wavelengths. In contrast, the rough samples are out of the GOA validity domain at longer wavelengths, and thus the predictions of specular and diffuse reflectances do not match the measurements. For rough samples, reflectance predictions made using Kirchhoff diffraction models approach the measurements at longer wavelengths as the diffraction effects dominate the wave-surface interaction. Diffuse and specular reflectances for the rough surfaces can also be estimated using the EM diffraction model at longer wavelengths, while the GOA model can predict the directional-hemispherical reflectance, where the values are subject to the surface slope.

These findings will be used to develop spectral emissivity models used in industrial pyrometers that account for the surface state variations of AHSS samples during industrial annealing, and may also elucidate the connection between changes in spectral emissivity and variations in the surface topography of the steel strip caused by various rolling and finishing operations. This information will improve precise thermal control of steel strip during processing, which is particularly important for emerging high strength steel alloys, thereby improving the efficiency of the steel-making process. Furthermore, since this chapter has been focused on the radiative properties of un-oxidized samples, it is expected that the following research will be performed on the AHSS samples having oxidized surface states.

Chapter 6 Effect of Annealing Atmosphere and Steel Alloy Composition on Oxide Formation and Radiative Properties of Advanced High Strength Steel Strip[7]

6.1 Introduction

Chapter 4 and Chapter 5 focus on unannealed AHSS samples. The radiative properties, however, will change significantly when there is an oxide film deposited on the substrate surface as discussed in Section 3.2. In addition, the effect of substrate surface roughness, alloy composition, and annealing atmosphere on the selective oxidation and radiative properties of AHSS needs to be clarified. As mentioned in Chapter 2 (Section 2.1), the alloy composition and annealing atmosphere would dominate the selective oxidation formed during annealing. In this chapter, we experimentally illustrate how these effects are linked to the oxide species, morphology, thickness and radiative properties of AHSS having polished and rough substate states, with more focus on the polished states. The correlation between the selective oxidation having different refractive indices and thickness, and the directional-hemispherical reflectance of the oxidized AHSS samples, is interpreted using the thin film interference theory discussed in Section 3.2.

As discussed in Chapter 2, the type, location and extent of oxidation depend on the chemical composition of the steel, the thermal processing history, and the annealing process atmosphere parameters. A variety of oxide morphologies, distributions, thicknesses, and chemistry have been reported across the family of AHSS alloys and process atmospheres in the literature.

[7] The content of this chapter is an extended version of a paper submitted to *Metall. Mater. Trans. B*:
K. Lin, M. Pourmajidian, F. K. Suleiman, J. R. McDermid, K. J. Daun, *Effect of annealing atmosphere and steel alloy composition on oxide formation and radiative properties of advanced high strength steel strip*. (2021)

For example, in a study conducted on a Si/Mn = 0.34 transformation-induced plasticity (TRIP)-aided steel, thin film external oxides were observed to form at low dew points, while at high dew points oxide nodules emerged on the steel surface [13]. Khondker et al. [7] studied how the oxidation potential of the annealing atmosphere influenced the selective oxidation of dual-phase steel alloyed with 2 wt.% Mn and 0.3 wt.% Mo. It was reported that Mn segregated to the surface and formed surface oxides under all experimental annealing atmospheres. The oxidation mode transitioned from external to internal with an increase in the oxidation potential of the atmosphere, i.e. as p_{H2O}/p_{H2} increased from 8.44×10^{-3} to 3.451×10^{-2} (i.e. p_{O2} from 4.39×10^{-23} to 8.07×10^{-22} atm.) Bellhouse and McDermid [19] found that Mn, Si and Al formed external oxides when a 1.5 wt.% Al TRIP steel was annealed at 862°C in N_2-H_2 atmospheres with p_{O2} ranging between 5.08×10^{-25} to 2.80×10^{-19} atm. Using XPS and Auger electron microscopy, surface segregation of Si and Al was shown to be most significant under the lowest dew point of −53°C. Pourmajidian et al. [25] investigated the effect of oxygen partial pressure on the selective oxidation and oxide morphology of a 6 wt.% Mn, 2 wt.% Si third generation advanced high strength steels (3G-AHSS) and discovered considerable enrichment of Mn and Si in the form of oxides at the steel surface. They found that nodule-like external oxides formed after annealing at 690°C under high dew point (+5°C) as opposed to continuous film-like external oxides when annealing at lower dew points (−50°C, −30°C).

A number of studies have investigated how these different oxide states may influence radiative properties. Ham et al. [12] experimentally studied the effect of annealing atmosphere on selective oxidation and radiative properties of TRIP steel. The dew point strongly influenced oxide formation and measured spectral emissivity, and the effect of local surface texture induced by the oxide morphology on spectral emissivity was illustrated. More recently, Suleiman et al. [187]

presented an empirical approach for modelling the spectral emissivity of dual-phase steels through factorial design-of-experiments. In their study, the variation of the measured spectral emissivity with alloy composition (Si/Mn=0.04, Si/Mn=0.10, Si/Mn=0.23), pre-annealed surface state, and annealing dew point (-30°C, +10°C) was analyzed using full factorial designs. They found that alloy composition and pre-annealed surface state dominates the spectral emissivity at shorter (1.1-2.5 μm) and longer (2.5-5.0 μm) wavelengths, while annealing atmosphere has minor effect on measured spectral emissivity over the entire spectra.

In some scenarios, the presence of a thin oxide film on a smooth metal surface has been shown to influence the spectral emissivity in a coherent way, as shown in Figure 6-1 (a), because the reflections from the top and bottom interface of the oxide film induce a phase shift in the scattered electromagnetic (EM) wave, leading to constructive and destructive interference [47, 188]. The extent of this effect depends on the film thickness relative to the EM wavelength, and may be significant when these two quantities are similar [33]. In contrast, EM waves become more sensitive to surface irregularities (e.g. oxide nodules, surface roughness) when the wavelength becomes much larger than the oxide film thickness [166]. In this scenario, shown in Figure 6-1 (b), the wave is scattered in a random way that can be predicted using geometric optics [189]. At longer wavelengths and shallow grazing angles, the wave/roughness interaction becomes dominated by diffraction effects.

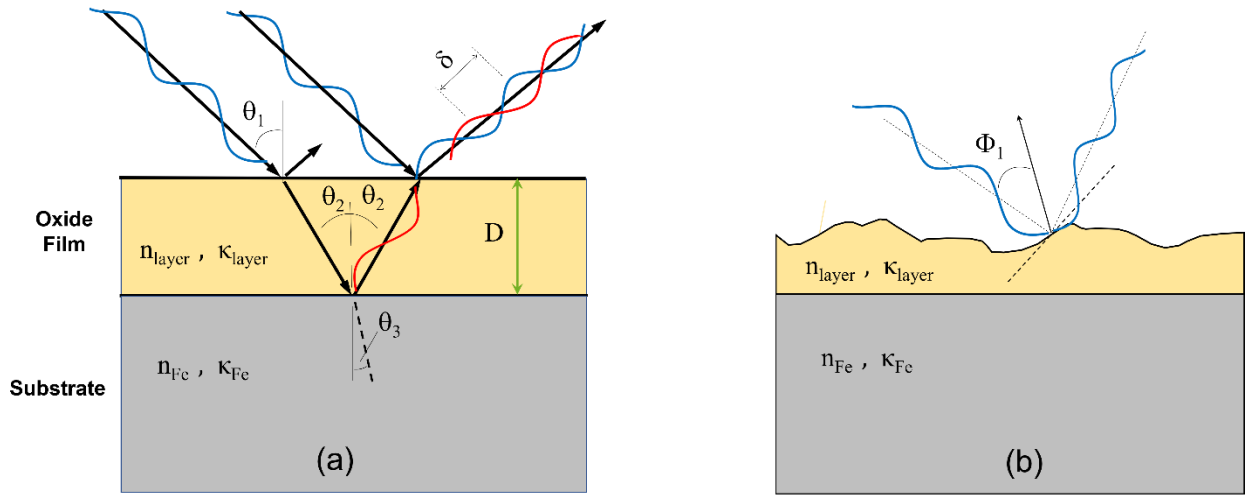

Figure 6-1. Schematic view of the thin film interference model where an oxide layer is formed on the metal surface; (b) surface topography (e.g. roughness) effect on EM wave scattering.

Within the thin film interference regime, many studies have shown that the spectral emissivity is sensitive to both annealing temperature and time as the oxide film grows. Brannon and Goldstein [190] experimentally investigated how total normal emissivity varies as a function of oxide thickness on a copper and aluminum substrate. Theoretical estimations of total normal emissivity based on interference wave optics were performed and compared to experimental results. While the theoretical estimations were lower than the measured values, they predicted the correct trend with respect to oxide layer thickness. Neuer and Guntert [56] showed that the spectral emissivity (λ = 0.71 μm) of an oxidized titanium surface oscillated as the oxide film grew until it plateaued once the film thickness exceeded 0.8 μm. Kobayashi et al. [55] investigated how the normal spectral emissivity of cold-rolled steel samples varies with wavelength and time during annealing in vacuum and oxidizing environments. They found that the spectral emissivity oscillates with respect to wavelength at shorter wavelengths, and the peaks and the valleys in the

oscillations caused by oxide film interference shifted to the longer wavelengths as the oxide became thicker.

Iuchi et al. [47] used a thin film interference model to investigate the spectral emissivity of oxidized cold-rolled steels. Both predicted and measured results showed that the peaks and valleys in spectral emissivity shift to longer wavelengths with annealing time and increasing oxide film thickness. Likewise, when measuring the spectral emissivity of iron heated in air, Del Campo et al. [188] found that the peaks and valleys shift to longer wavelengths with increasing annealing time. They later developed a quantitative model for the spectral emissivity that accounts for oxide film thickness, incident wavelength, and optical constants of the film [191]. King et al. [192] made similar observations on reactor pressure vessel alloys heated in air.

This chapter aims to elucidate the connection between the oxide formation, as determined by the alloy composition, annealing atmosphere oxygen potential, and the radiative properties of three dual phase (DP) steel alloys identical to those in Chapter 5, which is an important class of AHSS. Predictions are made through the thin film interference model, which incorporates the measured refractive indices and film thickness of the oxides formed on steel substrate. Samples are obtained from three cold-rolled DP alloys, each having a different Si/Mn mass ratio (DP980-Si/Mn = 0.04, DP780-Si/Mn = 0.10, DP980-Si/Mn = 0.23). A subset of these samples are polished, and all the samples are annealed in a 95%/5% (vol.) N_2/H_2 atmosphere at dew points of −30°C or +10°C using a galvanizing simulator. Surface profiles are characterized by optical profilometry, as well as optical and scanning electron microscopy. Ex-situ directional-hemispherical reflectance measurements are carried out using a UV-Vis-NIR spectrophotometer (0.25-2.50 μm) and a Fourier transform infrared (FTIR) infrared spectrometer (2-20 μm), both equipped with integrating spheres. Near-normal specular reflectance measurements are also carried out using the FTIR

spectrometer. Refractive indices and oxide film thicknesses are inferred through ellipsometry, while the oxide layer thickness is confirmed using a combination of focused ion beam (FIB) milling and scanning electron microscopy (SEM). These measurements are interpreted in the context of the thin film interference theory. Based on the studies presented in Section 2.1, surface oxides of the samples investigated in this chapter (Si/Mn=0.04, Si/Mn=0.10, Si/Mn=0.23) are likely to consist of Mn-rich oxide or Si-Mn ternary oxides depending on the annealing dew point and alloy Si/Mn ratio. For the alloy having the lowest Si/Mn ratio (Si/Mn=0.04), the oxide layer is likely to consist of MnO under both annealing dew points (−30°C, +10°C). Ternary oxides including $MnSiO_3$ and Mn_2SiO_4 may form alongside MnO on the other two alloys (Si/Mn=0.10, Si/Mn=0.23). This is because for low Si/Mn alloy, large amount of Mn tends to segregate onto to the surface and form Mn-rich oxides during annealing, while ternary oxides would appear on the surface for high Si/Mn alloy as more Si is available to segregate from the bulk onto the surface during annealing. The oxide composition of each sample is examined by using the X-ray photoemission spectroscopy (XPS).

It is found that alloy composition, annealing atmosphere oxygen potential, and pre-annealed surface state strongly influence oxide formation and, therefore, the spectral emissivity of the specimens. Samples annealed in a polished state exhibited a stronger interference effect compared to those annealed in their as-received, cold-rolled condition. Reflectance predictions using the thin film interference model are in line with the measurements over visible and near infrared wavelengths for most of the polished pre-annealed samples. These findings provide a potential means to estimate oxide formation *in-situ* through optical measurements during annealing, and can also be used to improve the pyrometry measurements carried out during the manufacturing process.

6.2 Sample preparation and measurement

The chemical compositions of the two cold-rolled DP980 alloys (alloys A1 and A2) and one cold-rolled DP780 alloy (alloy A3) used in this chapter are listed in Chapter 5 (Table 5-1). All alloys have elemental compositions consistent with ASTM standard (ASTM, A1079 - 17) [182]. Experimental conditions of the twelve samples analyzed in this study are shown in Table 6-1. 120 mm × 200 mm panels were cut from coils of cold-rolled DP980 and DP780. In order to investigate the influence of the pre-annealed surface state on oxide formation and radiative properties, half of the samples were annealed in their as-received state, while the other half were polished using a series of SiC polishing papers with progressively finer grit and particle size (240grit, 320grit, 400 grit, 600 grit), resulting in a mirror finish with identical roughness levels (σ=0.09 μm) obtained using an optical profilometer (WYKO NT1100). The samples were then annealed in a galvanizing simulator (Iwatani-Surtec) using a 95%/5% N_2/H_2 atmosphere and dew points of either +10°C or −30°C, corresponding to oxygen partial pressures of 2.56×10^{-20} atm (pH_2O/pH_2: 0.2408) and 4.39×10^{-23} atm (pH_2O/pH_2: 0.00998), respectively. The samples were heated according to the heating schedule illustrated in Figure 6-2. The surfaces of the processed samples were imaged using an optical microscope (×50). All samples were cleaned and rinsed with ethanol and acetone prior to microscopy analysis. FIB milling in combination with SEM analysis was carried out using an NVision 40 FIB-SEM microscope (Zeiss) to image the steel cross-sections using secondary electron imaging (SEI).

The surface oxide thickness of all samples were measured using ImageJ 1.48v software and the results are listed in Table 6-1, Two trenches, each having a length of 10 μm, were cut on distanced areas of all samples, and high-magnification electron images were captured along the

length of the cuts where a tilt correction of 36° was applied to the cross-sectional images in order to compensate for the 54° stage tilt required for the milling procedure. Finally, thicknesses were inferred using vertical lines at each point with approximately 100 nm intervals via ImageJ 1.48v software. For each sample, a minimum of 100 thicknesses were measured using a defined sampling grid to ensure random sampling of the oxide thickness. The FIB-measured thickness mean value and uncertainty associated with the margin of error at 95% confidence interval of the mean are shown in Table 6-1. These errors, however, would more or less affect the prediction even if they are generally small. Figure 6-3 (a)-(d) presented some of the critical images regarding to this process. It is found that both the mean thickness of oxide, μ_h, and the standard deviation of oxide thickness, σ_h, of samples annealed under the +10°C dew point are larger than those annealed under the -30°C dew point process atmosphere. Further details of this procedure can be found in Ref. [27].

X-ray photoemission spectroscopy was performed using a PHI Quantera II scanning XPS microprobe to obtain the surface oxide speciation of selected samples. The X-ray beam diameter was 100 μm and the take-off angle was set at 45°. High resolution spectra of the Mn2p and Mn3s peaks were collected with a pass energy and step size of 26 eV and 0.1 eV, respectively, and 112 eV and 0.2 eV for the Si2p. All data processing was performed using MultiPak software and the binding energies of the aforementioned peaks were used to speciate the surface oxides, shown in Table 6-1. The near-normal directional-hemispherical spectral reflectance of each sample was measured using a Varian Cary 5000 UV-Vis-NIR spectrophotometer (0.25-2.5 μm) and a Bruker Invenio-R spectrometer (2.5-20 μm) mentioned in Chapter 4. Refractive indices and thickness of the oxide films formed on the substrate were measured using a J. A. Woollam M-2000 ellipsometer (400-750 nm). It can be seen that the oxide film thicknesses measured by the ellipsometer and FIB

are close. For the polished samples in this study, the reflectance predictions through the thin film interference model (Eqs. (2.9)-(2.13)) are made using the ellipsometer-measured thickness.

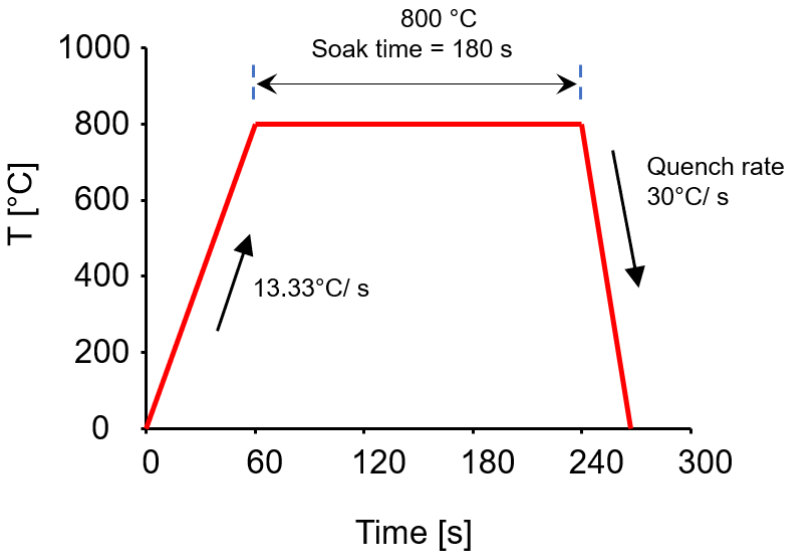

Figure 6-2. Annealing schedule for the tested samples. The samples were heated to 800°C and soaked for 180 s before quenching.

Table 6-1. Tested samples with different alloy compositions, annealing atmospheres, measured pre-annealed and post-annealed roughness, and measured oxide thickness and oxide species. The uncertainty in μ_h represents the margin of error at 95% confidence interval of the mean.

Sample No.	**DP**	**Si/Mn**	**Pre-annealed Surface State**	σ_{pre} [μm]	σ_{post} [μm]	σ/τ (post)	**Oxide thickness [nm]**		**Primary oxide (XPS)**
							Ellip.	**FIB**	
1 (A3)	−30°C	0.10	Polished	0.09	0.26	0.04	58.5	53.4±2.88	Mn_2SiO_4, Cr_2O_3, MnO
2 (A3)	−30°C	0.10	As-received	2.60	2.73	-	-	62.5±3.84	-
3 (A2)	−30°C	0.04	Polished	0.09	0.17	0.03	70.7	67.4±3.27	MnO, Cr_2O_3, $MnSiO_3$
4 (A2)	−30°C	0.04	As-received	0.65	0.71	-	-	91.2±5.08	-
5 (A1)	−30°C	0.23	Polished	0.09	0.28	0.04	74.1	70.5±5.85*	Mn_2SiO_4, Cr_2O_3, MnO
6 (A1)	−30°C	0.23	As-received	0.59	0.67	-	-	63.8±6.06*	-
7 (A3)	+10°C	0.10	Polished	0.09	0.21	0.04	112.8	101.7±7.05	MnO, Mn_2SiO_4
8 (A3)	+10°C	0.10	As-received	2.60	3.10	-	-	84.7±8.99	-
9 (A2)	+10°C	0.04	Polished	0.09	0.27	0.05	110.6	114.5±7.88	MnO, $MnSiO_3$
10 (A2)	+10°C	0.04	As-received	0.65	0.70	-	-	103.8±6.29	-
11 (A1)	+10°C	0.23	Polished	0.09	0.25	0.04	68.0	65.3±6.64*	Mn_2SiO_4, MnO
12 (A1)	+10°C	0.23	As-received	0.59	0.72	-	-	94.4±12.06*	-

*These measured thickness values contain significant nodule-like oxides as opposed to film-like oxides at the external surface region.

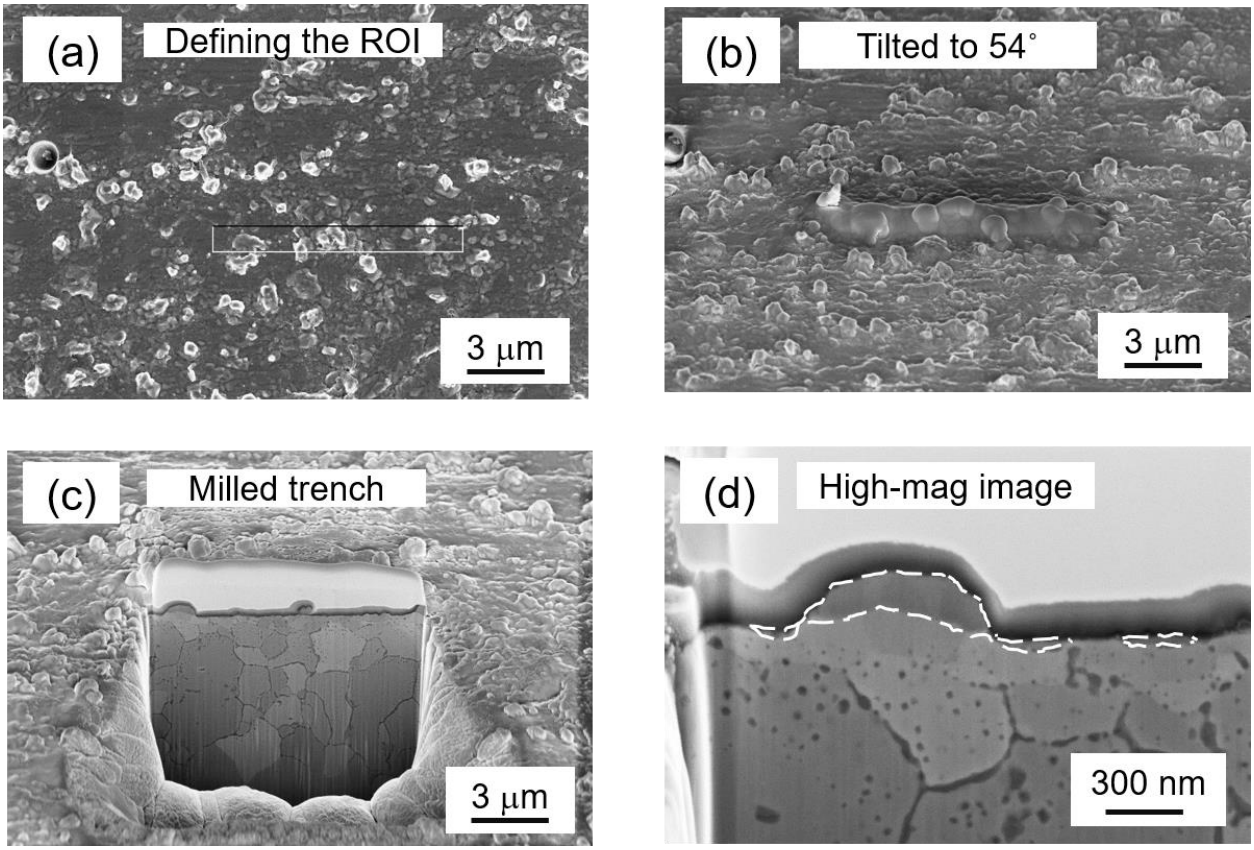

Figure 6-3. Images showing the process of Focused Ion Beam (FIB) technique (a) defining the region of interest (ROI) (b) tilted to 54˚ (c) trench milling (d) magnification of image for measurement. The dashed white lines denote the oxide.

6.3 Refractive indices of Fe and MnO

The refractive indices of MnO is derived from Ref. [193]. Figure 6-4 shows the literature-derived refractive indices of ferrite and MnO. In the present study, the refractive indices of other ternary oxides that are likely to form on the substrate, as discussed in Chapter 2, Section 2.1, are obtained through the ellipsometry measurements, since they are unavailable from the literature. Figure 6-5 shows that the measured spectral reflectance for all three alloys with polished surfaces closely matches predictions made using Fresnel's equation with refractive indices of iron shown in Figure 6-4. Consequently, it is reasonable to model substrate alloys as ferrite.

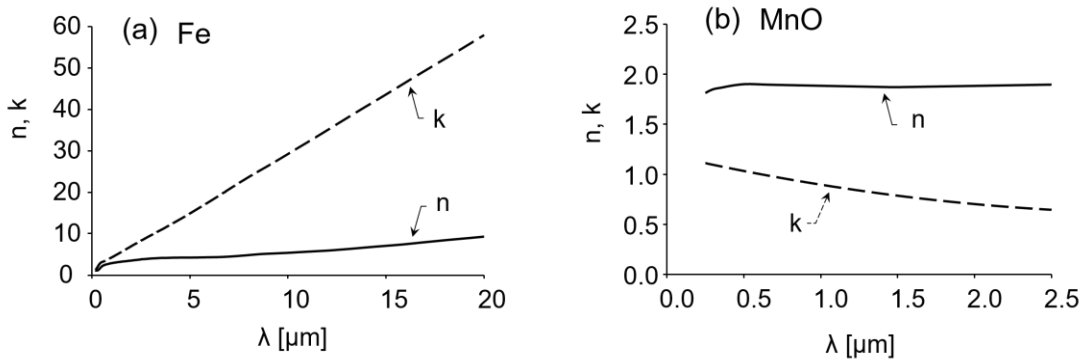

Figure 6-4. Refractive indices of (a) ferrite [194] and (b) MnO [193].

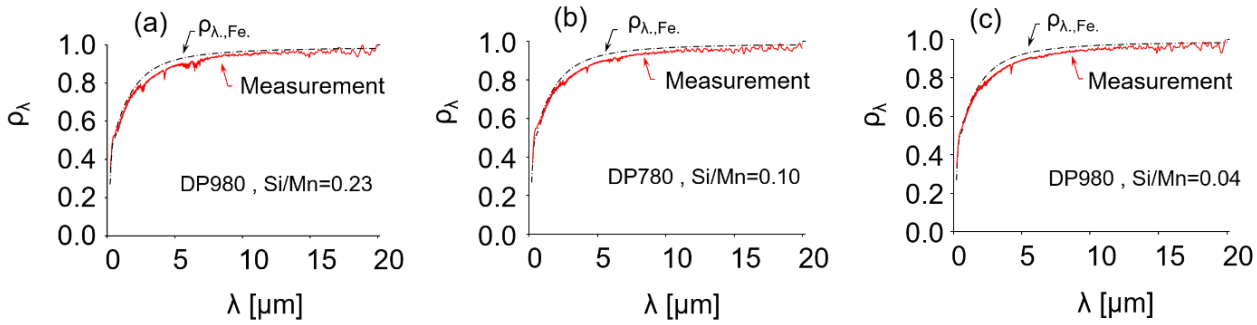

Figure 6-5. Comparison of measured reflectances of polished surfaces for different alloys: (a) DP980, Si/Mn=0.23; (b) DP780, Si/Mn=0.10; and (c) DP980, Si/Mn=0.04. The surfaces of the samples were polished to the same roughness scale (σ=0.09 μm) before the measurements. The dashed lines denote the reflectance of ferrite derived using Fresnel's equation with refractive indices from Ref. [194].

6.4 Results and discussion

6.4.1 Microscopy and optical profilograms

The surface roughness and surface slope of the polished samples are both smaller compared to those of the as-received samples, as shown in Table 6-1. The oxide thicknesses measured using

ellipsometry are consistent with those obtained *via* the FIB-SEM methodology. The alloy composition, process atmosphere, and pre-annealed surface topography significantly influence the oxide thickness formed during annealing. For samples annealed at dp =−30°C, thicker oxides are obtained on as-received samples, while for samples annealed at dp =+10°C, thicker oxides are found on polished samples except for the case of the high Si/Mn ratio alloy (Si/Mn =0.23).

Surface microstructure and topographical images of the samples are shown in Figure 6-6. The as-received surfaces are rougher and exhibit rolling artifacts. For the polished surfaces having the lowest Si/Mn ratio (Si/Mn=0.04), the one annealed at the higher dew point (sample #9) is rougher than the one annealed at the lower dew point (sample #3), while the opposite trend holds for alloys having a higher Si/Mn ratio.

The colors of samples having different alloy compositions (Si/Mn ratio) and pre-annealed surface topography are distinct from each other, while samples having identical Si/Mn ratio and pre-annealed surface condition have a similar color. This implies that alloy composition and surface topography have a stronger effect on radiative properties of AHSS in the visible spectra compared to that of the annealing atmosphere, which is consistent to what has been found in Ref. [187].

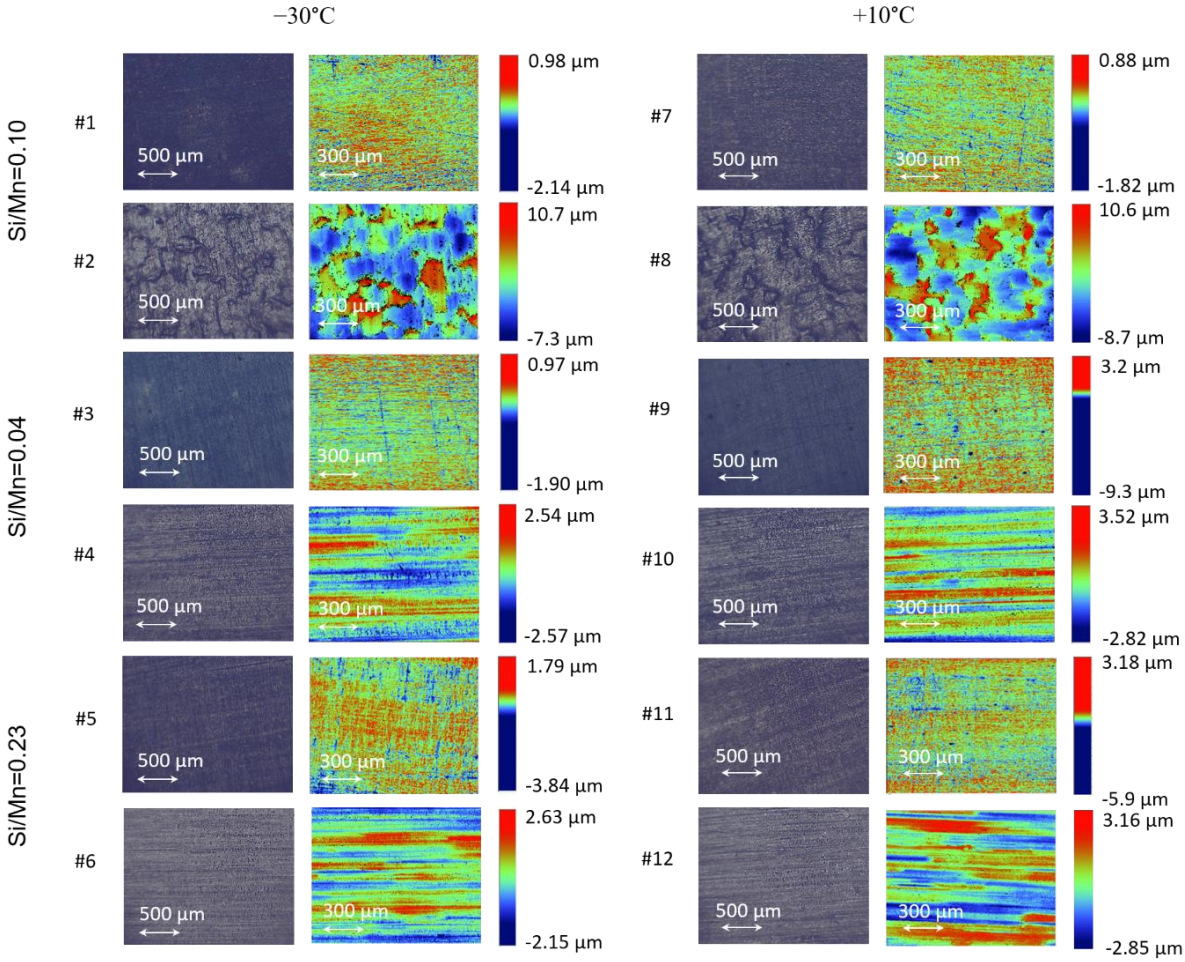

Figure 6-6. Optical microscopy and optical profilograms of the samples. Samples annealed in a polished state (sample #1, #3, #5, #7, #9, #11) have similar appearance, while artifacts from the cold-rolling process are evident in sample #2, #4, #6, #8, #10, #12. Note that samples #4, #6, #10, #12 underwent ground rolling in the last stand rolling finish, and appear different from sample #2 and sample #8, which underwent electro-discharge (EDT) rolling in the last stand. Overall, samples with identical Si/Mn share a similar color and brightness attributed to oxide speciation obtained during annealing. For polished substrates, samples annealed at low dew points (−30°C) appear darker compared to those annealed at high dew points (+10°C).

6.4.2 Measured reflectance of samples having polished and rough state

The observations in Section 6.4.1 are also borne out in the reflectance measurements shown in Figure 6-7, where the curves corresponding to samples having identical Si/Mn and pre-annealed surface state are generally similar over the visible spectra. In addition, the measured reflectances of samples annealed in their as-received state are generally higher among the visible spectra compared to those of the polished samples. These results are consistent with the brighter images of as-received surfaces shown in Figure 6-6.

Given the measured surface oxide thickness scale (50-115 nm) of all the samples, the radiative properties should be influenced by both oxide film and surface topography effects across the UV-Vis-NIR wavelengths [195, 196]. The interference effect is particularly distinct for samples annealed in the polished state, and especially for low Si/Mn alloys. This is likely due to the fact that, for polished surfaces, the oxide grows more uniformly across the smooth substrate, leading to a more coherent wave interference effect and a lower reflectance over the visible spectra. Conversely, the reflectance of samples annealed in their as-received state exhibit less oxide film interference. As the oxide film thickness increases, the interference effect shifts to longer wavelengths; this is particularly pronounced when comparing the reflectances of sample #3 and sample #9, where the minimum point of the curve shifts to longer wavelengths as the oxide thickness increases from 70 nm to 110 nm.

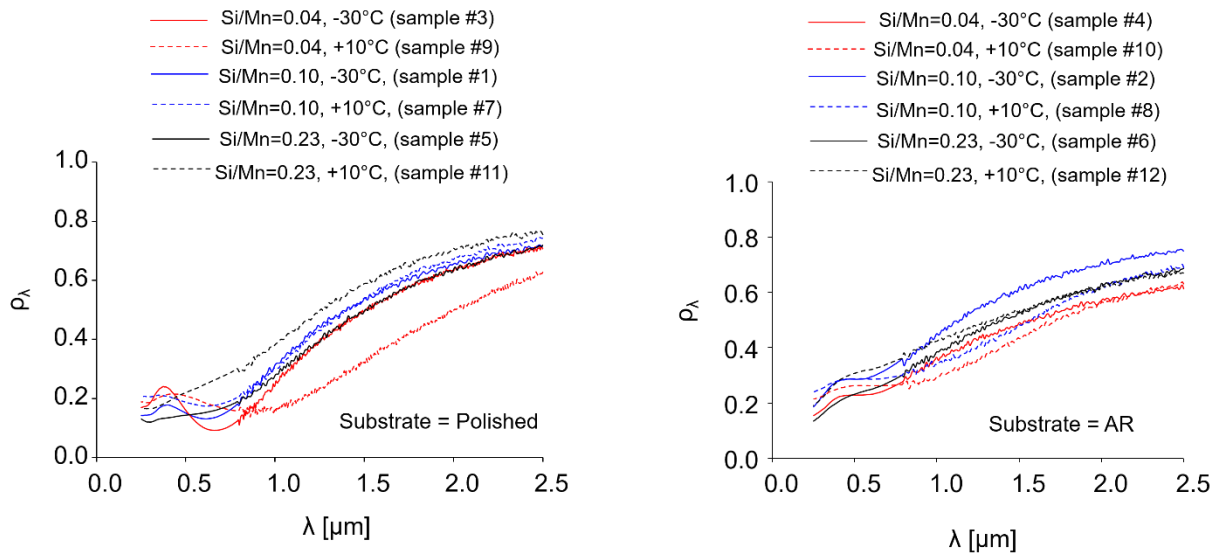

Figure 6-7. Comparisons of measured directional-hemispherical reflectances for samples annealed in their polished (left) and as-received (right) states. The thin film interference effect is more pronounced on the samples annealed in their polished state.

6.4.3 Scanning electron micrographs, measured refractive indices of oxides

Figure 6-8 shows SEM cross-sections of sample #1, #5, #7, #11, highlighting the effect of alloy composition and annealing dew point on the oxide structure. Sample #1 (Si/Mn=0.10, annealed at −30°C) has a uniform, continuous oxide film, while isolated oxide nodules are found on sample #5 (Si/Mn=0.23, annealed at −30°C) and sample #11 (Si/Mn=0.23, annealed at +10°C). The oxides on sample #7 (Si/Mn=0.10, +10°C) have a semi-continuous film-like appearance, while the ones observed on the surface of sample #11 are isolated nodules (Si/Mn=0.23, +10°C). The oxides formed on samples #3 and #9 (Si/Mn=0.04) were film-like and more comparable to those of the Si/Mn=0.1 alloy. In general, samples with Si/Mn=0.23 formed nodule-like oxides. On the other hand, the effect of dew point on oxide morphology was less pronounced, and oxide thickness and chemistry were more affected by this process parameter depending on the alloy composition.

Figure 6-9 shows the measured refractive indices for the oxide films obtained from ellipsometry. It can be seen that the measured refractive indices between the samples annealed with dp = −30°C and dp =+10°C are similar for the low Si/Mn alloy (Si/Mn=0.04, sample #3 and #9), and the measured values are close to that of MnO. This is in line with the XPS results of sample 3 (Table 6-1), which indicate that the surface oxides is mainly MnO, with minor $MnSiO_3$ and Cr_2O_3 as one would expect for low Si/Mn alloys. For the alloys of the intermediate Si/Mn ratio (Si/Mn = 0.1, sample #1 and #7) the measured refractive indices are sensitive to the dew point and are different from that of MnO. For the two samples having the highest Si/Mn ratio (Si/Mn=0.23, sample #5 and #11), the trends of measured curves are significantly different from the refractive index of MnO, and the refractive index is also sensitive to dew point. This implies the formation of distinct oxide species at different dew points. It is important to appreciate, however, that ellipsometry measurements are interpreted assuming that the oxide exists as a thin film; accordingly, the refractive indices for the Si/Mn = 0.23 samples, shown in Figure 6-9 (a), should be interpreted with some skepticism since the oxides formed on these surfaces are nodular-like.

In summary, as revealed in Figure 6-6, the alloy composition and surface topography have a greater impact on radiative properties of AHSS in the visible spectra compared to that of the annealing atmosphere. This is because the alloy composition, in addition to changing the surface oxide morphology, determines the oxide species having distinct refractive indices formed during annealing, as shown in Table 6-1 and Figure 6-9, which impacts the radiative properties. The pre-annealed surface would significantly affect the EM wave interference reflections due to different levels of uniformity of oxide layers between the polished and as-received surfaces. The annealing atmosphere, however, is found to have minor effect on the measured reflectance. This could be attributed to the fact that oxide morphology does not change significantly between the film-like

and nodular-like structure for samples having identical alloy composition and pre-annealed surface states, as observed in Figure 6-8.

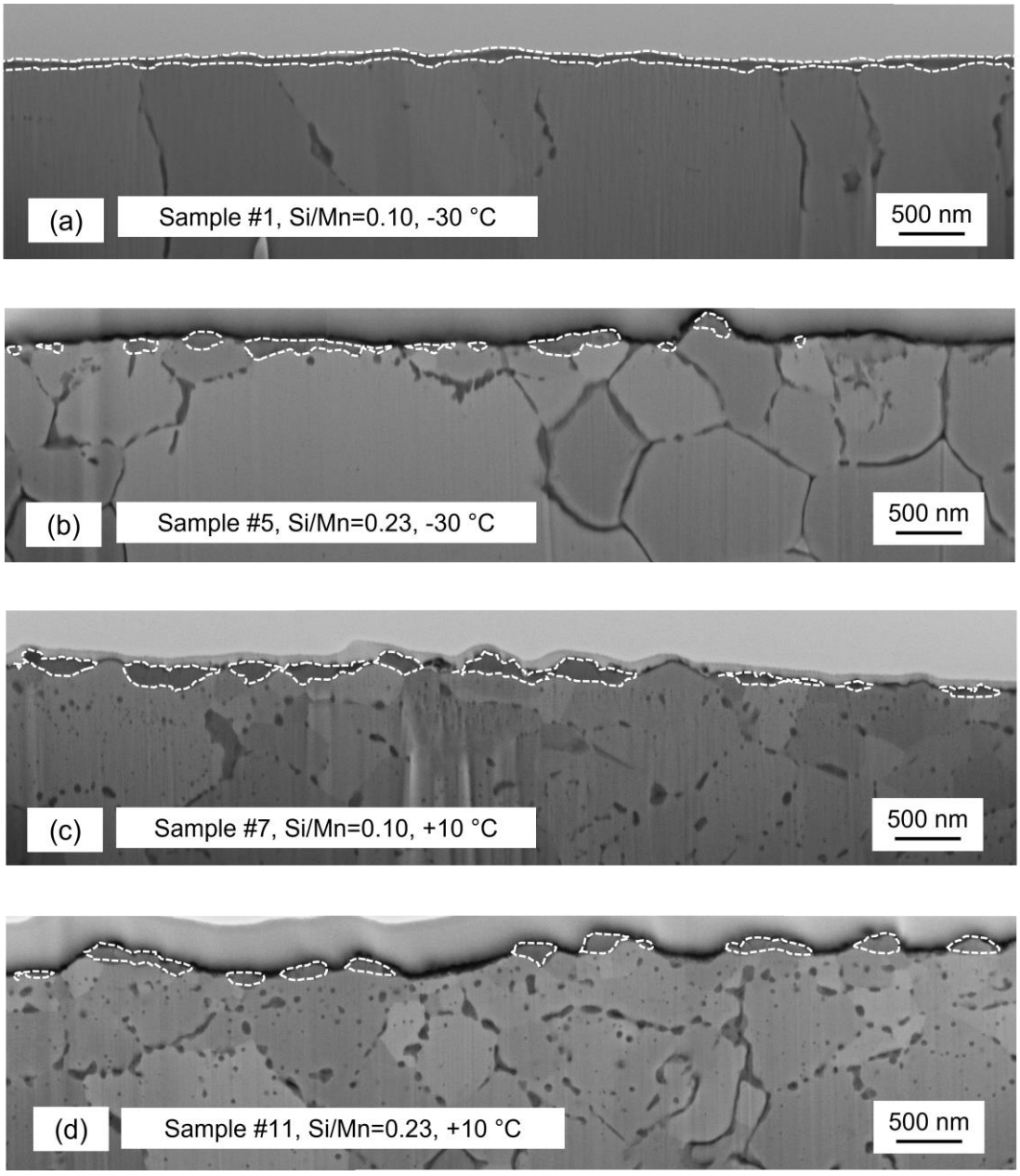

Figure 6-8. Scanning electron micrographs of cross-sectional surfaces of the annealed samples. (a) sample #1 (b) sample #5 (c) sample #7 and (d) sample #11. Oxides are outlined by the white dashed lines. Sample 1 has a film-like oxide, while isolated nodules oxides are formed on sample #5 and #11. The oxide structure of sample #7 shares characteristics of both a nodular and film-like structure, but more inclined towards film-like. Oxide formations of sample #3, #9 (not shown) are film-like.

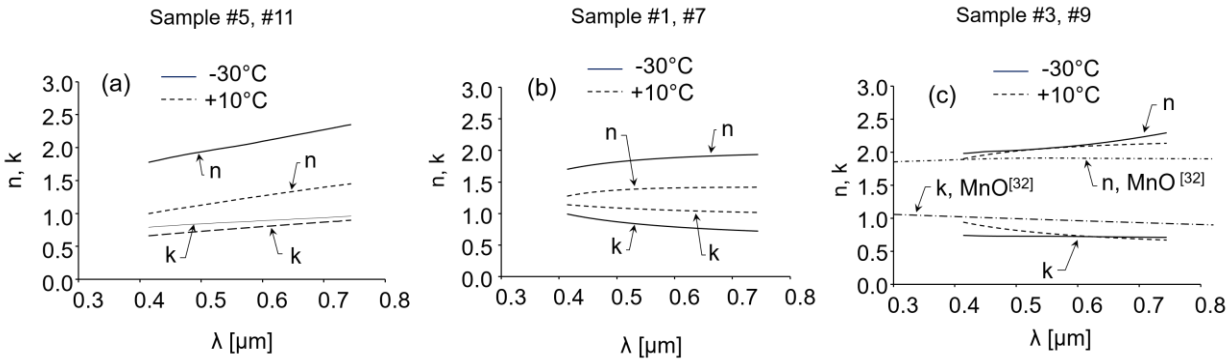

Figure 6-9. Measured refractive indices of oxide film via ellipsometry are shown for (a) Si/Mn=0.23, (b) Si/Mn=0.10, and (c) Si/Mn=0.04 for the samples annealed in a polished state. The solid and dash curves in the plots represent samples annealed at -30°C and +10°C atmosphere, respectively. The long-short dash lines in (c) are derived from [193]. The refractive indices shown in (a) should be interpreted with some skepticism, since the oxide has a nodular as opposed to a film-like morphology.

6.4.4 Comparison of thin film interference predictions and measurements

Figure 6-10 compares the reflectance measurements and model predictions over the UV-Vis-NIR spectra for all the polished samples. Since the thin film interference model (Eq. (2.9)-(2.13)) only applies to a smooth substrate and oxide layer, comparisons are only made using polished samples. For samples having low Si/Mn (sample #3, sample #9), the thin film interference predictions using the refractive indices of MnO from the literature can be made within a large spectrum (0.25-2.5 μm) since the refractive indices of MnO from the literature covers this wavelength range. In the case of samples having more complex oxide species, the thin film interference predictions using the measured refractive indices are limited to the visible spectrum because the ellipsometry measurements can only be done within this wavelength range. For all tested samples, the thin film interference model using ellipsometry-derived oxide refractive indices over visible spectra (0.4-0.75 μm) is consistent with the measurements, even though the predicted refractive indices slightly underestimate the measured values. This can be attributed to the slight roughness of these polished surfaces that scattered the light away from the specular directions when carrying out the

ellipsometry measurements. Accordingly, the intensities of reflected light received by the ellipsometry detector may be lower than the actual value.

When the oxide film thickness is on order of, or less than the EM wavelength, the radiative properties of oxidized steels are influenced by both the oxide film and surface topography [192, 195]. It can be seen from Figure 6-10 that the measured reflectance approaches the reflectance of ferrite as the wavelength increases and the surface becomes optically-smooth. This implies that the radiative properties are less affected by the oxide film as the EM wavelength becomes much longer than the film thickness. For sample #3 and #9, which have the lowest Si/Mn ratio (Si/Mn=0.04) in Figure 6-10 (b) and (e), one can see the predictions using the thin film interference model with MnO refractive indices from Ref. [193] (blue dashed lines) also match with the measurements over the entire spectra. An obvious interference effect can be observed in Figure 6-10 (a), (b), (d) and (e) for samples having low Si/Mn ratio (Si/Mn=0.04, Si/Mn=0.10).

Notably, neither sample #5 nor sample #11, Figure 6-10 (c) and (f), exhibit an oscillation due to thin-film interference, even though they were polished prior to annealing. As previously noted, the oxides are nodular as opposed to a homogeneous film as shown in Figure 6-10. Nevertheless, the thin film model predictions are still close to the measurements. Given the fact that the refractive indices in Figure 9 inferred from the ellipsometry using the thin film interference model, it is not a surprise that incorporating the ellipsometry-measured optical properties (oxide film refractive indices, thickness) into the thin film interference model can reproduce a spectral reflectance in line with the measurement, even though the thin film interference model should not be applied to a nodular oxide morphology. Accordingly, for samples having high Si/Mn, a model accounting for both the oxide nodulus and the roughness effect is needed to effectively predict the reflectance.

Overall, these results indicate that for AHSS samples having a polished pre-annealed surface and low Si/Mn, the effect of surface oxidation on radiative properties can be interpreted using the thin film interference model.

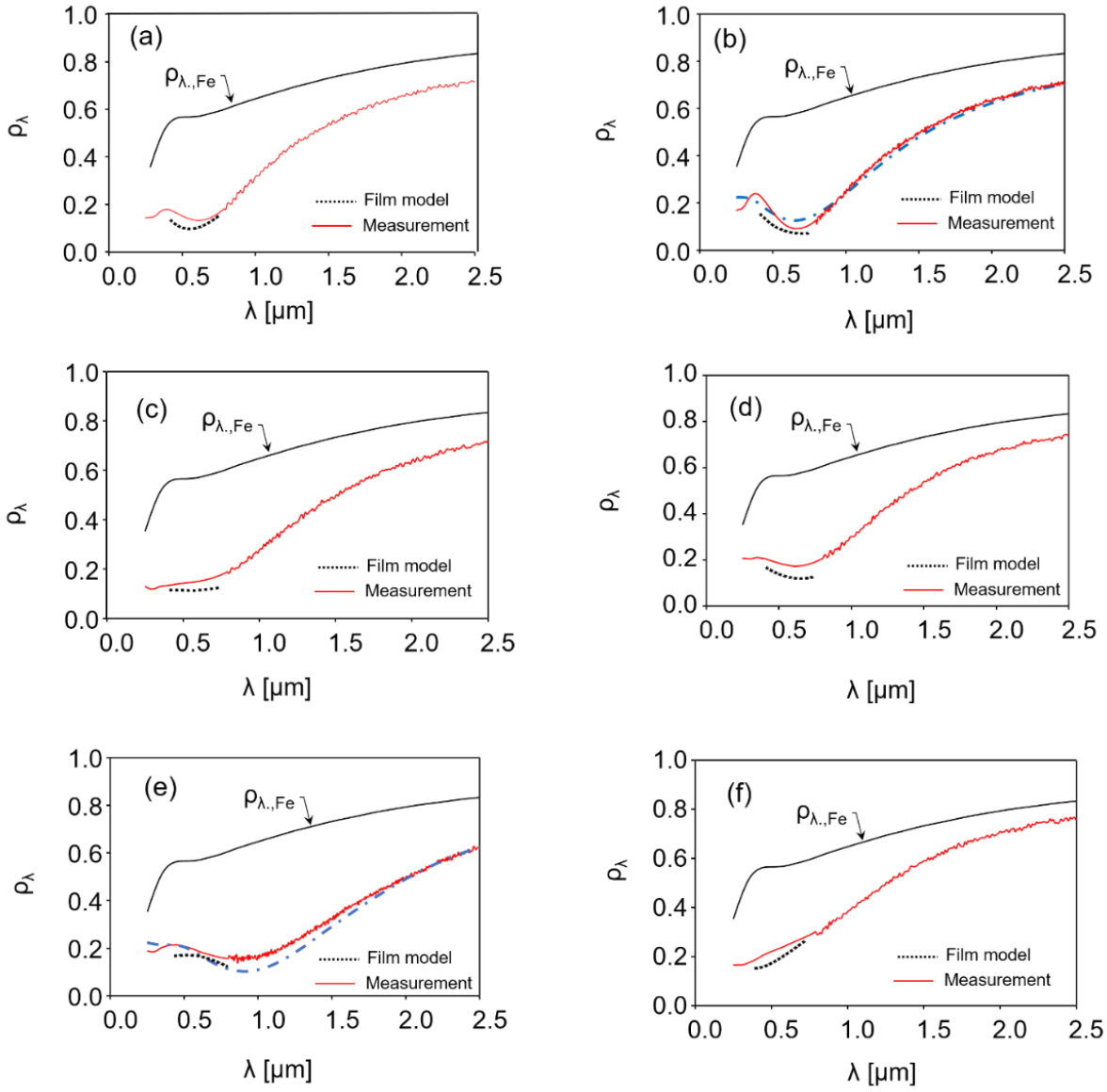

Figure 6-10. Comparisons of measured and predicted reflectances for samples annealed in their polished state: (a) sample #1, (b) sample #3, (c) sample #5, (d) sample #7, (e) sample #9, (f) sample #11. The black solid curves in the plots represent reflectance of ferrite derived using Fresnel's equation. The red curves and black dotted curves represent measurements and predictions using the thin film interference model, Eq. (2.9)-(2.13), with measured refractive indices, respectively. The blue dashed curves in (b) and (e) denote predictions via the thin film interference model with refractive indices of MnO obtained from reference [193].

6.5 Conclusions

This chapter examines the effect of alloy composition, annealing atmosphere, and pre-annealed surface states on radiative properties of dual-phase steels. Thin film interference effects are observed in the spectral reflectances of samples annealed in a polished and as-received surface state, although the effect is more pronounced for the polished samples, since the uniformity of the surface leads to more coherent wave interference effects. In the case of samples annealed in a polished state, the smoothness of the substrate and uniformity of the oxide layer permits a quantitative analysis using a thin film interference model. XPS measurements have revealed that Mn-rich oxide (MnO) was primarily formed on those low Si/Mn alloys, while ternary oxides were found on high Si/Mn alloys. Thin film interference effects are notably absent from two of the polished samples having high Si/Mn alloys, which had a nodular as opposed to film-like oxide morphology.

Ellipsometry measurements carried out on these samples reveal thicknesses consistent with values obtained through electron microscopy, and refractive indices that depend on the alloy composition and dew point of the annealing atmosphere. For samples having a low Si/Mn ratio (Si/Mn=0.04), the refractive indices matched published values for MnO at both dew points, suggesting that the oxide layer consists primarily of MnO, which is consistent with the XPS measurements. Alloys having a greater silicon content showed refractive indices are distinct from those of MnO and were also sensitive to dew point, due to the formation of more complex ternary oxides. In all cases, substituting the refractive indices and oxide thicknesses into the thin film interference model produced modeled spectral reflectances that closely match those measured using a spectrometer/spectrophotometer and integrating sphere, although the validity of this approach is questionable for the high Si/Mn samples having a nodular morphology.

Chapter 7 Interpreting the Radiative Properties of Advanced High Strength Steel Strip using Hybrid Thin Film/Geometric Optics Model[8]

7.1 Introduction

Chapter 6 focused on the AHSS samples that are annealed in their polished state, in which the correlation between the radiative properties and surface state are interpreted *via* the thin film interference theory. In most real cases, however, the substrates of steel samples are rough. Consequently, the radiative properties of oxidized steel strips may not only be influenced by the thin film effect, as the oxides may form less uniformly upon a rugged substrate surface. Following the previous chapter, this chapter is focused on estimating the radiative properties of AHSS samples oxidized in their as-received states. The radiative properties of these samples are estimated using the hybrid thin film/geometric optics model discussed in Section 3.4, with comparisons between the predictions and the measurements. The effects of alloy composition and annealing atmosphere on the oxide morphology of these samples are also investigated to elucidate the radiative behaviors.

As mentioned in Chapter 6, the presence of a uniform thin oxide film on a metallic surface may coherently influence the spectral emissivity, because an incident electromagnetic (EM) wave undergoes a phase shift as it enters the film, is reflected from the substrate, and exits the film, leading to constructive and destructive interference in the far field [47, 188]. The extent of this

[8] The content of this chapter is an extended version of a paper submitted to *J. Quant. Spectrosc. Radiat. Transf.*: K. Lin, M. Pourmajidian, F. K. Suleiman, J. R. McDermid, K. J. Daun, *Interpreting the radiative properties of advanced high strength steel strip using a hybrid thin film/geometric optics model*. (2021)

effect depends on the refractive index of the film as well as its thickness relative to the EM wavelength, and may be significant when the thickness is less than or on the order of the wavelength [33], as indicated in Figure 7-1 (a). The EM wave becomes more sensitive to the surface irregularities (e.g. oxide nodules, roughness) when the wavelength becomes much larger than the oxide film thickness [166] ($\lambda \sim 100D$). In this scenario, as shown in Figure 7-1 (b), the wave is scattered in a random way, leading to variations in bidirectional reflectance subject to each scattered direction. In the case of an oxide film deposited on a rough substrate, as illustrated in Figure 7-1 (c), radiative properties are governed by both the wave optics (thin film interference effect) and the surface roughness effect when the oxide film thickness is less than or on the order of the EM wavelength [195]. In the case of AHSS alloys, this scenario dominates over the wavelengths important to pyrometry (1.0-3.0 μm). This presents a pressing need for models that can connect the radiative properties over these wavelengths to the formation of oxide films and variations in surface topography imparted by cold rolling of oxide forms.

A number of hybrid models have been developed in the literature for other applications. Gunde and Aleksandrov [197] inferred the complex refractive indices for a rough silicon oxide film deposited on the silicon wafers via the measured transmittance and reflectance. They incorporated a roughness factor function into a flat-surface reflection model proposed in Ref. [50] which is correlated to the total transmittance and reflectance. Similar studies were carried out on various rough thin film materials [198, 199]. Tang et al. [195] combined geometric optics ray tracing with a thin film interference model (hybrid model) to predict the bi-directional reflectances of a rough oxidized aluminum surface. In their model, the coating on the rough substrate is treated as globally-uniform in thickness, and incident waves are ray-traced through multiple reflections with a two-dimensional random rough surface. Good agreement was observed between the

predicted and measured bidirectional reflectances. Lee et al. [200] used the hybrid model to estimate the radiative properties of coated rough silicon wafers. In their study, a weighted probability density function based on the surface slope distribution and the projected area is employed in the ray tracing scheme. Their model showed that both the roughness and coating strongly influence the bidirectional and directional-hemispherical radiative properties of the wafers.

The validity domain of the hybrid model was further delineated by Zhu et al. [196], who investigated SiO_2-coated rough silicon surfaces by comparing the predicted bi-directional reflectances with values obtained from a rigorous EM wave solution on a one dimensional surface. In the case of rough surfaces (i.e. large σ/τ) the hybrid method is only valid when the coating thickness is much smaller than the wavelength. They claimed that the hybrid method becomes invalid for rough surfaces with thick oxide layers due to the "corner effect", since multiple reflections of EM waves would occur inside the oxide film. In this case, reflections of ray bundles beneath the oxide layer, unaccounted for in the hybrid model, must also be considered. Lee and Zhang [201] used the hybrid model to predict the bi-directional reflectance of a SiO_2 coated rough silicon wafer, and compared these results with experimental measurements. Large deviations between the measurements and predictions were found on surfaces with large roughness slope and thick coatings, which they attributed to the corner effect and non-uniform film thickness across the surface.

Qiu et al. [202] further developed a novel hybrid partial coherence and geometry optics (HPCGO) model that incorporates the GOA raytracing and thin-film partial coherence effects to estimate the radiative properties of coated rough silicon surfaces. The incident EM wave was treated as partially coherent, depending on the given wavelength range. It was found that both

coating thickness and surface roughness can affect the estimations. The HPCGO model is highly accurate if the surface roughness and the ratio of film thickness to wavelength, h/λ, are both small. More recently, Jo et al. [179] employed a ray-tracing model described in [178] to evaluate the spectral emissivity of oxidized SA508 steel samples that were polished before they were oxidized in air. In their model, the surfaces were artificially generated according to a random roughness parameter, and the spectral-directional emissivity was set equal to the superposition of local emissivity at each ray tracing point. Model predictions were consistent with measured emissivity.

Most of the aforementioned studies account for interference reflections using thin film optics, as they assumed that the oxide layer is uniform in thickness across the rough substrate surface; this is required by the hybrid model, which considers only interference reflections as the ray bundle hits the surface (Figure 7-1 (c)). In the case of continuous galvanizing, however, the oxide layer formed on a rough substrate is usually nonuniform in thickness, as depicted in Figure 7-1 (d). In this scenario, the global oxide thickness should not be treated identical at each local point when performing the GOA ray tracing, and the unparallel ray bundles reflected from the top and bottom interfaces of the oxide may not overlap and form interference reflections. In Chapter 6, it has been shown that less interference was found on the measured reflectance of oxidized AHSS samples having cold-rolled artifacts compared to that of those having polished substrate [203], which could be attributed to the fact that the oxide formed across the surface during annealing is less uniform for the rough-substrate samples.

This chapter investigates the connection between surface morphology, as determined by alloy composition and annealing atmosphere, and the radiative properties of dual-phase steels having cold-rolled surface artifacts. Predictions are made through a hybrid thin film/geometric optics model described in Section 3.4 that incorporates thin film interference effects within the

framework of a GOA ray tracing model. It is found that the predicted values are very sensitive to surface roughness and oxide thickness profile; increasing the substrate roughness decreases the reflectance due to increased reflections of ray bundles. The hybrid model predictions generally underestimate the spectral reflectance compared to measured values, which also show less intense interference effects. These findings highlight the fact that the hybrid model is incapable of accurately capturing the radiative properties of oxidized AHSS samples having as-received surface states. A higher fidelity model, which precisely models wave interference underlying the robust oxide profiles, must be developed to recreate the radiative properties of these surfaces.

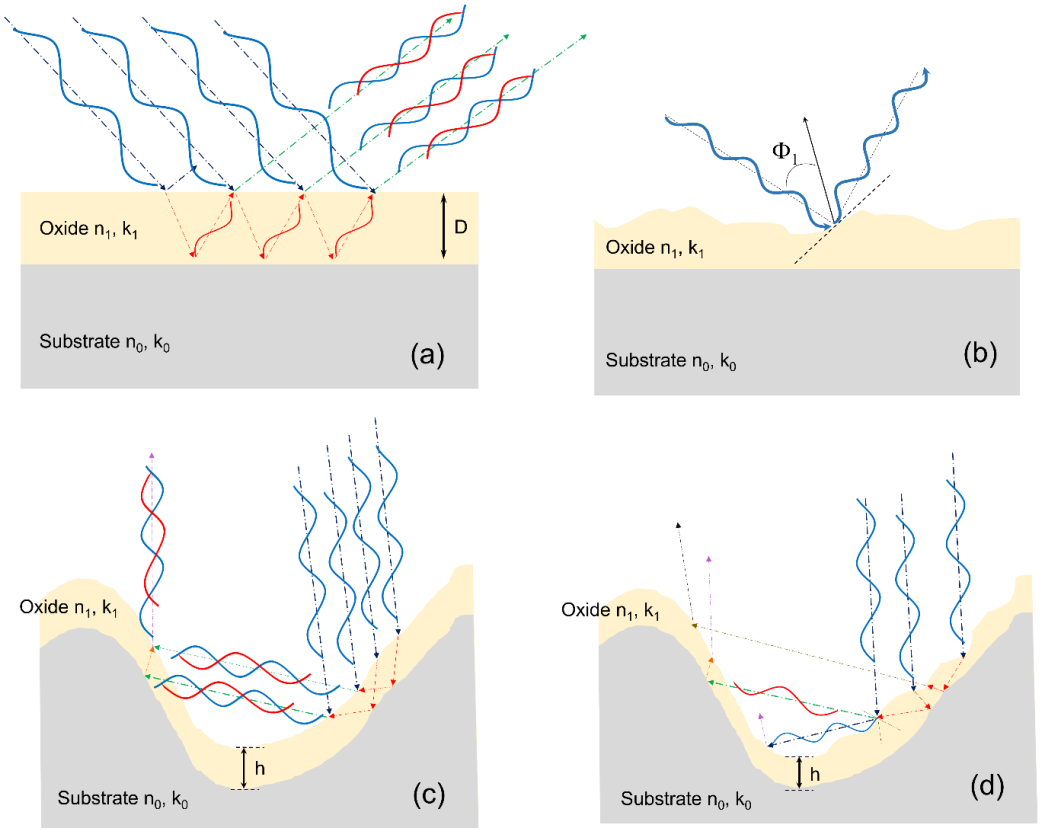

Figure 7-1. Schematic view of how EM waves interact with oxidized AHSS surfaces: (a) thin film interference effect; (b) surface topography dominates the wave/surface interaction when the wavelength is much larger than the oxide film thickness; (c) rough oxidized surface where the global oxide thickness across the surface area is uniform upon the substrate; and (d) rough oxidized surface where the global oxide thickness across the surface area is non-uniform upon the substrate. In scenarios (a) and (c), thin film interference dominates the wave/surface interaction. In scenario (d), both interference and non-interference reflections are important, depending on the profiles of the oxide and substrate.

7.2 Methodology, sample preparation and measurement

7.2.1 Methodology of hybrid model

The methodology of the hybrid thin film/geometric optics model is detailed in Section 3.4, with flowchart illustrated in Figure 3-13. The set of *x, y, z* data points obtained from an optical profilogram of the surface are used as surface nodes that form the 2D surface. The incident polar and azimuthal angles are set to be 10º and 45º, respectively, which match the FTIR measurement conditions. In present study, the substrates of all the samples are treated as ferrite, having refractive indices obtained from Ref. [194]. For the alloys considered in this study, surface oxides are likely to consist of Mn-rich oxide or Si-Mn ternary oxides and potentially chromium oxide, depending on the annealing dew point and Si/Mn ratio. The Si/Mn ratio of the alloys tests in this study are identical to the ones in previous chapter, as listed in Table 5-1. More detailed discussion about the oxide formation subject to annealing atmosphere and alloy composition is presented in Chapters 2 and 6.

The refractive indices of MnO is derived from Ref. [193]. Ellipsometry measurements cannot be carried out on rough samples, so the present study adopts the measured refractive indices of those having polished surface state, but with identical alloy composition and annealing conditions to those having as-received surface state. The oxide layer is composed primarily of MnO, Mn-Si ternary oxides, and/or Cr_2O_3 under the alloy composition and annealing conditions of this experiment, as mentioned in Chapters 2 and 6. The oxide components of all samples are also confirmed with XPS measurements.

7.2.2 Sample preparation

This study adopts AHSS samples that were examined in Chapter 6, as listed in Table 7-1. While the previous study focused on the samples that were oxidized in their polished states, the present study is focused on those annealed in their as-received states (sample #2, #4, #6, #8, #10, #12), which is more representative of industrial conditions. All the experimental methodology regarding the sample preparation, surface profile characterization, radiative property measurements, and surface oxide identification are detailed in Chapter 6 (Section 6.2). All the samples were annealed at 800°C in a 95%/5% (vol.) N_2/H_2 atmosphere at dew points of −30°C or +10°C, corresponding to oxygen partial pressures of 2.56×10^{-20} atm (p_{H2O}/p_{H2}: 0.2408) and 4.39×10^{-23} atm (p_{H2O}/p_{H2}: 0.00998), using the McMaster Galvanizing Simulator (Iwatani-Surtec) according to the annealing schedule illustrated in Figure 6-2.

7.2.3 Measurement techniques

The oxide thickness data were measured using Focused Ion Beam (FIB) milling technique as mentioned in Section 6.2. The predictions on the as-received samples were made with FIB-measured data via the thin film interference and hybrid thin film/geometric optics models. Refractive indices of oxide film formed on polished samples are characterized using a J. A. Woollam M-2000 ellipsometer over visible wavelengths [203]. It is assumed that oxides formed on various alloys processed within the same annealing atmosphere will be identical regardless of the pre-annealing surface roughness (polished vs. as-received), and, since the ellipsometer is unable to measure the samples having rough surface feature (sample #2, #4, #6, #8, #10, #12), the refractive indices of these samples are adopted from those of the polished samples having identical alloys and annealing conditions (sample #1, #3, #5, #7, #8, #11), respectively. The near-normal

directional-hemispherical spectral reflectance of each sample was measured using a Varian Cary 5000 UV-Vis-NIR spectrophotometer (0.25-2.5 μm) mentioned in Chapter 4.

The XPS measurements in Table 7-1 confirm that, in general, the surface oxides found between the polished and as-received samples have consistent speciation. Therefore, it seems reasonable to adopt the oxide refractive indices from the polished samples for those as-received samples in the model predictions. Sample #3, #4, #9, #10 are found to comprise Mn-rich oxides, whose refractive indices are close to that of MnO, as one would expect for low Si/Mn alloys [26], while the oxide species found on other high Si/Mn samples are mainly composed of ternary oxides. As mentioned in Ref. [203], the refractive indices of sample #5 and #11 obtained via the ellipsometry should be interpreted with skepticism, due to the nodule-like oxide morphology observed on the surface. In this scenario, ellipsometry cannot be used to correctly infer the refractive indices of the oxide, nor is the thin film interference model valid for predicting the radiative properties of the surface. Therefore, their related cases (sample #6, #12) are excluded from further analysis.

Table 7-1. Tested samples with different alloy compositions, annealing atmospheres, measured pre-annealed and post-annealed roughness, and measured oxide thickness and oxide species. The uncertainty in μ_h represents the margin of error at 95% confidence interval of the mean.

Sample No.	DP	Si/Mn	Pre-annealed Surface State	σ_{pre} [μm]	σ_{post} [μm]	σ/τ (post)	Oxide thickness [nm]			Primary oxide (XPS)
							Ellip.	FIB		
								μ_h	σ_h	
1 (A3)	−30°C	0.10	Polished	0.09	0.26	0.04	58.5	53.4 ±2.88	-	Mn_2SiO_4, Cr_2O_3, MnO
2 (A3)	−30°C	0.10	As-received	2.60	2.73	0.31	-	62.5 ±3.84	24.8	Mn_2SiO_4, Cr_2O_3, MnO
3 (A2)	−30°C	0.04	Polished	0.09	0.17	0.03	70.7	67.4 ±3.27	-	MnO, Cr_2O_3, $MnSiO_3$
4 (A2)	−30°C	0.04	As-received	0.65	0.71	0.42	-	91.2 ±5.08	34.1	$MnSiO_3$, Cr_2O_3, MnO
5 (A1)	−30°C	0.23	Polished	0.09	0.28	0.04	74.1	70.5 ±5.85*	-	Mn_2SiO_4, Cr_2O_3, MnO
6 (A1)	−30°C	0.23	As-received	0.59	0.67	0.32	-	63.8 ±6.06*	33.9	Mn_2SiO_4, Cr_2O_3, MnO
7 (A3)	+10°C	0.10	Polished	0.09	0.21	0.04	112.8	101.7 ±7.05	-	MnO, Mn_2SiO_4
8 (A3)	+10°C	0.10	As-received	2.60	3.10	0.34	-	84.7 ±8.99	48.9	MnO, Mn_2SiO_4
9 (A2)	+10°C	0.04	Polished	0.09	0.27	0.05	110.6	114.5 ±7.88	-	MnO, $MnSiO_3$
10 (A2)	+10°C	0.04	As-received	0.65	0.70	0.45	-	103.8 ±6.29	41.0	MnO, Cr_2O_3, $MnSiO_3$
11 (A1)	+10°C	0.23	Polished	0.09	0.25	0.04	68.0	65.3 ±6.64*	-	Mn_2SiO_4, MnO
12 (A1)	+10°C	0.23	As-received	0.59	0.72	0.35	-	94.4 ±12.06*	74.9	Mn_2SiO_4, MnO

*These measured thickness values contain significant nodule-like oxides as opposed to film-like oxides at the external surface region.

7.3 Results and discussion

7.3.1 Scanning electron micrographs and oxide thickness histograms

Figure 7-2 shows the cross-sectional SEM images of sample #2, #4, #6, #8, #10, #12 with oxide areas outlined by the white dashed lines. The images illustrate that the annealing atmosphere and

alloy composition significantly influence oxide formation. Film-like oxide structures tend to form across the surface of samples annealed at lower dew points (sample #2, #4, #6), while nodular oxides appear on the samples annealed at higher dew point (sample #8, #10, #12). For both annealing atmospheres (dp = -30°C, dp =+10°C), the oxide morphology also transforms from film-like to nodular-like structure as the alloy Si/Mn ratio increases. The oxide structure of Sample #12 (Figure 7-2-(f)) is particularly irregular, which is consistent with the statistical data obtained *via* the FIB-SEM measurements.

Figure 7-3 shows histograms of local oxide thickness obtained along each FIB-milled trench for each sample. The histograms also reflect the oxide morphology shown in Figure 7-2. Samples having film-like oxide morphology, which were annealed with lower dew point (dp=-30°C) shows more uniform (less deviation) histogram. Since the substrate is rough and the oxide thickness data are obtained over a 10 μm length, the measured values represent the local thickness instead of global thickness. Because the measurement interval (100 nm) is beyond the horizontal resolution of the optical profilometer (1.6 μm), the surface data needs to be regenerated using the measured parameters. In order to comply with the measurement conditions in present study, the 1.2 mm × 1.0 mm 2-D surface is reconstructed into two one-dimensional surfaces based on the measured σ and τ with a total length of 10 μm and interval of 0.1 μm (Δx=0.1 μm), assuming the surface heights obey Gaussian statistics [147]. With the measured μ_h and surface profile (surface inclination angle of each location), the global oxide thickness h can thus be approximated using Eq. (2.63). The calculated global thicknesses, h, are 67.4 nm (sample #2), 102.8 nm (sample #2), 69.6 nm (sample #6), 92.8 nm (sample #8), 121.2 nm (sample #10), 103.9 nm (sample #12).

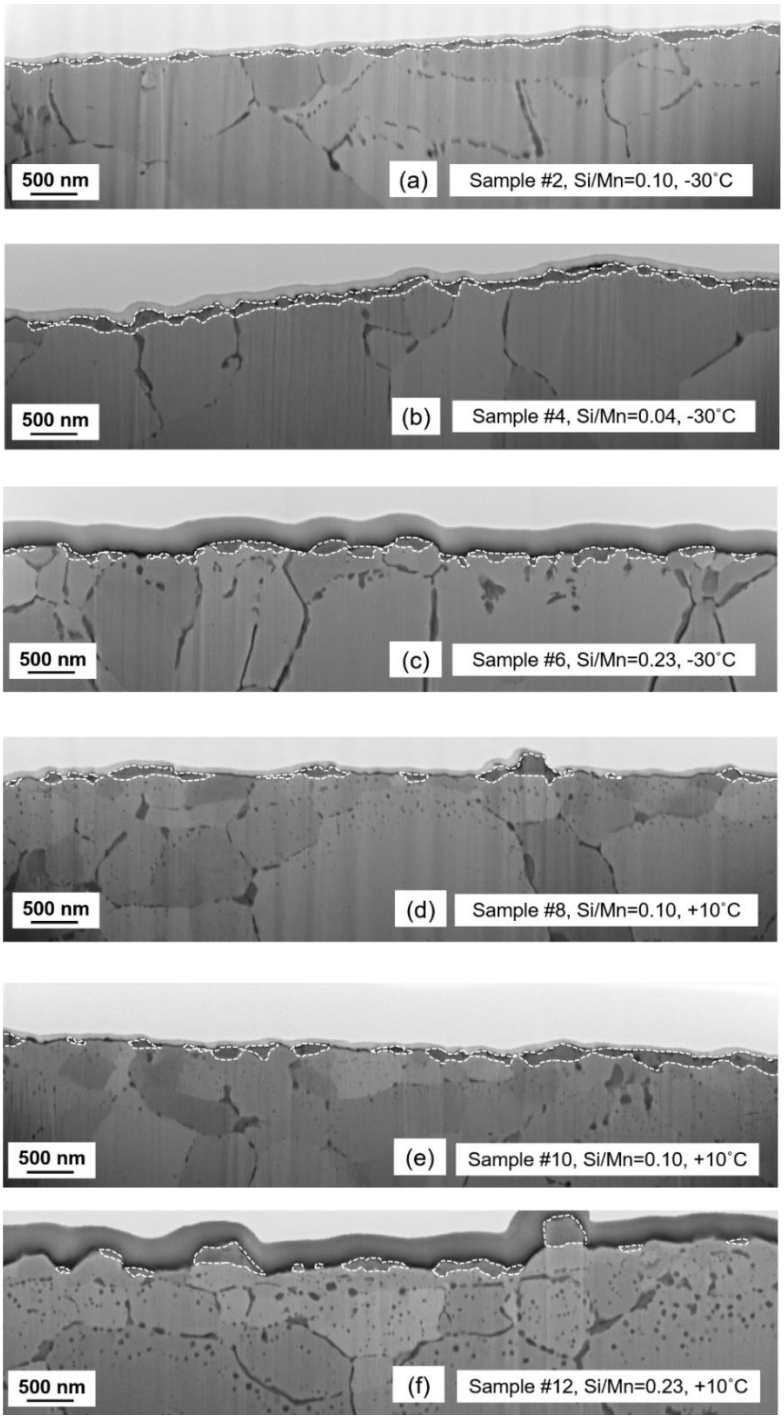

Figure 7-2. Scanning electron micrographs of cross-sectional surfaces of the annealed samples: (a) sample #2 (b) sample #4 (c) sample #6 and (d) sample #8 (e) sample #10 (f) sample #12. Oxides are outlined by the white dashed lines.

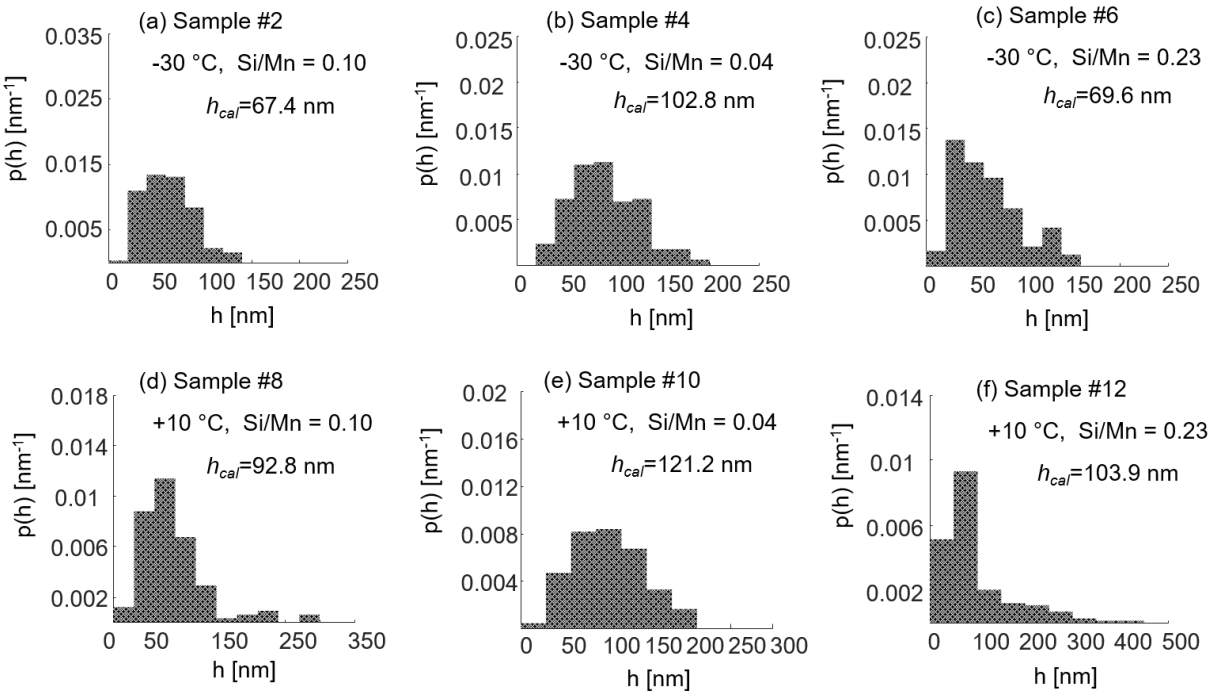

Figure 7-3. Measured local oxide thickness histogram for: (a) sample #2; (b) sample #4; (c) sample #6; (d) sample #8; (e) sample #10; and (f) sample #12. The grey bars denote the histogram of oxide thickness measured via FIB milling.

7.3.2 Comparisons of CDF curves for local oxide thickness

Figure 7-4 shows the cumulative density functions (CDF) of the measured and sampled local oxide thickness statistics. The red curve is the CDF of the local oxide thicknesses sampled over a 1.2 mm × 1.0 mm rough surface generated using the profilometry-measured data points and calculated *h*. It is apparent that the generated local oxide thicknesses do not follow the statistics of the measurements, where the measured thickness exhibits larger deviation, demonstrating a highly non-uniform oxide thickness across the surface. This implies that the oxide profile employed in the hybrid model, which assumes constant global thickness, may not be able to capture the real oxide morphology.

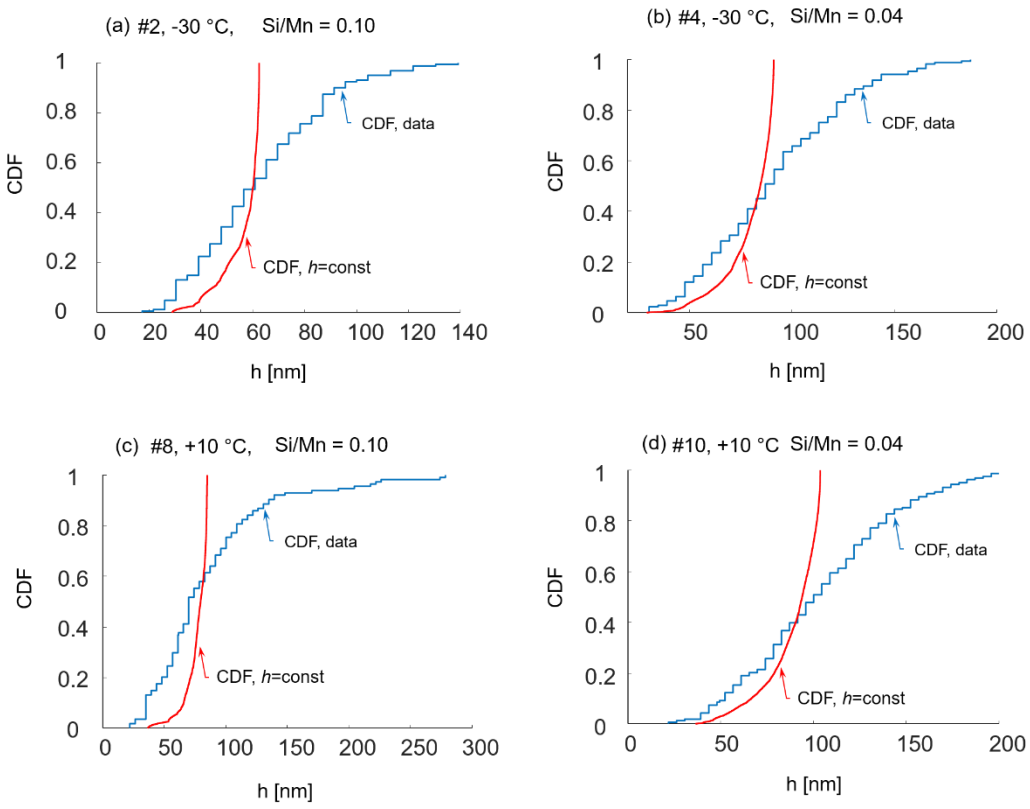

Figure 7-4. Comparisons of cumulative distribution function curves of local oxide thickness for: (a) sample #2; (b) sample #4; (c) sample #8; (d) sample #10; The blue curve represents the empirical CDF generated from the measured data. The red curve represents CDF generated by constant global oxide thickness, *h* and measured surface parameters, σ, τ listed in Table 7-1.

7.3.3 Constructed 1-D oxide profile employed in the hybrid model

Figure 7-5 (a)-(d) show the 1-D oxide and substrate surface profile for samples having as-received states (sample #2, #4, #8, #10) underlying the assumption of uniform oxide thickness employed in the hybrid model, although, in reality, the oxide is not uniform as shown in Figure 7-1 (c). The substrate surface profiles shown in black are generated using the profilometry-measured σ and τ from the 2-D surface. One can see that the level of irregularities of surface profile increases with σ/τ, leading to increased multiple scattering of ray bundles within the cavities. The oxide profiles shown in red are generated using the calculated *h*, as the constant global oxide thickness across

the surfaces. When the profile has both large σ/τ and oxide thickness, it was shown that the corner effect is likely to occur as the multiple reflected waves inside the oxide layer on a given microfacet escape from the microfacet before they interfere with each other [196]. It is seen in Figure 7-5 that, for all samples, given the substrate surface roughness, the oxide thickness is relatively thin across all the microfacets such that the corner effect can be neglected, as the red curves are intrinsically close to the black curves. Based on Ref. [196], the corner effect does not need to be considered for $0.2 \leq \sigma/\lambda \leq 1$, $\tau/\lambda \geq 2$ when $h/\lambda = 0.1$ or $h/\lambda = 0.5$. The samples tested in this study all follow this criterion. Consequently, it is reasonable to exclude the corner effect from the hybrid model employed in this study.

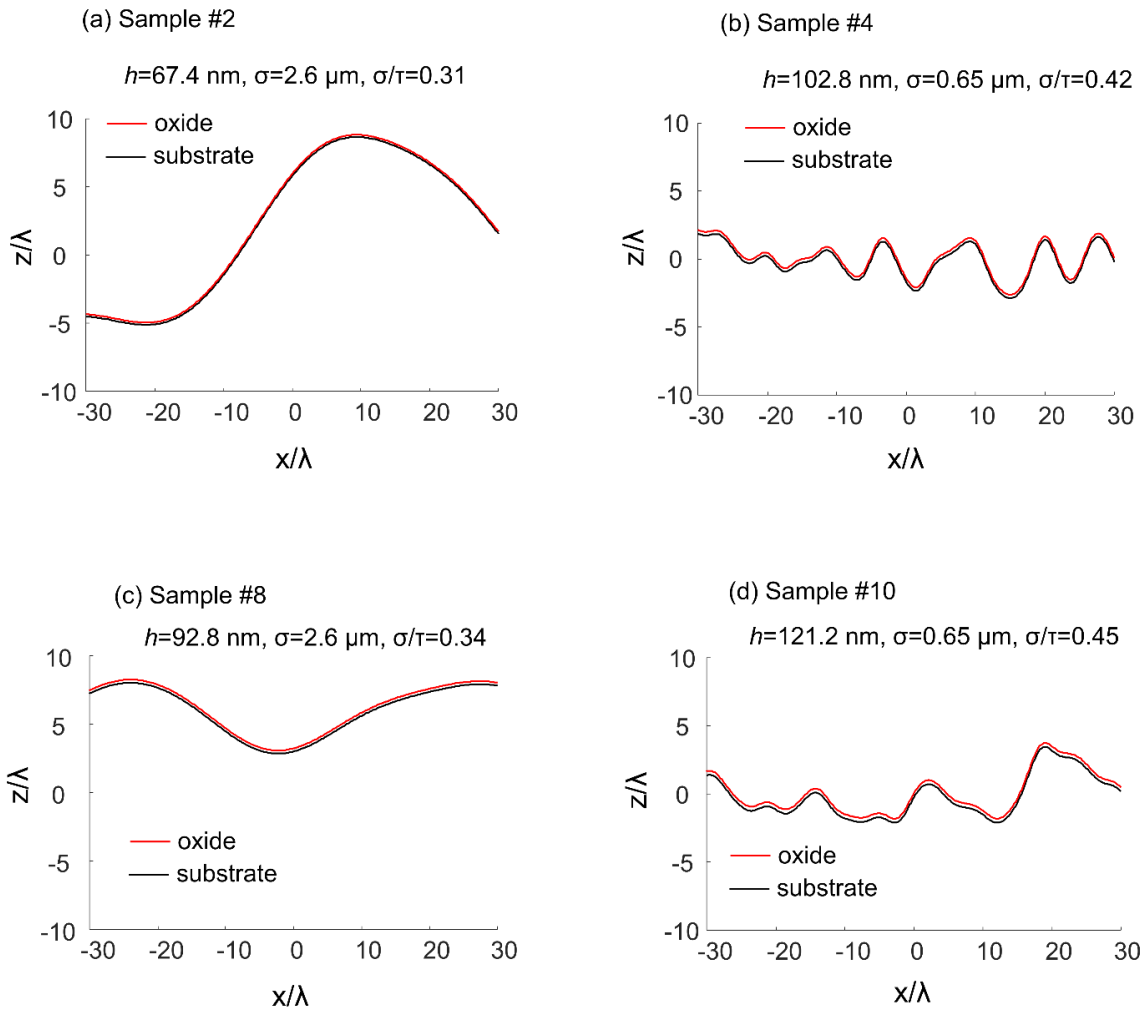

Figure 7-5. 1-D profiles of oxide and substrate for: (a) Sample 2; (b) Sample 4; (c) Sample 8; (d) Sample 10; The oxide profile is generated using the calculated universal (global) oxide thickness, *h*, while the substrate profile is generated using the measured surface parameters (σ, τ). The incident wavelength is fixed at λ=0.4 μm. The red and black curves represent the generated oxide and substrate profiles, respectively.

7.3.4 Comparisons of reflectance measurements and predictions

Figure 7-6 (a)-(e) compares the reflectance between the measurements and the predictions using the thin film interference model and hybrid model; Figure 7-6 (a) shows the case of the sample annealed in its polished state [203]. The hybrid model predictions are carried out using 2-D geometric optics. All the predictions are made using the oxide thickness and surface data derived

from the FIB/SEM analysis and optical profilometry, σ and τ. For all the samples, the calculated thickness, *h*, is employed in both the thin film interference model and hybrid model as the global oxide thickness (a constant value) over the surfaces. Figure 7-6 (a) shows that for the sample annealed in its polished state (sample #3) the spectral reflectance predicted using the thin film interference shows interference patterns that are consistent with the measured curve. For samples annealed in their as-received state, reflectances predicted using the hybrid model and thin film interference model are not in line with the measurements, as shown in Figure 7-6 (b). Among all the samples, sample #2 has the smallest σ_h, showing a nearly uniform oxide film across the surface as revealed in the SEM image, Figure 7-2 (a). The smoothness of this sample corresponds to an interference effect that is more pronounced than those of the other samples. Compared to the thin film interference predictions, the hybrid model predicts lower reflectance at shorter wavelength and higher values at longer wavelength. This is because the hybrid model accounts for multiple reflections, and the oxide local thickness in the hybrid model is smaller than the global thickness used in the thin film interference model. Accordingly, the interference occurs at longer wavelength in the thin film interference model, which gives rise to a lower reflectance.

The measured reflectance of Sample #4, Figure 7-6 (c), shows a much less pronounced interference pattern, and the reflectances predicted using the thin film interference and hybrid models are also lower compared to the measurement. The rugged, nonuniform oxide morphology of this sample, shown in Figure 7-2 (b), is reflected by the large value of σ_h in Table 7-1. This scenario corresponds to Figure 7-1 (d), where the non-uniform oxide layer across the surface leads to a weaker interference effect. Both the hybrid model and thin film interference model predict interference features that are absent in the measured reflectance. The lower reflectance predicted by the hybrid model compared to the thin film interference model can be attributed to the multiple

reflections of ray bundles accounted in the GOA framework of the hybrid model, and thinner local oxide thickness. The reflectance predicted by the hybrid model exceeds that of thin film interference model at longer wavelengths (λ>1 μm), where the thicker global oxide thickness in the thin film model induces interference effect to the EM waves.

Similar results can be found in Figure 7-6 (e), where the predictions using both the hybrid and thin film interference models show obvious interference features that are absent in the measurements. Although the oxide appears to have a film-like morphology shown in Figure 7-2 (e), the rugged and slightly discontinuous oxide layer causes a weak interference effect observed in the measured reflectance. The higher value of σ_h, in Table 7-1, supports this observation. Compared to Figure 7-6 (b), the measured reflectance in Figure 7-6 (d) shows a weaker interference effect and the predictions using both thin film interference and hybrid models also underestimate the reflectance compared to the measurements. Figure 7-6 (d) shows that the oxide has a nodular-like, non-uniform structure, so the EM waves interact with the surface in a manner similar to Figure 7-1 (d). Consequently, neither the thin film interference and hybrid models, which assume uniform oxide layer, can replicate the experimental measurements.

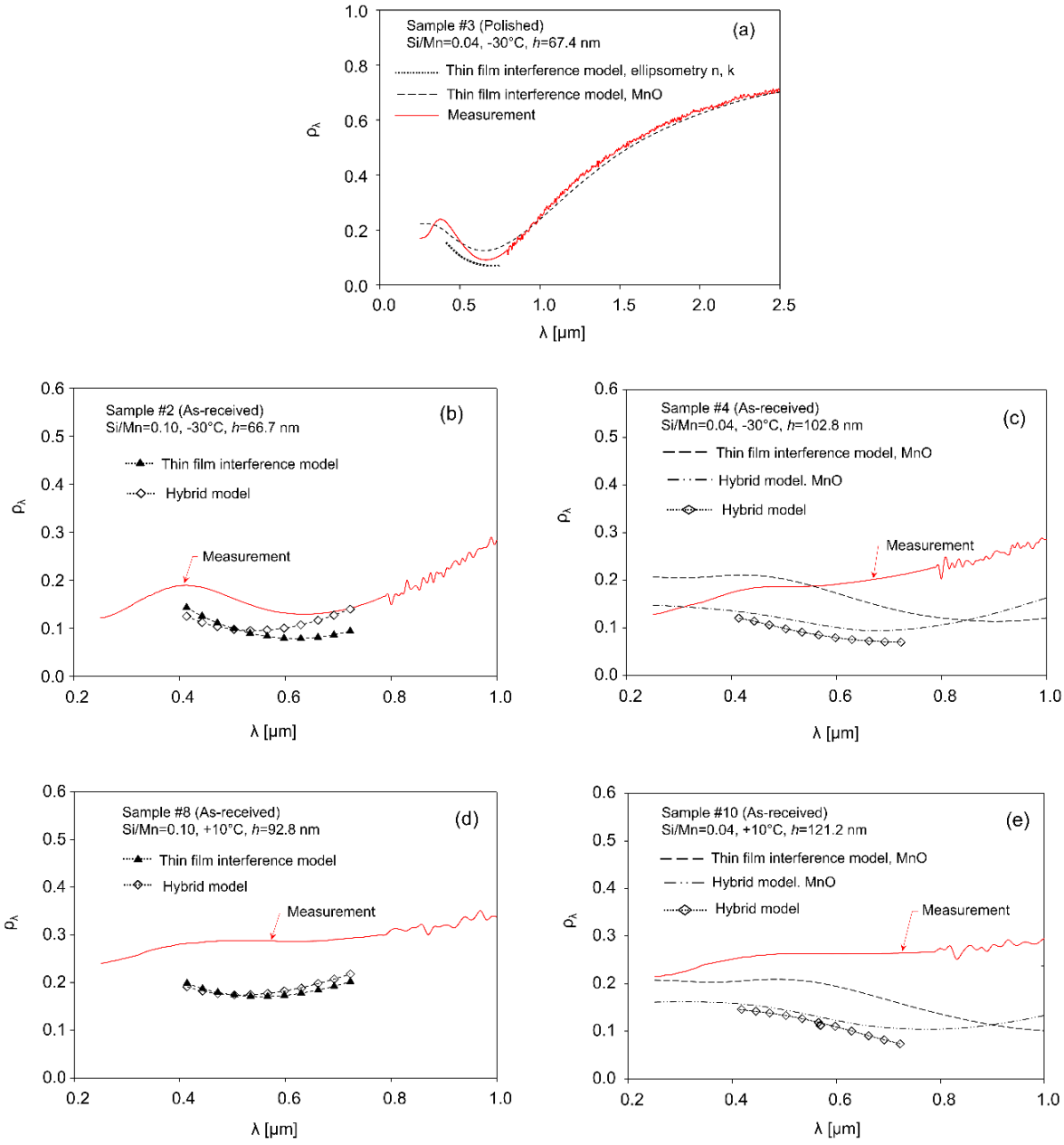

Figure 7-6. Comparisons of measurements and the predictions using thin film interference model, hybrid model, and modified hybrid model for (a) sample #2 (b) sample #4 (c) sample #8 (d) sample #10 and (e) sample #3. Predictions are made with measured surface parameters and measured averaged oxide thickness. Description of the thin film interference model, which assumes a uniform oxide layer deposited on a smooth surface, can be found in Ref. [203]. The refractive indices employed are from those of the samples having a polished surface state. The results for the sample having polished state (sample #3) shown in (e) are retrieved directly from Ref. [203].The refractive indices of MnO are derived from Ref. [193].

7.3.5 Effect of surface roughness parameters on the predictions

Figure 7-7 illustrates how the substrate surface roughness (σ; σ/τ) impacts the hybrid model predictions. The parametric analysis is carried out on sample #4 having measured parameters listed in Table 7-1. The 2-D surfaces were first generated based on profilometry-inferred σ and τ values assuming the surface roughness profile follows Gaussian statistics. The surfaces were incorporated into the hybrid model with derived global oxide thickness. Figure 7-7 (a) shows that increasing σ/τ decreases the predicted reflectance due to more multiple reflections of ray bundles within the rougher surface cavities. Furthermore, it is found that, when σ/τ is fixed, the effect of σ is trivial, as illustrated in Figure 7-7 (b). This result shows that reflectance is dominated by σ/τ, and not σ, which highlights the inadequacy of the root-mean-squared roughness as a surface parameter to predict radiative properties. Regardless of this result, however, no reasonable combination of (σ; σ/τ) exists that can be substituted into the hybrid model to explain the data, highlighting the fact that the hybrid model cannot explain the radiative properties of AHSS alloy annealed in its as-received state.

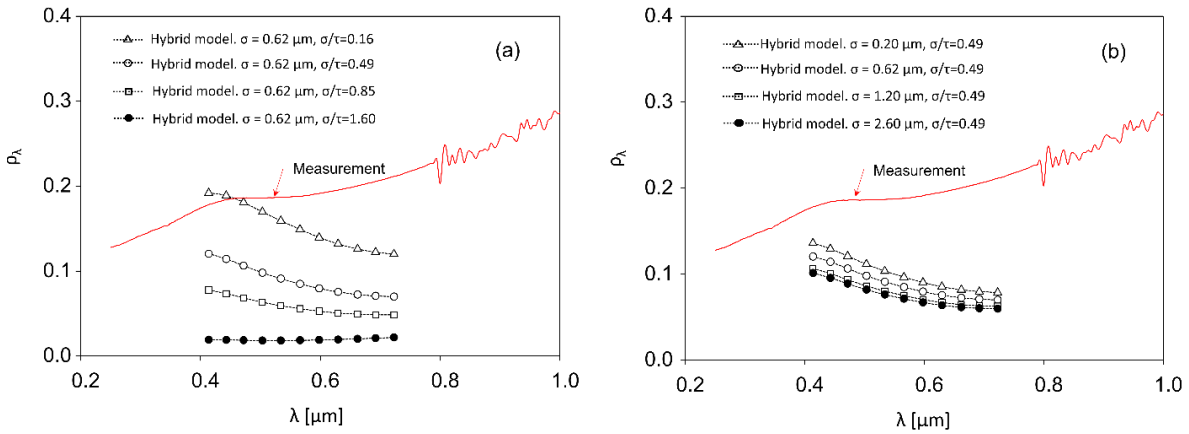

Figure 7-7. Comparisons of predictions using hybrid model through parametric analysis. Effect of (a) surface slope (b) root-mean-square roughness on the reflectance predictions. The analysis is performed on sample #4 having measured parameters μ_h=91.2 nm, σ_h=34.1 nm, σ=0.62 μm, σ/τ=0.49.

7.4 Conclusions

This chapter examines the radiative properties of oxidized AHSS samples having as-received artifacts underlying the thin film interference and hybrid models. In general, both models over-predict the interference effect due to the non-uniformity of the rough oxide layer, causing the reflectance to be under-predicted. The measured reflectances are well connected to the observed oxide morphologies in the SEM images. The results also indicate that the substrate roughness profile has a significant influence on the reflectance, highlighting the importance of accounting for these effects. Regardless the parameters chosen, the current hybrid model cannot replicate the measurements. This is attributed to the fact that the assumption of a uniform oxide thickness does not represent the intrinsic wave interference mechanism underlying the complex oxide and substrate topographies. Based on this, a higher fidelity model, which employs rigorous EM wave propagation theory, is required to solve the radiative properties of samples having non-uniform oxide structure upon a rough metal substrate.

Chapter 8. Conclusions and future work

Variation of spectral emissivity due to the changes of surface topography, subject to the “thin film effect” and “roughness effect”, affects temperature control in the industrial furnace. This is because the heat absorption ability of the steel strip is influenced as the spectral emissivity varies and thus the heating control is affected. In addition, the variation of spectral emissivity also causes errors to the pyrometry measurement. This thesis explores the correlation between the surface states, in terms of roughness and oxidation, and radiative properties of AHSS underlying the EM theories that may be used to improve the heating control and pyrometry measurement in the continuous galvanizing line.

8.1 Summary and key findings

8.1.1 Thin film effect

In the case of homogeneous, uniform oxide film deposits on a smooth metal surface, radiative properties over the wavelengths important to pyrometry are dominated by the wave interference effect due to the parallel, incoherent waves reflected from the top and bottom of the oxide interfaces. The radiative properties of oxidized AHSS, which are a function of the thickness and refractive indices of the oxide film arising from selective oxidation, are correlated to the AHSS alloy composition and annealing atmosphere.

This thesis explores the effect of alloy composition and annealing atmosphere on the selective oxidation and radiative properties of AHSS, as detailed in Chapter 6. Three types of

AHSS alloys having different Si/Mn with polished and as-received pre-annealed states are annealed according to the industrial heating schedule with two sets of annealing dew points, -30ºC and +10 ºC. Refractive indices and thickness of oxide layer are measured using an ellipsometer and FIB/SEM techniques. The oxide composition of each AHSS sample are confirmed using XPS measurement. Thin film interference effects are observed in the spectral reflectances of samples annealed in a polished and as-received surface state, although the effect is more pronounced for the polished samples, since the uniformity of the surface leads to more coherent wave interference effects. Predictions underlying thin film interference theory are made in comparison to the experimental results.

It is found that the alloy composition and annealing dew points have a significant effect on the oxide morphology and radiative properties of AHSS. For low Si/Mn alloys, the oxide appears to be continuous film-like under low dew point. For high Si/Mn alloys however, the surface forms nodular-like oxides regardless of the annealing atmosphere. XPS measurements confirm that Mn-rich oxide (MnO) was primarily formed on those low Si/Mn alloys, while ternary oxides were found on high Si/Mn alloys. The oxide morphology is found to correlate with the measured spectral reflectance over the UV-Vis-NIR spectrum. Telltale interference patterns in the measured reflectance is found on those samples having continuous film-like oxide, which are less pronounced or entirely absent on those having isolated, nodular-like oxide. The reflectance predictions *via* the thin film interference model with ellipsometry-measured refractive indices and FIB/SEM-measured thicknesses are consistent with the measurements, although the thin film interference effects are notably absent from two of the samples having high Si/Mn alloys, which had a nodular as opposed to film-like oxide morphology. These two samples, however, should be

excluded from analysis since the oxides are not thin films as revealed under the SEM and thus the validity of ellipsometry measurements for these two samples are questionable.

Overall, these results indicate that the effect of surface oxidation on radiative properties can be interpreted using the thin film interference model for oxidized AHSS samples having smooth pre-annealed surface state.

8.1.2 Surface roughness effect

Surface roughness also impacts the radiative properties of AHSS. For un-annealed and annealed AHSS samples, following Ham's work [12], it is found that the spectral, directional-hemispherical reflectance can be interpretated using the Davies' model with wavelet-filtered roughness scale, as illustrated in Chapter 4, despite that this methodology should not really work. Samples having different profilometer-measured roughness are first examined to assess the validity of Kirchhoff approximation. Next, the surface profiles of each sample obtained from the optical profilometer are wavelet-filtered with high-pass filtering to derive the "local roughness" that are compared to the optically-derived values. Finally, predictions made using Davies model with filtered roughness values are compared to the measurements. Agreeable estimations are found when the optical roughness parameters are within the Fraunhofer criterion, which determines whether the surface is optically-smooth.

Although this approach seems to work, we cannot explain explicitly why the Davies' specular reflectance model can be used to predict the hemispherical reflectance in terms of the physical aspects. In addition, this approach is unable to predict the reflectance at short wavelength region ($\lambda<2.5$ μm) where the surface becomes optically-rough and multiple reflections may occur.

Consequently, the geometric optics approximation (GOA) is employed in this thesis to deal with the radiative properties of rough AHSS samples. As illustrated in Chapter 5, the reflectance predictions of AHSS having different roughness levels follow the measured trends within the valid domain of GOA, demonstrating the applicability of using GOA to model the spectral emissivity at wavelengths important to pyrometry for as-received AHSS samples. At longer wavelengths, which is out of the GOA valid domain, diffraction models developed based on Kirchhoff approximation are found to be able to capture the radiative properties in both the specular and diffuse reflections. Diffraction effects become more prominent as the wavelength becomes longer. It can be concluded that using GOA and diffraction models can model the radiative properties of un-annealed, rough AHSS samples.

8.1.3 The hybrid effect

When oxides form on a rough surface, as is the case during intercritical annealing of AHSS, both the oxides and roughness effects should be considered when modeling the radiative properties. One existing approach is to combine the GOA and thin film optics by assuming a uniform oxide film deposited on a rough substrate.

This thesis explores the applicability of such hybrid thin film/geometric optics model by comparing the reflectance predictions with the experimental measurements (Chapter 7). Samples oxidized in their as-received (unpolished) state show less interference effect in the measured reflectance compared to those oxidized in a polished state. This could be attributed to the rugged oxide formed on the rough substrate that disrupts the coherent wave structure underlying the thin film interference effect. The measured reflectance of each sample correlates with the oxide

morphology shown in the SEM images. It is found that predictions using the hybrid model or the thin film interference model do not capture the measured trends, highlighting that the hybrid model is unable to model the radiative properties of AHSS samples annealed in their as-received state. This also implies that the assumption of uniform oxide layer made in the hybrid model does not comply to the real scenario of non-uniform oxide layer observed under the SEM images. It is concluded that a more rigorous model which accounts for the complex oxide profiles upon the substrate is required to improve the predictions.

8.2 Future work

8.2.1 Modeling the spectral emissivity variations across the surface underlying GOA

It has been reported by the industrial partner that there exist variations of radiative properties across the AHSS steel strip surfaces prior to heating. This phenomenon is attributed to different surface topography (roughness) at distinct locations across the strips, and will cause issues of heating control and pyrometry temperature measurement. It is thus important to investigate these surface features at different locations and correlate them with the measured radiative properties. Based on the findings of this thesis, using GOA with profilometry-derived surface profiles would be one effective way to address the issue. The proposed methodology is described in the following steps:.

i. First, the radiative properties and the surface profiles of each location of the steel strip (e.g. head, middle, tail) will be obtained using the FTIR spectrometer and profilometer. A laser beam device may be used to quantitatively identify the radiative properties along the coil and the results will be compared to the FTIR measurements. The digitized surface data points from

the AFM/ optical profilometer will be implemented into the GOA algorithm to derive the predicted radiative properties that are compared to the measurements.

ii. The surface statistical data of each location will then be constructed underlying the surface slope parameter (σ/τ), which dominates the GOA predictions. Consequently, the statistical distribution of σ/τ at each location of the coil is known and the surface profiles of each location can be modeled based on this. To reduce the calculation time, the empirical regression curve between the predicted spectral emissivity and σ/τ for AHSS will be developed according to the methodology in Ref. [181].

iii. Finally, the generated spectral emissivity of all locations *via* the regression model will be examined by comparing with the measurements. These findings should be useful to improve the heating control and temperature measurement as the strips enter the furnace.

8.2.2 Improving the reflectance predictions of oxidized AHSS having rough states

As mentioned in Chapter 7, the hybrid model cannot replicate the measurements for AHSS samples annealed in their as-received states. This is attributed to the fact that the assumption of a uniform oxide thickness does not represent the intrinsic wave interference mechanism underlying the complex oxide and substrate topographies. Accordingly, this effect requires a high-fidelity model which rigorously accounts for the EM wave propagation underlying the complex oxide geometry upon the rough substrate. First, since the oxide is not uniformly distributed, the oxide profiles of these samples are to be measured along the surface using the FIB/SEM techniques over a large area to ensure the development of a complete oxide profile model upon the substrate. Secondly, a more rigorous approach such as finite difference time domain (FDTD) will be implemented to solve the EM scattered field and corresponding radiative properties.

Although FDTD serves as a rigorous approach to the EM scattering, it is computationally expensive. Consequently, an alternative approach is needed to address the issue. One effective method is to use an efficient hybrid method which combines the finite-element boundary-integral method (FEM-BIM) with fast multipole method (FMM) [204, 205]. This approach can be used to efficiently solve the electromagnetic scattering characteristics for a double-layered rough surface having incoherent rough profiles. The field interactions between the three media (air/oxide/substrate) are formulated underlying rigorous EM propagation theory. Based on the finite-element boundary-integral method, the fields on the layered rough surface are discretized into segments and a FEM-BIM matrix equation correlating the incident field and the total field can be established. Finally, to speed up the matrix-vector multiplication, the fast multipole method is implemented to efficiently solve the FEM-BIM matrix with reduced computational time. Following the concept of FMM, the segments of each rough surface are divided into small groups based on their position on the *x* axis [206]. Then, the bistatic scattering coefficient (BSC) for the tapered incident wave can be obtained. More details about the approach can be found in Ref. [205].

Overall, this approach accounts for both rigorous EM propagation and computational efficiency in the derivation of the electromagnetic scattering characteristics of complex multi-layered rough surfaces. The following steps are proposed:

i. Both the substrate and the oxide profiles along the lateral direction of each sample are measured within a sufficiently large area *via* the 3D micrograph imaging technique. The complete profile of the rough, oxidized surface can thus be developed.

ii. Secondly, the optical constants of the oxides and substrate, as well the measured profiles are implemented in the FEM-BIM model. The electromagnetic scattering characteristics (bistatic

scattering coefficient, reflectance, etc.) can then be derived efficiently by solving the FEM-BIM matrix via FMM.

8.2.3 Investigation of temperature effect on radiative properties

It is mentioned in Section 4.4 that in addition to the surface state, the effect of temperature on spectral emissivity also needs to be accounted. The Hagen-Rubens relation of Eq. (2.38) can be used to model the temperature effect at long wavelength (λ>5 μm). However, Eq. (2.38) becomes less accurate when the wavelength is below 5 μm. It is suggested in the future work that the temperature effect is to be investigated through in-situ emissivity measurements with controlled atmosphere using the built-up chamber in the lab. The samples will be heated up to different annealing temperature and the variation in emissivity is measured by a spectrometer. It is expected to see how spectral emissivity would vary with temperature for the AHSS samples, and accordingly, empirical models correlating the emissivity and temperature could be developed to account for such effect.

8.2.4 Industrial impact of research

This thesis explores the connection between the surface states and radiative properties of AHSS samples via experiment and electromagnetic wave scattering theory. These findings are beneficial for the industrial partner in terms of the improvement of steel manufacturing *via* better understanding the heating control, and the approach to improve the pyrometry measurement. With respect to the future research project, algorithms correlating the surface variation to the radiative properties of AHSS strips in this thesis can be employed in the analysis of *in-situ* pyrometry measurements and see how much improvement can be achieved. In addition, the correlation

between surface roughness and radiative properties found in this thesis may be used in the analysis of heat absorption across the steel strip to optimize the heating control in the future. It is expected that the temperature control in the industrial furnace of CGL can be improved and thus reduce enormous costs to steel production annually for the local steel manufacturing companies.

References

[1] W.J. Joost, Reducing vehicle weight and improving US energy efficiency using integrated computational materials engineering, *JOM*, 64(9), 2012, 1032-1038.

[2] T.B. Glennan, Strategies for managing vehicle mass throughout the development process and vehicle lifecycle, *SAE Technical Papers*, 2007.

[3] N. Fonstein, Dual-phase steels, in: Automotive steels, *Elsevier*, 2017, 169-216.

[4] B. Ennis, A review of the effects of chemical and phase segregation on the mechanical behaviour of multi-phase steels, 2016. arXiv: 1604.06485.

[5] W.L. Roberts, Hot rolling of steel, *CRC Press*, 1983.

[6] A.A. Gorni, Steel forming and heat treating handbook, 24, 2011.

[7] R. Khondker, A. Mertens, J.R. McDermid, Effect of annealing atmosphere on the galvanizing behavior of a dual-phase steel, *Materials Science and Engineering: A*, 463(1-2), 2007, 157-165.

[8] H. Shirasawa, Y. Tanaka, M. Miyahara, Y. Baba, Japan, Production of formable TS98OMPa grade cold-rolled steel, *Transactions ISIJ*, 26(4), 1986, 310-314.

[9] 2021 American Galvanizers Association (https://galvanizeit.org/).

[10] R.G. Thiessen, E. Bocharova, D. Mattissen, R. Sebald, Temperature measurement deviation during annealing of multiphase steels, *Metallurgical and Materials Transactions B*, 41(4), 2010, 857-863.

[11] T. Larrick, Understanding modern infrared pyrometers for demanding steel mill applications, *Williamson Corporation*, Concord MA, USA, 2016.

[12] S.H. Ham, C. Carteret, J. Angulo, G. Fricout, Relation between emissivity evolution during annealing and selective oxidation of TRIP steel, *Corrosion Science*, 132, 2018, 185-193.

[13] H. Liu, Y. He, S. Swaminathan, M. Rohwerder, L. Li, Effect of dew point on the surface selective oxidation and subsurface microstructure of TRIP-aided steel, *Surface and Coatings Technology*, 206(6), 2011, 1237-1243.

[14] A.E. Morris, G. Geiger, H.A. Fine, Handbook on material and energy balance calculations in material processing, *John Wiley & Sons*, 2012.

[15] M.C. Rey, D.P. Kramer, W.R. Henderson, L. Abney, Dew point/temperature curves for selected metal/metal oxide systems in hydrogen atmospheres, *Monsanto Research Corp.*, Miamisburg, OH, 1984.

[16] G.S. Mousavi, J. McDermid, Selective oxidation of a C-2Mn-1.3 Si (Wt Pct) advanced high-strength steel during continuous galvanizing heat treatments, *Metallurgical and Materials Transactions A*, 49(11), 2018, 5546-5560.

[17] G.S. Mousavi, B. Langelier, J. McDermid, Effect of Sn addition, process atmosphere pO_2, and annealing time on the selective oxidation of a C-2Mn-1.7 Si (Wt Pct) advanced high-strength steel during continuous galvanizing, *Metallurgical and Materials Transactions A*, 50(6), 2019, 2898-2911.

[18] E. Bellhouse, J. McDermid, Analysis of the Fe–Zn interface of galvanized high Al–low Si TRIP steels, *Materials Science and Engineering: A*, 491(1-2), 2008, 39-46.

[19] E. Bellhouse, J. McDermid, Effect of oxygen partial pressure during annealing on the selective oxidation and galvanizing of a 1.5% Al TRIP-Assisted steel, in: Proc. Materials Science and Technology Conference and Exhibition, 2009, 913-924.

[20] E. Bellhouse, J. McDermid, Selective oxidation and reactive wetting of 1.0 pct Si-0.5 pct Al and 1.5 pct Si TRIP-Assisted steels, *Metallurgical and Materials Transactions A*, 41(6), 2010, 1539-1553.

[21] E.M. Bellhouse, A. Mertens, J.R. McDermid, Development of the surface structure of TRIP steels prior to hot-dip galvanizing, *Materials Science and Engineering: A*, 463(1-2), 2007, 147-156.

[22] Y.F. Gong, H.S. Kim, B.C.D. Cooman, Internal oxidation during intercritical annealing of CMnSi TRIP steel, *ISIJ international*, 49(4), 2009, 557-563.

[23] L. Cho, S.J. Lee, M.S. Kim, Y.H. Kim, B.C. De Cooman, Influence of gas atmosphere dew point on the selective oxidation and the reactive wetting during hot dip galvanizing of CMnSi TRIP steel, *Metallurgical and Materials Transactions A*, 44(1), 2013, 362-371.

[24] L. Cho, G.S. Jung, B.C. De Cooman, On the transition of internal to external selective oxidation on CMnSi TRIP steel, *Metallurgical and Materials Transactions A*, 45(11), 2014, 5158-5172.

[25] M. Pourmajidian, B. Langelier, J.R. McDermid, Effect of Process Atmosphere Dew Point and Tin Addition on Oxide Morphology and Growth for a Medium-Mn Third Generation Advanced Steel During Intercritical Annealing, *Metallurgical and Materials Transactions A*, 49(11), 2018, 5561-5573.

[26] Y. Suzuki, T. Yamashita, Y. Sugimoto, S. Fujita, S. Yamaguchi, Thermodynamic analysis of selective oxidation behavior of Si and Mn-added steel during recrystallization annealing, *ISIJ international*, 49(4), 2009, 564-573.

[27] M. Pourmajidian, J.R. McDermid, Selective oxidation of a 0.1 C-6Mn-2Si third generation advanced high-strength steel during dew-point controlled annealing, *Metallurgical and Materials Transactions A*, 49(5), 2018, 1795-1808.

[28] S. Alibeigi, R. Kavitha, R. Meguerian, J. McDermid, Reactive wetting of high Mn steels during continuous hot-dip galvanizing, *Acta Materialia*, 59(9), 2011, 3537-3549.

[29] J. Oh, L. Cho, M. Kim, K. Kang, B.C. De Cooman, The effect of Bi on the selective oxide formation on CMnSi TRIP steel, *Metallurgical and Materials Transactions A*, 47(11), 2016, 5474-5486.

[30] Z. Silvayeh, B. Götzinger, W. Karner, M. Hartmann, C. Sommitsch, Calculation of the intermetallic layer thickness in cold metal transfer welding of aluminum to steel, *Materials*, 12(1), 2019, 35.

[31] Z.Q. Tan, The effect of galvanized steel corrosion on the integrity of concrete, *PhD Thesis*, University of Waterloo, 2007.

[32] Performance of Hot-Dip Galvanized Steel Products, *American Galvanizers Association*, 2010. www.galvanizeit.org.

[33] J.R. Howell, M.P. Mengüç, K. Daun, R. Siegel, Thermal radiation heat transfer, CRC press, 2020.

[34] B.K. Tsai, R. Shoemaker, D. DeWitt, B. Cowans, Z. Dardas, W. Delgass, G. Dail, Dual-wavelength radiation thermometry: emissivity compensation algorithms, *International Journal of Thermophysics*, 11(1), 1990, 269-281.

[35] B. Tsai, D. DeWitt, G. Dail, Application of dual-wavelength radiation thermometry to the aluminum industry, *Measurement*, 11(3), 1993, 211-221.

[36] L. Zentner, D. DeWitt, D. White, Temperature measurements during the galvanneal process, *Thermochimica Acta*, 218, 1993, 317-328.

[37] M. Pellerin, Multispectral radiation thermometry for industrial applications, *PhD thesis*, Purdue University, 1999.

[38] G. Dail, M. Pellerin, D. DeWitt, Multispectral Radiation Method for Temperature Measurement of Aluminum Alloys, *Proceedings of International Aluminum Extrusion Technology Seminar*, 1993, 555-560.

[39] C.D. Wen, Investigation of steel emissivity behaviors: Examination of Multispectral Radiation Thermometry (MRT) emissivity models, *International Journal of Heat and Mass Transfer*, 53(9-10), 2010, 2035-2043.

[40] C.D. Wen, I. Mudawar, Mathematical determination of emissivity and surface temperature of aluminum alloys using multispectral radiation thermometry, *International Communications in Heat and Mass Transfer*, 33(9), 2006, 1063-1070.

[41] C.D. Wen, I. Mudawar, Experimental investigation of emissivity of aluminum alloys and temperature determination using multispectral radiation thermometry (MRT) algorithms, *Journal of Materials Engineering and Performance*, 11(5), 2002, 551-562.

[42] C.D. Wen, Experimental investigation of emissivity of aluminum alloys and application of multispectral radiation thermometry, *Applied Thermal Engineering*, 31(14-15), 2011, 2414-2421.

[43] C.D. Wen, Emissivity characteristics of aluminum alloy surfaces and assessment of multispectral radiation thermometry (MRT) emissivity models, *PhD thesis*, Purdue University, 2005.

[44] P. Beckmann, A. Spizzichino, *The scattering of electromagnetic waves from rough surfaces*, Pergamon Press, 1963.

[45] S.O. Rice, Reflection of electromagnetic waves from slightly rough surfaces, *Communications on Pure and Applied Mathematics*, 4(2-3), 1951, 351-378.

[46] H. Davies, The reflection of electromagnetic waves from a rough surface, *Proceedings of the IEE-Part IV: Institution Monographs*, 101(7), 1954, 209-214.

[47] T. Iuchi, T. Furukawa, S. Wada, Emissivity modeling of metals during the growth of oxide film and comparison of the model with experimental results, *Applied Optics*, 42(13), 2003, 2317-2326.

[48] C.D. Wen, I. Mudawar, Modeling the effects of surface roughness on the emissivity of aluminum alloys, *International Journal of Heat and Mass Transfer*, 49(23-24), 2006, 4279-4289.

[49] B. Bhushan, *Surface roughness analysis and measurement techniques*, Modern Tribology Handbook, CRC press, 2000, 74-144.

[50] O.S. Heavens, *Optical properties of thin solid films*, Courier Corporation, 1991.

[51] L. del Campo, R.B. Pérez-Sáez, M.J. Tello, Iron oxidation kinetics study by using infrared spectral emissivity measurements below 570°C, *Corrosion Science*, 50(1), 2008, 194-199.

[52] M.Q. Brewster, *Thermal radiative transfer and properties*, John Wiley & Sons, 1992.

[53] T. Makino, H. Wakabayashi, Thermal radiation spectroscopy diagnosis for temperature and microstructure of surfaces, *JSME International Journal Series B*, 46(4), 2003, 500-509.

[54] M. Kobayashi, A. Ono, M. Otsuki, H. Sakate, F. Sakuma, A database of normal spectral emissivities of metals at high temperatures, *International Journal of Thermophysics*, 20(1), 1999, 299-308.

[55] M. Kobayashi, M. Otsuki, H. Sakate, F. Sakuma, A. Ono, System for measuring the spectral distribution of normal emissivity of metals with direct current heating, *International Journal of Thermophysics*, 20(1), 1999, 289-298.

[56] G. Neuer, F. Güntert, Insitu measurements of layer thickness during oxidation of titanium, *Thermochimica Acta*, 133, 1988, 299-304.

[57] L. Rakotomanana, Connecting mesoscopic and macroscopic scale lengths for ultrasonic wave characterization of micro-cracked material, *Math. Mech. Solids*, 2002.

[58] R. Birkebak, E. Eckert, Effects of roughness of metal surfaces on angular distribution of monochromatic reflected radiation, *Journal of Heat Transfer*, 87(1), 1965, 85-93.

[59] K.E. Torrance, E.M. Sparrow, Off-specular peaks in the directional distribution of reflected thermal radiation, *Journal of Heat Transfer*, 88(2), 1966, 223-230.

[60] A.F. Gorton, Reflection from, and transmission through, rough surfaces, *Physical Review*, 7(1), 1916, 66.

[61] T. Chinmayanandam, On the specular reflection from rough surfaces, *Physical Review*, 13(2), 1919, 96.

[62] J.W.S.B. Rayleigh, *The theory of sound*, Macmillan, 1896.

[63] J. Ogilvy, Wave scattering from rough surfaces, *Reports on Progress in Physics*, 50(12), 1987, 1553.

[64] A. McGinn, J. Sykes, Microwave scattering from natural targets, *UKAEA Atomic Energy Research Establishment Engineering Sciences Division*, 1980.

[65] C.A. Guérin, M. Holschneider, M. Saillard, *Electromagnetic scattering from multi-scale rough surfaces, Waves in Random Media*, 7(3), 1997, 331-349.

[66] M. Fiaz, M. Ashraf, Scattering from PEMC rough surface using small perturbation method, *Waves in Random and Complex Media*, 27(1), 2016, 15-27.

[67] M. Saillard, D. Maystre, Scattering from metallic and dielectric rough surfaces, *JOSA A*, 7(6), 1990, 982-990.

[68] M. Nieto-Vesperinas, N. García, A detailed study of the scattering of scalar waves from random rough surfaces, *Optica Acta: International Journal of Optics*, 28(12), 1981, 1651-1672.

[69] M. Saillard, D. Maystre, Scattering from random rough surfaces: a beam simulation method, *Journal of Optics*, 19(4), 1988, 173.

[70] A. Ishimaru, J.S. Chen, Scattering from very rough metallic and dielectric surfaces: a theory based on the modified Kirchhoff approximation, *Waves in Random Media*, 1(1), 1991, 21-34.

[71] F. Bass, I. Fuks, Wave Scattering from Statistically Rough Surfaces (International Series in Natural Philosophy vol. 93), *Oxford: Pergamon*, 1979.

[72] N. Garcia, V. Celli, M. Nieto-Vesperinas, Exact multiple scattering of waves from random rough surfaces, *Optics Communications*, 30(3), 1979, 279-281.

[73] M. Nieto-Vesperinas, N. García, Non-circular gaussian speckle contrast in the exact theory of multiple scattering of waves from random rough surfaces, *Optics Communications*, 35(1), 1980, 25-30.

[74] J. Shen, A.A. Maradudin, Multiple scattering of waves from random rough surfaces, *Physical Review B*, 22(9), 1980, 4234.

[75] D. Maystre, M. Saillard, Rigorous solution of problems of scattering by large size objects, *Elsevier*, New York, 1989.

[76] M. Nieto-Vesperinas, J. Soto-Crespo, Monte Carlo simulations for scattering of electromagnetic waves from perfectly conductive random rough surfaces, *Optics letters*, 12(12), 1987, 979-981.

[77] J. Soto-Crespo, M. Nieto-Vesperinas, Electromagnetic scattering from very rough random surfaces and deep reflection gratings, *JOSA A*, 6(3), 1989, 367-384.

[78] A.R. McGurn, A.A. Maradudin, V. Celli, Localization effects in the scattering of light from a randomly rough grating, *Physical Review B*, 31(8), 1985, 4866.

[79] D. Maystre, Rigorous theory of light scattering from rough surfaces, *Journal of Optics*, 15(1), 1984, 43.

[80] J. Soto-Crespo, M. Nieto-Vesperinas, A. Friberg, Scattering from slightly rough random surfaces: a detailed study on the validity of the small perturbation method, *JOSA A*, 7(7), 1990, 1185-1201.

[81] L. Brekhovskikh, Diffraction of electromagnetic waves by a 'rough surface', in: Dokl. Akad. Nauk SSSR, 1951, O951b.

[82] M. Nieto-Vesperinas, J. Sanchez-Gil, Light scattering from a random rough interface with total internal reflection, *JOSA A*, 9(3), 1992, 424-436.

[83] V. Celli, A.A. Maradudin, A. Marvin, A.R. McGurn, Some aspects of light scattering from a randomly rough metal surface, *JOSA A*, 2(12) (1985) 2225-2239.

[84] A. Maradudin, T. Michel, A. McGurn, E. Méndez, Enhanced backscattering of light from a random grating, *Annals of Physics*, 203(2), 1990, 255-307.

[85] A. Sants, Enhanced backscattering and transmission of light from random surfaces on semi-infinite substrates and thin films, *Waves in Random Media*, 1(3), 1991, S129-S141.

[86] P. Phu, A. Ishimaru, Y. Kuga, Controlled millimeter-wave experiments and numerical simulations on the enhanced backscattering from one-dimensional very rough surfaces, *Radio Science*, 28(04), 1993, 533-548.

[87] J. Sanchez-Gil, M. Nieto-Vesperinas, Light scattering from random rough dielectric surfaces, *JOSA A*, 8(8), 1991, 1270-1286.

[88] R. Dimenna, R. Buckius, Electromagnetic theory predictions of the directional scattering from triangular surfaces, *Journal of Heat Transfer*, 116(3), 1994, 639-645.

[89] Z.-H. Gu, J.Q. Lu, A.A. Maradudin, A. Martinez, Enhanced backscattering from a free-standing dielectric film, *Applied Optics*, 34(18), 1995, 3529-3534.

[90] C. Macaskill, B.J. Kachoyan, Iterative approach for the numerical simulation of scattering from one-and two-dimensional rough surfaces, *Applied Optics*, 32(15), 1993, 2839-2847.

[91] P. Tran, A. Maradudin, The scattering of electromagnetic waves from a randomly rough 2D metallic surface, *JOSA A*, 11(5), 1994, 1686-1689.

[92] A. Voronovich, Non-local small-slope approximation for wave scattering from rough surfaces, *Waves in Random Media*, 6(2), 1996, 151-168.

[93] A. Voronovich, Small-slope approximation for electromagnetic wave scattering at a rough interface of two dielectric half-spaces, *Waves in random media*, 4(3), 1994, 337-368.

[94] K. Zaki, A. Neureuther, Scattering from a perfectly conducting surface with a sinusoidal height profile: TE polarization, *IEEE Transactions on Antennas and Propagation*, 19(2), 1971, 208-214.

[95] D. Maystre, O.M. Mendez, A. Roger, A new electromagnetic theory for scattering from shallow rough surfaces, *Optica Acta: International Journal of Optics*, 30(12), 1983, 1707-1723.

[96] D. Maystre, M. Saillard, Enhanced backscattering and blazing effect from gratings, quasi-gratings and randomly rough surfaces, *Waves in Random Media*, 4(4), 1994, 167-402.

[97] L. Tsang, C.H. Chan, K. Pak, Backscattering enhancement of a two-dimensional random rough surface (three-dimensional scattering) based on Monte Carlo simulations, *JOSA A*, 11(2), 1994, 711-715.

[98] J.T. Johnson, L. Tsang, R.T. Shin, K. Pak, C.H. Chan, A. Ishimaru, Y. Kuga, Backscattering enhancement of electromagnetic waves from two-dimensional perfectly conducting random rough surfaces: A comparison of Monte Carlo simulations with experimental data, *IEEE Transactions on Antennas and Propagation*, 44(5), 1996, 748.

[99] C.A. Guerin, M. Holschneider, Scattering on fractal measures, *Journal of Physics A: Mathematical and General*, 29(23), 1996, 7651.

[100] R. Axline, A. Fung, Numerical computation of scattering from a perfectly conducting random surface, *IEEE Transactions on Antennas and Propagation*, 26(3), 1978, 482-488.

[101] S.T. McDaniel, A. D. Gorman, An examination of the composite-roughness scattering model, *The Journal of the Acoustical Society of America*, 73(5), 1983, 1476-1486.

[102] A. McGurn, A. Maradudin, An analogue of enhanced backscattering in the transmission of light through a thin film with a randomly rough surface, *Optics Communications*, 72(5), 1989, 279-285.

[103] R.A. Dimenna, R.O. Buckius, Microgeometrical contour contributions to surface scattering, *Therm. Sci. Eng.*, *2*, 1994, 166-171.

[104] H. Chan, A. Fung, A numerical study of the Kirchhoff approximation in horizontally polarized backscattering from a random surface, *Radio Science*, 13(5), 1978, 811-818.

[105] L. Tsang, C.H. Chan, K. Pak, H. Sangani, A. Ishimaru, P. Phu, Monte Carlo simulations of large-scale composite random rough-surface scattering based on the banded-matrix iterative approach, *JOSA A*, 11(2), 1994, 691-696.

[106] K. Pak, L. Tsang, C.H. Chan, J. Johnson, Backscattering enhancement of electromagnetic waves from two-dimensional perfectly conducting random rough surfaces based on Monte Carlo simulations, *JOSA A*, 12(11), 1995, 2491-2499.

[107] A. Madrazo, M. Nieto-Vesperinas, Scattering of electromagnetic waves from a cylinder in front of a conducting plane, *JOSA A*, 12(6), 1995, 1298-1309.

[108] P. Tran, A. Maradudin, Scattering of a scalar beam from a two-dimensional randomly rough hard wall: enhanced backscattering, *Physical Review B*, 45(7), 1992, 3936.

[109] S. Agababov, Effect of the roughness of the surface of a solid body on its radiation properties and methods for their experimental determination(Solid body surface roughness influence on radiative properties, deriving expressions relating radiative properties to surface roughness parameters), *High Temperature*, 6, 1968, 76-85.

[110] A.G. Voronovich, Wave scattering from rough surfaces, *Springer Science & Business Media*, 2013.

[111] E. Harper, F. Labianca, Scattering of sound from a point source by a rough surface progressing over an isovelocity ocean, *The Journal of the Acoustical Society of America*, 58(2), 1975, 349-364.

[112] E.I. Thorsos, The validity of the Kirchhoff approximation for rough surface scattering using a Gaussian roughness spectrum, *The Journal of the Acoustical Society of America*, 83(1), 1988, 78-92.

[113] J.F. McDonald, R.C. Spindel, Implications of Fresnel Corrections in a Non-Gaussian Surface Scatter Channel, *The Journal of the Acoustical Society of America*, 50(3A), 1971, 746-757.

[114] J. McDonald, P. Schultheiss, Asymptotic frequency spread in surface− scatter channels at large Rayleigh numbers, *The Journal of the Acoustical Society of America*, 57(1), 1975, 160-164.

[115] A. Houchens, R. Hering, Bidirectional reflectance of rough metal surfaces, *Progress in Aeronautics and Astronautics*, 20, 1967, 65-90.

[116] K. Tang, R.A. Dimenna, R.O. Buckius, , Regions of validity of the geometric optics approximation for angular scattering from very rough surfaces, *International Journal of Heat and Mass Transfer*, 40(1), 1997, 49-59.

[117] Y.M. Govaerts, M.M. Verstraete, Raytran: A Monte Carlo ray-tracing model to compute light scattering in three-dimensional heterogeneous media, *IEEE Transactions on geoscience and remote sensing*, 36(2), 1998, 493-505.

[118] C. Argento, D. Bouvard, A ray tracing method for evaluating the radiative heat transfer in porous media, *International Journal of Heat and Mass Transfer*, 39(15), 1996, 3175-3180.

[119] B. Rousseau, H. Gomart, D.D.S. Meneses, P. Echegut, M. Rieu, R. Dugas, P. Lenormand, F. Ansart, Modelling of the radiative properties of an opaque porous ceramic layer, *Journal of electroceramics*, 27(2), 2011, 89-92.

[120] R. Coquard, B. Rousseau, P. Echegut, D. Baillis, H. Gomart, E. Iacona, Investigations of the radiative properties of Al–NiP foams using tomographic images and stereoscopic micrographs, *International Journal of Heat and Mass Transfer*, 55(5-6), 2012, 1606-1619.

[121] Q. Zhu, Z. Zhang, Anisotropic slope distribution and bidirectional reflectance of a rough silicon surface, *Journal of heat transfer*, 126(6), 2004, 985-993.

[122] K. Fu, P.-f. Hsu, Modeling the radiative properties of microscale random roughness surfaces, *Journal of Heat Transfer*, 129(1), 2007, 71-78.

[123] K. Tang, R.O. Buckius, The geometric optics approximation for reflection from two-dimensional random rough surfaces, *International Journal of Heat and Mass Transfer*, 41(13), 1998, 2037-2047.

[124] D. Hensler, Light scattering from fused polycrystalline aluminum oxide surfaces, *Applied Optics*, 11(11), 1972, 2522-2528.

[125] H.E. Bennett, Scattering characteristics of optical materials, *Optical Engineering*, 17(5), 1978, 175480.

[126] H. Bennett, J. Porteus, Relation between surface roughness and specular reflectance at normal incidence, *JOSA*, 51(2), 1961, 123-129.

[127] T.J. Love, R.E. Francis, Experimental Determination of Reflectance Function for Type 302 Stainless Steel, *Progress in Astronautics and Aeronautics*, 20, 1967, 115-135.

[128] R. Birkebak, Optical and mechanical RMS surface roughness comparison, *Applied Optics*, 10(8), 1971, 1970-1970.

[129] C. Depew, R.J.A.O. Weir, Surface roughness determination by the measurement of reflectance, *Applied Optics*, 10(4), 1971, 969-970.

[130] S. Agababov, Effect of secondary roughness on the emissive properties of solid bodies, *Teplofizika Vysokikh Temperatur*, 8(1), 1970, 220-222.

[131] S. Agababov, Effect of the roughness factor on radiation properties of solids (experimental check), *Teplofizika Vysokikh Temperatur*, 8(4), 1970, 770-773.

[132] S. Agababov, Effect of roughness factor on the radiation properties of a solid body with random roughness, *Teplofizika Vysokikh Temperature*, 13(2), 1975, 314-317.

[133] B.B. Mandelbrot, *The fractal geometry of nature*, WH freeman New York, 1983.

[134] D.L. Jordan, R.C. Hollins, E. Jakeman, Measurement and characterization of multiscale surfaces, *Wear*, 109(1-4), 1986, 127-134.

[135] A. Majumdar, C. Tien, Fractal characterization and simulation of rough surfaces, *Wear*, 136(2), 1990, 313-327.

[136] A. Majumdar, B. Bhushan, Role of fractal geometry in roughness characterization and contact mechanics of surfaces, *Journal of Tribology*, 112(2), 1990, 205-216.

[137] S. Ganti, B. Bhushan, Generalized fractal analysis and its applications to engineering surfaces, *Wear*, 180(1-2), 1995, 17-34.

[138] M.V. Berry, Z. Lewis, J.F. Nye, On the Weierstrass-Mandelbrot fractal function, *Proceedings of the Royal Society of London. A. Mathematical and Physical Sciences*, 370(1743), 1980, 459-484.

[139] M. Berry, Diffractals, *Journal of Physics A: Mathematical and General*, 12(6), 1979, 781.

[140] M. Berry, T. Blackwell, Diffractal echoes, *Journal of Physics A: Mathematical and General*, 14(11), 1981, 3101.

[141] W. Gordon, Far-field approximations to the Kirchoff-Helmholtz representations of scattered fields, *IEEE Transactions on Antennas and Propagation*, 23(4), 1975, 590-592.

[142] K. Reuther, M. Rettenmayr, A comparison of methods for the calculation of interface curvature in two-dimensional cellular automata solidification models, *Computational Materials Science*, 166, 2019, 143-149.

[143] K. Tang, R.O. Buckius, A statistical model of wave scattering from random rough surfaces, *International Journal of Heat and Mass Transfer*, 44(21), 2001, 4059-4073.

[144] N. Pinel, C. Boulier, *Electromagnetic wave scattering from random rough surfaces: Asymptotic models*, John Wiley & Sons, 2013.

[145] A. Soubret, Diffusion des ondes électromagnétiques par des milieux et des surfaces aléatoires: étude des effets cohérents dans le champ diffusé, *Aix-Marseille 2*, 2001.

[146] J.A. Ogilvy, Wave scattering from rough surfaces, *Reports on Progress in Physics*, 50(12), 1987, 1553.

[147] E. Thorsos, The validity of the Kirchhoff approximation for rough surface scattering using a Gaussian roughness spectrum, *The Journal of the Acoustical Society of America*, 83(1), 1988, 78.

[148] A. Houchens, R. Hering, Bidirectional reflectance of rough metal surfaces, *Thermophysics of spacecraft and planetary bodies*, 1967.

[149] D. Bergström, J. Powell, A. Kaplan, The absorption of light by rough metal surfaces—A three-dimensional ray-tracing analysis, *Journal of Applied Physics*, 103(10), 2008, 103515.

[150] L. Tsang, J. Kong, Energy conservation for reflectivity and transmissivity at a very rough surface, *Journal of Applied Physics*, 51(1), 1980, 673-680.

[151] P. Beckmann, A. Spizzichino. *The Scattering of Electromagnetic Waves from Rough Surfaces*, Pergamon Press, Oxford, 1963.

[152] C.D. Wen, I. Mudawar, Modeling the effects of surface roughness on the emissivity of aluminum alloys, *International Journal of Heat and Mass Transfer*, 49(23-24), 2006, 4279-4289.

[153] A. Majumdar, C.L. Tien, Reflection of radiation from rough fractal surfaces, *Radiation Heat Transfer: Fundamentals and Applications, ASME*, 1990, 205-216.

[154] Q. Somveille, P. Mosser, M. Brochu, K.J. Daun, Effect of Oxidation on Emissivity for DP780 and DP980 Steels, *11th International Conference on Zinc and Zinc Alloy Coated Steel Sheet* Tokyo, Japan, 2017.

[155] S. Ham, M. Ferté, G. Fricout, L. Depalo, C. Carteret, In-situ spectral emissivity measurement of alloy steels during annealing in controlled atmosphere, *13th Quantitative Infrared Thermography Conference*, Gdańsk, Poland, 2016.

[156] S.H. Ham, C. Carteret, J. Angulo, G. Fricout, Relation between emissivity evolution during annealing and selective oxidation of TRIP steel, *Corrosion Science*, 2017.

[157] E.M. Bellhouse, A. Mertens, J.R. McDermid, Development of the surface structure of TRIP steels prior to hot-dip galvanizing, *Materials Science and Engineering: A*, 463(1-2), 2007, 147-156.

[158] K. Lin, K.J. Daun, Impact of roughness length scale on spectral emissivity during intercritical annealing of advanced high strength steels, *Material and Science Technology 2018*, Columbus, Ohio, 2018.

[159] Standard ASTM A1079-17, 2017.

[160] J. Davis, K. Mills, S. Lampman, Metals handbook. Vol. 1: properties and selection: irons, steels, and high-performance alloys, *ASM International*, Ohio 44073, USA, 1990.

[161] A. Graps, An introduction to wavelets, *IEEE computational science and engineering*, 2(2), 1995, 50-61.

[162] Y. Meyer, *Wavelets and applications*, Springer-Verlag, 1992.

[163] F. Ticconi, L. Pulvirenti, N. Pierdicca, Models for scattering from rough surfaces, *Electromagnetic Waves*, 2011.

[164] K.E. Torrance, E.M. Sparrow, Theory for off-specular reflection from roughened surfaces, *JOSA*, 57(9), 1967, 1105-1114.

[165] W.M. Haynes, *CRC handbook of chemistry and physics*, CRC press, 2014.

[166] K. Lin, K. Daun, Interpreting the spectral reflectance of advanced high strength steels using the Davies' model, *Journal of Quantitative Spectroscopy and Radiative Transfer*, 242, 2020, 106796.

[167] R.A. Dimenna, R.O. Buckius, Quantifying specular approximations for angular scattering from perfectly conducting random rough surfaces, *Journal of Thermophysics and Heat Transfer*, 8(3), 1994, 393-399.

[168] Q. Zhu, Z. Zhang, Anisotropic slope distribution and bidirectional reflectance of a rough silicon surface, *J. Heat Transfer*, 126(6), 2004, 985-993.

[169] K. Tang, R.A. Dimenna, R.O. Buckius, Regions of validity of the geometric optics approximation for angular scattering from very rough surfaces, *International Journal of Heat and Mass Transfer*, 40(1), 1996, 49-59.

[170] N. Bruce, Scattering of light from surfaces with one-dimensional structure calculated by the ray-tracing method, *JOSA A*, 14(8), 1997, 1850-1858.

[171] K. Tang, Y. Yang, R.O. Buckius, Theory and experiments on scattering from rough interfaces, *Annual Review of Heat Transfer*, 10, 1999, 101-140.

[172] K. Fu, P.F. Hsu, New regime map of the geometric optics approximation for scattering from random rough surfaces, *Journal of Quantitative Spectroscopy & Radiative Transfer*, 109, 2008, 180-188.

[173] D. Bergström, J. Powell, A. Kaplan, A ray-tracing analysis of the absorption of light by smooth and rough metal surfaces, *Journal of applied physics*, 101(11), 2007, 113504.

[174] K. Tang, R.O. Buckius, The geometric optics approximation for reflection from two-dimensional random rough surfaces, *International Journal of Heat and Mass Transfer*, 41(13), 1998, 2037-2047.

[175] H. Parviainen, K. Muinonen, Bidirectional reflectance of rough particulate media: ray-tracing solution, *Journal of Quantitative Spectroscopy and Radiative Transfer*, 110(14-16), 2009, 1418-1440.

[176] B. Zhang, C. Zhao, Geometric optics approximation with considering interference for reflection from random rough surface, *Journal of Thermophysics and Heat Transfer*, 27(3), 2013, 458-464.

[177] Y. Sekiguchi, H. Kaneko, Simple ray-tracing model for a rough surface including multiple scattering effects, *Applied Optics*, 56(1), 2017, 35-45.

[178] J.L. King, H. Jo, S.K. Loyalka, R.V. Tompson, K. Sridharan, Computation of total hemispherical emissivty from directional spectral models, *International Journal of Heat and Mass Transfer*, 109, 2017, 894-906.

[179] H. Jo, J.L. King, K. Blomstrand, K. Sridharan, Spectral emissivity of oxidized and roughened metal surfaces, *International Journal of Heat and Mass Transfer*, 115, 2017, 1065-1071.

[180] T. Warren, N. Bowles, K. Donaldson Hanna, J. Bandfield, Modeling the angular dependence of emissivity of randomly rough surfaces, *Journal of Geophysical Research: Planets*, 124(2), 2019, 585-601.

[181] H.J. Lee, Simple Regression Model for Estimating Reflectance Reduction due to Random Surface Roughness, *International Journal of Thermophysics*, 40(6), 2019, 1-12.

[182] Standard ASTM A1079-17, 2017.

[183] H. Stanley, T. Kato, An FFT-based method for rough surface contact, *Journal of Tribology-transactions of The Asme*, 1997.

[184] P. Johnson, R. Christy, Optical constants of transition metals: Ti, V, Cr, Mn, Fe, Co, Ni, and Pd, *Physical review B*, 9(12), 1974, 5056.

[185] M.A. Ordal, R.J. Bell, R.W. Alexander, L.A. Newquist, M.R. Querry, Optical properties of Al, Fe, Ti, Ta, W, and Mo at submillimeter wavelengths, *Applied optics*, 27(6), 1988, 1203-1209.

[186] V.U. Zavorotny, A.G. Voronovich, Comparison of geometric optics and diffraction effects in radar scattering from steep and breaking waves, *2007 IEEE International Geoscience and Remote Sensing Symposium*, 2007, 1350-1353.

[187] F.K. Suleiman, K. Lin, K.J. Daun, Development of a multivariate spectral emissivity model for an advanced high strength steel alloy through factorial design-of-experiments, *Journal of Quantitative Spectroscopy and Radiative Transfer*, 271, 2021, 107693.

[188] L. del Campo, R.B. Pérez-Sáez, X. Esquisabel, I. Fernández, M.J. Tello, New experimental device for infrared spectral directional emissivity measurements in a controlled environment, *Review of Scientific Instruments*, 77(11), 2006, 113111.

[189] K. Lin, F.K. Suleiman, K.J. Daun, Interpreting the radiative properties of advanced high strength steel using the geometric optics ray-tracing approximation, *International Journal of Heat and Mass Transfer*, 176, 2021, 121429.

[190] R. Brannon, R.J. Goldstein, Emittance of oxide layers on a metal substrate, *J. Heat Transfer*, 92(2), 1970, 257-263.

[191] L. Del Campo, R.B. Perez-Saez, M.J. Tello, Iron oxidation kinetics study by using infrared spectral emissivity measurements below 570°C, *Corrosion Science*, 50(1), 2008, 194-199.

[192] J. King, H. Jo, R. Tirawat, K. Blomstrand, K. Sridharan, Effects of surface roughness, oxidation, and temperature on the emissivity of reactor pressure vessel alloys, *Nuclear Technology*, 200(1), 2017, 1-14.

[193] J. Hugel, C. Carabatos, Band structure and optical properties of MnO, *Solid State Communications*, 60(4), 1986, 369-372.

[194] M. Querry, Optical Constants, *Contractor Report, US Army Chemical Research, Development and Engineering Center (CRDC)*, 418, 1985.

[195] K. Tang, P.A. Kawka, R.O. Buckius, Geometric optics applied to rough surfaces coated with an absorbing thin film, *Journal of Thermophysics and Heat Transfer*, 13(2), 1999, 169-176.

[196] Q. Zhu, H. Lee, Z. Zhang, Validity of hybrid models for the bidirectional reflectance of coated rough surfaces, *Journal of thermophysics and heat transfer*, 19(4), 2005, 548-557.

[197] M.K. Gunde, B. Aleksandrov, Infrared optical constants and roughness factor functions determination: the HTHRTR method, *Applied Optics*, 30(22), 1991, 3186-3196.

[198] K. Tsuji, T. Yamada, T. Utaka, K. Hirokawa, The effects of surface roughness on the angle-dependent total-reflection x-ray fluorescence of ultrathin films, *Journal of Applied Physics*, 78(2), 1995, 969-973.

[199] J. Pawlikowski, Determination of the absorption coefficient of a real semiconductor film: application to ZnSe, *Thin Solid Films*, 125(3-4), 1985, 213-220.

[200] H. Lee, B.J. Lee, Modeling the radiative properties of semitransparent wafers with rough surfaces and thin-film coatings, *J. Quant. Spectrosc. Radiat. Transf.*, 93, 2005, 185-194.

[201] H. Lee, Z. Zhang, Measurement and modeling of the bidirectional reflectance of SiO_2 coated Si surfaces, *International Journal of Thermophysics*, 27(3), 2006, 820-839.

[202] J. Qiu, Y. Ting Wu, Z. Huang, P.F. Hsu, L.H. Liu, H.C. Zhou, A hybrid partial coherence and geometry optics model of radiative property on coated rough surfaces, *Journal of heat transfer*, 135(9), 2013, 091503.

[203] K. Lin, M. Pourmajidian, F.K. Suleiman, J.R. McDermid, K.J. Daun, Effect of annealing atmosphere and steel alloy composition on oxide formation and radiative properties of advanced high strength steel strip, *Metallurgical and Materials Transactions B*, 2021.

[204] H.J. He, L.X. Guo, W. Liu, An efficient hybrid method for 3D scattering from inhomogeneous object buried beneath a dielectric randomly rough surface, *International Journal of Antennas and Propagation*, 2017.

[205] H.J. He, L.X. Guo, Efficient hybrid method for electromagnetic scattering from a coated object above a two-layered rough surface, *Applied Optics*, 57(25), 2018, 7102-7108.

[206] N. Engheta, W.D. Murphy, V. Rokhlin, M.S. Vassiliou, The fast multipole method (FMM) for electromagnetic scattering problems, *IEEE Transactions on Antennas and Propagation*, 40(6), 1992, 634-641.